Editorial Office
Department of Science and Technology
Hanoi Architectural University
Km10, Nguyen Trai Road, Thanh Xuan Dist, Hanoi
Tel: 024 3854 2521
Email: tapchikientruchn@gmail.com

Publishing license No. 268/GP-BTTTT on 27.5.2022
by Ministry of Information and Communications
Graphic design and Desktop Publishing
at Department of Science and Technology,
Hanoi Architectural University
Print at INVESCO., JSC

Contents

Number 46/2022 - Science Journal of Architecture & Construction



Khoa học và công nghệ

4 The relationship among technology, equipment and space organization in designing hospital architecture
Pham Trong Thuat

8 Sound barrier wall to reduce traffic noises in Vietnam
Nguyen Tuan Anh

15 Limit and shakedown analysis of kirchhoff-love plates under uncertainty of strength
Tran Ngoc Trinh

18 Workability analysis of lightweight aggregate concrete mixture use air entrainment admixture
Nguyen Duy Hieu, Truong Thi Kim Xuan

23 The effect of aging and slurry density on triaxial shear properties of liquefied stabilized soil mixed with fiber material cured at the indoor and in-situ
Hung Khac Le, Yukihiro Kohata

28 Strength reduction of mudstone embankment due to change in water content
Tetsuo Abe, Yuki Hashimoto, Nobuo Mishima, Shima Kawamura

31 One-dimensional compressibility and shrinkage behavior of an initially saturated clay
Manh Cuong Le, Diethard König, Yukang Wang and Gunnar Heibrock

35 Prediction of bearing capacity of shallow strip foundation: a case study in Binh Dinh-Vietnam
Thi Khanh Ngan Nguyen and Tuan Thanh Tran

39 Development of static P-Y curves from experimental measurements based on lateral load tests on onshore drilled shafts
Minh D. Uong and J. Erik Loehr

45 Application of mixed reality technology in geotechnical industry
Nguyen Thi Thao Van, Yasuo Miyagi and Junichiro Odaka

49 Experimental and numerical investigation of the fire performance of densified spruce wood
Tran Trong Tuan

54 Yielding novel k-factor formula according to the aisc standard by machine learning
Nguyen Thanh Tung

59 Application of convolutional neural network for detecting concrete cracks
Tu T. Nguyen, Hiep H. Vu and Kien T. Doan

63 Finite element modeling of reinforced concrete shear wall subjected to static loading
Khiem Van Giang, Hien Manh Nghiem and Chuong Tien Nguyen

67 Estimating the face-to-face reinforcement ratio of short rectangular reinforced concrete columns based on two uniaxial bendings separately
Vu Huy Hoang

73 Study on a novel exterior RCS hybird joint by ABAQUS
Nguyen Viet Phuong

79 Real situation and solutions for solid waste management in Tien Yen district (Quang Ninh province)
Bui Thi Ngoc Lan

84 Road development reality in Dienbien province, Vietnam
Nguyen Cong Giang, Bui Thi Ngoc Lan

92 Cultural heritage conservation and sustainable development - Case study of Tien Yen, Quang Ninh, Vietnam
Ngo Thi Kim Dung

97 Kinetic ofammonium removal by anammox rocessusingbiomass carrier felibendy
Nguyen Thi My Hanh, Tran Thi Hien Hoa

The relationship among technology, equipment and space organization in designing hospital architecture

Pham Trong Thuat

Abstract

Technology advancement directly affects the way of providing medical services, in terms of both management and architecture facilities, namely space organization. The trend of hospital architecture now is heavily influenced by technological revolutions of medical equipment, mostly in terms of changing machinery size, and consequently providing more efficiency and less requirement of space. The emergence of new technology and the import of medical machinery and equipment actively accelerate these changes.

The role of management and the capability to examine and provide medical care is reflected in the availability of advanced diagnostic and treatment equipment, integrated with information technology systems to transmit data and images. This article focuses on analyzing the effects of science and technology, the digital revolution, and medical equipment on space organization for providing medical services in modern hospitals.

Key words: *Hospital Architecture; designing hospital; medical technology; hospital IT system; medical equipment*

Assoc. Prof. Arch. Pham Trong Thuat
Hanoi University of Architecture
Phone: +84.903.442.174.
Email: thuat@hau.edu.vn

Date of receipt: 17/9/2022
Editing date: 03/10/2022
Post approval date: 05/10/2022

1. Introduction

According to the World Health Organization (WHO), a hospital is a part of a medical and social organization whose function is to ensure that people receive comprehensive medical care, both curative and preventative care. The hospital's outpatient work extends to the family in its environment. The hospital is also a center for medical teaching and sociobiological research[10]. By this definition, the hospital is not only a health care provider, but the hospital assumes a range of functions and harmoniously links health care to society. This new concept changes the mission, functions, organizational structure, and method of hospital management.

With the rapid development of science and technology, medical imaging technology creates multiple advanced medical equipment, including diagnosis and treatment equipment. Modern technologies are invented regularly and continuously every year – it is completely changing many healthcare methods, and also significantly affecting organizational principles such as the architecture of space for examination and treatment.

2. Hospital information system with healthcare communication

Through the digital transformation process, hypothetical/test situations are considered as input data to create response scenarios; and via the virtual reality system, the interaction between hypothetical situations and the medical tasks of robots is established. Functional probe devices which are capable to check the function of the patient's body such as electroencephalogram, electrocardiogram, respiratory, diagnostic-oriented devices, endoscopes, etc.

Figure 1. New North Hospital – New Zealand[4]

Figure 2. Helsingborg Schmidt Hammer Lassen Hospital – Sweden[3]

are connected to a central processing unit to offer optimal treatment options and provide doctors with full analysis to evaluate and choose the best capable treatment.

Technology advancements in medical fields in recent years are also provided tools to collect, search, store, transmit, retrieve, query, and ensure the privacy of each medical record, in the field of medical examination, treatment, and health care. These data also support doctors to forecast and analyze the patient's disease stages to find correlations with the disease patterns. Hospital information systems bring many benefits to medicine, most notably assisting to store and analyze data for medical research, remote medical support, and helping doctors to make clinical decisions.

For example, the Mayo Clinic Foundation in Phoenix, Arizona, USA, is remotely connected to a hospital that is located 12 miles away for access to information, data, and patient monitoring.

Middlemore Hospital in Auckland, New Zealand builds a network of outpatient clinics with telecommunications systems. The first trial of its kind in New Zealand enables outpatient clinic centers to transmit diagnostic images to radiologists working at Middlemore Hospital for consultation. [2]

In Georgia, USA, a project to connect 55 small cities and their rural hospitals with major medical centers is implemented to create opportunities for examination and consultation among local specialists, patients, and hospital doctors.

In Finland, the University of Helsinki is connected with hospitals scattered throughout the territory to integrate their mobile institutions of C.T. (computed tomography) and M.N.R. (nuclear magnetic resonance), so that they can effectively respond to the problem of emergency magnetic resonance testing in the field of nerve trauma. [3]

In Italy, an interesting initiative of adopting orthopedic telephone consultations is being launched since 1996 at the Istituto Rizzoli of Milano [4]. This initiative offers patients who reside in the southern regions of Italy and are required to have a first visit to the hospitality can have the pre-consultation through postal services. This consultation is also extended to outpatients and programmed control after-surgery patients.

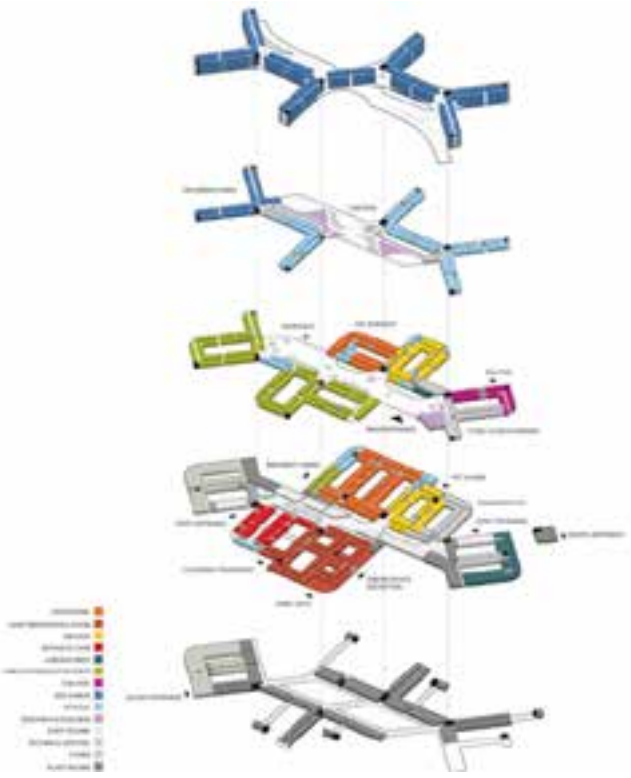

Figure 3. The diagram of the hospital function chain Lynd Park– Germany[3]

In Vietnam, TeleHealth technology allows Hanoi Medical University Hospital to provide remote medical examination and treatment to a range of hospitals across the country. Medical consultation sessions are also held between Hospital 199 and Hanoi Medical University Hospital with the participation of doctors at the two hospitals, resulting in optimal efficiency of treatment.

In Thua Thien Hue province, the Department of Health applies GIS to perform remote medical examinations and treatment. Hospitals in the province create and manage health records online, and as a result, most people in the area are now registered with electronic medical records.[6]

Information technology supports connecting local medical centers with central specialized hospitals in primary medical examination and treatment, and to raise community awareness in disease prevention. Additionally, the media serves a critical role in guiding and propagandizing information about disease control and prevention, consequently reducing the number of patients required to visit the hospital.

Medical equipment

The rapid advancements of technology in medical equipment assist hospital architectural design standards seamlessly keep to pace with such medical changing development.

Figure 4. Surgery preparation room - Johns Hopkins University Hospital- Maryland- USA[1]

- Equipment for emergency resuscitation: in addition to common emergency equipment such as monitor multi-parameter emergency beds, and surgical instruments, hospitals are also equipped with specialized equipment classified by emergency specialties, such as Respiratory Resuscitation, Cardiovascular Resuscitation, Urological Resuscitation, Gastrointestinal Resuscitation, Toxic Resuscitation, and Intensive Care Unit (ICU).

- Equipment of the operating room is renovated with modern equipment because the operating room is the center of focus where high technology and medical techniques are developed for medical intervention and treatment. Therefore, the working space in the operating room must be comfortable and not interfere with the operation of the surgery. Other microclimate environmental conditions in the operating room (for example clean water, sterile, cold light, high illuminance, cool, clean temperature, air) are continuously circulated and at higher pressure (++) compared to the surrounding, but the noise level must be at the allowable level; and transfusion, blood, medical gas, and necessary consumables must be ready all the time.[7]

- Functional probe devices: many new types of equipment that support easily checking the ability of body functions are available, such as electroencephalogram, electrocardiogram, and spirometer, especially with diagnostic equipment, endoscopic equipment…

Equipment for emergency resuscitation: in addition to the usual emergency equipment such as monitor multi-parameter emergency beds, and surgical instruments, hospitals are equipped with specialized equipment classified by emergency specialties, such as Resuscitation,Cardiovascular Resuscitation, Urological Resuscitation, Gastrointestinal Resuscitation, Toxic Resuscitation, and Intensive Care Unit (ICU).[8]

4. New requirements in hospital design adapting to technology and medical equipment

- Instead of visiting hospitals to take a medical test or examination, patients can take medical samples at various functional departments at different locations. Further, the deployment of telehealth by applying info-communication technologies changes the way of medical examination and treatment. Moreover, designs of the medical examination lines require architects to arrange spaces for patients in a convenient location, so that medical staff can access the patients for conducting operations and the patients do not have to move. This is the core point of view that asks architectural design to change to better satisfy new needs of examination and treatment when information technology and diagnostic technology are changing.

- The core health providers, who should be developed as community hospitals, offer a new perspective on primary treatment. Specifically, these community hospitals provide short-term examination and treatment; deliver re-examination and follow-up patients who completed emergency procedures at major hospitals. With the support of Telehealth, it is possible to maintain an optimal number of doctors who are capable of providing basic healthcare, monitoring the health of patients with special medical needs, and supervising elderly patients or those who require intensive care.

- Solution to divide space: Currently, most hospitals are designed to divide space based on rigid modules. This type of division is less flexible and creates a lot of spread spaces in large sizes without a high frequency of use. With modern medical equipment, medical machinery and equipment are integrated with many functions, making spaces for departments such as general examination, ultrasound, preparation, auxiliary procedures, and auxiliary tests convenient. Functions are "borrowed" among these departments from time to time to maximize the efficiency of the working area. The removal of most of the hard partitions such as brick walls and concrete walls reduces the workload, lowers construction costs, and minimizes the infiltration of water and polluting chemicals over time.

- With the help of telemedicine consultation, online patient classification will significantly reduce the area of outpatient examination and treatment areas. Patients who are screened before coming to the hospital need to be

Figure 5. The modern equipment in the operating room. Medical equipment for neurosurgery[2]

Figure 6. Novant Clemmons Extensive Clinic Transitional care clinic helps to stabilize patients before returning home[8]

designed with an appropriate approach to reduce clutter in the clinic and outpatient treatment.

- The application of information technology in the management and administration of the medical examination and treatment process also reduces the excess movement of patients and their family members, and medical staff will be able to optimize the common areas.

- The height requirements in operating, testing, and scanning rooms need to be updated according to the requirements of medical machinery and equipment. Hospital architecture design also needs to make efforts to optimize power use through the application of energy-saving solutions and devices (automation, smart management, integrated heat recovery air conditioners, led lights, etc.). Architectural and landscape design solutions ensure thermal balance and natural air convection (such as narrow slit ventilation, corridor ventilation, facades with active radiation control, hybrid covering materials, indoor plants, and vertical gardens). These views in architectural design contribute to maximizing the use of clean energy sources (solar energy, wind energy, heat recovery ... for hot water supply and navigation equipment, and passenger lighting corridor, and basement).

5. Conclusion

Technology and equipment create requirements for fundamental changes in hospital architectural design. Hospital architecture has a critical role in creating space to meet the needs of implementing and applying new medical examinations, treatment processes, and technologies in the hospital. Therefore, shortly hospital design work needs to take important breakthroughs and major changes, reflecting and selectively absorbing major changes in modern technology and equipment. A hospital that performs well in healthcare needs to have the right architectural design, the right technology line design, and the right medical equipment./.

References

1. *American Society of Anesthsiologists (2013), Operating Room Design Manual, http://asahq.org.*
2. *ASHE Seattle Annual Conference (2011), Equipment for Smart Hospitals. Seattle.*
3. *Christine Nickl-Weller, Hans Nickl (Eds.) (2007), Hospital Architecture, Verlagshaus Braun, Deutsche.*
4. *Francesca Giofrè, (2005), Hospital Architecture and the Digital Revolution, Italia*
5. *Ministry of Construction (2012), Vietnamese design TCVN 4470:2012, Design standards for general hospitals*
6. *Nguyễn Thanh Tùng (2012), IT system in hospital, 1. University of Science and Technology, Vietnam National University, Ho Chi Minh City.*
7. *Nguyễn Trọng Quỳnh (2012), Hospital architecture with impact factors, Vietnam Architecture Magazine.*
8. *The American Institute of Architects (A1A), The Facility Guidelines Institute (2006). Guidelines for Design and Construction of Hospital and Health Care Facilities, USA.*
9. *Ulrich. R.S. (2000), Effects of Healthcare Environmental Design on Medical Outcomes. Design & Health -The therapeutic benefits of design. proceedings of the 2nd Annual International Congress on Design and Health. Karolinska Institute. Stockholm.*
10. *WHO (2004), Practical guidelines for infection control in health care facilities.*

Sound barrier wall to reduce traffic noises in Vietnam

Nguyen Tuan Anh

Abstract

This paper presents the applying of sound barrier wall for highways in Viet Nam studied from existing experiments in the world. Nowadays, pollution sources come from traffic noises, water sources and air environment. Especially, traffic noises such as transportations, trains and airplanes are much serious and effect population and country. On road traffic systems, noise generated by vehicles is always in high level and give discomfort to residents who live around both sides of highways. In the world, noise barrier walls are being built along the highway to minimize impact of traffic noise to the surrounding environment. However, such solution has not been properly considered in Viet Nam yet.This paper deals with sound transmission mechanism in roads as well as experiences of countries around the world in building the noise barrier system along highways, contributing to ensure the best urban comfort for the surrounding environment and create a friendly traffic landscape.

Key words: *Noise source; sound transmission; sound barrier wall; noise pollution; highway; urban comfort; traffic landscape*

1. Introduction

Sounds are a natural phenomenon that manifests the diversity of the living environment, a transmission of information to living entities through the absorption of the sound of the human ears. Sounds in the environment are quite various and originated from any activity that creates a sound source. Especially in the urban environment, the sources of soundsare mainly from human voices, from urban activities and particularly from the operation of transportation means. For urban traffic, due to the low motor vehicle speed, generally noise sources generated from the friction between tires and the road surface and noises from small engines do not much impact to the urban environment. However, in Viet Nam and particularly in urban areas, the greatest source of noise pollution is the horn of cars and motorbikes. In the context of this article, we briefly introduce noise level in urban areas in order to understand and evaluate greater noise level on the highways system in Viet Nam (including the ring roads system around the large cities with motor vehicle speed above 80km/h). We also analyze experiences of using noise barriers to prevent traffic noise in the world for proposing solutions to reduce traffic noise on the highways in Viet Nam.

2. Sound environment

2.1. Urban sound environments

The sound environment is a concept proposed by R.M. Schafer[1], a Canadian musician who describes the sound environment by synthesizing all of the sound sources in the environment. Most of these sources are negative for the environment, such as sound from road friction, from car horns, from motorbike noise and from trains… We can approach the sound environment as Kevin Lynch describes in his work "L'image de la cité" [2].

Talking about noise in urban areas, we should analyze its three basic elements that are closely related to each others, those are:

- Sound sources;
- Urban space; and
- Urban residents.

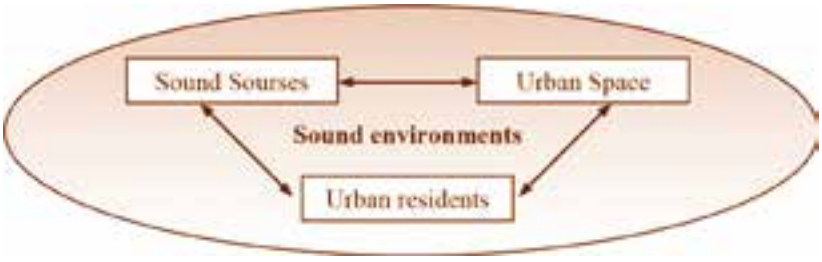

Figure 1: The organic relationship among noice elements in cities

Figure 2: The role of the acoustic channel between the sound source and the sound acquisition

Assoc. Prof. Nguyen Tuan Anh
Hanoi Architectural University
Email: tuananh310866@gmail.com

Date of receipt: 17/9/2022
Editing date: 03/10/2022
Post approval date: 05/10/2022

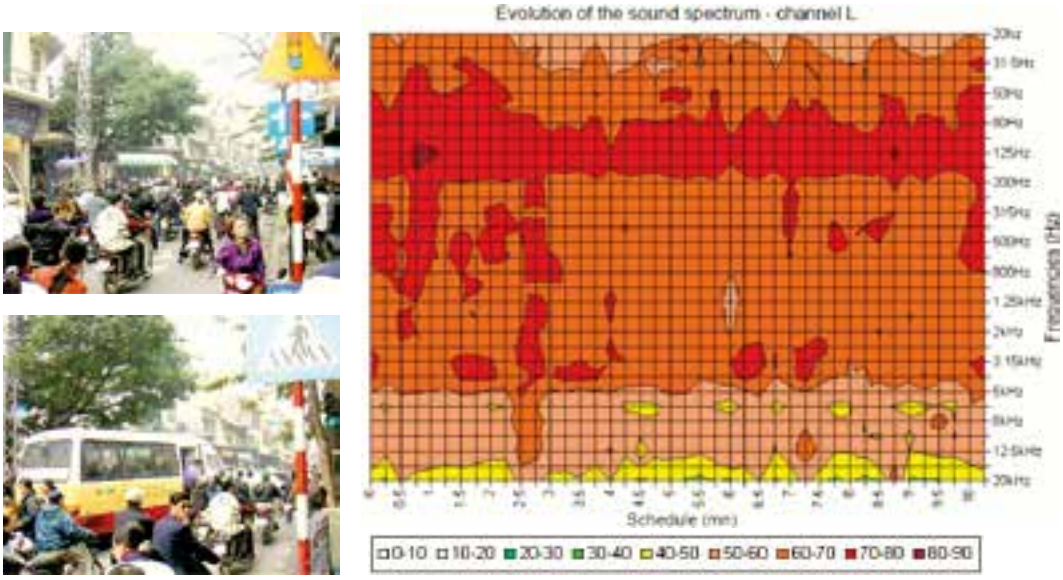

Figure 3: Spectral images in Ha Noi Down-town Area

These elements are introduced in the following diagram:

These three elements are relevant to various research fields; they explain the complexity of aggregated phenomena. To describe more accurately about the urban sound environment, we can combine each of these elements with a phenomenon that creates an organic link below:

In this diagram, we can obviously realize the important role of researching the acoustic channel in urban space. In fact, the elements illustrated in Figure 2 determine sound aquisitions that the sound environment will be received.

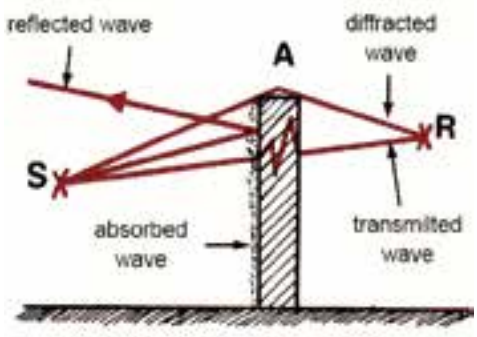

S: Sound Source; R: Virtual sound source

Figure 4: Sound transmission when facing barriers

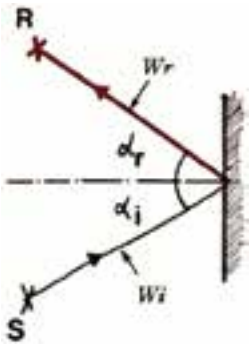

S: Sound Source

Figure 5: Reflective phenomena

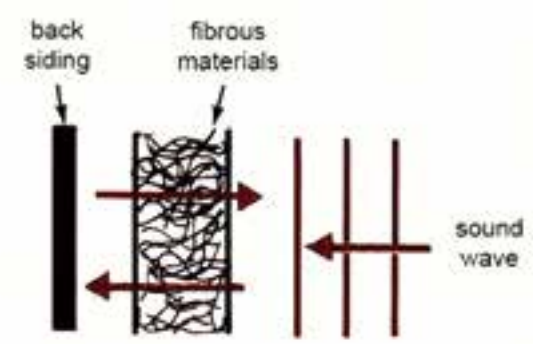

Sound waves lose energy when transmitting through fiber material by absorbing sound

Figure 6: Exemple for sound absorption phenomena

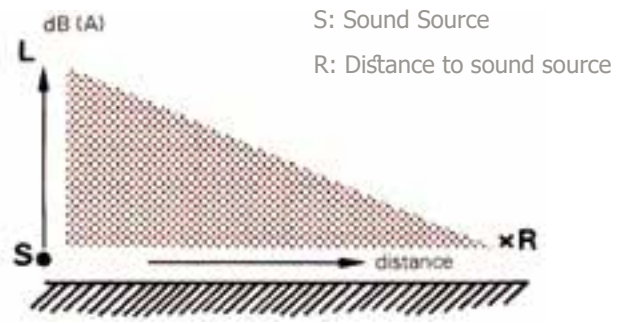

S: Sound Source

R: Distance to sound source

Sound level decreases when distance increases from the sound source S

Figure 7: Sound level depends on distance

2.2. Sound level in Ha Noi Down-town Area

Sound level in Ha Noi Down-town area is a combination of sound levels emitted from various sound sources: from people, from urban activities and especially from the means of transportation. Ha Noi is the capital of Viet Nam, then the transportation system is subjected to high pressure from high traffic. The diversity of transportation meanscauses to frequent traffic congestion, and consequently causes negative urban noise level. In Ha Noi Down-town area, the common sound level is from 70-90dB, in which the highest

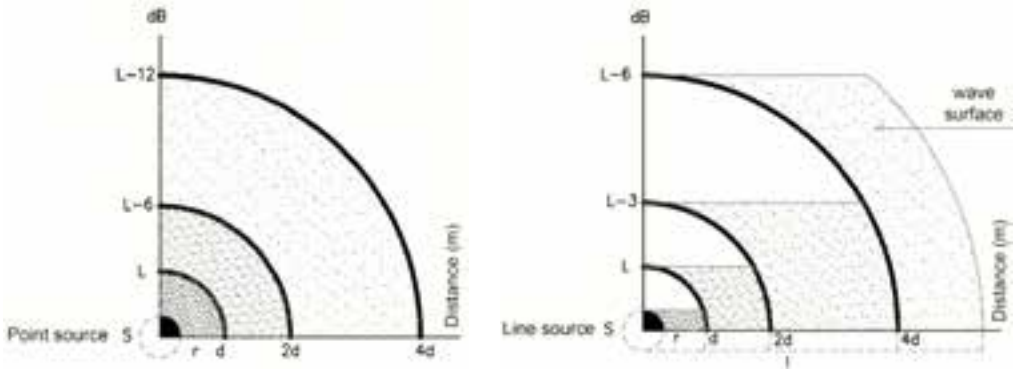

Point sound source Linear sound source

Figure 8: Sound level depends distance to the point sound source and linear sound source

sound level is derived from the horns of cars and motorbikes [3] [4].

The image of the sound spectrum in the Ha Noi Downtown area (the typical area of the sound environment in Ha Noi metropolis) shows that the noise level is quite loud and constant (effect at the frequency of 20Hz - 5kHz with a sound level of 60-80dB.) This causes to constant stressed and discomfortable state for human beings.The sound level in the center of Hanoi as in the example above is a measure of the high sound level on the highways system

3. Sound transmission in the air

Sound transmission in the air is characterized by the nature of the relationship between the sound sources and the air environment, as well as the shielding of the transmision path of the sound waves[5].

3.1. Sound transmission when facing barriers

When facing barriers during the transmission, sound energy is divided into four parts: reflexion, absorption, transmission and diffraction. Each part represents a different physical characteristic as shown in the Figure 4 below:

*Sound reflection:

If a sound wave faces an object during its transmission, it can reflect as a way that light reflects through a mirror. In acoustics, we apply the principles as in optics.

* Sound absorption:

When a sound wave faces a barrier, sound energy may be reduced by sound absorption capability of that barrier.

* Sound transmission:

We hear sound through a barrier means that the sound has been transmitting through this barrier. Or, more precisely, the sound is partially reflected, partially absorbed by the material of the barrier and partially penetrated by the barrier and passed to the ears of the listeners.

3.2. Free sound transmission with no barrier

Free sound transmission with no barrier is a common

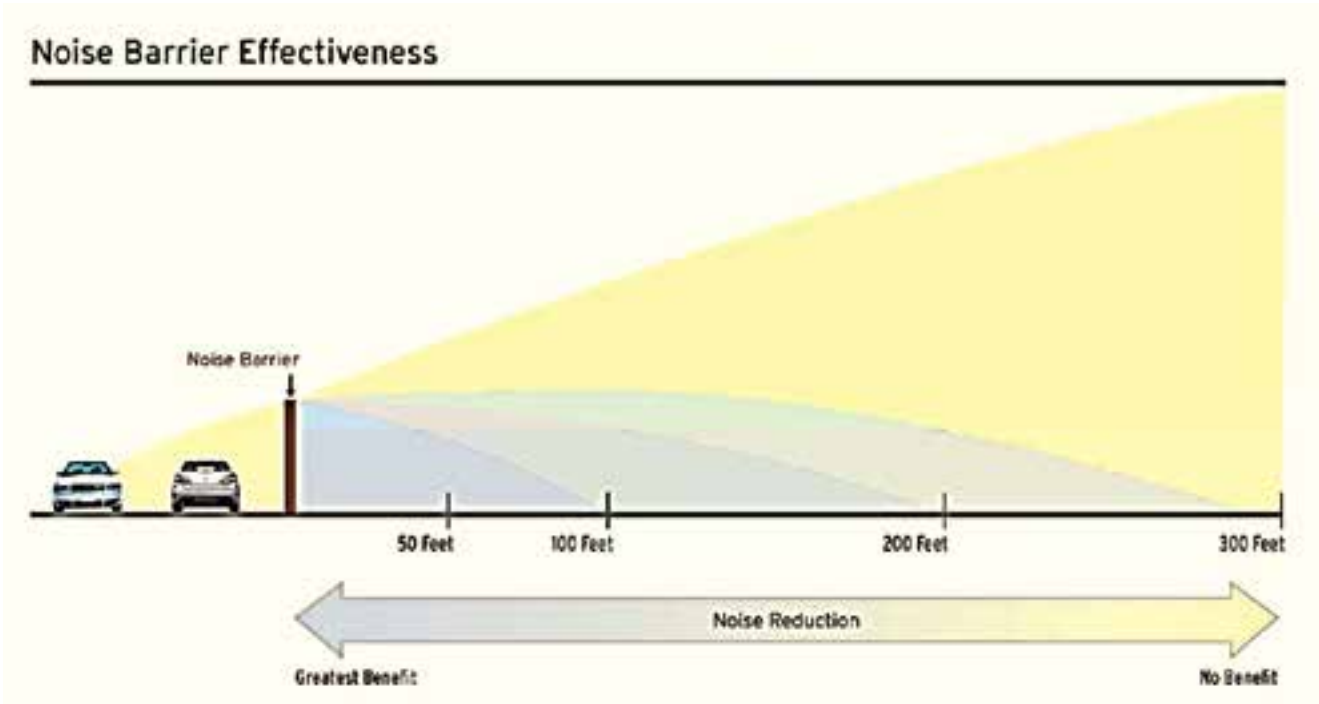

Figure 9: The spread of traffic noise level after sound barrier wall

transmission in the environment. Sound level decreases when the sound source is further away. In free of barrier environment, sound is being transmitted from the sound source, spreads to surrounding space, and shuts off until the energy is negative. In this paper, we would like to analyze the phenomenon of sound transmission in air freely without clarifying the physical nature of the sound transmission.

3.3. Free sound transmission faces barrier on the transmission line

As mentioned above, when the sound source emits sound to the surrounding environment, the sound level decreases when the sound source is distant. Point sound source attached to fixed sound source. The sound source emitted by the road traffic (also known as the linear sound source) creates a sound line along the road [6].

Thus, the phenomenon of sound transmission on the road will form a stream of sound transmitted to both sides. Therefore, when facing a sound barrier wall, the sound level will be significantly reduced for the two sides of the road.

4. Highwaysand Sound barrier wall solutions in the world

Countries in the world have being used various solutions to reduce noise from traffic such as creating sound barrier walls made from concrete, wood, glass, aluminum or building mud dikes. These solutions minimize traffic noise to ensure the best comfort for the areas along the roads. Sound barrier walls have been building both on highways,ring highways and highways from the outerto city centers. This is an effective solution to reduce traffic noise, as well as a decorative solution to creating landscape architecture on the roads. Each country has different solutions to build sound barrier walls, but all aim to reduce traffic noise to ensure sustainable environmental development.

* InJapan: Japan is very interested the sound environment on the transportation system. The sound barrier walls built by glass have significantly reduced noise and created urban landscapeaesthetic.

* In Hungary: Hungary builds wooden sound barrier walls to increase sound absorption and fit with the surrounding terrains.

* In Russia: Mud dikes with grass in

Sound barrier

Arts creativity

Figure10: Sound barrier walls in Korea

Figure 11: Sound barrier walls in Japan

Figure12: Sound barrier walls in Hungary

Figure13: Sound barrier walls in Moscow - Russia

Figure14: Sound barrier walls in Paris - France


Figure 15: Sound barrier walls in Czech


Figure 16: Sound barrier walls in the U.S


Figure 17: Sound barrier walls in Vancouver, Canada

The Highway System in Viet Nam consists of 31 highways with a total length of 6410 km

1. North-South Highways:

   - 02 highways with are 3083 km long

2. Highway system in the North:

   - 14 highways with 1368 km long

3. Highways system in the Central and Highlands:

   - 03 highways with 264 km long

4. Highways system in the South:

   - 7 highways with 983 km long

5. Highways ring road system in Ha Noi and Ho Chi Minh city:

   - HaNoi: Ring highways No.3, 4 and 5 with 425 km long

   - Ho Chi Minh: Ring highways No. 3 and 4 with 287 km long

Figure 18: Master-plan of the highway system in Viet Nam to 2030


Figure 19: Highway Ha Noi-Hai Phong-Ha Long


Figure 20: Highways Ha Noi - Ninh Binh (Cao Bo - Mai Son)


Figure 21: Highway Ha Noi - Thai Nguyen


Figure 22: Highway Đa Nang-Quang Ngai


Figure 23: Highway Ha Noi-Hai Phong-Ha Long

Moscow are built to prevent and absorb sounds. This solution can prevent noise levels quite well. However, this solution requires large are for the walls construction and does not harmonize with the urban landscape.

* In France: Sound barrier walls in Paris are built from concrete with art-shapes to reduce the heavy and monotonous scenes. The solutions are being used depend on the terrains and surrounding spaces.

* In Czech: sound barrier wallshave both functions; those are preventing negative noise and creating art-scenes to the urban landscape.

* In the United States: the U.S. is one of the countries has the largest highway system. The pace of economic development is fast and the demand for road traffic is high, so that many highways in the U.S. run through many residential areas. Therefore, minimizing noise levels from road traffic is a strict requirement in the U.S.

* In Canada: the Canada is one only of the countries has the largest highway system.The city of Vancouver has a special geographical position, so the north-south highway runs through many residential areas. Therefore, a sound barrier solution has been designed along the route.

5. Sound barrier walls on highways in Việt Nam

The Master-plan for highways system in Viet Nam toward 2020 and 2030 shows that Viet Nam will have 31 highways spread across the country [7]. This highway-system creates as important backbone for road traffic in Viet Nam. This system also forms continuous connections with other transportation systems. Each region in Viet Nam will construct its highway-system based on the Master-plan and available financial resources.

5.1. Highways in Viet Nam

The highway system in Viet Nam is built by either renovating, expanding the old ones or constructing new highways. For that reason, many highways are still running through various residential areas. Particularly, the ring-highway-systems in the two largest cities, Ha Noi and Ho Chi Minh, are all run through residential areas and seriously impact to the surrounding environment.

Many highways in Viet Nam have been or are being constructed under the master-plan of the national highway system in order to promote economic development, though the construction also creates challenges for the environment around the roads.

The East Highway Hanoi - Ho Chi Minh City (1nd highway) is being implemented with many sections already in use (Ha Noi-Cau Gie-Cao Bo-Mai Son).

The new highway construction of the road and surrounding infrastructure has been putting into operation to satisfy traffic demand. However, there is almost no evaluation on the impact of traffic noise to the surrounding environment and solutions to reduce noise from traffic are undertaken.

5.2. Sound barrier walls in highways in Viet Nam

Sound barrier walls are contructed in some roads only in Viet Nam due to difficulties in mobilizing financial resources. The number and length of sound barrier walls is too small in comparison to the length of the highways and the status of residential areas surrounding the roads.

Currently, some highways have speeds up to 120 km/h such as Ha Noi - Hai Phong - Ha Long, Ha Noi - Lao Cai and Phap Van - Cau Gie, cause tohigh noise level to surrounding areas. On the other hand, since there are many residential areas along the routes so in the near future, when the traffic increases,negative noise will be more serious. It requires carrying out necessary surveys and constructing sound barrier wall systems to reduce noice level affects to the population along the roads.

5.3. The ring highways in Ha Noi city

Ring-highway-system in Ha Noi runs through many residential areas in the city. The distance from the residential area to the road is too short, causes to serious pollution level. The lack of soundproofing solutions from the traffic to the residential area causes negative feelings to the residents; and high traffic and congestions on the roads destroys hamorniztion of the urban landscape.

The 2nd route ring is also under construction and is the closest road in centre of Hanoi.

Some roads which connect between the city center and the suburbs have been improved in terms of environmental landscapes but no solutions to reduce traffic noise are being employed. In the near future, when the constructionsalong the road Vo Nguyen Giap is finished as planned, noise pollution will become more serious.

6. Conclusion

The diversity of sound environment brings flavor to our life but also brings several negative affect. In particular, traffic noise is a source of pollution and cause discomfortability to environment and human beings. Applying different solutions to minimizing noise pollution, such as constructing sound barrier walls in roadsides is a popular and effective solution in the world. Viet Nam is constructing and renovating the highway system, but does not yet carefully to create sound barrier walls along the road to reduce noise pollution. It therefore is a requirement to urban-planners, architecturers and constructors in Viet Nam to understand the modes of sound transmission;analyze noise level causes from urban transportation and learn experiencesfrom countries in the world in building sound barrier walls with the aim at bringing a more comfortable living environment to Viet Nam./.


Figure 24: Highways Ha Noi-Lao Cai và Phap Van - Cau Gie


Figure 25: 3nd highway ring to Thanh Tribrige and to Thang Long brige in Ha Noi


Figure 26: 2nd route ring to Nga Tu Vong and Nga Tu So in Ha Noi


Figure 27: HighwayVo Nguyen Giap connects between Hanoi Center and Noi Bai Airport

References

1. *SCHAFER. R. M, Le paysage sonore, Ed. J-C.Lattès, Paris, 1979.*
2. *LYNCH. K., L'image de la Cité, Dunod, Paris, 1999.*
3. *NGUYEN. T. A., C. SEMIDOR, Relationship between urban activities and soundscape: commercial areas in Bordeaux and Hanoi, 23th PLEA, Geneva, Switzerland, 6-8 September 2006.*
4. *NGUYEN. T. A, Comparison of soundscape on the ground floor of tube house in Hanoi and open urban space in Bordeaux, 23th PLEA, Geneva, Switzerland, 6-8 September 2006.*
5. *BAR. P et al, Bruit et Formes Urbaines: propagation du bruit routier dans les tissus urbains, Centre d'Etude des Transports Urbains, Paris, 1981.*
6. *NGUYEN. T. A, Caractérisations des particularités dominantes de la morphologie urbaine à travers l'environnement sonore: Etude dans le vieux quartier de HaNoi et dans le quartier Saint-Michel à Bordeaux, PhD, University of Bordeaux I, France, 2007.*
7. *[7]The Prime Minister, Approving the planning on development of Vietnam's highway networkup to2020 and orienting to 2030, Decision No 326/QĐ-TTg, 2016.*

Limit and shakedown analysis of kirchhoff-love plates under uncertainty of strength

Tran Ngoc Trinh

Abstract

A new formulation to calculate the shakedown limit load of Kirchhoff plates under stochastic conditions of strength is developed. Direct structural reliability design by chance constrained programming is based on the prescribed failure probabilities, which is an effective approach of stochastic programming if it can be formulated as an equivalent deterministic optimization problem.

We restrict uncertainty to strength, the loading is still deterministic. A new formulation is derived in case of random strength with lognormal distribution. Upper bound and lower bound shakedown load factors are calculated simultaneously by a dual algorithm.

Key words: *Kirchhoff Plate, Limit Analysis, Shakedown Analysis, Primal Dual Programming, Stochastic Programming, Chance Constrained Programming*

Tran Ngoc Trinh
PhD, Lecturer, Faculty of Civil Engineering, Hanoi Architectural University
Email: <trinhdhkt@gmail.com>

Date of receipt: 24/03/2022
Editing date: 14/04/2022
Post approval date: 5/9/2022

1. Introduction

Plates are very important structural elements, that are widely used in civil and mechanical engineering. The common examples of plates are slabs in civil engineering structures, bearing plate under columns, many parts of mechanical components. In this paper, we consider bending of such plates subjected to lateral loads. The bending stiffness of a plate depends on the cube of its thickness. The classical theory divides plates into following groups: thin plates with small deflection, thin plates with large deflections, and thick plates.

The thin plate assumptions on which A.E.H. Love based his plate theory were proposed by Gustav R. Kirchhoff [1]. Consequently, thin plates with small deflections theory are called Kirchhoff-Love plate or Kirchhoff plate for short. This theory is suitable for plates with length of span at least 10 times the thickness. Many engineering problems lie in the above category and satisfactory results are obtained by the classical thin plates theory.

Limit analysis of plates in bending has been studied analytically and numerically [8]–[16]. Due to limitations of analytical methods, alternative numerical approaches such as finite element methods (FEM), meshfree methods or isogeometric analysis (IGA) have been developed.

Limit and shakedown analysis state problems as a mathematical programming. If the strength of a plate is a random variable, we may consider the problems as a stochastic programming problem. Many models of stochastic programming have been proposed such as approximate polyhedral dynamic programming [16-18], measurement-based optimization [19], worst-case and distributional robustness analysis [20], Cost horizons and certainty equivalence [21] and chance constrained optimization (CCOPT) [22]. In this paper the CCOPT approach is used to treat the problem of shakedown analysis of plate under uncertainty condition of strength. If the thickness deterministic and the yield stress is distributed normally or lognormaly a deterministic equivalent formulation can be derived which allows a most effective numerical solution for prescribed reliability of the structure.

2. Static approach with chance constrained programming

Consider a convex polyhedral load domain D and a special loading path consisting of all load vertices $\hat{P}_k (k = 1,...,m)$ of $\mathcal{L}$. The total moment $\mathbf{m}(\mathbf{x},t)$ at a point $\mathbf{x} \in \Omega$ of the considered plate at time t is decomposed into an elastic reference moment $\mathbf{m}^E(\mathbf{x},t)$ and a residual moment $\boldsymbol{\rho}(\mathrm{x},t)$. Here, $\mathbf{m}^E(\mathbf{x},t)$ denotes the fictitious moment that would appear in a purely elastic reference structure $\mathcal{P}^E$ under the same loading conditions as the original structure, and $\boldsymbol{\rho}(\mathrm{x},t)$ represents a residual moment field that is induced by the evolution of plastic strains

$$\mathbf{m}(\mathbf{x},t) = \mathbf{m}^E(\mathbf{x},t) + \boldsymbol{\rho}(\mathbf{x},t) \quad (2.1)$$

According to Melan's static shakedown theorem the structure will shakedown, if there exists a time-independent residual moment field $\bar{\boldsymbol{\rho}}(\mathbf{x})$ such that the yield condition is satisfied for any loading path at any time t and in any point $\mathbf{x}$ of the plate. Based on this lower bound theorem, for a plate made up of elastic perfectly plastic material, the maximum enlarging of the load domain allowing still for shakedown, characterized by load factor α^- that can be obtained by solving the following optimization problem (in FEM form)

$$\alpha^{-} = \max \alpha$$
$$\text{s.t.:} \begin{cases} \sum_{i=1}^{NG} w_i \mathbf{B}_i^T \overline{\boldsymbol{\rho}}_i = 0 \\ f(\alpha \mathbf{m}_{ik}^E + \overline{\boldsymbol{\rho}}_i) \le m_0 \quad \forall i = \overline{1, NG} \quad \forall k = \overline{1, m} \end{cases} \quad (2.2)$$

in which $\mathbf{B}_i$ is the deformation matrix, w_i is integration weight at Gauss point i and NG denotes the total number of Gauss points of the structure.

Let us now consider the situation that the plastic moment of the plate is not given but must be modelled $m_0=m_0(\omega)$ a random variable on a certain probability space. Under uncertainty, the inequalities in (2.2) are not always satisfied, the probability of the i^{th} yield condition is required to be satisfied is greater than some reliability level ψ_i. Problem (2.2) becomes a chance constraint stochastic program:

$$\alpha^{-} = \max \alpha$$
$$s.t.: \begin{cases} \sum_{i=1}^{NG} w_i \mathbf{B}_i^T \overline{\boldsymbol{\rho}}_i = \mathbf{0} \qquad \text{in } \Omega \\ \text{Prob}\left[f(\alpha \mathbf{m}_{ik}^E + \overline{\boldsymbol{\rho}}_i) - m_{0i}(\omega) \le 0 \right] \ge \psi_i \\ \qquad \forall i = \overline{1, NG} \quad \forall k = \overline{1, m} \end{cases} \quad 2.3)$$

Let the plastic moment $m_i(\omega)$ be distributed normally with mean μ_i and standard deviation σ_i, in short $m_i(\omega) \sim \mathcal{N}(\mu_i, \sigma_i^2)$. Based on the methodology of chance constrained programming, problem (2.3) can be converted into a equivalent deterministic program as shown in [10,11]:

$$\alpha^{-} = \max \alpha$$
$$\text{s.t.:} \begin{cases} \sum_{i=1}^{NG} w_i \mathbf{B}_i^T \overline{\boldsymbol{\rho}}_i = 0 \qquad \text{in } \Omega \\ f(\alpha \mathbf{m}_{ik}^E + \overline{\boldsymbol{\rho}}_i) \le \mu_i - \kappa \sigma_i \quad \forall i = \overline{1, NG} \quad \forall k = \overline{1, m} \end{cases} \quad (2.4)$$

where $\kappa = \Phi^{-1}(\psi_i)$ is the inverse normal cumulative distribution function (normal quantile function) of the plastic moment at Gauss point i.

Let the plastic moment $m_i(\omega)$ be distributed lognormally. This means that $\ln[m_i(\omega)]$ is distributed normally with mean μ_i and standard deviation σ_i, in short $\ln[m_i(\omega)] \sim \mathcal{N}(\mu_i, \sigma_i^2)$. The stochastic program (2.3) can be relaxed into an equivalent deterministic optimization problem after some transformations [2,3]:

$$\alpha^{-} = \max \alpha$$
$$\text{s.t.:} \begin{cases} \sum_{i=1}^{NG} w_i \mathbf{B}_i^T \overline{\boldsymbol{\rho}}_i = 0 \qquad \text{in } \Omega \\ f(\alpha \mathbf{m}_{ik}^E + \overline{\boldsymbol{\rho}}_i) \le e^{\mu_i - \kappa \sigma_i} \quad \forall i = \overline{1, NG} \quad \forall k = \overline{1, m} \end{cases} \quad (2.5)$$

3. Kinematic approach with chance constrained programming

An upper bound to the shakedown limit of plates can be obtained using the kinematic shakedown theorem. In this investigation, we use von Mises yield criterion.The plastic dissipation power of the plate domain Ω can be written in form of curvature vector χ

$$\dot{D}_{\text{int}}(\dot{\boldsymbol{\chi}}) = m_0 \int_{\Omega} \sqrt{\dot{\boldsymbol{\chi}}^T \mathbf{Q} \dot{\boldsymbol{\chi}}} \, \mathrm{d}\Omega \quad (3.1)$$

In which

$$\mathbf{Q} = \frac{1}{3} \begin{bmatrix} 4 & 2 & 0 \\ 2 & 4 & 0 \\ 0 & 0 & 1 \end{bmatrix} \quad (3.2)$$

m_0 is the plastic limit moment per unit length of a plate section.

We introduce here an admissible cycle of a plastic curvature field $\Delta\boldsymbol{\chi}^p$. At each load vertex, the plastic curvature rate may not necessarily be compatible at each instant during the time cycle, but the plastic curvature accumulation over the cycle is required to be kinematically compatible such that

$$\Delta\boldsymbol{\chi}^p = \sum_{k=1}^{m} \dot{\boldsymbol{\chi}}^p = \nabla^2 \dot{w} \quad (3.3)$$

Based on the above statements and the mathematical programming theory, an upper bound of the shakedown load factor can be found by solving the following convex nonlinear programming:

$$\alpha^{+} = \min \sum_{k=1}^{m} \sum_{i=1}^{NG} w_i m_0 \sqrt{\dot{\boldsymbol{\chi}}_{ik}^{\mathrm{T}} \mathbf{Q} \dot{\boldsymbol{\chi}}_{ik}}$$
$$\text{s.t.:} \begin{cases} \sum_{k=1}^{m} \dot{\boldsymbol{\chi}}_{ik} = \mathbf{B}_i \dot{\mathbf{u}} \qquad \forall i = \overline{1, NG} \\ \sum_{k=1}^{m} \sum_{i=1}^{NG} w_i \dot{\boldsymbol{\chi}}_{ik}^{\mathrm{T}} \mathbf{m}_{ik}^E = 1 \end{cases} \quad (3.5)$$

If the yield stress of the material is random, then the plastic moment is an uncertain quantity and the objective function of (3.5) is a stochastic variable. Firstly, we must properly define the minimum of a random function. This can be done in such a way that one looks for a minimum lower bound of the objective function under the constraint that the probability of violation of that bound is prescribed in [22]

$$\min \eta$$
$$\text{s.t.:} \begin{cases} \text{Prob}\left(\sum_{k=1}^{m} \sum_{i=1}^{NG} w_i m_0(\omega) \sqrt{\dot{\boldsymbol{\chi}}_{ik}^{\mathrm{T}} \mathbf{Q} \dot{\boldsymbol{\chi}}_{ik}} \ge \eta \right) = \psi \\ \sum_{k=1}^{m} \dot{\boldsymbol{\chi}}_{ik} = \mathbf{B}_i \dot{\mathbf{u}} \qquad \forall i = \overline{1, NG} \\ \sum_{k=1}^{m} \sum_{i=1}^{NG} w_i \dot{\boldsymbol{\chi}}_{ik}^{\mathrm{T}} \mathbf{m}_{ik}^E = 1 \end{cases} \quad (3.6)$$

Problem (3.6) is a stochastic program, it can be converted into an equivalent deterministic program by using a chance constrained program technique [10,11].

$$\alpha^{+} = \min \sum_{k=1}^{m} \sum_{i=1}^{NG} w_i \left(\mu_i - \kappa \sigma_i \right) \sqrt{\dot{\boldsymbol{\chi}}_{ik}^{\mathrm{T}} \mathbf{Q} \dot{\boldsymbol{\chi}}_{ik}}$$
$$\text{s.t.:} \begin{cases} \sum_{k=1}^{m} \dot{\boldsymbol{\chi}}_{ik} = \mathbf{B}_i \dot{\mathbf{u}} \qquad \forall i = \overline{1, NG} \\ \sum_{k=1}^{m} \sum_{i=1}^{NG} w_i \dot{\boldsymbol{\chi}}_{ik}^{\mathrm{T}} \mathbf{m}_{ik}^E = 1 \end{cases} \quad (3.7)$$

In case of a lognormal distribution of strength, the stochastic problem (3.6) can be converted into the equivalent deterministic program (3.8) by using the duality property:

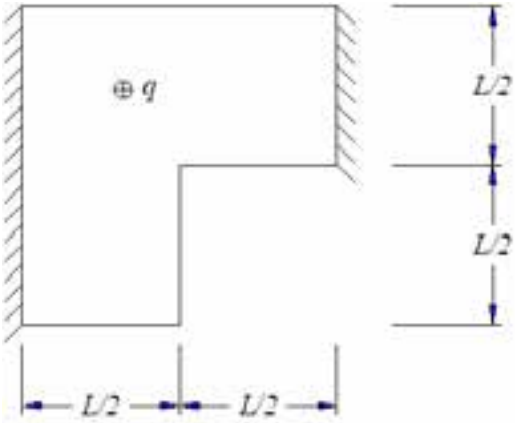

Figure 1: L-shape plate loaded by a uniform pressure

$$\alpha^+ = \min \sum_{k=1}^{m}\sum_{i=1}^{NG} w_i e^{(\mu_i - \kappa\sigma_i)} \sqrt{\dot{\boldsymbol{\chi}}_{ik}^{\mathrm{T}} \mathbf{Q} \dot{\boldsymbol{\chi}}_{ik}}$$

$$\text{s.t.}: \begin{cases} \sum_{k=1}^{m} \dot{\boldsymbol{\chi}}_{ik} = \mathbf{B}_i \dot{\mathbf{u}} \qquad \forall i = \overline{1, NG} \\ \sum_{k=1}^{m}\sum_{i=1}^{NG} w_i \dot{\boldsymbol{\chi}}_{ik}^{\mathrm{T}} \mathbf{m}_{ik}^{E} = 1 \end{cases} \tag{3.8}$$

4. A dual algorithm for shakedown analysis of Kirchhoff plate

For the sake of simplicity, we set some new notations:

$$\dot{\mathbf{k}}_{ik} = w_i \mathbf{Q}^{1/2} \dot{\boldsymbol{\chi}}_{ik}, \ \mathbf{t}_{ik} = \left(\mathbf{Q}^{-1/2}\right)^T \mathbf{m}_{ik}^{E}, \ \hat{\mathbf{B}}_i = w_i \mathbf{Q}^{1/2} \mathbf{B}_i, \tag{4.1}$$

where

$$\mathbf{Q}^{1/2}\mathbf{Q}^{-1/2} = \mathbf{I}, \ \ \mathbf{Q} = \left(\mathbf{Q}^{1/2}\right)^T \mathbf{Q}^{1/2}. \tag{4.2}$$

By substituting (4.1) into (3.8) one obtains a simplified version for the upper bound of the shakedown limit load (primal problem)

$$\alpha^+ = \min \sum_{k=1}^{m}\sum_{i=1}^{NG} e^{(\mu_i - \kappa\sigma_i)} \sqrt{\dot{\mathbf{k}}_{ik}^{T} \dot{\mathbf{k}}_{ik}}$$

$$\text{s.t.}: \begin{cases} \sum_{k=1}^{m} \dot{\mathbf{k}}_{ik} - \hat{\mathbf{B}}_i \dot{\mathbf{u}} = \mathbf{0} \quad \forall i = \overline{1, NG} \\ \sum_{i=1}^{NG}\sum_{k=1}^{m} \dot{\mathbf{k}}_{ik}^{T} \mathbf{t}_{ik} - 1 = 0 \end{cases} \tag{4.3}$$

Using a penalty method to eliminate the first constraint in (4.3) leads to the penalty function

Table 1: Limit load factor in comparison for case of simple supported plate $\left(\frac{m_0}{qL^2}\right)$

Author	Lower bound	Upper bound	
Le et al. [7]	--	6.219	
Tran et al.[15]	6.044	6.173	deterministic
	6.022	6.190	
Present	3.785	3.882	normal
	4.135	4.242	lognormal

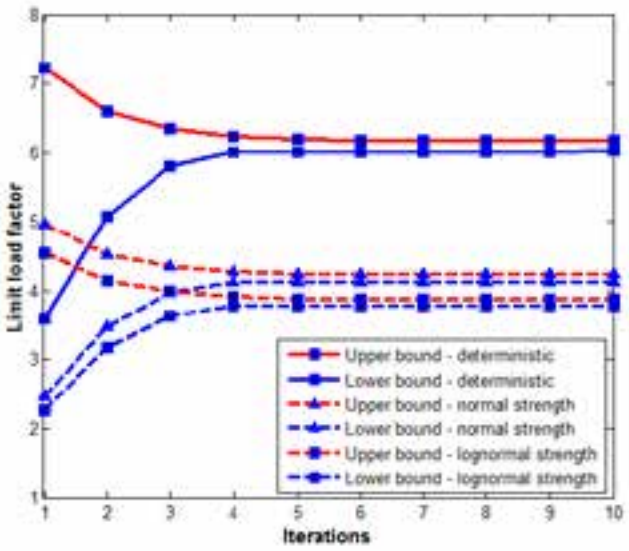

Figure 2: Convergence of limit load factors

$$F_p = \sum_{i=1}^{NG} \left\{ \begin{array}{l} \sum_{k=1}^{m} e^{(\mu_i - \kappa\sigma_i)} \sqrt{\dot{\mathbf{k}}_{ik}^{T} \dot{\mathbf{k}}_{ik} + \varepsilon_0^2} + \\ + \frac{c}{2} \left(\sum_{k=1}^{m} \dot{\mathbf{k}}_{ik} - \hat{\mathbf{B}}_i \dot{\mathbf{u}} \right)^T \left(\sum_{k=1}^{m} \dot{\mathbf{k}}_{ik} - \hat{\mathbf{B}}_i \dot{\mathbf{u}} \right) \end{array} \right\} \tag{4.4}$$

where c is a penalty parameter such that $c>>1$. The corresponding Lagrange function of (4.4) is

$$L = F_p - \alpha \left(\sum_{i=1}^{NG}\sum_{k=1}^{m} \dot{\mathbf{k}}_{ik}^{T} \mathbf{t}_{ik} - 1 \right) \tag{4.5}$$

By employing Newton method to solve the Karush-Kuhn-Tucker (KKT) conditions of the Lagrange function (4.5), we have the incremental vectors of nodal variables $\dot{\mathbf{u}}$, curvature rate $\dot{\mathbf{k}}_{ik}$ and $\boldsymbol{\beta}_i$ as follows :

$$\begin{aligned} d\dot{\mathbf{u}} &= d\dot{\mathbf{u}}_1 + d\dot{\mathbf{u}}_2 \left(\alpha + d\alpha\right) \\ d\dot{\mathbf{k}}_{ik} &= (d\dot{\mathbf{k}}_{ik})_1 + (d\dot{\mathbf{k}}_{ik})_2 \left(\alpha + d\alpha\right) \\ d\boldsymbol{\beta}_i &= (d\boldsymbol{\beta}_i)_1 + (d\boldsymbol{\beta}_i)_2 \left(\alpha + d\alpha\right) \end{aligned} \tag{4.6}$$

$$\left(\alpha + d\alpha\right) = \frac{1 - \sum_{i=1}^{NG}\sum_{k=1}^{m} \mathbf{t}_{ik}^{T} \left[\dot{\mathbf{k}}_{ik} + \left(d\dot{\mathbf{k}}_{ik}\right)_1 \right]}{\sum_{i=1}^{NG}\sum_{k=1}^{m} \mathbf{t}_{ik}^{T} \left(d\dot{\mathbf{k}}_{ik}\right)_2} \tag{4.7}$$

The vectors $d\dot{\mathbf{q}}, d\dot{\mathbf{k}}_{ik}, d\boldsymbol{\beta}_i$. and $d\alpha$ are actually Newton directions, which assure that a suitable step along them will lead to a decrease of the objective function of the primal problem (3.8) and to an increase of the objective function of the objective function of the dual problem (2.5). Based on (4.6 - 4.7) we can update the vectors of $\dot{\mathbf{q}}, \dot{\mathbf{k}}_{ik}$, $\boldsymbol{\beta}_i$ and α. The dual algorithm for limit and shakedown analysis is presented in detail in [2-6].

5. Numerical examples

We investigate a L-shape plate subjected to uniform pressure. Length $L=10m$, plate thickness $t=0,1m$, the mean value of yield stress $E(\sigma_i)=250\text{MPa}$ and the standard deviation $\sigma = 0.1E(\sigma_0)$ .The reliability level is assumed $\psi = 0.9999$. Let

(xem tiếp trang 22)

Workability analysis of lightweight aggregate concrete mixture use air entrainment admixture

Nguyen Duy Hieu[(1)], Truong Thi Kim Xuan[(2)]

Abstract

In the production of lightweight aggregate concrete, there is always a tendency to stratify the lightweight aggregates during transportation and construction, because the unit weight of lightweight aggregates is often much smaller than that of the cement mortar in the mix. This paper presents some analysis results on workability, calculating relative stratification reduction and quality factor of LC when using Air Entrainment Admixture (AD) that most of experimental results presented on the referent [5]. Experimental and analytical results show that the effect of AD depends on the amount of use; significantly reduce the stratification of the mix, reducing the density without much effect on the quality factor of the concrete when it is used at the appropriate concentration, in this study it was about 0.02%.

Key words: *Lightweight Aggregate Concrete (LC), Air Entrainment Admixture (AD), Workability of Fresh Concrete, Stratified Index, Quality Factor*

(1) Assoc. Prof. PhD. Lecturer, faculty of civil engineering, Hanoi Architectural University,
Email: hieund@kientruchanoi.edu.vn

(2) MA., Lecturer, Hanoi Architectural University,
Email: xuanttk@kientruchanoi.edu.vn

Date of receipt: 15/4/2022
Editing date: 6/5/2022
Post approval date: 5/9/2022

1. Introduction

Lightweight aggregate (LA) in lightweight concrete helps reduce its bulk density, increase the insulation and sound-proofing of the structure, but fresh concrete is easily stratified because lightweight aggregates always tend to float upwards. This can be overcome by using air entrainment additives [1, 2].

The theoretical basis for the use of air entrainment admixtures in Lightweight aggregate Concrete (LC) is Stock's law and component principle of composite material. In viscous plastic multi-component system like fresh concrete, particles of different sizes and densities can cause sedimentation or stratification that can be described by the Stock equation [1, 4]:

$$v = \frac{2r^2.g.\Delta\rho}{9.\eta} \quad (1)$$

In which:

v – the movement rate of spherical grains, (m/s); r – the radius of grain, (m);

g - acceleration of gravity, (m/s^2);

ρ_m- bulk density of cement paste, (kg/m^3);

ρ_{LA} - particle density of aggregate, (kg/m^3); $\Delta\rho = \rho_m - \rho_{LA}$

η - dynamic viscosity of cement paste, (Ns/m^2);

Considering that lightweight aggregate concrete is as a two-phase composite material, in which, the reinforced phase is aggregates and the matrix phase is cement paste, its bulk density, strength and elastic modulus are described according to the equations (2), (3) and (4) as follows [1, 4]:

$$\rho_{co} = \rho_{LA}\phi + \rho_m(1 - \phi) \quad (2)$$

$$\log R_{co} = \phi.\log R_{LA} + (1- \phi).\log R_m \quad (3)$$

$$E_{co} = v_m.E_m+\phi.\zeta.E_{LA} = v_m.E_m+(1-v_m).\zeta.E_{LA} \quad (4)$$

In which:

ρ_{co}, ρ_{LA}, ρ_m: dry density of concrete, LA, dry mortar, respectively (kg/m^3);

vm : The volume of mortar, (m3); Em: elastic modulus of mortar;

ϕ : Volume part of LA in fresh concrete, (m^3/m^3).

$0< \zeta \leq 1$: coefficient depends on the link between mortar and LA;

R_{co}, R_{LA}, R_m: the strength of concrete, LA and mortar, respectively.

From the above relationships, it can be seen that, when replacing a part of cement with mineral admixtures whose density is smaller than that of cement, such as fly ash or silica fume, combined with air entrainment admixture, the specific density of the binder will be reduced, thereby limiting the stratification of fresh concrete; However, the mechanical properties of concrete can be changed.

Based on empirical data, much of which has been published in ref. [5], this paper presents the results of analysis and evaluation of the relative stratification reduction of fresh concrete and the quality coefficient of hardened concrete when using air entrainment admixtures with different content.

2. Materials and Concrete Compositions

2.1. Cement (C)

Cement PC50 Nghi Son is produced according to Vietnam standard, TCVN -2009. The properties of cement are shown in Table 1.

Table 1: Properties of cement

Water demand, %	Setting time, min		Compressive strength, MPa		Fineness, cm^2/g	Density, g/cm^3
	Initial	Final	3 days	28 days		
29.5	115	230	33.0	60.7	3870	3.09

2.2. Fine aggregates - Sand (S) and Lightweight Aggregate (LA)

Sand from the Lo River, according to standard TCVN 7570-2006, is used. LA used for the research with two grain sizes: 10 - 20 mm (No 1), 4 – 8 mm (No 2). Mechanical-physical properties of aggregates are shown in Table 2 and Table 3.

Table 2: Properties of fine aggregate

Properties	Result
Specific density, g/cm^3	2.47
Bulk density, kg/dm^3	1.57
Porosity, %	37.2
Scale module	2.65

Table 3: Properties of lightweight aggregate

Properties	No 1	No 2
Particle size, mm	10 – 20	4 – 8
Bulk density, kg/dm^3	0.63	0.75
Compacted density, kg/dm^3	0.69	0.81
Particle density), kg/dm^3	1.44	1.35
Compressive strength in cylinder, MPa	1.4	1.9
Water absorption 24h, %	25	23

2.3. Fly ash (FA) and Silica Fume (SF)

Fly ash is floated from Phalai thermo-electric plant's coal ash, F type according to TCVN 10302:2014. The chemical compositions of Phalai fly ash are shown in Table 4.

SF used in this study is granular, according to ASTM C1240-00, properties of SF are shown in Table 5.

Table 4: Properties of Phalai fly ash

Properties	Symbol	Result
Specific density, g/cm^3	ρ_{fa}	2.3
Moisture, %	w	0.5
Loss of weight on ignition, %	LOI	4.5
Sieve remission (screen size 45μm), %	-	23
Fineness (Blaine), cm^2/g	S	3250
Activity intensity index after 28 days, %	-	84
(SiO_2+ Al_2O_3+ Fe_2O_3) content, %	-	81
SO_3 content, %	-	0.15

Table 5: Properties of Silica Fume

Properties	Result
Specific density, g/cm^3	2.2
Moisture, %	2.76
Loss of weight on ignition, %	2.82
SiO_2 content, %	88.15
SO_3 content, %	0.05
CaO content, %	0.66
Cl^- content, %	0.01

2.4. Super-plasticizer (SP)

Super-plasticizer based on Polycarboxylate, type F according to TCVN 8826:2011. Its properties are as follows:

liquid form; pale yellow; specific density: 1.1-1.2 g/cm^3; pH = 6.6

2.5. Air-entraining admixture (AD)

This study uses Bifi, meeting TCVN 12300:2018 with the following characteristics: liquid form; pale yellow; solute content: 40-45%; Specific density: 1.02 – 1.06kg/l.

2.6. Water (W)

Clean water, meeting the requirement of TCVN 4506:2012.

2.7. Lightweight Aggregate Concrete Compositions

After the process of calculation and experiment, experimental concrete compositions as follows (Binder is total of cement, fly ash and silica fume by mass ratio 70, 25 and 5%, respectively): [5]

Table 6: Concrete Compositions

Symbol	Binder	S	LA (kg)		SP	W	AD
	(kg)	(kg)	No1	No2	(%)	(kg)	(%)
LC0	540	870	255	170	0.8	195	0
LC2	540	870	255	170	0.8	195	0.02
LC4	540	870	255	170	0.8	195	0.04
LC6	540	870	255	170	0.8	195	0.06
LC8	540	870	255	170	0.8	195	0.08

3. Results and Discussion

3.1. Effects of air entrainment additive on bulk density of fresh concrete

Table 8 shows the results of the study on the effect of air-entraining admixture on the properties of fresh concrete, such as: dry bulk density (ρvd), bulk density (ρv), slump (SN) and slump after 1 hour (SN1).

Table 7: Bulk density (ρ_v) and slump (SN) of fresh concrete

Symbol	AD content, %	ρ_v, kg/m^3	SN, mm	SN1, mm
LC0	0	1895	78	63
LC2	0.02	1725	80	75
LC4	0.04	1714	85	70
LC6	0.06	1627	95	60
LC8	0.08	1595	105	68

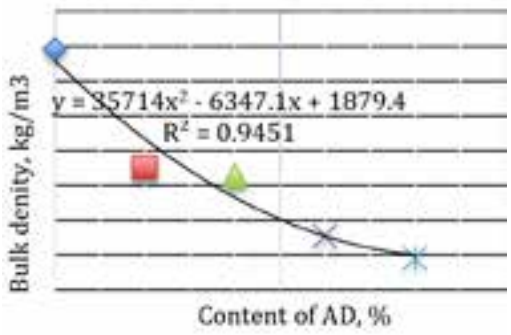

Figure 1: Bulk density of fresh concrete, kg/m^3

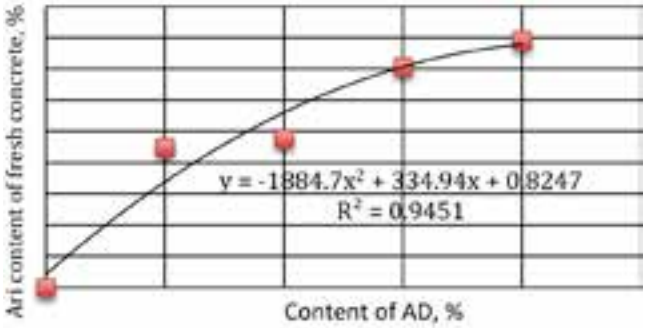

Figure 2: The amount of air entrained into the fresh concrete, %

Table 9 shows the amount of air entrained into the fresh concrete (air content) according to AD content used (Ignore air content in LC0 mixture). [5]

Table 8: The amount of air entrained into fresh concrete

Symbol	LC0	LC2	LC4	LC6	LC8
AD content, %	0	0.02	0.04	0.06	0.08
Bulk density, kg/m^3	1895	1725	1714	1627	1595
Air content, %	-	9.0	9.6	14.1	15.8

The research results show that the amount of air entrained into the fresh concrete reduces its bulk density. The bulk density decreases markedly when the Bifi content is from 0.04 – 0.06%. Experiments also show that when the air-entraining admixture content is more than 1% by mass (compared to the amount of binder), the bulk density of fresh concrete decreases slightly.

3.2. Workability Analysis of fresh concrete

The results of the study on the effect of air-entraining admixture on the slump of fresh concrete are shown in Table 8. Its slump is tested according to TCVN 3016 : 1993, measured immediately after mixing and 1 hour later. The slump loss is also calculated, the results are shown in Figure 3 and 4. [5]

We can see that when the air-entrained admixture content in concrete, the slump of mixtures increases. This result is most evident when measuring intermediately after mixing. The reason may be due to the small evenly distributed air bubbles creating a "ball bearing" effect to reduce internal friction, on the other hand, it limits the stratification of aggregates, so the slump increases. However, when the air-entrained admixture content in concrete is greater than 0.02% by mass, the slump after 1 hour (SN1) tends to decrease quite clearly. It can be explained that the air bubbles entrained into concrete only exist for a short time if we do not mix the mixture continuously. When these bubbles escape, a part of the "ball bearing" effect disappears, so the slump decreases sharply.

The above results show that the air-entraining admixture content should be used in minimum quantities.

Through experiments measuring the stratification of fresh concrete and visual observations, we can see that when using air-entraining admixture, the homogeneity of fresh concrete is significantly improved, so mixing, molding and shaping concrete samples are much easier than samples without this

Table 9: Stratified index of fresh concrete

Symbol	AD content, %	Volume part of LA in LC	Density of fresh LC, ρ_{oc}, kg/m^3	Mortar density, Dm, kg/m^3	Relative Stratified Index, v_i/v_0, %
LC0	0	0.30	1920	2108	100
LC2	0.02	0.30	1725	1864	65
LC4	0.04	0.30	1714	1849	63
LC6	0.06	0.30	1627	1724	45
LC8	0.08	0.30	1595	1678	39

Table 10: Compressive strength of hardened concrete

Symbol	AD content, %	Dry density, ρ_{co}, g/cm^3	Compressive strength, MPa,			Quality factor, R_{28}/ρ_{co}
			R_3	R_7	R_{28}	
LC0	0	1.870	21.3	27.3	33.5 (*)	17.9
LC2	0.02	1.630	21.5	25.3	28.8	17.7
LC4	0.04	1.600	16.3	19.0	23.0	14.4
LC6	0.06	1.550	15.9	17.7	21.9	14.1
LC8	0.08	1.530	16.4	17.4	21.2	13.9

(*) This value has been checked and adjusted, different from the reference [5], after a writing error was detected.

Figure 3: Effect of AD on slumps

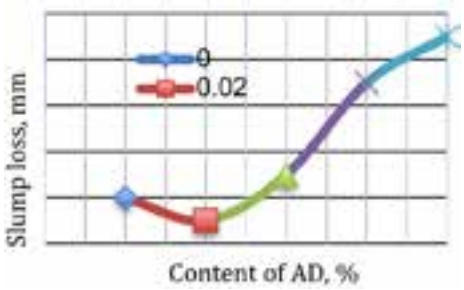

Figure 4: Effect of AD on slumps loss

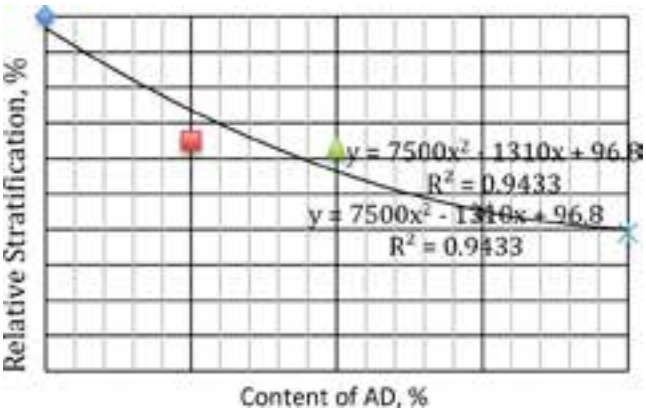

Figure 5: Effect of AD on Stratification of fresh concrete

additive. Figure 6 visually shows the sample surface using (a) and not using Bifi (b).

The results in Table 7, the graphs in Figure 3 and Figure 4 show that the impact of AD on the slump of fresh concrete is not much: in the range of 8-10 cm for SN; 6-7cm for SN1. Research experience shows that the presence of AD does not significantly change the flowability of the cement paste, that is, has a negligible effect on the dynamic viscosity of the cement slurry [3]. The slight increase in slump of the concrete mix when the presence of AD may be mainly due to the stratification reduction effect of the lightweight aggregates. In the subsequent analysis, it can be considered that the relative change ratio of the viscosity (η) of the mixtures LC to the viscosity of the mixture LC0 is negligible.

Obviously, the movement rate of LA in fresh concrete can be used to assess the stratification of the mix. Call the movement speed of LA in the mixtures of LC0, LC2, LC4, LC6, LC8 is vi (i = 0, 2, 4, 6, 8), from equation (1) we have

$$\frac{v_i}{v_0} = \frac{\Delta\rho_{(i)}}{\Delta\rho_0} = \frac{\rho_{m(i)} - \rho_{LA}}{\rho_{m0} - \rho_{LA}} \quad (5)$$

In which:

$\rho_{m(i)}$ - bulk density of cement mortar in LC(i), (kg/m^3);

ρLA - particle density of aggregate, (kg/m^3)

From equation (2) infer to:

$$\rho_{m(i)} = \frac{\rho_{co(i)} - \varphi\rho_{LA}}{1 - \varphi} \quad (6)$$

In which: $\rho_{co(i)}$ - bulk density of LC(i), (kg/m^3)

From (6) and (5) assuming that stratification of LC0 is 100%, we calculate the relative stratified index of LC mixes (i) as shown in Table 9 and shown in Figure 5.

Calculation results show that, when using air-entraining admixtures with the content of 0.02 - 0.08%, the stratification of the concrete mixture has been reduced by about 35 - 60% compared to the control sample LC0. From the graph or regression equation in the Figure 5, it is possible to approximate the AD content for the purpose of reducing stratification; and then, estimate the bulk density and the rate of entrained air and slump of the fresh LC according to the graph or the regression function in Figure 1, Figure 2 and Figure 3.

3.3. Quality factor analysis of hardened concrete

Compressive strength and dry density of hardened concrete is determined according to TCVN 3118:1993 and TCVN 3115:1993 respectively. The research results about Factor of quality of LC are presented in Table 10.

In the range of air-entraining admixture content studied in this report, when the additive content increases, compressive strength of hardened concrete decreases, but the level of reduction is not the same at different ages. The reason is that the porosity of concrete is significantly increased by the presence of entrained air bubbles.

Concrete strength at the early ages (3 and 7 days) is not much reduced when air-entraining admixture content is at 0.02% as well as at 0.04 – 0.08%. The strength at 28 days of age is the largest decrease, which is evident in all samples using air-entraining admixture when compared to the control sample (about 30% reduction). This may be due to the effect of intensity reduction with increasing porosity at different strength levels, whereby the higher the concrete strength, the higher the reduction at a certain porosity.

When the air-entraining admixture content increases from 0.04% to 0.08%, the level of strength reduction slows down. This may be due to the air entraining performance of this additive has nearly reached saturation threshold.

The quality factor of concrete is calculated as the ratio of strength to dry density. The results show that at the level of using AD 0.02%, the quality coefficient of LC does not change, but this coefficient will decrease when the content of AD increases higher.

4. Conclusions

The results of this study show that the use of air-entraining admixture in lightweight aggregate concrete reduces bulk density and the aggregate stratification of fresh concrete. This additive helps fresh concrete easier to work, shaping without floating lightweight aggregate on top.

Air-entraining admixture reduces bulk density and the strength of LC, the level of reduction depends on the amount of additive and curing time. Specifically, the level of intensity

reduction at the age of 3 and 7 days is significantly lower than that of the 28 days.

Therefore, air-entraining admixture should be used at the minimum content, depending on the purpose of strength and bulk density as well as the ease of construction of fresh concrete. In this study, the most reasonable AD content is at 0.02% by weight of the binder.

And it is worth noting that the method as presented can be used to evaluate the relative stratification reduction effect of AD for lightweight concrete mixes./.

References

1. *Hieu Nguyen Duy, High quality lightweight concrete technology, Construction Publishing House, 2016.*
2. *Hieu Nguyen Duy, Viet Tran Ba, Lu Phung Van, Studying methods for reducing segregation of Self-Compacting Keramzit Concrete Mixture, Journal of Building Science and Technology, N0 1/2009 (Vo 146), 2009.*
3. *Hieu Nguyen Duy, Kim Xuan T. Truong, Research on manufacturing high-strength lightweight concrete with self-compacting features used in renovating and constructing urban constructions, Report on scientific research results of Hanoi Architectural University, 2009.*
4. *Satish Chandra and Leif Berntsson, Lightweight Aggregate Concrete – Science, Technology and Applications, William Andrew Publishing, Norwich, New York, U.S.A, 2003.*
5. *Hieu Duy Nguyen, Pham Thanh Mai, Truong T. K. Xuan, Phan Viet Anh and Trinh T. Trang, Effects of air entraining admixture on the properties of lightweight aggregate concrete, 2020 IOP Conf. Ser.: Mater. Sci. Eng. 869 032026, 2020.*

Limit and shakedown analysis of kirchhoff-love plates...

(tiếp theo trang 17)

us calculate limit load fators. This example is investigated in [5-6] for case of normal distribution of strength.

In this analysis, the plate is modelled by 768 DKQ (discrete kirchhoff quadrilateral) elements. Figure 2 shows the convergence of the upper bound and lower bounds for simple supported case. Table 1 shows the results in comparison with Le [7] and Tran [15]./.

References

1. *G. Kirchhoff, Über das Gleichgewicht und die Bewegung einer elastischen Scheibe. J. für die Reine und Angew. Math., 40: 51-88, 1850.*
2. *N.T. Trần, M. Staat, Direct plastic structural design under random strength and random load by chance constrained programming. Eur J Mech A Solids, 85(1), art. no. 104106, 2021.*
3. *N. T. Trần, M. Staat, Direct plastic structural design under lognormally distributed strength by chance constrained programming. Optim. Eng. 21(1), 131-157, 2020.*
4. *Ngọc Trình Trần, Limit and Shakedown analysis of structures under stochastic conditions. PhD thesis, Technische Universität Carolo-Wilhelmina zu Braunschweig, Braunschweig, Germany, 2018.*
5. *N.T. Trần, T.N. Trần, H.G. Matthies, G.E. Stavroulakis, M. Staat, Shakedown analysis of plate bending under stochastic uncertainty by chance constrained programming. Proc. VII Eur. Congr. Comput. Methods Appl. Sci. Eng. (ECCOMAS Congr. 2016), no. June, pp. 3007–3019, 2016.*
6. *N.T. Trần, T.N. Trần, H.G. Matthies, G.E. Stavroulakis, M. Staat, Shakedown analysis of plate bending analysis under stochastic uncertainty by chance constrained programming. M. Papadrakakis, V. Papadopoulos, G. Stefanou, V. Plevris eds. ECCOMAS Congress 2016, VII European Congress on Computational Methods in Applied Sciences and Engineering. Crete Island, Greece, 5–10 June 2016, Vol. 2, pp. 3007-3019, 2016.*
7. *C.V Le, M. Gilbert, H. Askes, Limit analysis of plates using the EFG method and second-order cone programming. Int. J. Numer. Meth. Engng, 78, 1532-1552, 2009*
8. *T. Belytschko, P.G. Hodge, Numerical methods for the limit analysis of plates. Trans. ASME, J. Appl. Mech., 35, 796-801, 1968.*
9. *C.T. Morley, The ultimate bending strength of reinforced concrete slabs. PhD thesis, Cambridge University, 1965.*
10. *L. Capsoni, A. Corradi, Limit analysis of plates-a finite element formulation. Struct. Eng. Mech., 8(4), 325-341, 1999.*
11. *E.N. Fox, Limit analysis for plates: the exact solution for a clamped square plate of isotropic homogeneous material obeying the square yield criteron and loaded by uniform pressure. Math. Phys. Eng. Sci., 277(1265), 121-155, 1974.*
12. *R.H. Wood, A partial failure of limit analysis for slabs, and the consequences for future research. Mag.Concr. Res., 21, 79-90, 1969.*
13. *W.C. McCarthy, L.A. Traina, A plate bending finite element model with a limit analysis capacity. Math. Model., 8(Supplement C),486-492, 1987.*
14. *S. Timoshenko, S. Woinowsky-Krieger, Theory of plates and shells. 2nd Edition. McGraw Hill,1959.*
15. *T.N. Tran, A dual algorithm for shakedown analysis of plate bending. Numer. Methods Eng., 86(7), 862-875, 2011.*
16. *J. Björnberg and M. Diehl, Approximate robust dynamic programming and robustly stable MPC. Automatica, 42(5), 777-782, 2006.*
17. *L. Zéphyr, P. Lang, B. F. Lamond, P. Côté, Approximate stochastic dynamic programming for hydroelectric production planning. Eur. J. Oper. Res., 262(2), 586-601, 2017.*
18. *B. Srinivasan, S. Palanki, D. Bonvin, Dynamic optimization of batch processes: I. Characterization of the nominal solution. Comput. Chem. Eng., 27(1), 1-26, 2003.*
19. *G. Francois, D. Bonvin, Chapter One - Measurement-based real-time optimization of chemical processes. S. Pushpavanam ed. Control and Optimisation of Process Systems, vol. 43, Academic Press, 1-50, 2013.*
20. *S. Rasoulian, L.A. Ricardez-Sandoval, Worst-case and distributional robustness analysis of a thin film deposition process. IFAC-PapersOnLine, 48(8), 1126-1131, 2015.*
21. *A. Charnes, W. Cooper, G.H. Symonds, Cost horizons and certainty equivalence: An approach in stochastic programming of heating oil. Manage. Sci., 4, 235-263, 1958.*
22. *A. Charnes, W.W. Cooper, Chance-constrained programming. Manage. Sci., 6(1), 73-79, 1959.*

The effect of aging and slurry density on triaxial shear properties of liquefied stabilized soil mixed with fiber material cured at the indoor and in-situ

Hung Khac Le[(1)], Yukihiro Kohata[(2)]

Abstract

In this study, a series of Consolidated–Undrained triaxial compression tests were conducted at a constant axial strain rate, with a small unloading and reloading during the monotonic loading to investigate the effect of various densities and curing times on the mechanical properties of Liquefied Stabilized Soil (LSS). The comparison of LSS mixed with fiber material in the amounts of 0 and 10 kg/cm3 cured at the indoor and in-situ was discussed. Based on the test results, the effect of slurry density on the strength of LSS was found to be greater than the effect of curing time. The pre-peak behavior of q~εa curve became more non-linear under the effect of changing slurry density, in contrast to the effect of curing time. Moreover, the damage degree of LSS with shearing becomes smaller with curing time, while it seems to be rather independent of slurry density.

Keywords: *liquefied stabilized soil, fiber material, cured at indoor and in-situ, triaxial shear property*

(1) Graduate School of Engineering, Muroran Institute of Technology, Muroran Japan

(2) Professor, Muroran Institute of Technology, Muroran, Japan

Date of receipt: 15/4/2022
Editing date: 6/5/2022
Post approval date: 5/9/2022

1. Introduction

Nowadays, environmental issues are arising from growing urbanization, especially in developing countries. Urban construction generates large amounts of construction waste soil that may not be appropriate for reuse in construction and may be harmful to the environment if not properly treated. Moreover, due to its small land area, the city confronts environmental issues such as a lack of ultimate waste disposal sites and resource limitations, such as concerns about the potential exhaustion of mineral resources, and the waste and recycling problem has become a societal issue. The problem has received considerable attention. Therefore, it is desirable to use recycled-oriented materials. The Liquefied Stabilized Soil (LSS)[1]) is one of of cement-stabilized soil, improves the soil properties by the effect of cementation arising in an excavated soil mixed with cement and water, and has been extensively used in Japan. However, there is concern that the increased use of cement solidifiers in LSS increases their strength and causes them to behave brittlely, reducing their seismic resistance. In order to improve brittle property, Kohata et al 2), 3). proposed using pulverized newspaper as a fibered material to reinforce LSS, and conducted a series of unconfined and triaxial compression tests. The study found that after the peak of the stress-strain curve, LSS mixed with fibered material had improved brittle properties. Afterward, numerous investigations into the strength and deformation properties of LSS with fiber were conducted [2), 3)]. Nevertheless, no comprehensive investigation of LSS with fiber under a variety of combination conditions has been performed. Especially, the effect of various slurry densities and longer curing times on the strength and deformation properties of LSS cured at in-situ conditions is not clearly. In this study, a series of undrained triaxial compression tests were performed to investigate the effects of slurry density and curing time on the triaxial shear properties of LSS under various conditions. Base on the test results, the comparison between the strength and deformation properties of LSS cured at indoor and in-situ were discussed.

2. Test procedure

2.1. Test material

In this study, the New Snow Fine Clay (NSF-Clay), which is a commercially cohesive soil, was used as the homogenous base material. The physical property of NFS- clay are shown in Table 1. The cement stabilizer (Geoset 200 by Taiheiyo Cement Co., Ltd.) was used as the solidification agent. For the fiber material, newspaper, which is easy to obtain, was pulverized with water by a food processor and made into a cotton-like material.

Table 1 : Physical parameters of NSF-CLAY

Particle density ρ_s (g/cm^3)	2.762
Liquid limit w_L (%)	60.15
Plastic limit w_P (%)	35.69
Plasticity Index I_P	24.46

2.2. Mixing and specimen preparation

There are two types of mixing methods for LSS, that is, the “slurry method” and the “adjusted slurry method”. In this study, LSS were

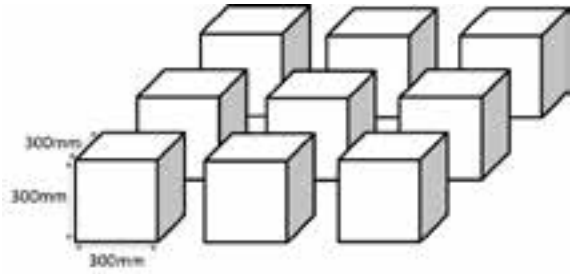

Figure 1: Schematic diagram of pits

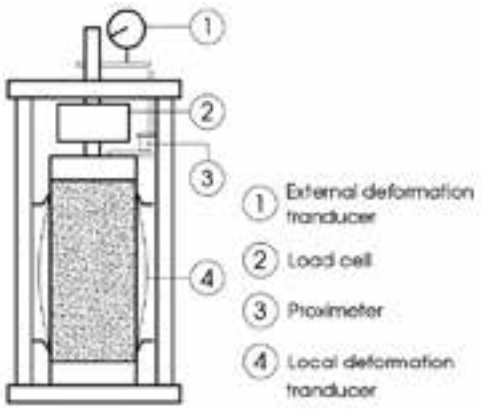

Figure 2: Schematic diagram of test apparatus

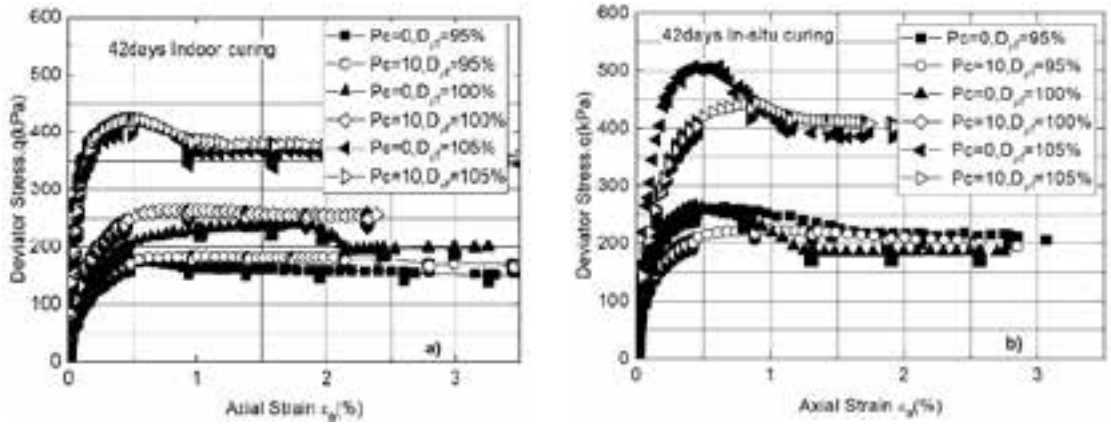

Figure 3: q vs ε_a relation at 42 days indoor curing

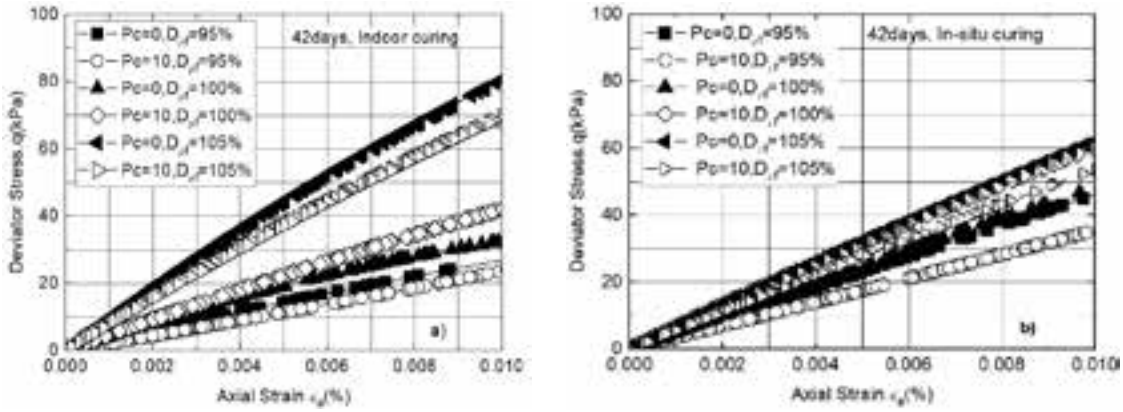

Figure 4: q vs ε_a relation at 42 days in-situ curing

prepared by the "slurry method" because it is easier for preparation, in which NSF-Clay is mixed with an appropriate amount of water to produce a density-controlled slurry, which is then mixed with cement stabilizer and fiber material.

In order to investigate the effect of various slurry density on the strength and deformation of LSS reinforced fiber material, the basic slurry density was decided to be 1.280g/cm^3, the density was base on the standard mix proportion design figure[2]), and the slurry density changing rate D_{pf} (actual slurry density)/ (basic slurry density) x 100% was defined as, D_{pf}=100% (ρ_f=1.280g/cm^3), D_{pf}=105% (ρ_f=1.344g/cm^3), D_{pf}=95% (f=1.216 g/cm^3), respectively. To achieve the desired slurry density, this slurry was poured into a stainless steel container (AE mortar container) of 400cm^3 in volume and the excess portion was slipped off with a glass plate to measure its density. After adjusting the slurry several times to obtain the required density, cement stabilizer in the amount of 100 kg/m^3 was added to the slurry. The amount of fiber material added was referenced as being 10 kg/m^3 based on a previous study[2), 3)] (1.963g/specimen). After adding the fiber material, the Liquefied Stabilized Soil (LSS) was mixed with a hand-type mixer. Before filling the mold, the indoor-cured specimens were deaired by a negative pressure of about -90kPa for 30 minutes and put in a 50×100mm commercial plastic mold with fabric tape on top for extra filler. After filling the container with treated soil, a plastic film was attached to the top edge. The excess portion of fill was trimmed off after 3 hours of curing. The top surface was flattened, re-covered with polymer film, covered with a wet towel, and cured in moist air at 20±3°C. For the in-situ cured specimens, they

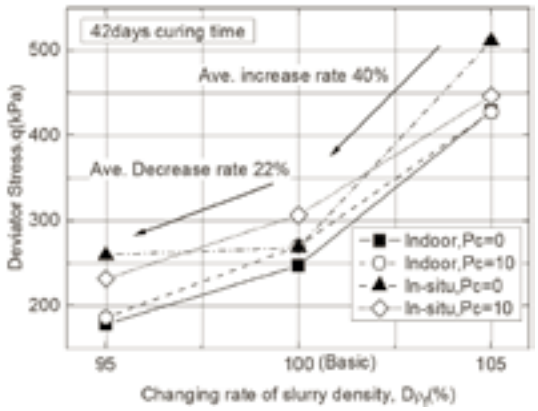

Figure 5: Relationship between the deviator stress q vs changing rate of slurry density

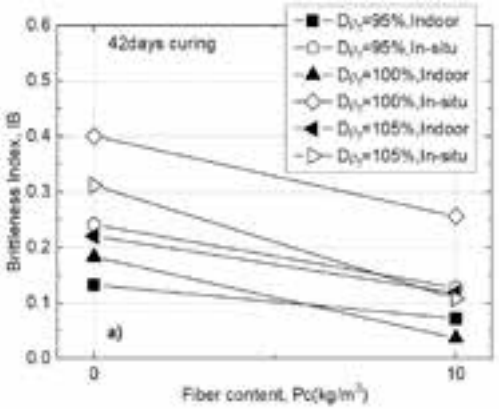

Figure 6: Fiber content vs IB

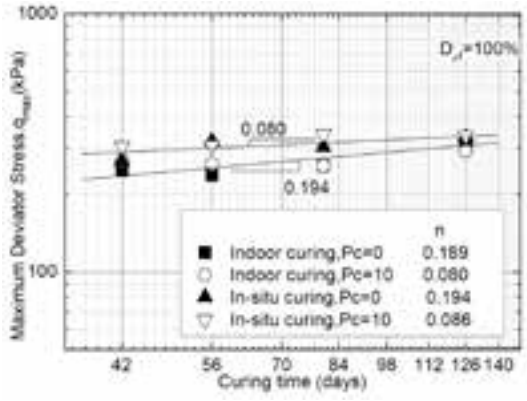

Figure 7: q_{max} vs. t relations

were poured into isolated pits excavated on the campus grounds and allowed to cure for the prescribed days (42, 56, 80, and 126 days). Figure 1 illustrates a schematic diagram of the pits. After placement, the LSS surface was covered with a polymer sheet and cured at in-situ. Using a trimmer and straight edge, the LSS blocks were excavated and formed into cylindrical specimens in the laboratory.

2.3. Testing method

In this study, a triaxial compression test apparatus with a pair of local deformation transducers (LDTs)[4] installed on each side of the specimen was used to measure axial displacement at the small strain level and to avoid the bedding errors caused by loose layers at the top and bottom edges of the specimen and filter paper compression. A dial gauge and a proximity transducer (Gap sensor) were used to determine the axial displacement when LDTs exceeded a certain range. A series of undrained triaxial compression tests were performed at an axial strain rate of 0.054%/min, with a small unloading and reloading during the monotonic loading process. The experiments were conducted on specimens that had been cured in-situ and indoors for 42, 56, 80, and 126 days, respectively. For 15 hours, the specimens were isotropically consolidated at 98kPa confining pressure and 196 kPa back pressure before being subjected to undrained triaxial shear. Figure 2 illustrates the triaxial compression test apparatus schematically.

3. Results and discussion

3.1. Stress and strain relationships

3.1.1. Effect of slurry density

Figures 3 and 4 show the relationships between deviator stress q and axial strain εa based on locally measured axial strain by LDTs for undrained triaxial compression tests at 42 days of indoor and in-situ curing. Figure 3 shows the relationship up to εa=3.5%, Figure 4 shows up to 0.01% at the small strain level. It is clear from the figures that the change in slurry density influences significantly the strength of LSS both indoor and in-situ at 42 days of curing. By defining the average decreasing or increasing of maximum deviator stress as (the value that decreased or increased in maximum deviator stress)/ (maximum deviator stress with basic slurry density)×100%[3]), the data in Figure 5 is considered that in case of larger slurry densities, the average increasing rate in indoor and in-situ curing are calculated to be about 40%, whereas the average decreasing rate with lower slurry densities are shown 30% and 14% for indoor and in-situ curing, respectively. Moreover, the maximum deviator stress, q_{max}, of in-situ LSS specimens substantially tend to be larger than that of indoor LSS ones, irrespectively of slurry density. However, in Figure 4, the gradient of the q and ε_a relationship at small strains for in-situ specimens is less than that of indoor specimens, whereas in Figure 3, the q_{max} of in-situ specimens for large slurry density is large than that of indoor specimens. This indicates that when increasing slurry density at the indoor, the stiffness at small strain increased significant in comparison to the other specimens of lower slurry density that tends to only slightly increase at in-situ conditions. It caused the magnitude of viscous resistance appears to decrease with an increasing of plasticity and water content at in-situ[5]. As a result, increases or decreases in slurry density have a greater influence on the stiffness of LSS at the indoor than when it is cured at in-situ.

In order to estimate the brittleness property after the peak, the brittleness index (I_B)[6] was defined in this study.

$$I_B = (q_{max} / q_{res}) - 1 \quad (1)$$

Where qmax is the maximum deviator stress and qres is the residual deviator stress. As the value of brittleness index (I_B) decreases and approaches zero, the failure behavior becomes increasingly ductile and brittleness property is improved.

Figure 6 shows that when LSS (Pc=0) and LSS with fiber (Pc=10) are compared, the IB value decreased roughly twice as fast in the specimens mixed fiber. This result can be seen as the most effective method to mix fiber into LSS to improve the brittleness mechanical property and to increase ductile performance.

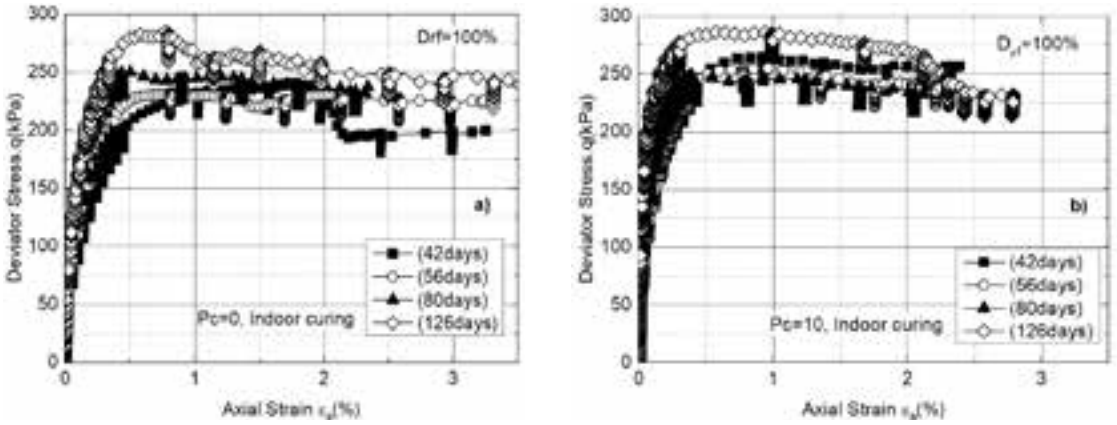

Figure 8: q vs ε_a relation with $D_{\rho f}$= 100 %, Pc=0

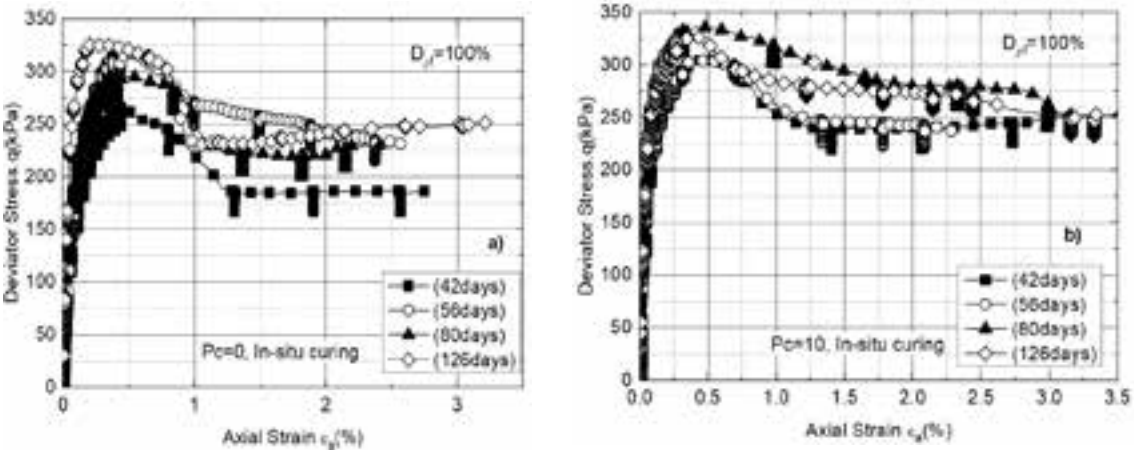

Figure 9: q vs ε_a relation with $D_{\rho f}$= 100 %, Pc=10

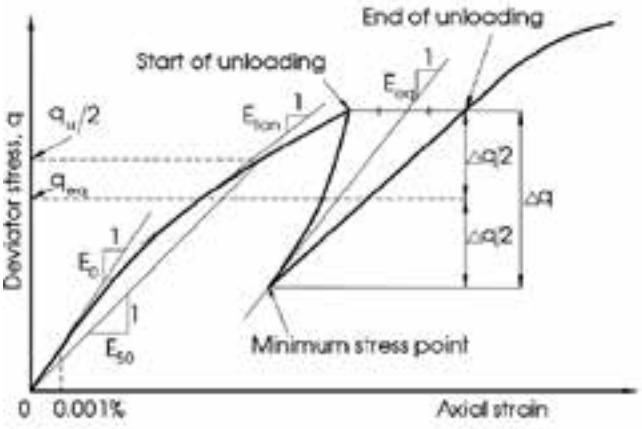

Figure 10: Definitions of E_0, E_{tan}, E_{eq}.

3.1.2. Effect of curing time

As shown in Figure 7 that the relationship between q_{max} and curing time t by both logarithms is linear[7] $q_{max}=a\times(t)^b$. In both logarithm plots, the value of "n" represents the slope of the line created by a linear fit. This value becomes smaller than in cases of added fiber material (Pc=10) and cured in-situ. It means that the effect of aging on the increasing rate of strength of LSS becomes small due the addition of fiber material and cured in-situ. Figure 8 and 9 show the relationship between q and ε_a up to ε_a=3.5% based on LDTs measurement for various conditions (mixture, curing) with a changing rate of slurry density $D_{\rho f}$=100% at prescribed curing time. It was found that the maximum deviator stress q_{max} increased with increasing curing time in most cases.

3.2. The normalized relationships between E_{tan}/E_0, E_{eq}/E_0 and q/q_u

Various Young's moduli are defined as shown in Figure 10 in this study. The initial Young's modulus E_0 is defined as an initial stiffness at of ε_a less than about 0.001% measured with LDTs. The E_{tan} is defined as a tangential gradient in q~ε_a curve. This value was obtained by deviating from the fitted quadratic equation for q~ε_a relation at a small εa range, and it indicates the non-linearity of the deformation property in q~ε_a curve. The value of peak-to-peak secant modulus from an unload/reload cycle is defined as the equivalent Young's modulus, E_{eq}[7]), as shown in Figure 10.

Figures 11 to 14 show the normalized relationship between E_{tan}/E_0 vs. q/q_{max} and E_{eq}/E_0 vs. q/q_{max}, respectively, in different cases.

3.2.1. Effect of slurry density

Figures 11 a) and 11 b) showed that there was a remarkably increasing or decreasing tendency in the non-linearity of the normalized relationship between E_{tan}/E_0 vs. q/q_{max} when the decreasing/increasing rate of slurry density with specimens cured at indoors was Pc = 0, 10 at 42 days of curing. By contrast, the normalized tangent modulus E_{tan}/E_0 exhibits a strong nonlinearity tendency when the slurry density rate is decreased and increased in in-situ specimens, as shown in Figure 11 d).

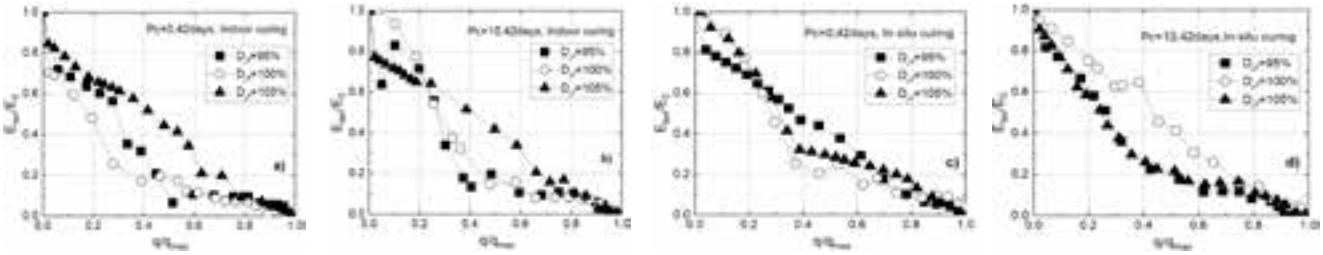

Figure 11 : Effect of slurry density on normalized relations between E_{tan}/E_0 vs. q/q_{max}

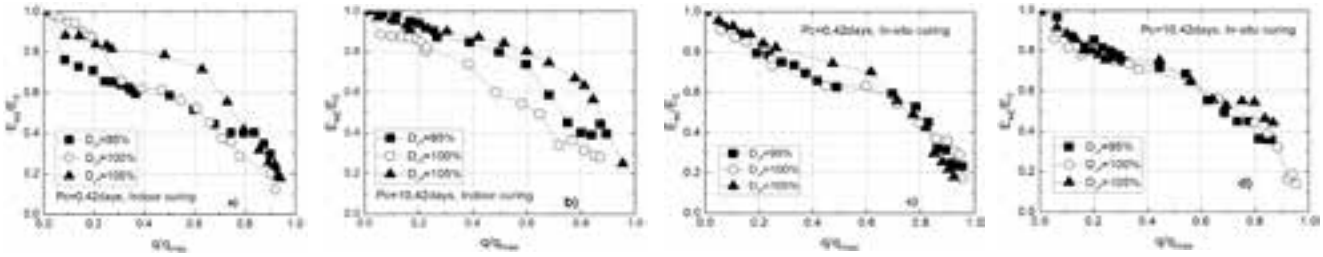

Figure 12: Effect of slurry density on normalized relations between E_{eq}/E_0 vs. q/q_{max}

Figure 12 shows the normalized relationship between E_{eq}/E_0 and $q/_{qmax}$. The E_{eq}/E_0 value almost often increases with increasing slurry density, whereas the trend with decreasing densities is the same. However, as seen in Figure 12 d), the normalized relationship between E_{eq}/E_0 and q/q_{max} seems to be generally independent of slurry density when fiber material is mixed at in-situ. As a result, the effect of changing the slurry density on the in-situ LSS added fiber material is much more non-linear in the pre-peak region, more ductile in the post-peak region, and more stable in terms of damage degree.

3.2.2. Effect of curing time

Figures 13 and 14 show the influence of aging time on the pre-peak non-linearity deformation property of the stress-strain relationship. There was a slightly increased normalized relation of E_{tan}/E_0 with increasing curing time for LSS in both the indoor and in-situ cases, as shown in Figures 13 a) and c). The decreasing tendency of non-linearity of pre-peak deformation property is large at a long time of curing (126 days) in most cases. However, by adding fiber material into specimens cured at in-situ, the tendency of pre-peak non-linearity behavior of the stress-strain curve seems to become rather independent of curing time in Figure 13 b) and d). Moreover, it can be seen that it is difficult to predict the influence of curing time on the non-linearity of pre-peak deformation property due to uncontrolled environmental conditions.

Figure 14 showed that the damage degree under shear stress level for indoor curing in both cases of no fiber and adding fiber seems to become more independent of curing time. Meanwhile, the E_{eq}/E_0 for in-situ curing is larger than when compared with indoor cases. In particular, by mixing fiber material at in-situ, the remarkable effect of aging on the normalized relation between E_{eq}/E_0 and q/qmax is large, as shown in Figure 14 d). In which, there was a remarkably increase in E_{eq}/E_0 by curing time with normalized shear stress level due to both a decrease in the viscous deformation component during small unload/reload cycle by curing time

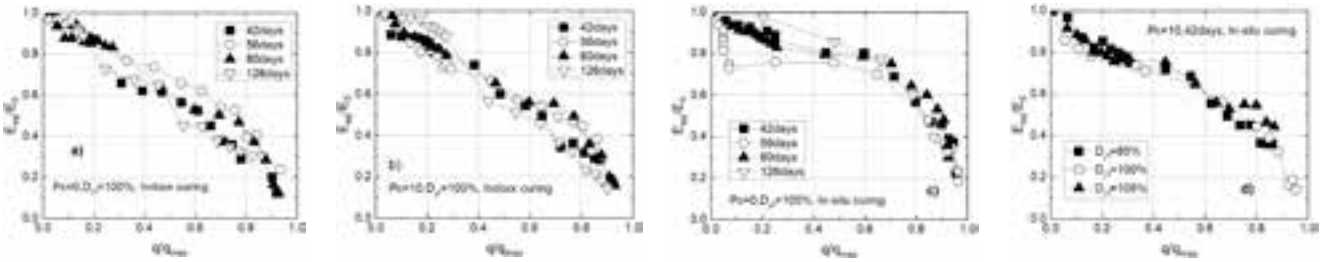

Figure 13: Effect of curing time on normalized relations between E_{tan}/E_0 vs. q/q_{max}

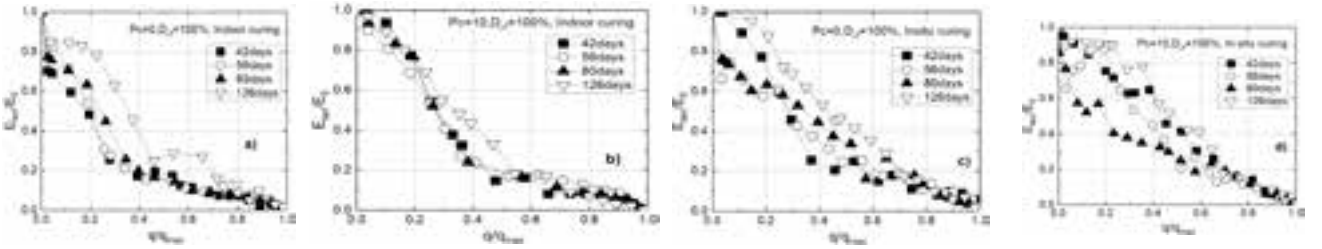

Figure 14: Effect of curing time on normalized relations between E_{eq}/E_0 vs. q/q_{max}

(xem tiếp trang 38)

Strength reduction of mudstone embankment due to change in water content

Tetsuo Abe[(1)], Yuki Hashimoto[(2)], Nobuo Mishima[(3)], Shima Kawamura[(4)]

Abstract

In August 2009, the Suruga Bay earthquake caused the collapse of an embankment on the Tomei Expressway, Japan. According to later investigation, the main cause was the embankment materials with slaking property became finer due to the seepage of rainwater and groundwater, and the embankment caused a decrease in strength. However, since it has been known that the fine granulation of the embankment materials by slaking will be completed in about 10 years after the construction, in actual, the collapsed embankment has been in service for 40 years. The authors do not evaluate that the fine granulation is the only cause of the collapsed embankment. Instead, we focused on the fact that the water content increased with the granulation, and confirmed the effect of the increase in water content on strength behavior by experiments. The results indicated that the reduction in strength of embankments made of slaking materials depends not only on the fine granulation of the embankment materials, but also on the increase in water content.

Key words: *mudstone, embankment, slaking, fine granulation, water content, strength reduction*

(1) Chief, Geotechnics Division, Road Research Department, Nippon Expressway Research Institute Company Limited, Email: <t.abe.af@ri-nexco.co.jp>

(2) Researcher, Geotechnics Division, Road Research Department, Nippon Expressway Research Institute Company Limited, Email: <y.hashimoto.ab@ri-nexco.co.jp>

(3) Special senior researcher, Geotechnics Division, Road Research Department, Nippon Expressway Research Institute Company Limited

(4) DE, Professor, Graduate School of Engineering, Muroran Institute of Technology, Email: <skawamur@mmm.muroran-it.ac.jp>

Date of receipt: 15/4/2022
Editing date: 6/5/2022
Post approval date: 5/7/2022

1. Introduction

In August 2009, a magnitude 6.5 earthquake that occurred in Suruga Bay off the coast of Omaezaki, Shizuoka Prefecture, Japan, caused a disaster that resulted in the collapse of the embankment of the Tomei Expressway. Later investigation, clarified that the main cause was the embankment materials with slaking property. Neogene mudstone, became gradually finer and finer over time due to repeated dry and wet conditions caused by seepage of rainwater and groundwater, this process resulted in a decrease in the strength of the embankment (Takagi et al., 2010). However, it has been generally said that the fine granulation of embankment materials by slaking is completed about 10 years after the embankment construction (Nakamura, 2014). Since the embankment that collapsed was already in service 40 years ago, therefore, we evaluated that the fine granulation of the embankment materials was not the only cause of the embankment collapse. In this study, we focused on the fact that the water content of embankment materials made of slaking materials such as mudstone increases as the materials become finer due to slaking, and confirmed the effect of the increase in water content on strength behavior by experiments.

2. Experiments

2.1. Soil materials used in the experiments

The physical properties of the soil used in the experiments are shown in Table 1. This soil material (referred to as "Kobe 5") was sampled from the ground near the Kobe Junction during the construction of the Shin-Meishin Expressway between Takatsuki and Kobe, which was in service in March 2018, and is mainly mudstone with slaking property. The stratum containing this mudstone has been called the "Kobe Group", which was formed 32-35 million years ago during the late Eocene to Oligocene period of the Cenozoic Era. The mudstone of the Kobe Group is a geomaterial characterized by a high slaking rate and a low crushing rate. In the construction of the Sanyo Expressway between Kobe Junction and Miki-Ono Interchange, which is near this area, embankments were constructed without sufficient crushing and compaction of the embankment materials. The high slaking rate and low crushing rate of the embankment materials were a problem, after that, the slaking caused the embankment materials to become fine-grained, leading to large-scale compressive settlement in service (Shima and Imagawa, 1980). The "slaking rate" is a physical property determined by “NEXCO Test Method 110: Test method for slaking of rocks”. This test is used to evaluate the durability of weak rocks. After measuring the mass of the sample in its natural state, it is oven dried at 110± 5°C for 24 hours to measure the mass, and then it is immersed in water for 24 hours. After 5 cycles of dry and wet repetition of the same operation, the "slaking rate" is defined as the ratio of the dry mass passing the 9.5 mm sieve to the total dry mass. The greater the reduction, the lower the slaking resistance is evaluated. The "crushing rate" is a physical property value obtained by “NEXCO Test Method 109: Test method of crushing of rocks”. In this test, rocks remaining on a 37.5mm to 19mm sieve are placed in a mold with an inner diameter of 150mm and loaded until the axial load reaches 2MN/m^2 to determine the degree of crushing.

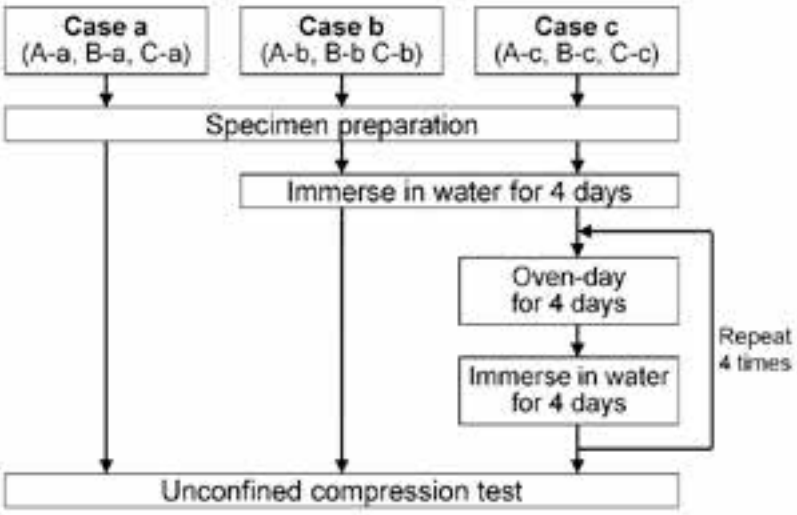

Figure 1: Flow chart of experiments

The ratio of the mass passing through the 9.5mm sieve after crushing to the total mass before loading is defined as the "crushing ratio. The higher the crushing ratio, the weaker the rock is.

Table 1: Physical properties of "Kobe 5" mudstone used in the experiments

Natural water content	w_n	17.4	%
Soil particle density	ρ_s	2.701	Mg/m^3
Slaking rate		100	%
Crushing rate		44.0	%
Optimum water content	w_{opt}	22.5	%
Maximum grain size		300	mm

2.2. Experimental method

In the experiments, some of cylindrical specimens of 100mm in diameter and 200mm in height were prepared using this mudstone material (but with a maximum grain size of 37.5mm or less), and unconfined compression tests were conducted to determine those of unconfined compression strength. The conditions for preparing the specimens are shown in Table 2. Three different dry densities (ρd) were set for the preparation of the specimens: ρ_{dA}, ρ_{dB}, and ρ_{dC}. Thereafter, they are called the A series, B series, and C series, in each series. Three specimens under the same dry density were provided for each series. In preparing the specimens, the mudstone material was prepared so that the dry density (ρ_d) was set for each series and the air content (υ_a) was 15%, and was statically compacted in four layers, one layer at a time, using an Amsler-type load testing machine. After that, unconfined compression tests were performed on three specimens, in each series, as shown in Figure 1. The unconfined compression test is specified in JIS A 1216 (2020) and applies compression to a cylindrical specimen continuously at a rate of 1% compressive strain per minute. During compression, a displacement meter measures the amount of compression ΔH (mm) and a load cell measures the compressive force p (N). From the results, the compressive stress σ (kN/m^2) and compressive strain ε (%) are calculated and a stress-strain curve is drawn to determine the unconfined compressive strength qu (kN/m^2) from the maximum compressive stress. One specimen was tested in its as-is condition (Case a) after specimen preparation, and the other one was tested after being immersed in water for four days (Case b). This Case b simulates the increase in water content in the embankment due to the infiltration of rainfall and groundwater into the embankment. The last other specimen was immersed in water for four days after specimen preparation, and then tested after five cycles of "four days of oven drying (110°C) and four days of water immersion" as one cycle (Case c). This Case c simulates how mudstone materials become finer due to the repeated action of drying and wetting after rainfall or groundwater infiltrates in the embankment.

Figure 2 illustrates the concept of these experiments. The compaction control standard for mudstone embankments (embankments using mudstone materials with a slaking rate of 30% or more and a crushing rate of 50% or less) on expressways managed by East Nippon Expressway Company, Central Nippon Expressway Company, and West Nippon Expressway Company (referred to as "NEXCO") requires that the dry density (ρ_d) in the field be 90% or greater than the maximum dry density (ρ_{dmax}) obtained by method B of "JIS A 1210 (2020): Test method for soil compaction using a rammer" and that the air content (υ_a) be 15% or less (the red hatch in Figure 2 (compaction curve) is applicable).

Table 2: Dry density and air content for each series of experiments

Series	Dry Density ρ_d (Mg/m^3)	Air Content υ_a (%)	Initial water content w_0 (%)
A	ρ_{dA}	15	w_A (=w_n)
B	ρ_{dB} (ρ_{dmax} x 0.93)	15	w_B
C	ρ_{dC} (ρ_{dmax} x 0.90)	15	w_C

The condition that satisfies this minimum compaction control standard is at point C-a (ρ_{dC} =ρ_{dmax}×0.9, υ_a =15%) in Figure 2. In addition to point C-a, there are points A-a and B-a on the 15% air content curve. Point A-a is the dry density at natural water content (ρ_{dA}= ρ_{dwn}), and Point B-a is the dry density between points A-a and C-a (ρ_{dB} was set to ρ_{dmax} x 0.93 for this test) to complement point A-a and point C-a. The condition of these specimens is the initial state (Case a) and is regarded as the condition immediately after the construction of the embankment. From these initial conditions, the process moves to the water absorption and retention process (Case b), which assumes rainwater and groundwater seepage, and the slaking process (Case c), which assumes fine graining of the mudstone materials by slaking.

The detailed explanation using the C series is as follows; Point C-a is the embankment that has been under the condition that satisfies the minimum compaction control standard. Subsequently, by immersing the specimen in water for four days, the dry density (ρ_{dC}) does not change, but point C-a moves to point C-b as water seeps into the specimen and the water content increases (representing the

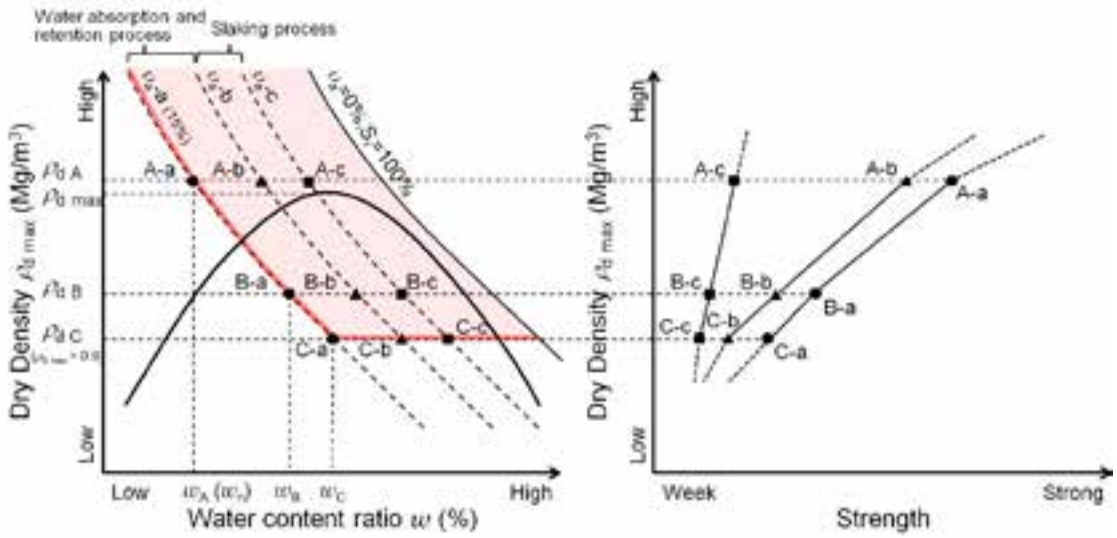

Figure 2: Conceptual diagram of experiments

water absorption and retention process of the embankment material). Furthermore, it is expected that the mudstone material in the specimen will become finer and water seepage will occur further in the specimen by repeating the drying and wetting process five times afterwards. At this time, the dry density does not change, but the water content increases, so the condition of the specimen changes from point C-b to point C-c, as shown in Figure 2 (representing the slaking process of the embankment material). By then determining the strength characteristics of each specimen, it would be possible to distinguish whether the reduction in strength of the mudstone embankment constructed was caused by the increase of water content due to rainwater and groundwater seepage, or whether the reduction in strength due to slaking.

2.3. Experimental results

Figure 3 shows the results of the experiments. Figure 3 embodies the conceptual diagram of the experiment shown in Figure 2 based on the results of the experiments. This one is also explained using the C series (point C-a, point C-b and point C-c) as an example. When the condition of the specimen changes from point C-a to point C-b, which is the water absorption and retention course, the unconfined compression strength of the specimen decreases by about 40%. Furthermore, when the condition of the specimen changed from point C-b to point C-c, which assumes a fine-grained course due to slaking, the unconfined compression strength of the specimen was further decreased by about 30%. Similar trends were seen in the A series and B series.

3. Conclusions

The test results indicated that the reduction in strength of embankments constructed from slaking materials (referred to as "weak rock embankments") depends not only on the finer grain size of the embankment materials but also on the increase in water content. When slaking materials such as mudstone are excavated from the ground, they are on the dry side of the optimum water content. It is expected that the water content of weak rock embankments will naturally increase after the embankment is constructed due to water absorption and retention by rainwater and groundwater seepage. Since it is not easy to completely block the seepage of rainwater and groundwater, which are the sources of water supply, and a decrease in the strength of the weak rock embankments

(xem tiếp trang 62)

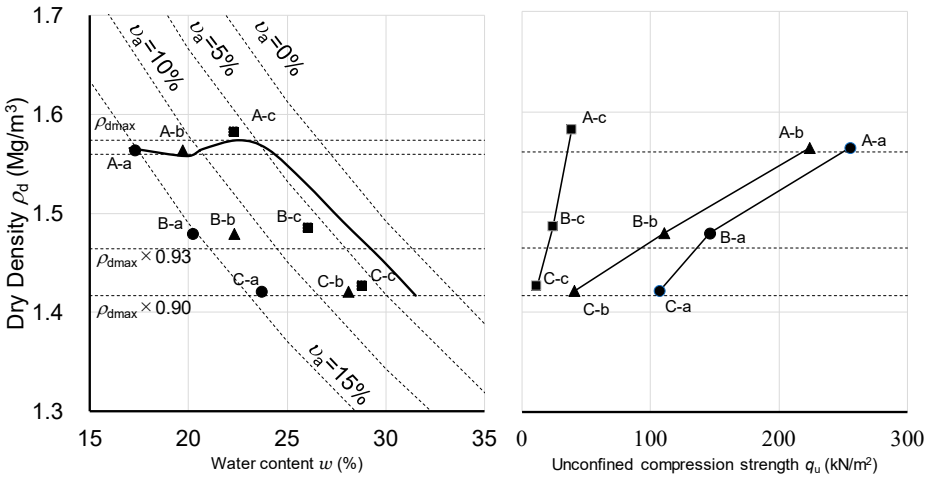

Figure 3: Relationship among dry density and water content and unconfined strength for each series

One-dimensional compressibility and shrinkage behavior of an initially saturated clay

Manh Cuong Le[(1)], Diethard König[(2)], Yukang Wang[(3)] and Gunnar Heibrock[(4)]

Abstract

This paper presents the experimental study on one-dimensional compressibility behavior, soil water characteristic and soil shrinkage behavior of slurry Amberger kaolin. Soil water characteristic curve (SWCC) (Sr-ψ) was determined using conjunction between SWCC (w-ψ) and soil shrinkage curve (w-e). The oedometer test was performed with a maximum applied vertical stress of 6.4 MPa. The volume change behavior of sample due to the suction and that due to applied vertical stress demonstrated a similarity within the saturation domain.

Key words: *Oedometer test, unsaturated soil, suction, shrinkage*

(1)Doctoral candidate, Chair of Soil Mechanics, Foundation Engineering and Environmental Geotechnics, Ruhr-Universität Bochum, 44801 Bochum, Germany. E-mail: manh.le@rub.de

(2)Senior Lecturer, Chair of Soil Mechanics, Foundation Engineering and Environmental Geotechnics, Ruhr-Universität Bochum, 44801 Bochum, Germany. E-mail: diethard.koenig@rub.de

(3)Doctoral candidate, Dep. Of Civil Engineering and Design, Univ. Applied Sciences, 67659 Kaiserlautern, Germany. E-mail: Yukang.Wang@hs-kl.de

(4)Professor, Dep. Of Civil Engineering and Design, Univ. Applied Sciences, 67659 Kaiserlautern, Germany. E-mail: Gunnar.Heibrock@hs-kl.de

Date of receipt: 15/4/2022
Editing date: 6/5/2022
Post approval date: 5/9/2022

1. Introduction

Consolidation process concerns the mechanical process in which volume of the soil changes due to a change in applied pressure. Tezaghi (1943) was the first to introduce a theory to describe the consolidation process. At first, when the soil is subjected to an increase in applied pressure, the liquid phase which is considered as an incompressible phase absorbs almost entirely the external pressure, this results in excess pore water pressure. With time, as the seepage occurs, the soil skeleton which is virtually compressible starts to carry the applied pressure gradually. The effective stress is mathematical expressed as (Tezaghi 1936):

$$\sigma' = \sigma - u_w \quad (1)$$

Oedometer tests are used widely commonly to determine one-dimensional compressibility of the clays. A number of studies have been carried out in an attempt to understand various aspect of compressibility behavior of clays (Sridharan et al. 1986, Burland 1990, Fleureau et al. 1993, Mitchell 1993, Nagaraj et al. 1994, Bo et al. 2002, Marcial et al. 2002, Hong et al. 2010, Baille et al. 2014, Baille et al. 2016).

However, soils under partially saturated conditions comprise of three phases. The volume changes of unsaturated soil due to the change of applied pressure is a complex mechanism of interaction between solid, air and water phase (Yidong and Lu 2020). The volume change of the soil is virtually dominated by the effective stress. Bishop (1959) and Bishop (1960) were the first who tried to extend the effective stress concept of Tezaghi to unsaturated soil which has been considered as single stress variable approach.

$$\sigma' = (\sigma - u_a) + \chi \cdot \psi \quad (2)$$

where σ' is the effective stress, σ is the total normal stress, ψ is the matric suction and equal to the difference between ua (pore air pressure) and uw (pore water pressure). χ is the effective stress parameter which has been considered as the upscaling function capturing the contribution of suction to the effective stress.

On the other hand, Fredlund and Morgenstern (1977) suggested an approach of two stress state variables when dealing with volume change and shear strength behavior of unsaturated soil. From a micromechanical point of view, Lu and Likos (2006) introduced the term of suction stress which could be defined as the sum of interparticle forces per unit area intersecting a representative elementary volume of the soil. Fleureau et al. (1993) investigated the drying and wetting path behavior of clayey soils and compared the result with the void ratio – applied pressure relationship obtained from oedometer tests in saturated condition. They concluded that the volume change behavior of the soil from drying path and oedometric compression path are equivalent. Baille (2014) performed water retention and oedometer compression tests at high pressure regime on three types of clays. The author pointed out the validity of Tezaghi's effective stress concept within the saturated regime. To establish the relationship between void ratio and suction following the drying path, the precise volume measurement plays a crucial role.

The primary objective of this paper is to establish soil water characteristic curve (SWCC) and soil shrinkage curve (SSC)

of slurry clay. The secondary objective is to perform the oedometer compression tests on the slurry clay with the applied pressure up to 6,4 MPa. Afterward, the validity of effective stress concept within the saturated domain was examined based on the volume change behavior of the studied clay obtained from drying path of SWCC and the one achieved from oedometric compression path.

2. Material

Amberger kaolin was used in this study. The kaolin was exploited from the mines located in Germany by Amberger Kaolinwerke Eduard Kick company. The main component of kaolin is about 80% of mineral kaolinite. The basic properties of the soil are summarized in Table 1. The soil was mixed with the predetermined amount of water corresponding to 1.1wL (slurry mixture). Afterward, the mixture was stored in some sealed bags and a closed bucket for 4 days to achieve homogeneous condition in water content distribution. Eventually, using the mixture, the sample preparation was performed for the soil shrinkage test, SWCC and the oedometer compression test.

Table 1: Material properties of Amberger kaolin

Properties	Amberger kaolin (AK)
Specific gravity, G_s	2.639
Liquid limit, w_L [%]	56.6
Plastic limit, w_P [%]	40.1
Plasticity index, I_P [%]	16.5
$1.1 \cdot w_L$ [%]	62.26
USCS	MH

3. Apparatus used and test procedure

The apparatus used for establishment the SWCC was the chilled mirror hygrometer (Aqualab) which is based on the dew point technique to measure the total suction of a soil sample. Leong EC et al. (2003) described the detail of this technique as a precise manner to measure the water potential of a soil sample. A desiccator with Natri Hydroxide (NaOH) corresponding to 330MPa suction was used in this study.

First of all, the dry Amberger kaolin was mixed with predetermined amount of 1,1wL. After storing phase in 4 days as mentioned in the manuscript, the cups with known dimension and weight were filled with the mixture. The criterion used to assess the identical condition of the samples was based on the known dimension of the cups (3 cm in diameter and 0.5 cm in height), the initial water content, the weight of samples after pasting and therefore the initial void ratio of the sample. The samples were weighted to determine the initial condition and immediately transferred to the desiccator. Afterward, the sample was measured the weight using a precise digital balance and the relative humidity using the Aqualab regularly. Adopting the Kelvin's equation (see eq. 3), the total suction can be calculated from the measured relative humidity.

$$\psi_{tot} = -\frac{RT}{M_w(1/\rho_w)}\ln\left(\frac{RH}{100}\right) \quad (3)$$

Where ψ_{tot} is the total suction (kPa), R is the universial gas constant (8.314 J/mol K), T is the absolute temperature (K), Mw is the molecular weight of water (18.016 kg/kmol), ρ_w is the unit weight of water (kg/cm^3) as the function of temperature and RH is the measured relative humidity in percent. The total suction is significantly sensitive to temparature changes. Therefore, the desiccator with the samples and the Aqualab were placed in the relative humidity and temperature-controlled room. Figure 1 shows the device used for SWCC determination.

In order to determine soil shrinkage curve, the immersion weighing method was adopted. A series of samples which were identical to the samples of SWCC were prepared. The samples were placed in some large ceramic trays and were allowed to air dry slowly using plastic membrane covering on top of the tray. To maintain the constant condition, the test was conducted in the controlled relative humidity and temperature room. At predetermined certain values of water content, a sample was submerged into paraffin oil to measure the volume of sample and therefore the void ratio. The experimental setup for soil shrinkage curve is shown in Figure 2.

The ELE oedometer device was adopted to investigate the one-dimensional compressibility behavior of the

Figure 1: (a) Chilled mirror hygrometer and (b) Samples in the desiccator

Figure 2:

(a) Samples under drying process and

(b) A precise balance and paraffin oil

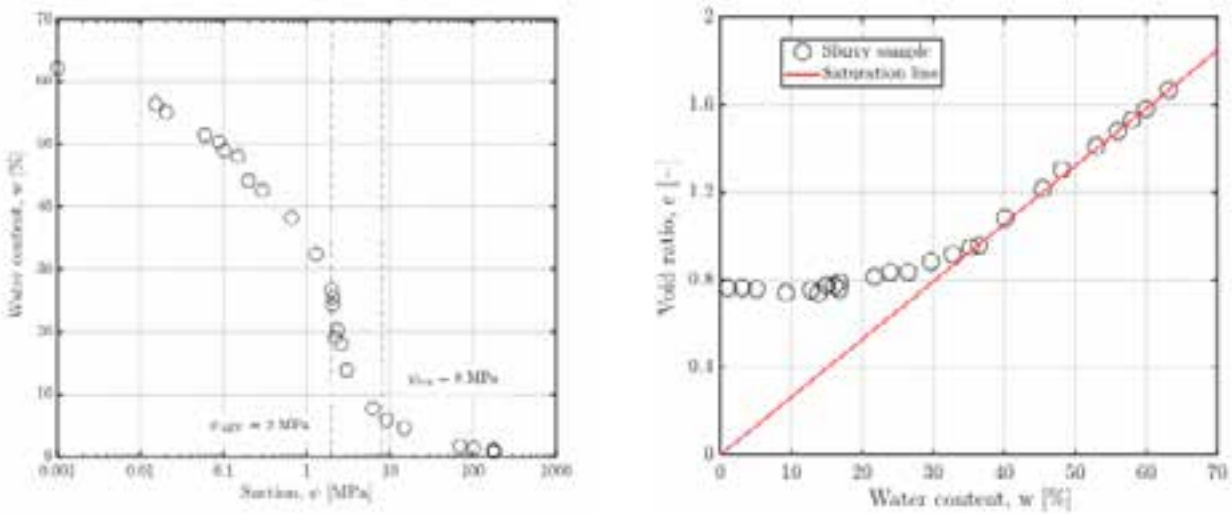

Figure 3: (a) SWCC of the slurry sample and (b) SSC of the slurry sample

slurry sample. The slurries were carefully pasted into the oedometer ring which has dimension of 5cm in diameter and 2cm in height. The initial condition of sample was calculated from the initial volume and water content. After placing the oedometer ring containing the sample in the oedometer cell, the loading frame was assembled. The vertical displacement of sample was monitored using a high precise displacement sensor. A series of successive loads equal to 6.25, 12.5, 25, 50, 100, 200, 400, 800, 1600, 3200 and 6400 kPa were applied.

4. Results and Discussion

The effect of applied suctions on the water content are shown in Figure 3a. Using the conjunction between water content, void ratio and degree of saturation, the degree of saturation was determined and are shown in Figure 4a with respect to suction. Generally, three zones were observed in the SWCC. The saturated zone was the zone between soil suction ψ = 0kPa and the air-entry value (ψ_{AEV} = 2.0MPa) which was determined based on the best-fit of the Sr-ψ data using the model of Fredlund and Xing (1994). The relationship between the degree of saturation and the suction was virtually linear in the saturation domain. In the transition zone (>(ψ_{AEV}), a pronounced increase in the rate of reduction in the water content and also the degree of saturation of sample could be seen. In the residual zone (ψ>10MPa), the increase in applied suction resulted in inconsiderable decrease in the degree of saturation.

Figure 3b depicts the soil shrinkage curve of the slurry sample. When the soil was in saturation condition, the decrease in void ratio due to the reduction of water content was a linear relationship. After passing a value about 40% in water content, the shrinkage curve started deviating from the saturation line followed by a mostly constant value in the void ratio which is related to the shrinkage limit of sample. This phenomenon has been explained by Sridharan and Prakash (1998). The surface tension which increase as the radius of meniscus increase is the main component of capillary stresses. During drying process, the sample is in desaturation range, the suction stress which contributes to effective stress and therefore shear strength of the soil is mainly dominant by the capillary stresses. As a result of reduction water in the pore system, the process of equalization between the shear strength and the shear stresses induced by the capillary stresses occurs and the void ratio reachs a constant value when the stress equilibrium achieves.

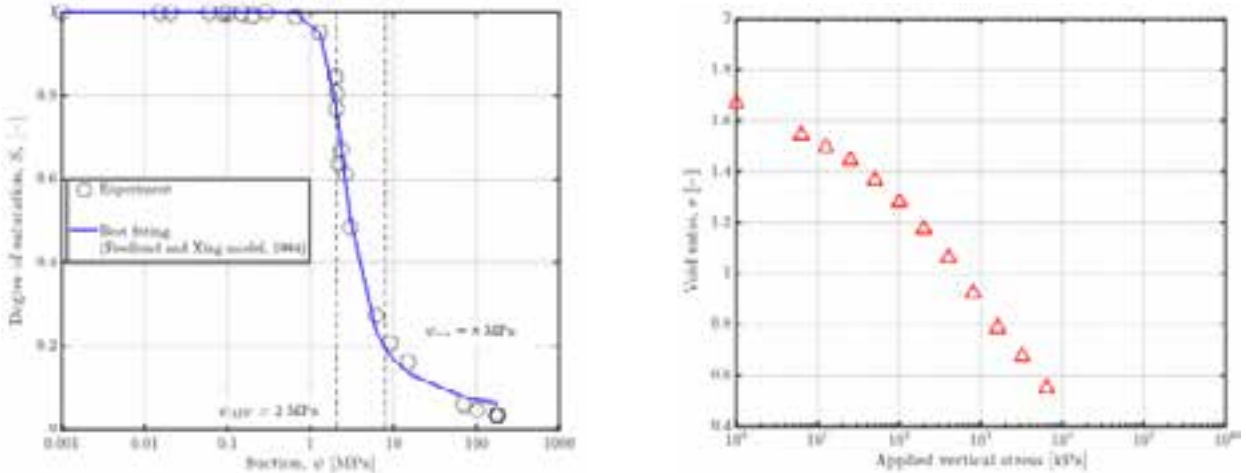

Figure 4: (a) SWCC (Sr-ψ) and (b) Oedometer test result

The oedometer test result of the slurry sample is shown in Figure 4b. The void ratio of slurry sample decreased significantly as the applied vertical stress increased. The compression path of the sample exhibited a slight curve at streses smaller than 300kPa, while a linear behavior was found at stresses greater than 300kPa.

Figure 5 shows a comparison between one-dimensional compressibility path and the suction versus void ratio relationship. For the suction or applied vertical stress below 800kPa, there was an equivalent correlation between two curves which indicated that both applied vertical stress and suction had similar effect on the volume change of the sample. For the suction from 800kPa to 2000kPa, the volume change of the sample due to the external loading (i.e. applied vertical stress in oedometer test) was found to be slightly smaller than that due to the internal loading (i.e. suction stress). Such behavior may be due to the oriented fabric or the rearrangement of pore system of sample which is more sensitive to the high applied vertical load (above 800kPa).In general, this indicated the validity of Tezaghi's effective stress concept within saturation regime. The results coincide with the test results published by some researchers for different types of clay (Baille 2014, Tripathy et al. 2010).

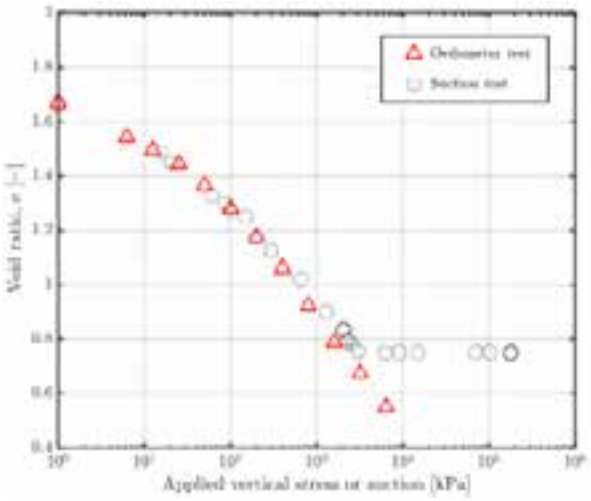

Figure 5: Influence of applied vertical stress and suction on volume change behavior of slurry Amberger kaolin

5. Conclusions

The one-dimensional compressibility, soil water characteristic and soil shrinkage behavior of slurry Amberger kaolin was studied. Using the conjunction between SWCC (w-ψ) and soil shrinkage curve (w-e), the SWCC (Sr-ψ) was established. The oedometer test was performed with a maximum applied vertical stress of 6.4 MPa. For the slurry Amberger kaolin, the volume change behavior of sample due to the suction and that due to applied vertical stress was found to be very similar within the a range of suction smaller than air entry value./.

References

1. *Baille, W., Tripathy, S. & Schanz, T. (2014), 'Effective stress in clays of various mineralogy', Vadose Zone Journal 13(5), 1–10.*
2. *Baille, W., Lang, L.Z.,Tripathy, S. & Schanz, T. (2016), Influence of effective stress on swelling pressure of expansive soils, 3rd European Conference on Unsaturated Soils September 12–14, 2016, Paris, France, E3S Web Conf. 9, 14016.*
3. *Bo, M.W., Choa, V. and Wong, K.S. Compression tests on a slurry using a small-scale consolidometer. Canadian Geotechnical Journal. 39(2): 388-398. https://doi.org/10.1139/t01-112*
4. *Burland, J. B. 1990. On the compressibility and shear strength of natural clays. Geotechnique 40(3): 329–378.*
5. *Bishop, A. W. (1959), "The Principle of Effective Stress," Teknisk Ukeblad, Oslo, Norway, Vol. 106, No. 39, pp. 859-863.*
6. *Bishop, A. W. (1960), "The Measurement of Pore Pressure in Triaxial Test," in Proc. Conf Pore Pressure and Suction in Soils. London: Butterworths, 1960, pp. 38-46*
7. *Dong, Y., N. Lu. And Patrick J.Fox. 2020. "Drying-induced Consolidation in Soil"J. Geotech. Geoenviron. Eng. 146 (9): 04020092.*
8. *Hong, Z., J. Yin, and Y. Cui. 2010. Compression behavior of reconstituted soils at high initial water contents. Geotechnique 60(9): 691–700.*
9. *Fredlund, D. & Morgenstern, N. (1977), 'Stress state variables for unsaturated soils', J.Geotech. Eng. Div. Am. Soc. Civ. Eng. 103, 447–466.*
10. *Fredlund, D. & Xing, A. (1994), 'Equation for the soil-water characteristic curve', Can. Geotech. J. 31, 521–532.*
11. *Fleureau, J.-M., Kheirbek-Saoud, S., Soemitro, R. & Taibi, S. (1993), 'Behaviour of clayey soils on drying-wetting paths', Can. Geotech. J. 30, 287–296.*
12. *Leong, E., Tripathy, S. & Rahardjo, H. (2003), 'Total suction measurement of unsaturated soils with a device using the chilled-mirror dew-point technique', Géotechnique 53(2), 173–182.*
13. *Lu, N. & Likos, W. J. (2006), 'Suction stress characteristic curve for unsaturated soil', Journal of Geotechnical and Geoenvironmental Engineering 132(2), 131–142.*
14. *Marcial, D., Delage, P. & Cui, Y. J. (2002), 'On the high stress compression of bentonites', Canadian Geotechnical Journal 39(4), 812–820.*
15. *Mitchell, J. K. (1993), Fundamentals of Soil Behaviour, 2 edn, John Wiley & Sons, Inc.*
16. *Nagaraj, T. S., N. S. Pandian, and P. S. R. Narasimha Raju. 1994. Stress-state-permeability relations for overconsolidated clays. Geotechnique 44(2): 349–352*
17. *Terzaghi, K. (1943), Theoretical soil mechanics, Wiley, New York.*
18. *Terzaghi, K. (1936), The sehearing resistance of saturated soils and the angle between the planes of shear, in 'International Conference on Soil Mechanics and Foundation engineering', Harvard University press, Cambridge, MA.*
19. *Tripathy, S., Bag, R. & Thomas, H. (2010), Desorption and consolidation behavior of intially saturated clays, in E. Alonso & A. Gens, eds, 'Proceedings of the 5th International Conference on Unsaturated Soils', Taylor & Francis, Barcelona, Spain, pp. 381–386*
20. *Sridharan, A., Rao, S. & Murthy, N. (1986), 'Compressibility behaviour of homoionized bentonites', Géotechnique 36(4), 551–564.*
21. *Sridharan, A and Prakash, K., (1998), 'Mechanism controlling the Shrinkage limit of Soils', Geotechnical Testing Journal, GTJODJ, 21(3), 240-250.*

Prediction of bearing capacity of shallow strip foundation: a case study in Binh Dinh-Vietnam

Thi Khanh Ngan Nguyen[1] and Tuan Thanh Tran[2]

Abstract

The bearing capacity (BC) of a shallow foundation is an important parameter to design economic structures. This study aims to propose a safety factor for BC of the strip footings. By utilizing, several geologies to calculate the shallow strip footing of the mid-rise buildings in central Viet Nam. The bearing capacity of the foundation is first calculated using the different available methods such as Terzaghi, Meyerhof, Hansen, and Vesic theories. Then the three-dimensional finite element analysis of the foundation is performed using PLAXIS software. Results indicate that there is a clear difference in the bearing capacity from the theory and numerical model. Additionally, a safety factor is proposed for the design purposes of the shallow strip foundation.

Key words: *Bearing capacity, Shallow Foundation, Strip Footing, PLAXIS*

(1)MS, Lecturer, Faculty of Technology and Technique, Quy Nhon Univesity, Email: <ntkngan@fit.edu.vn>

(2)Ph.D, Institute of Offshore Wind Energy, Kunsan National University, Email: <tranthanhtuan@kunsan.ac.kr>

Date of receipt: 15/4/2022
Editing date: 6/5/2022
Post approval date: 5/9/2022

1. Introduction

The bearing capacity (BC) of shallow foundations is one of the important parts of soil mechanics relevant to foundation design for structures (i.e., buildings, nuclear power plants) [1,2]. Many studies have been conducted to estimate the ultimate bearing capacity of the foundation soil [3-9]. For example, the BC of the liquefied sandy ground under the raft foundation was assessed by Vo and Nguyen [10]. Later, the BC of footing subjected to horizontal load, vertical load, and moment combination was calculated by Nguyen et al. [11]. Unfortunately, the load capacity of the footing under the complexity of soil conditions and loadings has not been particularly pointed in the published studies [6,9]. For instance, geology in Binh Dinh province (Viet Nam) is known as a complex site with limited research on designing the BC of the shallow foundations.

This study aims to evaluate the allowable bearing capacity of the strip footing subjected to uniform vertical loading. Finite element modeling is implemented to analyze the behavior of soil the ground under the strip footing. These results of numerical analysis are verified with existing solutions. The results are useful for engineers to reduce computational time in structural design.

2. Methodology

a. Existing theory for predicting the bearing capacity of the foundation

Ultimate bearing capacity can be expressed as the maximum pressure that a foundation soil can withstand without undergoing shear failure. For the static analysis, the shallow strip footing under vertical central loading can be calculated using different approaches.

Terzaghi's theory.

The bearing capacity equation developed by Terzaghi for the strip foundation is defined as follows [3]:

$$q_u = cN_c + qN_q + 0.5\gamma BN_\gamma \quad (1)$$

where B and D_f are the width and depth of the foundation, repectively; c, γ and q are cohesion, the weight of soil and surcharge at the ground level, respectively; N_c, N_q, N_γ are Terzaghi's bearing capacity factors for a strip foundation depend on angle of internal friction (φ) [1] and are given by equations (2 - 4)

$$N_q = \frac{e^{2\left(\frac{3\pi}{4}-\frac{\varphi}{2}\right)\tan\phi}}{2\cos^2\left(45+\frac{\varphi}{2}\right)} \quad (2)$$

$$N_c = \cot\varphi\left(N_q - 1\right) \quad (3)$$

$$N_\gamma = \frac{1}{2}K_{p\gamma}\tan^2\varphi - \frac{\tan\varphi}{2} \quad (4)$$

Meyerhof's bearing capacity theory

The superposition method is used to determine the contribution c, q and γ. The ultimate bearing capacity (q_u) of the continuous

foundation is expressed as [3]:

$$q_u = cN_c + qN_q + \frac{1}{2}\gamma BN_\gamma \quad (5)$$

where N_c, N_q, and N_γ are variations of Meyerhof's bearing capacity factors, given by Eqs (6 – 8)

$$N_q = e^{\pi \tan\varphi}\left(\frac{1+\sin\varphi}{1-\sin\varphi}\right) \quad (6)$$

$$N_c = \left(N_q - 1\right)\cot\varphi \quad (7)$$

$$\frac{Q_p}{B} = cN_c + \gamma D_f N_q + 0.5\gamma BN_\gamma \quad (8)$$

Hansen's bearing capacity theory

Hansen [5] proposed the equation for the bearing capacity of strip footing as follows

$$\frac{Q_p}{B} = cN_c + \gamma D_f N_q + 0.5\gamma BN_\gamma \quad (9)$$

where Q_p is ultimate bearing capacity; the Hansen's bearing capacity factors N_c, N_q, and N_γ were presented in graphical form in Figure 1.

b. General bearing capacity

The bearing capacity formula for the soil under a shallow strip footing can be calculated by incorporating the shape factors and depth factors. It can be expressed by the following equation [3]

$$Q_u = cN_c\chi_{cs}\chi_{cd} + qN_q\chi_{qs}\chi_{qd} + 0.5\gamma BN_\gamma\chi_{\gamma s}\chi_{\gamma d} \quad (10)$$

where χ_{cs}, χ_{qs}, $\chi_{\gamma s}$ and χ_{cd}, χ_{qd}, $\chi_{\gamma d}$ are shape factors and depth factors, respectively. These factors were determined through empirical and semi-empirical studies; N_c and N_q are obtained from equations (6) and (7), respectively; white N_γ is given by equation (11)

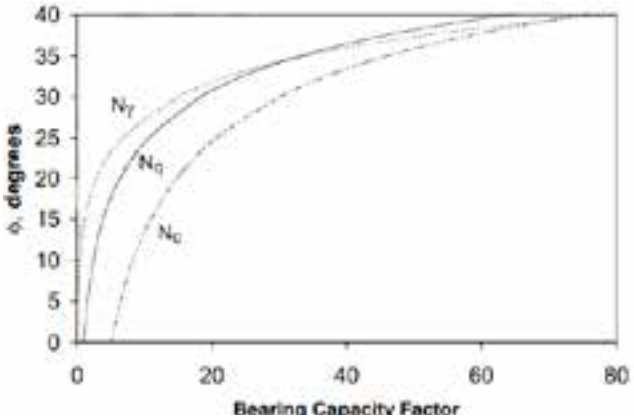

Figure 1: Hansen's bearing capacity factors [3]

$$N_\gamma = 2\left(N_q + 1\right)\tan\phi \quad (11)$$

Gross allowable bearing capacity

Gross allowable bearing capacity (q_{all}) is fomulated to consider both shear failure and settlement of the soil, and it is defined as [5]

$$q_{all} = \frac{q_{ull}}{FS} \quad (12)$$

where (q_{all}) is the ultimate bearing capacity, FS is the safety factor ranging from 3 to 4. [5]

2.2. Finite element modeling

PLAXIS 2D is a well-known software for geotechnical engineering projects, which is used to accomplish the deformation and flow analysis of soil behavior. The 2D analysis can be modeled by a plain stain or symmetrical model.

In this study, Plaxis software is used to analyze the BC of the ground under the continuous foundation. Modeling of

Table 1: Geotechnical input data for the bearing capacity calculations

Site	Soil type	Description	γ(kN/m^3)	γ_{sat}(kN/m^3)	φ(^{0})	c(kN/m^2)	E(kN/m^2)
1	Clayey sand	Soft	20.2	20.6	17.25	17.1	3021.6
2	Fine-grained sand	Medium dense	-	17.5	32	-	6300
3	Medium-grained sand	Medium dense	-	18.4	34.28	-	13200

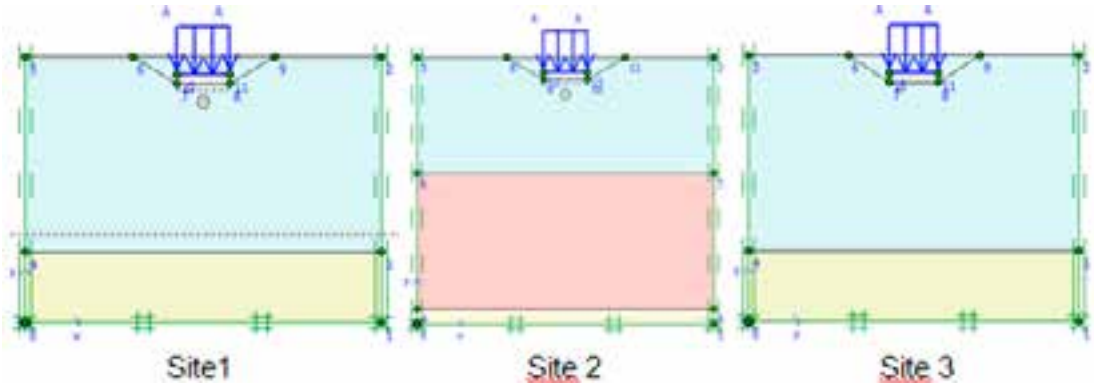

Figure 2: Geometry model in Plaxis 2D. (Site 1) BIDV Bank, (Site 2) Quy Nhon University, and (Site 3) Quy Hoa National leprosy dermatology hospital

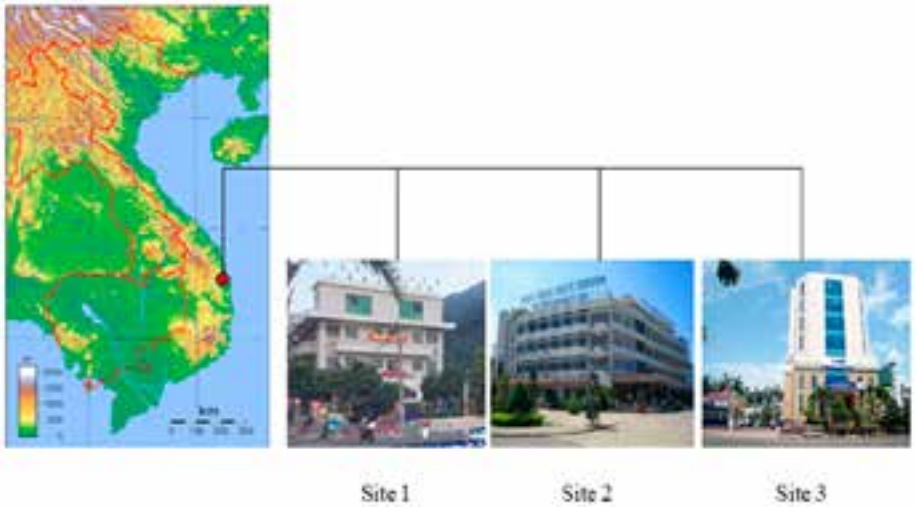

Figure 3: Site Location. (Site 1) BIDV Bank, (Site 2) Quy Nhon University, and (Site 3) Quy Hoa National leprosy dermatology hospital

the shallow strip footing under loading is shown in Figure 2. It is noted that the Mohr-Coulomb model is used for soil, and elastic model behavior is assigned for strip footing. The foundation was divided by a strip footing subjected to vertical and uniform load. The groundwater level is at the ground surface.

3. Numerical example

Binh Dinh is a coastal province of South Central Vietnam, and it is known as a zone of coastal creeks and lagoons. The earth structures were developed by beaches associated with sand deposition. The surface geology was made up of the fine sand or medium sand.

We only mentioned the geological conditions in 3 buildings in Binh Dinh province to analyze the BC of the shallow foundation in this study were illustrated in Figure 3, including Quy Hoa National leprosy dermatology hospital, Quy Nhon University, and BIDV bank. The geotechnical parameters of the investigated sites are listed in Table I. These sites are utilized for designing the mid-rise buildings. The foundation dimensions corresponding to values of 3m, 1.5m, and 0.5m for width, depth, and thickness were selected for this purpose. An analysis is performed for the applied foundation pressure of 50kN/m^2.

4. Results and discussions

The bearing capacity failures for strip footing were calculated by finite element analyses and existing approaches. Note that the effect of shape and depth factors for variations of allowable bearing capacity to each soil group is skipped in this study. The comparison of the permissible bearing capacity for strip footing at a shallow depth of 1.5m for all sites is shown in Figure 4 and Figure 5. In each figure, the obtained results from the existing solutions are compared with those from the numerical modeling. As seen, the allowable bearing capacity of the shallow strip foundation varies from 80 to 300kN/m^2. While, for medium dense sands, these values range from 200 to 300kN/m^2.

Another finding is that outcomes for all cases vary slightly. The variations between theoretical and numerical modelling values range from 6 to 10%, depending on soil types. It is seen that the variation obtained from the Meyerhof method is less than 6% (FS = 4) [5], indicating the best estimations of allowable bearing pressure of the strip footing.

Through the analysis results, the safety factor of 4 for the gross allowable bearing capacity of the strip foundation is recommended for the investigated sites.

5. Conclusions

In this study, a finite element model was made to calculate the BC of shallow strip footing. The Mohr-Coulomb model with drained behavior was used to analyze soil behavior. Material parameters were obtained based on the results from field tests and laboratory tests. A comparison of the numerical and theoretical outcomes are introduced. The following conclusions are drawn:

- The Meyerhof method was the most promising one since it gave only an approximation to the numerical modeling.

- A safety factor of 4 for the allowable footing pressures of the strip footing is recommended for mid-rise buildings.

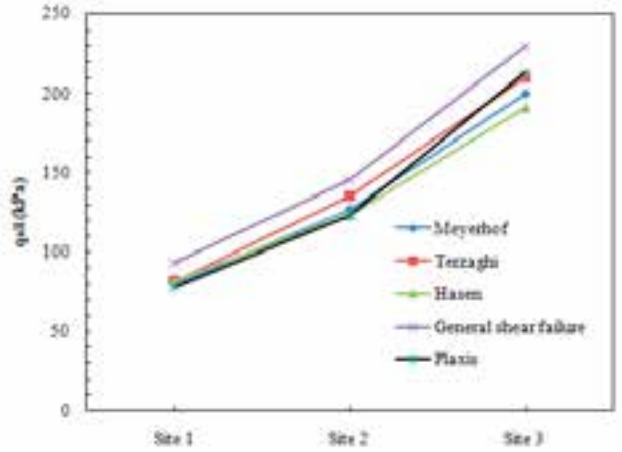

Figure 4: Allowable bearing capacity FS = 4 [5]

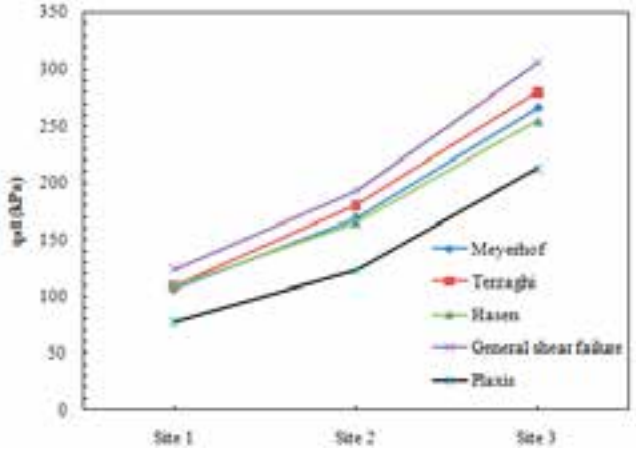

Figure 5: Allowable bearing capacity FS = 3 [5]

The effects of foundation depth and footing geometry are known as significant parameters, which are ignored in this study. Therefore, it is recommended that these effects will be considered for further investigation./.

References

1. *Tran, T. T., Cao, A. T., Kim, D., & Chang, S. (2020). Seismic Vulnerability of Cabinet Facility with Tuned Mass Dampers Subjected to High-and Low-Frequency Earthquakes. Applied Sciences, 10(14), 4850.*
2. *Tran, T. T., Salman, K., Han, S. R., & Kim, D. (2020). Probabilistic Models for Uncertainty Quantification of Soil Properties on Site Response Analysis. ASCE-ASME Journal of Risk and Uncertainty in Engineering Systems, Part A: Civil Engineering, 6(3), 04020030.*
3. *M. D. Braja. Shallow Foundation Bearing Capacity and Settlement, 2th Edition. Taylor & Francis Group, 2009.*
4. *M. D. Braja. Advanced Soil Mechanics, 3th Edition. Taylor & Francis Group, 2008.*
5. *C. R. Lymon, M. I. William, Shin-Tower Wang. Analysis and Design of Shallow and deep Foundations. Taylor & Francis Group, 2006.*
6. *H. A. Taiebat, J. P. Carter. Bearing capacity of strip and circular foundation on undrained subjected to eccentric loads. Geotechnique 52(1) (2002) 61 – 64.*
7. *S. Gupta, A. Mital. Numerical analysis of bearing capacity of rectangular footing. Journal of Physics: Conference Series 1240(1) (2019) 012039.*
8. *B. Móczár, J. Szendefy. Calculation of presumed bearing capacity of shallow foundation according to the principles of Eurocode 7. Periodica Polytechnica civil engineering 61(3) (2017) 505 – 515.*
9. *C. Atala, C. R. Patra, B. M. Das, N. Sivakugan. Bearing capacity of shallow foundation under eccentrically inclined load. Proceedings of the 18th intermational coference on Soil mechanics and Geotechnical engineering (2013) 3439-3442.*
10. *P. Vo, D. D. Nguyen. Assessment of load bearing capacity of liquefied sandy ground under raft foundation. Journal of Science Ho Chi Minh City Open University 51(6) (2016) 68-79.*
11. *D. L. Nguyen, S. Ohtsuka, K. Kaneda. Utimate bearing capacity of footing on sandy soil against combined load of vertical, horizontal and moment loads. Int. J. of Geomate 10(1) (2016) 1649-1655.*

The effect of aging and slurry density on triaxial shear properties...

(tiếp theo trang 27)

with shear stress, and an increase in the elastic component of strain by aging in in-situ specimens. This property is similar to that of cement-treated gravelly soil[5]).

4. Conclusions

Base on the results of a series of undrained triaxial compression tests on LSS mixed with fibered materials and LSS, the following conclusions were obtained.

1) The slurry density had a considerable effect on the strength of LSS. When slurry density is increased, the strength increases by about 40% for both indoor and in-situ curing, whereas reducing slurry density decreases the strength by about 30% and 14% for indoor and in-situ curing, respectively.

2) The influence of shear stress level on the degree of damage appears to be independent of slurry density in case of in-situ curing. This result has practical implications for the application of LSS to increase seismic resistance.

3) By both logarithms, the relationship between qmax and the curing time t of LSS is linear. The effect of curing time on the increasing rate of strength is small in compared to indoor specimens of LSS.

4) By adding fiber into in-situ cured LSS, the effect of curing time on the degree of damage is found to be largely due to a decrease in viscous deformation and an increase in the elastic component of strain.

5. Acknowledgement

The authors express deep gratitude to Mr. Moteki, Mr. Onodera (formerly, graduate and undergraduate student), and Ms. Watanabe, Mr. Okada, and Ms. Xi (undergraduate student of Muroran Institute of Technology) for sample preparation, experiments and data analysis. This work was supported by JSPS KAKENHI Grant Number JP19K04590 (Grant-in-Aid for Scientific Research(C))./.

References

1. *G. Kuno, eds. Liquefied stabilized soil method Recycling technology of construction-generated soil and mud. Gihodo publication, 1997 (in Japanese).*
2. *K. Ito, Y. Kohata, and Y. Koyama. Influence of additive amount of cement solidification on agent on mechanical characteristics of Liquefied Stabilized Soil mixed with fibered material. Japanese Geotechnical Society Hokkaido Branch Technical Report Papers, Vol.51, 131-136, 2011 (in Japanese).*
3. *Y. Cui and Y. Kohata. Influence of cement solidification agent and slurry density on mechanical property of liquefied stabilized soil. International Journal of GEOMATE, Vol.19, Issue 73, 177-184, 2020.*
4. *S. Goto, F. Tatsuoka, S. Shibuya, Y-S. Kim, and T. Sato. A simple gauge for local small strain measurements in the laboratory. Soils and Foundations, Vol. 31, No. 1. 169-180, 1991.*
5. *F. Tatsuoka, and L. Kongsukprasert. Small strain stiffness and non-linear stress-strain behavior of cement-mixed gravelly soil. Soils and foundations, Vol.47, No.2, 375-394, 2007.*
6. *NC. Consoli, JP. Montardo, PDM. Prietto, and GS. Pasa. Engineering behavior of a sand reinforced with plastic waste. J Geotech and Geo Environ Eng., Vol. 128, Issue6, 462-472, 2002.*
7. *F. Tatsuoka and Y. Kohata. Stiffness of hard soils and soft rock in engineering aplications. Pre-failure deformation of Geomaterial, Balkema, Vol.2, 1030-1035, 1995.*

Development of static P-Y curves from experimental measurements based on lateral load tests on onshore drilled shafts

Minh D. Uong[1] and J. Erik Loehr[2]

Abstract

Lateral load tests were performed at two geotechnical research sites. Drilled shafts were instrumented using both strain gages and shape acceleration array devices. Lateral deflection and bending moment profiles were interpreted from strain gages data as well as shape acceleration array data. p-y models were derived from the collected data using a Finite Element Method (FEM) code to match the measured experimental data. Linear and non-linear bending stiffness methodologies were used to develop the p-y curves. These analyses show that significantly different interpretations result when the non-linear bending stiffness is accurately modeled. A computational tool using FEM to incorporate non-linear bending stiffness is described along with analyses performed to compare the predicted lateral deflection and bending moment with experimental results. The evaluation described in this paper indicates the difference between the predicted p-y curves considering cracking and non-cracking concrete sections, as well as significant differences in lateral deflection and bending moment when non-linear bending stiffness is considered.

Key words: *lateral load test, p-y curve, FEM, non-linear bending stiffness*

(1) Ph.D., Faculty of Civil Engineering, Hanoi Architectural University
Geotechnical Engineer, Burns & McDonnell Engineering Company, Inc., Email: muong@burnsmcd.com
(2) Ph.D., P.E., Professor, University of Missouri-Columbia

Date of receipt: 15/4/2022
Editing date: 6/5/2022
Post approval date: 5/9/2022

1. Introduction

One common objective for performing lateral load tests is to establish appropriate p-y models for design of laterally loaded deep foundations. However, the net lateral pressure, p, cannot be directly measured, but rather must be inferred from other measurements via some form of back-calculation to fit some modeled response to the measured response of the deep foundation. This process often requires a number of assumptions regarding the expected structural response of the deep foundation. As illustrated in this paper, such assumptions can have a significant influence of the inferred p-y response.

This paper documents the methodology that was used to develop static p-y curves from experimental measurement results for onshore long flexible drilled shaft, not for the case of cyclic loading or for short rigid pile or for offshore conditions. Background information on the test sites, test instrumentation and test procedure is briefly described. An example of experimental shaft responses in terms of lateral displacements and bending moments along the length of the shaft is presented. Computational program using finite element method developed by the author is used to interpret and derive new p-y curves from the load tests and from the experimental measurement results. Two different methodologies of bending stiffness have been used to verify the reasonable procedure when considering cracking and non-cracking concrete sections. Finally, conclusions drawn from development and evaluation of the proposed procedures and recommendations for implementation and for future work are provided.

2. Lateral Loaded Testing

2.1. Testing Site and Testing Instrumentation

Twenty-five drilled shafts were constructed in Warrensburg and Frankford, Missouri, with diameters ranging from 3 to 5 ft (0.9 to 1.5m) and lengths ranging from 20 to 50 ft (6 to 15m). Each shaft was instrumented with six levels of vibrating wire strain gages, a ShapeAccelArray (SAA), vibrating wire displacement transducers (LVDTs) and dial gages.

All shafts were instrumented with four strain gages at each of six level (24 gages per shaft). The ShapeAccelArray (SAA) devices were used to measure deflection profiles in lieu of a conventional inclinometer. The displacement transducers were connected between the steel casing of the shaft and the reference beam. Mounting the transducers above one another allowed for interpretation of shaft head rotation and displacement at the ground surface. One dial gage was mounted on each shaft during each test. Like the displacement transducers, the dial gages were mounted between the drilled shaft casing and the reference beam. Dial gage measurements were recorded manually in one-minute intervals during testing.

2.2. Lateral Loaded Testing Procedure

The primary focus of the lateral loaded testing program was to measure the response of the foundations subjected to static lateral loading. All tests were performed by pulling two shafts together, so that two foundations were loaded and monitored simultaneously, producing two sets of shaft test results for one individual lateral load test.

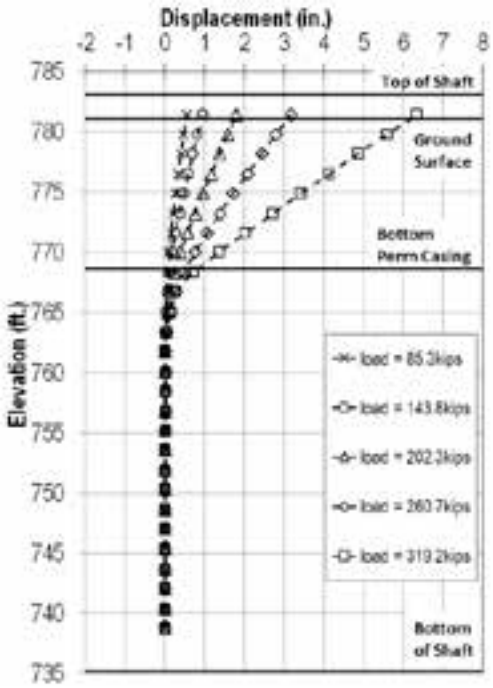

Figure 1: Displacement profiles from SAA measurements (shaft W-9)

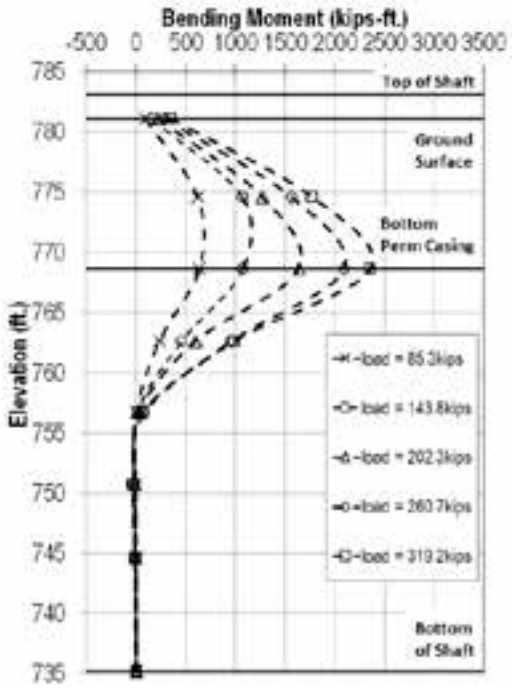

Figure 2: Bending moment profiles from strain gage measurements (shaft W-9)

In general, the lateral load testing program followed ASTM D3966 (2007). The loads were applied for each test following the loading sequence of Procedure B for Static Excess Loading. Loads were applied using the hydraulic system. For each load test, the load was increased in 200-psi increments, corresponding to approximately 30 kips (133.5 kN) using four jacks. The raw data from strain gages, SAA and LVDTs were recorded continuously with data acquisition devices. Readings from dial gages were recorded every minute.

2.3. Experimental Results

Shaft responses were interpreted from the load test data. The shaft response is characterized by the load-displacement behavior at the top of the shaft, the displacement profiles and the bending moment profiles along the shaft length. Figure 1 represents example of displacement profiles interpreted from SAA measurements. Figure 2 shows example of bending moment profiles obtained using strain gage measurements. Only representative data are presented and discussed in this paper, additional displacement and bending moment profiles are included in Boekmann et al. (2014).

The shapes of the displacement profiles in Figure 1 and the shapes of bending moment profiles in Figure 2 are consistent for all load steps. Increasing of lateral load results in increasing of displacements as well as maximum bending moment. Each displacement profile indicates the respective shaft is essentially fixed around elevation 765, which is 2 to 3 ft (0.6 to 0.9m) below permanent casing.

3. Analysis of Experimental Results

A computational program has been developed using finite element method to analyze drilled shafts subjected to lateral loading. The program derives p-y models to produce the best match of experimental measurements shaft responses for a given shaft geometry and loading.

3.1. Methodology to derive p-y curve models

The program employs the conventional p-y models (Reese et al., 2006; Isenhower and Wang, 2011) to predict the response of a drilled shaft subjected to lateral loading. The p-y model can be implemented through the finite element method (FEM), with the shaft modeled with elastic beam elements and the soil modeled as a series of nonlinear springs. Each spring is governed by a p-y curve, where p is the soil resistance on a unit length of the shaft (force/length) and y is the relative lateral deflection between the soil and the shaft (length).

The shaft responses are governed by:

$$([K_p] + [K_s])\{y_p\} = \{F\} \quad (1)$$

in which the code solves using the finite element method to produce shaft deflections and rotations.

In Equation 1:

$[K_p]$ = soil stiffness matrix represented by p-y model

$[K_s]$ = stiffness matrix for all the beam elements forming the drilled shaft

$\{y_p\}$ = vector of shaft deflections and rotations at the shaft nodes

$\{F\}$ = vector of induced lateral forces acting on the shaft

The bending moments are then calculated based on the following equation:

$$\{M\} = [EI] \times \{\kappa\} \quad (2)$$

In Equation 2, bending moments, M, is derived from bending stiffness, EI, and curvature, κ. Finite element method implemented in the program uses shape functions, nodal deflections and nodal rotations to calculate the curvature.

The program applies a p-multiplier to the assumed conventional p-y curve in order to match the experimental measurement shaft responses. The p-multiplier simply factors the values of p on the p-y curves. The program is capable

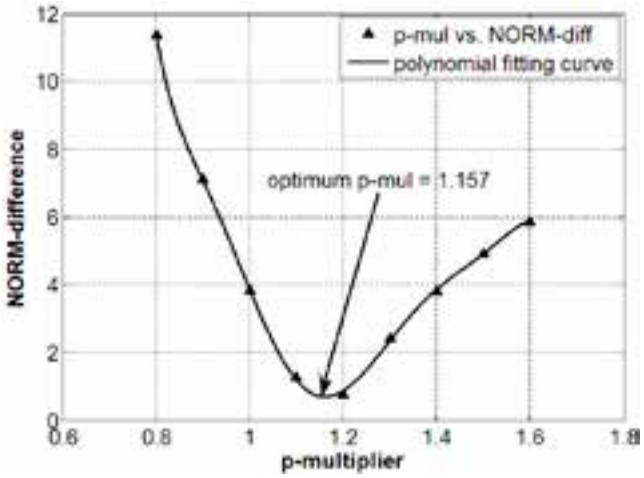

Figure 3: p-multiplier optimization (shaft W-9, load = 319.2kips or 1,420kN)

of matching predicted shaft responses with experimental results, which are displacement profiles from SAA or bending moments from the strain gages. The matching process is outlined in the steps below:

1. A range of p-multiplier values is an input for the program.

2. For each value of the p-multiplier, calculate the difference between the measured and predicted shaft responses values for each node and store the values in a vector. Calculate the norm of each difference vector.

3. Plot the norm of the difference vector versus the p-multiplier as shown in Figure 3. The example would output an optimum p-multiplier value between 1.1 and 1.2.

4. If the curve does not have a minimum, adjust the range of p-multiplier values and repeat steps 2 and 3.

5. Fit a high-order polynomial through the norm versus p-multiplier scatter points. It is called the polynomial fitting curve as shown in Figure 3.

6. The value of the p-multiplier that minimizes the norm corresponds to the best fit of the measured data and will be the optimum p-multiplier.

In Figure 4, several shaft responses in term of lateral displacement and bending moment profiles have been presented for different values of p-multiplier. For a given shaft configuration and at a given load, the optimum p-multiplier obtained from the process above shows the best match between the predicted shaft responses and the experimental measurements.

The methodology of the computational program to establish p-y models starts with adjusting the conventional p-y curves using values of p-multiplier (p-mul) to produce the best fit of experimental measurement shaft responses. After having the optimum p-multiplier, the back-calculation process has been operated to perform the final structural responses in terms of lateral deflections and bending moments. Under a given load and at a given depth, a value of lateral deflection, y, is relative to the lateral soil resistance, p. From series of applied loads, the new p-y model for that given depth will be derived.

The example shown in Figure 5 is performed with shaft W-9, for series of applied loads starting from 26.8kips (120kN) to 348.5kips (1,550kN) and at depth is equal to 2ft (0.6m). For each given load, value of optimum p-multiplier is presented, and each data point represents value of lateral deflection between the soil and the shaft, y, and the corresponding soil resistance on a unit length of the shaft, p.

(a) (b)

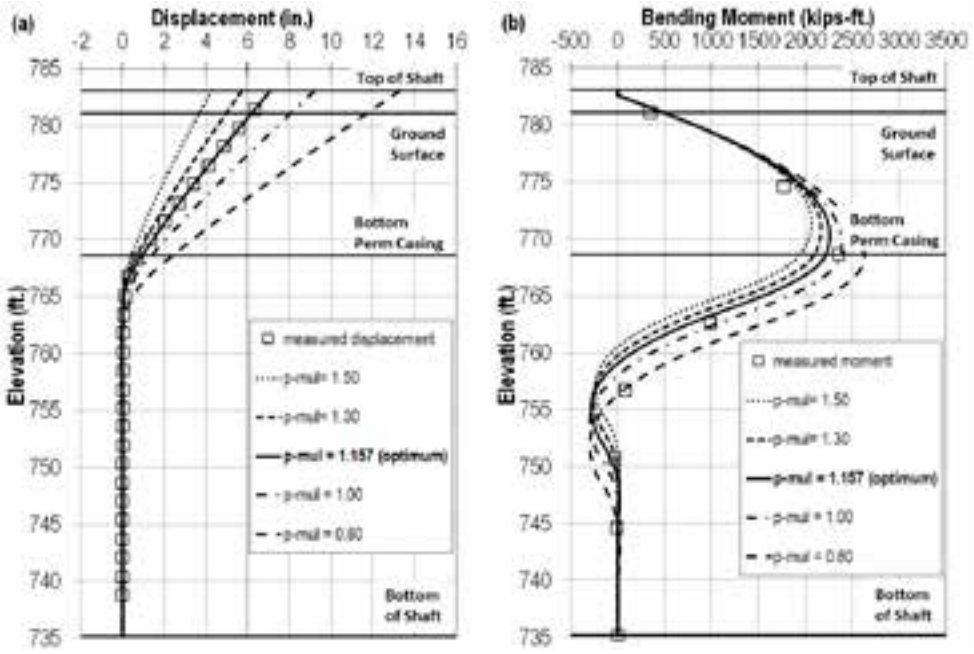

Figure 4: Shaft responses for different values of p-multiplier (shaft W-9, load = 319.2kips or 1,420kN)

(a) Displacement **(b) Bending Moment**

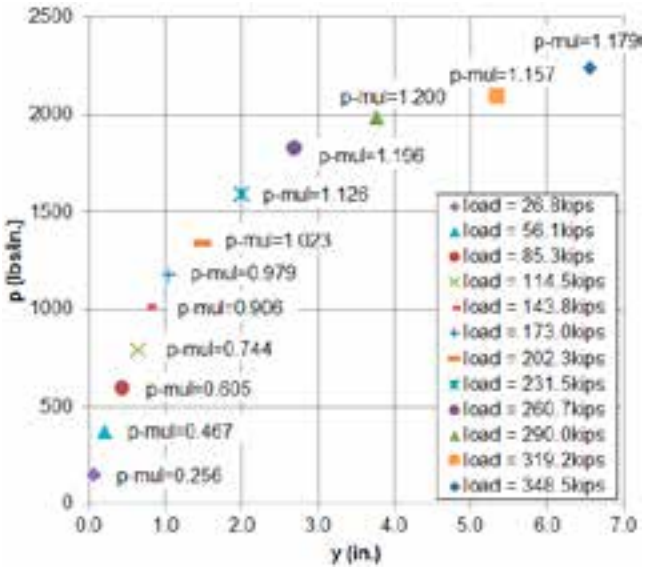

Figure 5: Predicted p-y curve derived from the experimental results (shaft W-9, depth z=2ft or 0.6m)

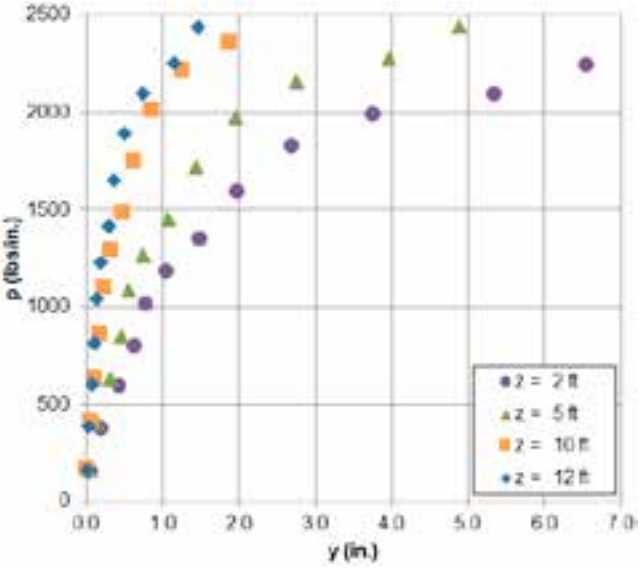

Figure 6: Different predicted p-y curves derived from the experimental results for different depths (shaft W-9, z=2ft (0.6m), 5ft (1.5m), 10ft (3m), 12ft (3.6m))

Different predicted p-y models for the same shaft but at different depths can be derived easily since the optimum p-multiplier and the shaft responses are unchanged. The lateral deflection, y, for a different depth need to be obtained from the shaft responses and new value of lateral soil resistance, p, is calculated. Repeat the procedure for all the applied loads to derive the predicted p-y models for different depths.

Figure 6 shows different predicted p-y curves for the same shaft W-9 at four different depths of 2ft, 5ft, 10ft and 12ft (0.6m, 1,5m, 3m and 3.6m).

3.2. Methodologies for bending stiffness

The bending stiffness, EI, is nonlinear and greatly influenced by concrete cracking, which is difficult to predict. Two methodologies of using bending stiffness have been presented to illustrate the reasonable procedure implementation in the computational program to derive the p-y models.

The first methodology of bending stiffness simply considers the cross-section geometry and material properties of the drilled shaft. Assume that no cracking of concrete is given during the lateral loaded test, the bending stiffness will be linear along both casing and non-casing sections as shown in Figure 7.

The second methodology of bending stiffness considers the nonlinear properties due to the cracking of concrete sections. The routine employed by LPile is documented in the program's technical manual (Isenhower & Wang, 2011). In summary, LPile iterates the location of the neutral axis until force equilibrium is satisfied, accounting for concrete cracking. Cracking of the concrete is predicted as a function of the compressive strength of the concrete, which was estimated from compression tests performed on cylinders from each shaft pour.

An example of the nonlinear shaft bending stiffness predicted by LPile as a function of the bending curvature is shown in Figure 7. The nonlinear bending stiffness decreases abruptly at small values of curvature, which initiate cracking of the concrete. After the concrete cracks, the decrease in stiffness is more gradual as the steel yields.

The procedure used here predicted values of bending stiffness along the length of the shaft as a function of the bending curvature, which was interpreted from computational program using initial assumed value of bending curvature. Predicted values for bending stiffness as a function of curvature were computed using Ensoft LPile. These values were used to implement in the computational program, especially in the iteration process presented below:

1. An initial bending stiffness is assigned to each element of the shaft.

2. Calculate the bending curvature from the deflection derived from that initial EI.

3. Obtain improved values of bending stiffness EI using the calculated bending curvatures from Step 2 and the predicted EI curves as shown in Figure 7.

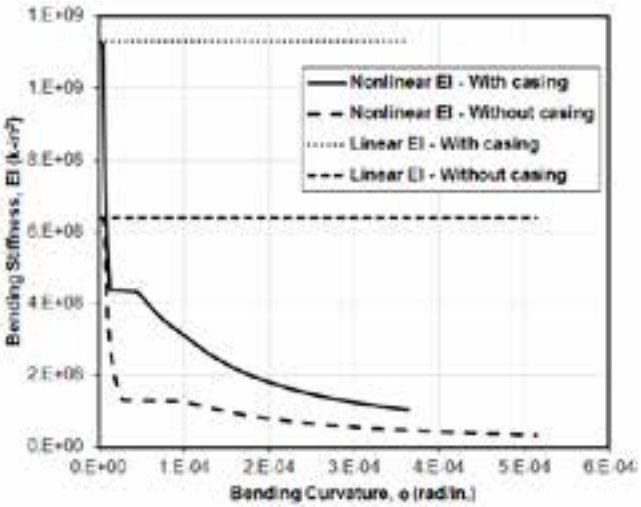

Figure 7: Example of linear and nonlinear bending stiffness for shaft W9

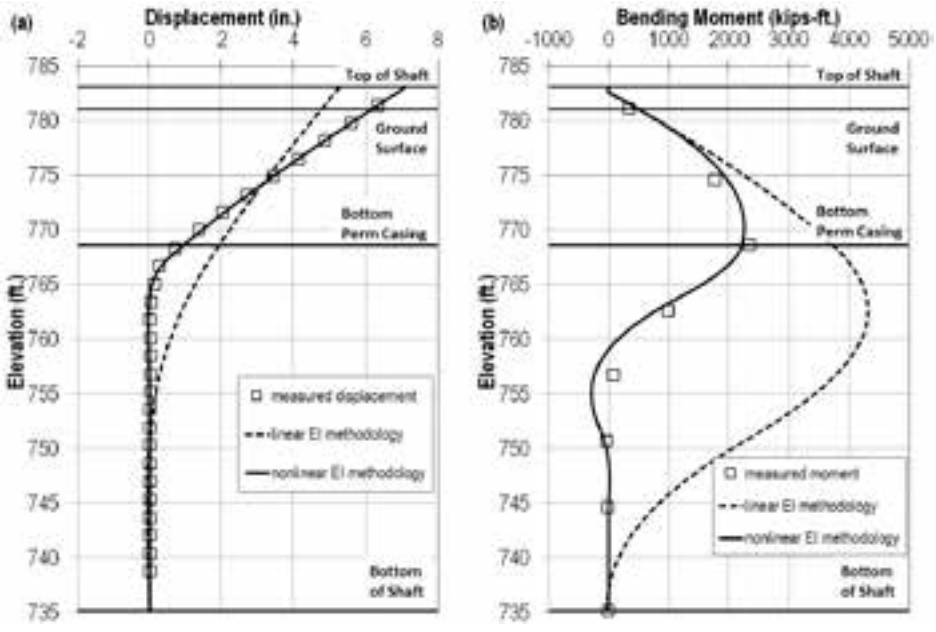

(a) Displacement profiles (b) Bending moment profiles

Figure 8: Predicted and measured shaft responses (shaft W-9, load = 319.2kips or 1,420kN)

4. Repeat steps 2 and 3 until the approximate relative error in EI values is negligible.

4. Predicted Responses

The analyses of experimental measurements explained in the previous section were applied to all 25 test shafts to produce predicted displacement, bending moment and p-y models considering linear and nonlinear EI. Example results are presented and discussed below.

4.1. Predicted lateral deflections

Figure 8a shows the difference between predicted lateral deflections using two different methodologies of bending stiffness: linear and non-linear. The measured lateral deflection obtained from SAA measurements has been presented also in order to compare with the predicted ones.

The shapes of the predicted displacement profiles indicate that by using nonlinear bending moment methodology, the predicted displacements are closely fit with the measured ones. While the linear bending stiffness methodology shows the substantial differences between predicted and measured ones.

Predicted displacement profiles obtained using nonlinear bending moment methodology show that the respective shaft is essentially fixed around the elevation 765 below the top

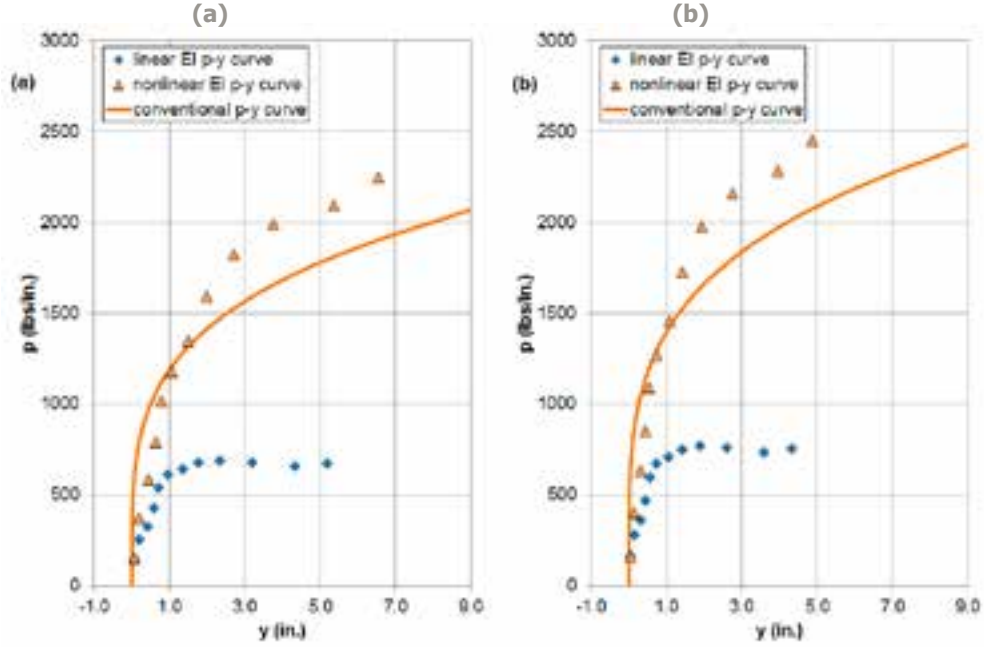

Figure 9: Predicted p-y curves using different stiffness methodologies vs. conventional p-y curve at: (a) depth = 2ft or 0.6m ; (b) depth = 5ft or 1.5m

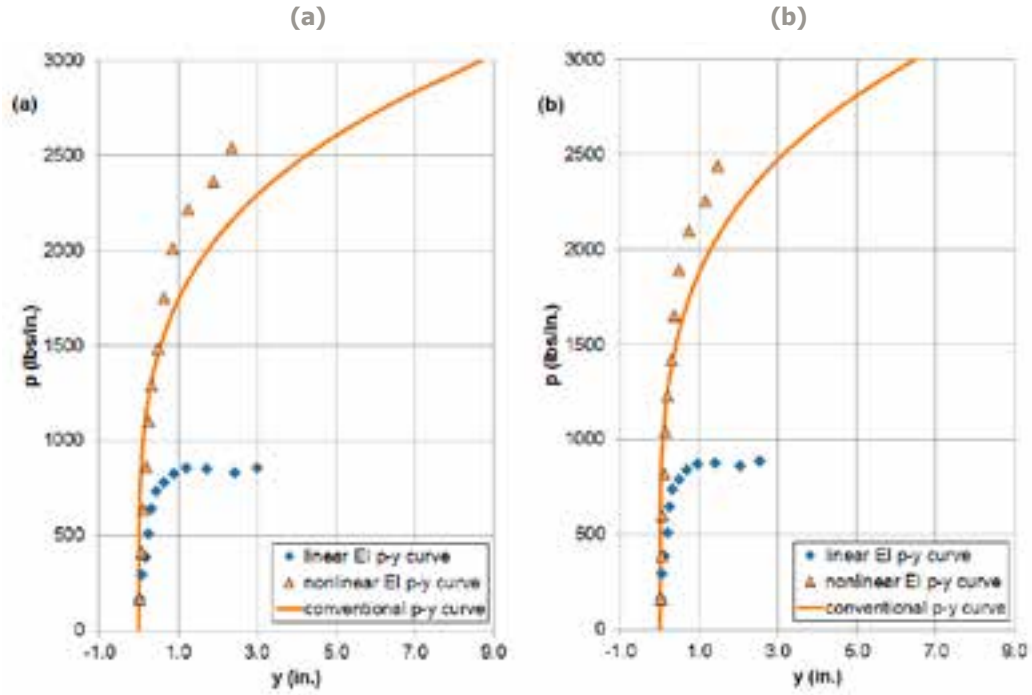

Figure 10: Predicted p-y curves using different bending stiffness methodologies vs. conventional p-y curve at:

(a) depth = 10ft or 3m **(b) depth = 12ft or 3.6m**

of the shaft, which is the same as the shaft responses fixed elevation obtained from experimental measurements.

4.2. Predicted bending moments

Figure 8b shows values of the bending moment interpreted from the strain gage measurements as well as values predicted by the computational program using linear and nonlinear bending stiffness methodologies.

The predicted bending moments using the methodology of nonlinear bending stiffness show a reasonably good fit to the bending moments interpreted from the strain gage measurements. While the linear bending stiffness methodology shows many differences between predicted and measured displacements. Reason is the much higher values of linear bending stiffness results in higher values of bending moments

4.3. Predicted p-y curves

Figure 9 and Figure 10 shows the difference between predicted p-y curves at a given depth using two different methodologies of bending stiffness: linear and non-linear. The conventional p-y curves (Reese et al., 2006; Isenhower and Wang, 2011) have been presented to compare with the predicted ones.

There is a significant difference between the predicted p-y curves using two different methodologies of bending stiffness as shown in Figure 9 and Figure 10. The predicted p-y curve using nonlinear bending stiffness methodology has much higher ultimate value of lateral response since the nonlinear bending stiffness reasonably represents the actual stiffness of the shaft, especially when the concrete is cracked.

The predicted p-y curves derived from experimental measurements are compared to the conventional p-y curves for stiff clay model (Reese et al., 2006; Isenhower and Wang, 2011). Interpretation of data from Figure 9 and Figure 10 indicate close agreement between the predicted p-y curves using nonlinear bending stiffness methodology and the conventional p-y curves.

The initial slopes are similar for predicted p-y curves using nonlinear bending stiffness and conventional p-y models, while predicted p-y curves using linear bending stiffness methodology have much lower initial slopes.

Data generally indicates slightly greater values of ultimate lateral soil responses for nonlinear bending moment methodology but much lower values for linear bending stiffness methodology, compared with the conventional p-y curves values.

As the depths increase in Figure 9a, 9b, 10a and 10b, the initial slopes as well as the ultimate lateral soil responses of predicted p-y curves increase, which shares the same characteristic with the conventional p-y curves.

5. Conclusion

Shaft responses in terms of lateral deflection and bending moment profiles were interpreted from strain gages and shape acceleration array (SAA) measurements. A methodology of matching predicted and collected data has been established and implemented in the computational program using Finite Element Method in order to generate experimental p-y response from measurements of displacement and strain. Moreover, in the case when bending stiffness (EI) is nonlinear and greatly influenced by concrete cracking, the importance of using nonlinear bending stiffness is represented by comparing the difference of shaft responses as well as predicted p-y curves using two different methodologies of bending stiffness. Among the most important observations:

- The computational program using Finite Element Method written to fit p-y model parameters by using p-multiplier to the experimental measurements obtained from geotechnical instrumentations was similarly effective.

(xem tiếp trang 48)

Application of mixed reality technology in geotechnical industry

Nguyen Thi Thao Van[(1)], Yasuo Miyagi[(2)] and Junichiro Odaka[(3)]

Abstract

Over the past decade virtual reality (VR), augmented reality (AR), and mixed reality (MR) technologies have been applied to the construction industry. The 3D geological models are also used to visualize the ground information for revealing the risk of geology in the geotechnical industry, and new approaches using VR/AR/MR technology are useful in understanding the relationship between the ground and structures. In this paper, examples of the application of MR technology will be introduced to further clarify how this technology changed the geotechnical industry.

Key words: *3D geological model, BIM/CIM, risk communication, mixed reality, HoloLens 2*

(1) (2) (3) Kiso-Jiban Consultants Co.,Ltd.
Email: <nguyen.van@kiso.co.jp>

Date of receipt: 15/4/2022
Editing date: 6/5/2022
Post approval date: 5/9/2022

1. Introduction

With the acceleration of the use of BIM/CIM (Building/ Construction Information Modeling, Management) in the construction industry have been, three-dimensional (3D) geological models are used as the BIM/CIM models in the geotechnical industry. 3D geological models are expected to visualize the ground information such as the risks of geology affecting seriously construction structures and to support the risk assessment process which is very meaningful to the design/construction phases. In this paper, an example of the use of 3D geological model and mixed reality (MR) technology as communication tools in risk assessment is introduced.

2. Mixed Reality Technology and HoloLens 2

In recent years, virtual reality (VR), augmented reality (AR), and mixed reality (MR) have brought about drastic changes in many industries, most notably in the entertainment industry, film, video game, retail, etc. Mixed reality (MR) is the merging of real and virtual worlds to produce new environments and visualizations, where physical and digital objects co-exist and interact in real time. Mixed reality does not exclusively take place in either the physical world or virtual world but is a hybrid of augmented reality and virtual reality. In addition, all such real-and-virtual combined environments and human-machine interactions generated by computer technology and wearables are collectively called extended reality (XR) including VR/ AR/MR and the areas interpolated among them.

HoloLens 2 (Fig. 1(a)) is an HMD (head-mounted display) developed by Microsoft Corporation in the United States and is an MR device that can display a 3D model in a hologram (Fig. 1(b)). HoloLens 2 allows you to freely enlarge, reduce, and rotate the hologram with your fingers, and you can also move it by touching it. It is equipped with an infrared LiDAR scanner that can perform spatial mapping of the real world up to 5 to 10 m away. This allows the hologram displayed by HoloLens 2 to be superimposed at an accurate position in the real space.

In the construction field, the introduction of HoloLens 2 was being promoted in advance by displaying a full-scale BIM model of piping, mechanical equipment, and steel skeleton of a building, etc. in a hologram. The designed equipment layout in the building is visualized and the constructed layout is examined. In addition, tools and services that support the inspection process of buildings by displaying the inspection points of the building in the hologram have been put into practical use. In this way, work efficiency is improved. By using HoloLens 2, remote assistance services in which skilled technicians provide remote support to young technicians who are working at the site through a video conference system are also being provided.

3. Hologram of the 3D geological model

Confirmation of the 3D geological models, for example, the 3D geological model of an erosion control dam (Fig.2), which is a BIM / CIM model in the geology/soil field, is usually performed on 3D model viewer software that can review 3D models. The 3D geological model was created by the AEC collection (Autodesk) [2] and GEORAMA, a 3D-geological modelling software provided by

HoloLens 2

b) Hologram of a 3D object in real space
(Microsoft Corporation 2022 [1])

Figure 1: HoloLens 2 and hologram generated by HoloLens 2

ITOCHU Techno-Solutions Corporation (CTC) [3]. And then the 3D models were imported into Rhinoceros, a 3D-CAD software developed by Robert McNeel & Associates [4], and holographically displayed by HoloLens 2. To display holograms with HoloLens 2, we used an add-on software for Rhinoceros named Fologram which was developed by Fologram Pty Ltd [5]. Figure 3 shows an example of a 3D geological model of an erosion control dam with a hologram display on HoloLens 2. By utilizing MR technology, now 3D geological models can be displayed right before our eyes, and actively the actively viewing and interacting of all or each layer in real space can be done (Fig.4). Moreover, the 3D geological model can be viewed from different angles for many viewers at the same time. These are the advantages of using MR, which are impossible with 3D model viewer software.

Although the 3D model (BIM/CIM) is displayed as a full-scale (1: 1 scale) hologram for a relatively large model such as a 3D geological model in general, by using the scale function of Fologram, the displayed hologram can be scaled down to any size. Therefore, it is possible to display the created 3D geological model on the desk in the conference room. In the case of a scaled-down hologram, to intuitively grasp the true size of the 3D model, a guide ruler such as a 3D scale bar that shows the actual size of the model should be added to the 3D models. Since HoloLens 2 does not have a device for acquiring position information like GPS, the hologram is aligned using a marker (QR code).

4. Hologram of 3D rockfall source models

Dangerous slopes with rockfall sources are spots where many unstable rocks and floating rocks exist, and most of them are steep slopes with a slope of 60° or more [6]. In many cases, the approach to the inspection point of the outcrops of the rockfall source is a difficult and dangerous

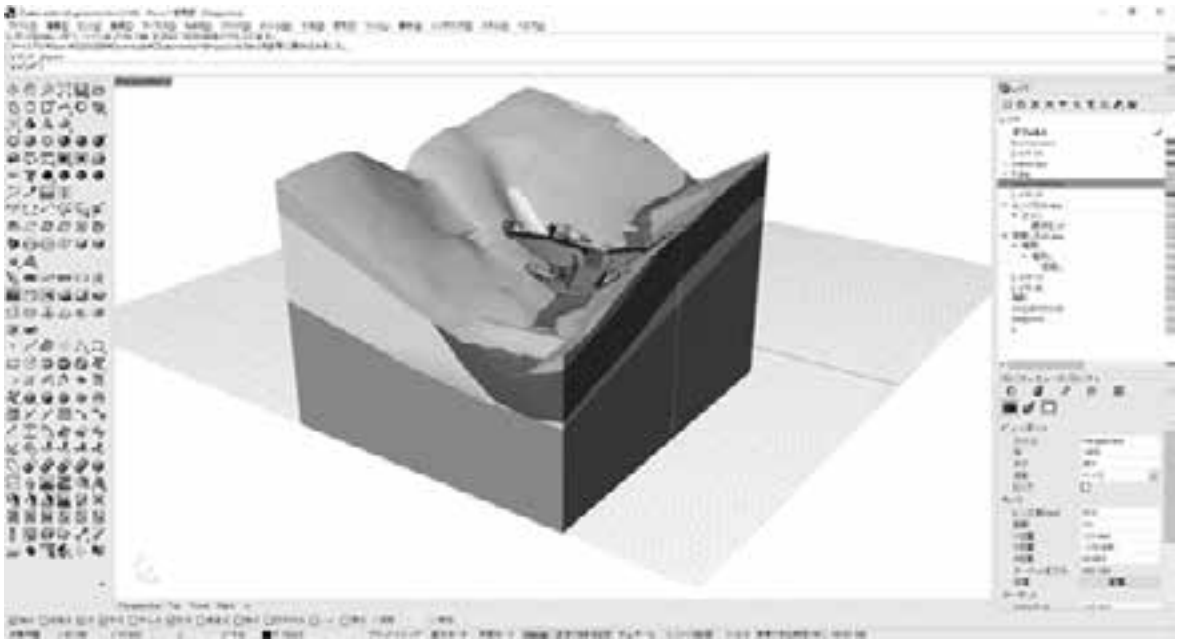

Figure 2: 3D geological model imported in Rhinoceros

task for investigators. But by utilizing MR technology, it is possible to realistically reproduce the situation at the site as a hologram without going to the site. As a result, engineers and experts can see the rockfall source situations as they are on-site and get a realistic recognition of the site situation. Through such advanced communication methods, they can share information, discuss disaster risks, and create various ideas for countermeasures.

The 3D rockfall source model was created with photogrammetry software that requires 50 or more digital photographs of the rockfall source from all directions. The created 3D rockfall source model was then opened and displayed with Rhinoceros, after that the hologram of the 3D rockfall source model was displayed on HoloLens 2 using Fologram in real scale in real space (Fig. 5).

The advantages of displaying a hologram of a 3D rockfall source model are as follows.

(1) It is possible to safely check the rockfall source situation and its danger without going to the site in the case of unstable and risky rockfall sources.

(2) Since the hologram of the 3D rockfall source model allows you to check the detailed situation while walking around the hologram as in the field. In this way, it can easily check the opening cracks on the slope with the hologram.

(3) Advanced communication can be conducted. For example, a skilled technician or expert wearing HoloLens 2 and observing the hologram of the 3D rockfall model can share his/her viewpoint while streaming the hologram through the PC screen.

On the other hand, the problems related to the hologram display of the 3D rockfall source model are as follows.

To create a 3D rockfall source model, it is necessary to take many photographs of the rockfall source from all angles. If some parts of the rockfall source model cannot be photographed or that can only be taken from a limited angle, the data is insufficient to convert to a 3D model. As a result, the model quality is inferior.

When a realistic and too detailed 3D rockfall source model is created, it takes much time to display the hologram on HoloLens 2 because the mesh data is too large.

While such issues are recognized, it can be said that the benefit of being able to safely confirm dangerous sites of the rockfall sources is extremely great.

5. Summary

In this paper, we introduced the hologram display of the 3D geological and 3D rockfall source models by utilizing MR technology and HoloLens 2. The hologram display makes it easier and more intuitively to understand the geological composition in the 3D geological model. In the case of the hologram of the 3D rockfall source model, it allows an experience of the situation of the

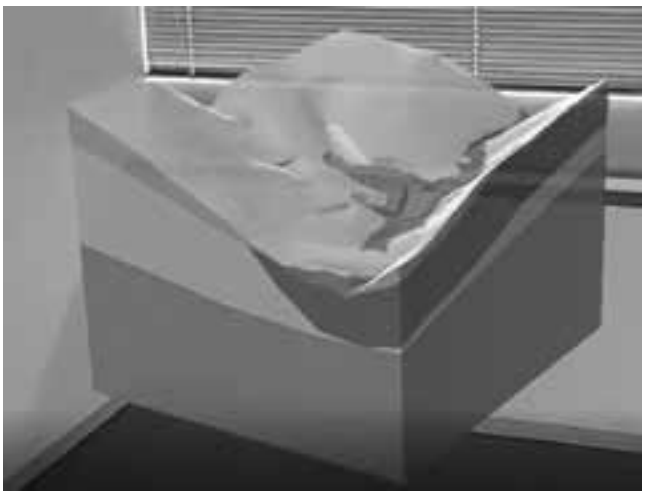

Figure 3: Hologram of a 3D geological model displayed in real space (1/1,000 scale)

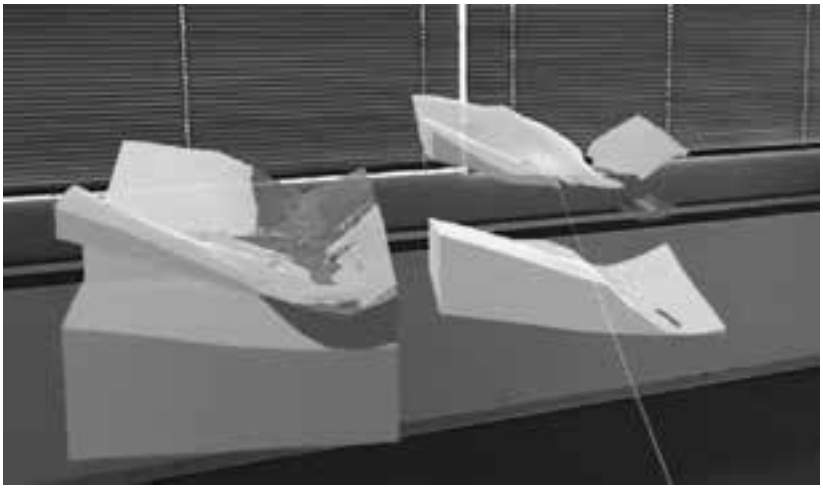

Figure 4: User interacting with the hologram of the geological model displayed in real space

Figure 5: Hologram of a 3D rockfall source model displayed indoors

rockfall source in a realistic manner.

However, HoloLens 2 itself has the following problems:

(1) Since the device itself does not have position information like GPS, it is not easy to align the BIM/CIM model of slopes with the position in real space.

(2) It takes time to load the 3D data with a large file size to display the hologram with HoloLens 2.

(3) The device itself is not dust-proof or drip-proof, and the system is likely to go down under conditions where the temperature is 30° C or higher.

Regarding the solutions for the above-stated issues, for (1), it is possible to perform accurate alignment by combining it with the position correction technology of the quasi-zenith satellite "MICHIBIKI" [7], which is operated by JAXA [8]. Regarding (2), the 3D model should be optimized to reduce the size as much as possible before being displayed with HoloLens 2. For the issue stated in (3), we expect that next-generation devices developed in the future can withstand use under harsh conditions such as in the civil engineering and construction site. Some cooling equipment for HoloLens 2 was also introduced and we hope that these accessories will be developed further to help HoloLens 2 work better in multiple types of environments./.

References

1. *Microsoft Corporation 2022, digital image, accessed 2022 Feb 14th, <https://docs.microsoft.com/en-us/windows/mixed-reality/design/core-concepts-landingpage>.*
2. *Autodesk Inc. Architecture, Engineering & Construction Collection, accessed 2022 May 19th, <https://www.autodesk.com/collections/architecture-engineering-construction/overview?term=1-YEAR&tab=subscription >.*
3. *ITOCHU Techno-Solutions Corporation. Solution and Products, accessed 2022 May 19th, <https://www.engineering-eye.com/en/category/45/index.html>.*
4. *Robert McNeel & Associates. Rhinoceros 3D, accessed 2022 May 19th, < https://www.rhino3d.com/en/>.*
5. *Fologram Pty Ltd. "Fologram for Rhino and Grasshopper" and "Fologram for HoloLens", accessed 2022 May 19th, <https://fologram.com/download >.*
6. *K. Miura, N. Komuro, N. Kuramoto. Extraction of rock-fall danger points related to road disaster prevention using laser profiler data. Journal of JGS, Vol.69□No.6□30-33, 2021. (Japanese)*
7. *Construction IT World. Quasi-zenith satellite "MICHIBIKI", HoloLens2, BIM / CIM are linked. Challenge to construction management of construction site by MR (Informatics), accessed 2022 Jan 17th, <https://ken-it.world/success/2021/03/michibiki-mr-collaboration.html#>.*
8. *Japan Aerospace Exploration Agency. Overview of the First Quasi-Zenith Satellite "MICHIBIKI", accessed 2022 April 14th, <https://global.jaxa.jp/countdown/f18/overview/michibiki_e.html>.*

Development of static P-Y curves from experimental measurements...

(tiếp theo trang 44)

- Optimization p-multiplier process produces closed fit between the predicted shafts responses and the collected measurements.

- Nonlinear characteristic of bending stiffness is important and significantly impacts the predicted shaft responses in terms of lateral displacements and bending moments, as well as the predicted p-y models.

- Linear and nonlinear methodologies of applying bending stiffness to the computational program show the substantial differences in both shapes and magnitudes of predicted shaft responses and the significant differences of predicted p-y models.

- By using nonlinear bending stiffness considered the cracking of concrete section and the methodology to derive p-y models implemented in the computational program, the experimental p-y curves can be established reasonably and practicably.

- The p-y curves derived from experimental measurements are compared to the conventional p-y curves. The comparisons are useful for perspective on how the test data align with models commonly assumed in practice.

The proposed approach is limited to the static p-y curves for onshore long flexible drilled shafts, not for the case of cyclic loading or for short rigid pile or for offshore conditions. Further readings should refer to API RP 2A-WSD, 22nd Edition, November 2014 and DNVGL-RP-C212, 2019 Edition, September 2019./.

References

1. *ASTM Standard D3966. Standard Test Methods for Deep Foundations Under Lateral Load. ASTM International, West Conshohocken, PA, 2007, DOI: 10.1520/D3966-07, www.astm.org, 2007.*
2. *Boeckmann, A.Z., Myers, S.G., Uong, M. and Loehr, J.E. Load and Resistance Factor Design of Drilled Shafts in Shale for Lateral Loading. Report to Missouri Department of Transportation, 2014.*
3. *Isenhower, W.M. and Wang, S.-T. Technical Manual for L-Pile, Ensoft, Inc., Version 6, 2011.*
4. *Reese, L.C., Isenhower, W.M. and Wang, S.-T. Analysis and Design of Shallow and Deep Foundations, John Wiley & Sons, Hoboken, New Jersey, 2006.*

Experimental and numerical investigation of the fire performance of densified spruce wood

Tran Trong Tuan[(1)]

Abstract

This paper presents experimental and numerical investigations to assess the relative fire structural resistance of thermo-mechanically compressed (or densified) spruce wood. First of all, both compressed and uncompressed spruce samples of dimensions of 100 mm x 100 mm x 19 mm have been subjected to fire in a cone calorimeter under 20 kW/m2 and 75 kW/m^2. Finally, a predictive finite element model based on three-step multi-reactions of pyrolysis is proposed for the thermal transfer and degradation analyses of timber material. The simulated thermal profiles, the mass loss as well as the charring depths were compared to the experimented results showing a fairly good agreement.

Key words: *Wood, Fire Performance, Finite Element Method, Pyrolysis, Thermal Transfer*

(1) PhD. Lecturer, faculty of civil engineering, Hanoi Architectural University, Email: tuan87kta@gmail.com

Date of receipt: 15/4/2022
Editing date: 6/5/2022
Post approval date: 5/9/2022

1. Introduction

Fire resistance should be understood as the characteristic times involved in the degradation, burning and loss of density and mechanical properties of the material. Among other timber species, spruce timber is known for its lower thermo-physical properties (thermal conductivity, specific heat and density) thanks to its porosity level. However, information on the thermo-physical properties of compressed spruce timber is not available. In fact, the objective of the thermomechanical compression process is to increase the density of spruce timber by reducing as much as possible its porosity, which in turn can greatly affect the thermal conduction.

It has been found that the densification process increases the fire performance of wood material by modifying the thermal properties [1–2], including heat release rate and flammability. Gan et al. [3] presented a study showing how delignification and densification of wood can substantially improve the fire-retardant properties of wood materials. Yue et al. [4] combined resin impregnation and densification of Chinese fir to improve its combustion performance. Chen et al. [5] combined delignification, bentonite impregnation, and densification of wood to enhance flame-retardancy of wood.

Pyrolysis is a crucial process to understand the fire behavior of wood [6–8]. In recent years, pyrolysis modeling is extensively used to predict the thermal degradation of polymers in general and wood in particular. Several numerical pyrolysis models have been formulated for wood including basic and more detailed chemical schemes to represent the transformation of the virgin components of wood, namely hemicellulose, cellulose, and lignin. Readers can referr to [1–16] for a better reading on the pyrolysis chemical schemes and related modeling aspects.

In this paper, the heat transfer and thermal degradation of both compressed and uncompressed spruce have been studied experimentally and compared. The pyrolysis process suggested by Blasi et al. [17], was modified and extended to a three-steps multi-reactions pyrolysis finite element model to deal with the thermal behavior of wet wood under fire conditions. The developed pyrolysis finite element (FE) model was calibrated with regard to the experimental database and used to simulate the thermal behavior of uncompressed and compressed wooden plates under fire conditions.

2. Fire tests under a cone calorimeter

2.1. Materials

Spruce timber plates without visible defects, either compressed or uncompressed, having the dimensions of 100mm x 100mm x 19mm were used in this study (Figure 1). The initial density of the uncompressed spruce plates was 449 kg/m^3 (±3%). The compressed wood plates were obtained by thermomechanical compression of spruce blocks (cut from the same wood as for the uncompressed plates) in the radial direction [18] up to a compression ratio (CR) of 68% (the CR is defined as the ratio between the final and initial thickness). For a better reading of the compression process, readers can referr to [18]. Thanks to the thermomechanical compression process, the mean density of the spruce plates was increased from 449 kg/m^3 to 1210 kg/m^3 (±1.4%).

2.2. Experimental set-up

Experiments on thermal decomposition of both compressed and uncompressed spruce were undertaken using a cone calorimeter (Figure 2) using the samples depicted in Figure 1 with dimensions of 100mm x 100mm and 19mm thick, with moisture content (MC) ranging from 7 to 8%. All the samples were heated on one side using two different uniform heat fluxes, namely 20kW/m^2 and 75kW/m^2, with a potential of maximal temperatures at the exposed surfaces of 600°C and 850°C, respectively. The unexposed surfaces (one opposite and four lateral surfaces) were protected from direct heating to allow exchange with the room temperature. K-type thermocouples were placed on both the exposed and the unexposed surfaces to record the temperature rise during the thermal decomposition. The mass of samples was continuously recorded using a precise electronic balance every one second. In addition, an infrared camera was used to control the distribution of the heat flux on the exposed surface. The tests were carried out according to the standard ISO 5660-1.

2.3. Experimental results

Figures 3 and 4 display the mean experimental mass loss curves over the fire exposure time under 20kW/m^2 and 75kW/m^2 heat fluxes, respectively, for both the uncompressed and compressed spruce samples. It can be observed from Figure 3 that both the uncompressed and compressed samples exhibit a similar plateau-like mass loss up to about 300°C, which corresponds to the isotherm point of the pyrolysis. The beginning of this plateau corresponds to the drying stage up to about 100°C.

Beyond the temperature level of 300°C, corresponding to about 5 min exposure time to fire, the thermal decomposition of both uncompressed and compressed samples starts but the uncompressed samples pyrolyzed very quickly as compared to the compressed samples. However, in the case of heat flux of 75kW/m^2 (Figure 4), both uncompressed and compressed samples do not exhibit the plateau-like mass loss, and the thermal decomposition of both starts from the beginning of heating, and no obvious drying process was observed at this heating level (75kW/m^2) because probably, this has occurred very quickly. This result is coherent with that reported in [19]. Moreover, it can be clearly seen that the pyrolysis (charring rate) of the compressed samples is very slow by comparison to the uncompressed samples.

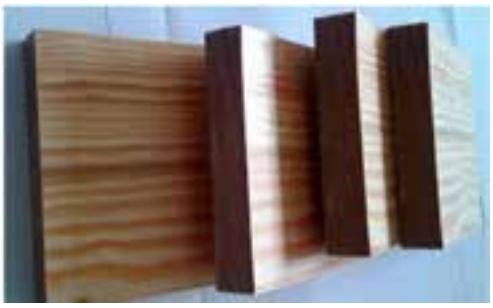

(a) Uncompressed samples

(b) 68% compressed samples

Figure 1: Typical studied spruce timber plates

Furthermore, the experimental charring layers for both uncompressed and compressed samples are depicted in Figure 5. The experimental observation of the charring depths confirms the results depicted in Figures 3 and 4. It can, therefore, be concluded that the compressed samples exhibit low charring rate than the uncompressed ones.

3. Numerical simulation

3.1. Finite element modeling

A finite element model for the thermal behaviour (pyrolysis) of timber under fire based on three-steps multi-reaction kinetics is proposed. The model is inspired by the three-steps kinetic model proposed by Blasi et al. [17] to analyze the thermal decomposition of wood. That model states that dry wood is composed of three pseudo-components A_1, A_2, and A_3, each of them corresponds to specific kinetic law and a mass fraction α_1, α_2, and α_3, respectively [17].

The general flowchart of the proposed three-steps pyrolysis model is given in Figure 6, including the drying

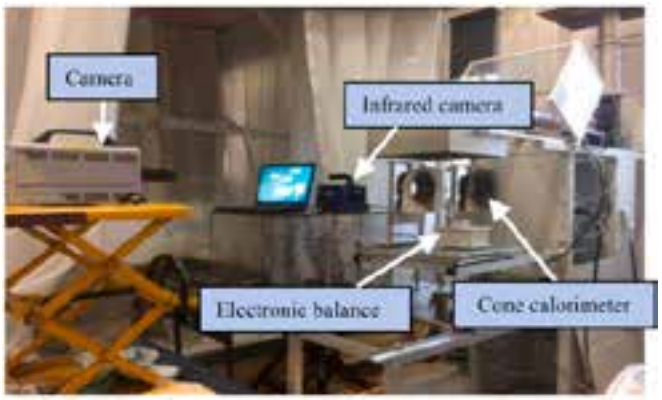

Figure 2: Experimental set-up for cone calorimeter test

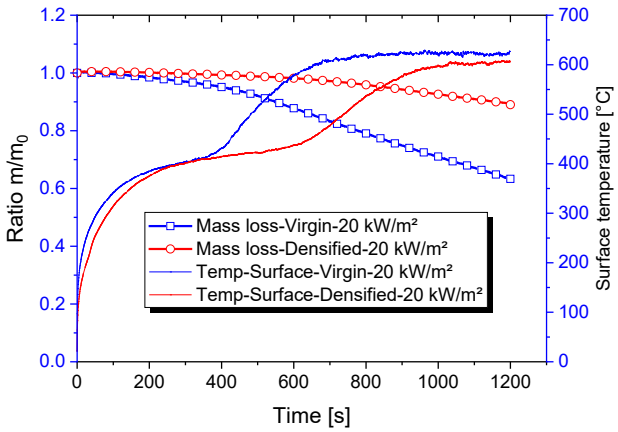

Figure 3: Experimental mass loss under exposure to 20 kW/m^2 heat flux

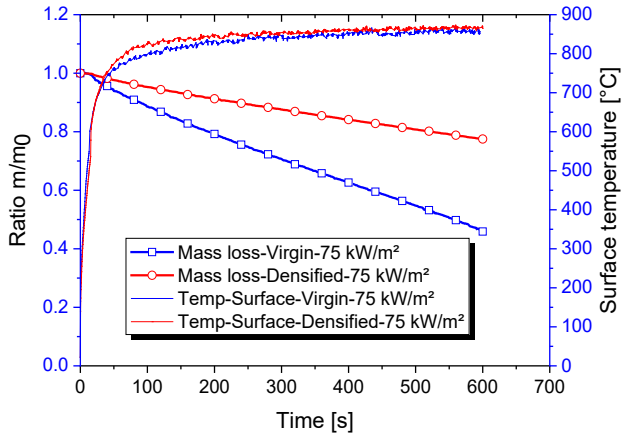

Figure 4: Experimental mass loss under exposure to 75 kW/m² heat flux

process. As shown in Figure 6, the kinetic mechanisms involved in the three parallel decompositions of the pseudo-components A_1, A_2, and A_3 are associated with the rate constants of reactions k_1, k_2, and k_3. By assuming that the kinetic is described by first-order laws for the three reactions, the mass balance of the wet solid and associated components can be expressed as follows:

$$\frac{dm_l}{dt} = -k_v.m_l \quad (1)$$

$$\frac{dm_{A1}}{dt} = -k_1.m_{A1} \quad (2)$$

$$\frac{dm_{A2}}{dt} = -k_2.m_{A2} \quad (3)$$

$$\frac{dm_{A3}}{dt} = -k_3.m_{A3} \quad (4)$$

Eqs. (1) to (4) show that the mass of the sample during the pyrolysis at a fixed temperature in an inert atmosphere depends on six parameters (α_1, α_2, α_3, k_1, k_2, and k_3), which are defined based on experimental data, including inverse approach analysis using the gravimetric test data.

The energy conservation equation for the pyrolysis of the wet wood was adapted from the one-dimensional model by Shen et al. [20] and modified to consider 3D heat transfer model as well as the different pyrolysis reactions involved in the three-steps thermal decomposition model as follows [21-22]:

$$\frac{\partial\left[\left(\rho_{A1}+\rho_{A2}+\rho_{A3}\right)Cp_w+\rho_c Cp_c+\rho_l Cp_l\right]}{\partial t} = \frac{\partial}{\partial x}\left[\lambda_x.\frac{\partial T}{\partial x}\right]+\frac{\partial}{\partial y}\left[\lambda_y.\frac{\partial T}{\partial y}\right]+\frac{\partial}{\partial z}\left[\lambda_z.\frac{\partial T}{\partial z}\right]+Q_r^{"} \quad (5)$$

By introducing the mass fractions of the pseudo-components A_1, A_2, and A_3, the Eq. (5) becomes:

$$\frac{\partial\left[\left(\alpha_1+\alpha_2+\alpha_3\right)\rho_w Cp_w+\rho_c Cp_c+\rho_l Cp_l\right]}{\partial t} = \frac{\partial}{\partial x}\left[\lambda_x.\frac{\partial T}{\partial x}\right]+\frac{\partial}{\partial y}\left[\lambda_y.\frac{\partial T}{\partial y}\right]+\frac{\partial}{\partial z}\left[\lambda_z.\frac{\partial T}{\partial z}\right]+Q_r^{"} \quad (6)$$

where $Q_r^{"}$ is the energy source resulting from the sum of reaction heat of the three pyrolysis reactions (endothermic and exothermic), including the drying at temperature T, which can be expressed as:

$$\begin{aligned} Q_r^{"} &= k_v.\rho_l.\left[\Delta h_o^v+\left(Cp_v-Cp_l\right).\left(T-T_0\right)\right] \\ &+k_1.\rho_{A1}.\left[\Delta h_o^1+\left(Cp_G-Cp_w\right).\left(T-T_0\right)\right] \\ &+k_2.\rho_{A2}.\left[\Delta h_o^2+\left(Cp_G-Cp_w\right).\left(T-T_0\right)\right] \\ &+k_3.\rho_{A3}.\left[\Delta h_o^3+\left(Cp_G-Cp_w\right).\left(T-T_0\right)\right] \end{aligned} \quad (7)$$

Cp_G=2.4, Cp_C=1.39, Cp_l=4.18, Cpv=1.58 (kJ.kg^{-1}.K^{-1}) are the specifc heat for gas, char, liquid, and vapor [20]. Specific heat values, Cp_w, for both compressed and uncompressed wood are taken from experiment of thermogravimetric test at 60 oC (1382 and 1405). Δhi (kJ.kg^{-1}) represent constants of the standard resulting heat for resultants and reactants per unit mass (enthalpy) and they are taken from [20] as follows: $\Delta h_1^0 = \Delta h_2^0 = \Delta h_3^0 = -420$ (for pyrolysis reactions: transformation of wood to char and gas), $\Delta h_v^0 = -2440$ (for drying process: transformation of moisture to vapor).

$\lambda_x, \lambda_y = \lambda_z$ are the variable thermal conductivity coefficients,

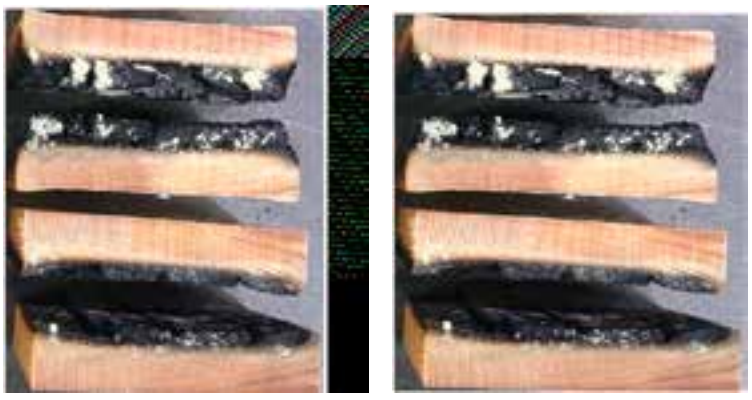

(a) Uncompressed spruce (b) Compressed spruce

Figure 5: Experimental charring layer under 20 kW/m² and 20 min exposure

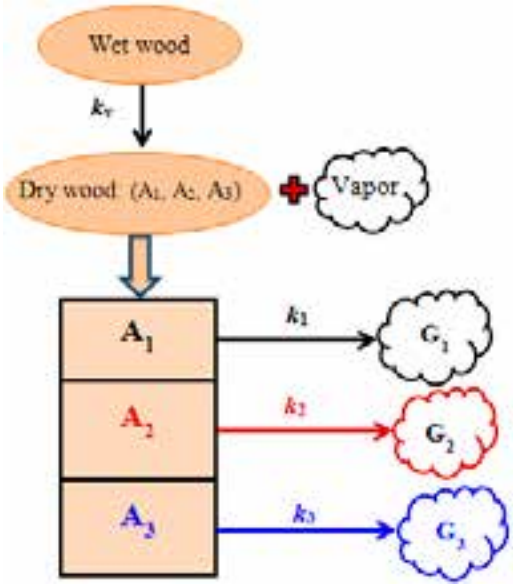

Figure 6: The three-steps multi-reactions of pyrolysis of wet wood

in the transverse and longitudinal directions, of the equivalent solid depending on the solid conversion η and on the thermal conductivity coefficients of char, λ_c, and wet wood λ_w [20]:

$$\lambda_i = \eta.\lambda_{ci} + (1-\eta).\lambda_{wi} \quad (8)$$

$$\lambda_c = 0,07 \quad (9)$$

$$\eta = \frac{\rho_c}{\rho_c + \rho_w} \quad (10)$$

Conductivity reference values for compressed and uncompressed wood are taken from hot plate method (λ_w=0,096 for native wood and λ_w=0,175 for compressed wood), and assumed to evolve as a function of the humidity according to the relation by [20]: λ_w=0.096+0.369X and λ_w=0.175+0.369X, respectively, for uncompressed and compressed wood. X represents the moisture content (in %). Here, the thermal conductivity of wood in the two transverse directions, namely tangential and radial directions, is assumed identical (λ_x=λ_y). While the longitudinal thermal conductivity is assumed to be the same (λ_z=0.2W/(m.K)) as for native wood (uncompressed).

The rate constants of reactions k_1, k_2, and k_3 are assumed to obey the first-order Arrhenius law, depending on the temperature T, the activation energy Ei (J.mol^{-1}) of reaction i, the gas constant R=8.314 J/(mol.K) and the pre-exponent factor Ai (s^{-1}) of the reaction i, as follows:

$$k_i = A_i.\exp\left(\frac{E_i}{RT}\right) \quad (11)$$

Table 1: Identified kinetic parameters for the three-steps pyrolysis model

Reaction	E_i [kJ/mol]	A_i [1/s]	α_i
(1)	102	1,15×10^7	0,25
(2)	220,9	1,16×10^{16}	0,37
(3)	30	5,85×10^{-1}	0,2

The parameters related to fractions α_1, α_2, α_3, the activation energy E_i and the pre-exponent Ai are obtained using the inverse approach based on the mass loss curves and their derivatives obtained from the TGA-type tests. The identified parameter values are summarized in Table 1.

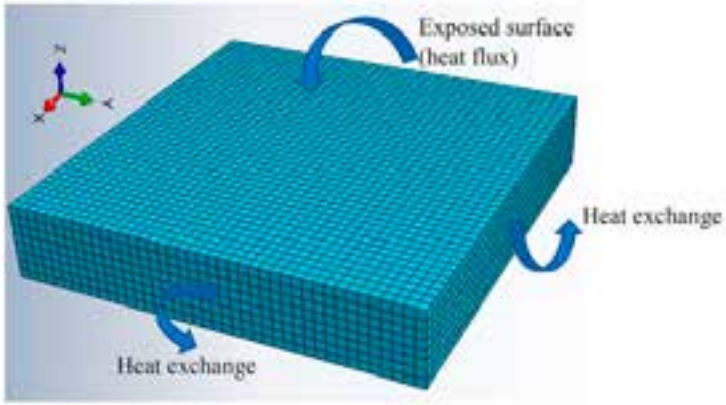

Figure 7: Finite element model of the spruce plate

The developed three-steps pyrolysis reactions finite element model was successfully implemented in the Abaqus commercial software via the user-defined UMATHT.

3.2. Numerical simulation and validation of the FE model

Both uncompressed and compressed spruce square plates were simulated using the developed finite element model. 3D solid quadratic elements of Abaqus (CD320) were used to generate the finite element mesh (Figure 7). It is worth noting that even if the FE-model is a 3D formulation, at this stage of the study the application considered is a one-dimensional problem. Heat exchange, by radiation and convection, was used for the unexposed surfaces to allow exchange with the temperature room (23°C). A heat transfer coefficient of 12.5W/m^2.K and radiative transfer coefficient of 0.92 was used in the simulations.

The thermal profiles for both uncompressed and compressed spruce plates were simulated and compared to the experimentally recorded temperatures (Figure 8). In addition, the Eurocode 5 [23] model was applied for comparison purposes using the surface temperature recorded experimentally on the sample exposed surface (see Figures 3 and 4) as the boundary condition (the imposed temperature). This is similar to the ISO-834 fire curve [24] suggested by the Eurocode. Modified thermo-physical

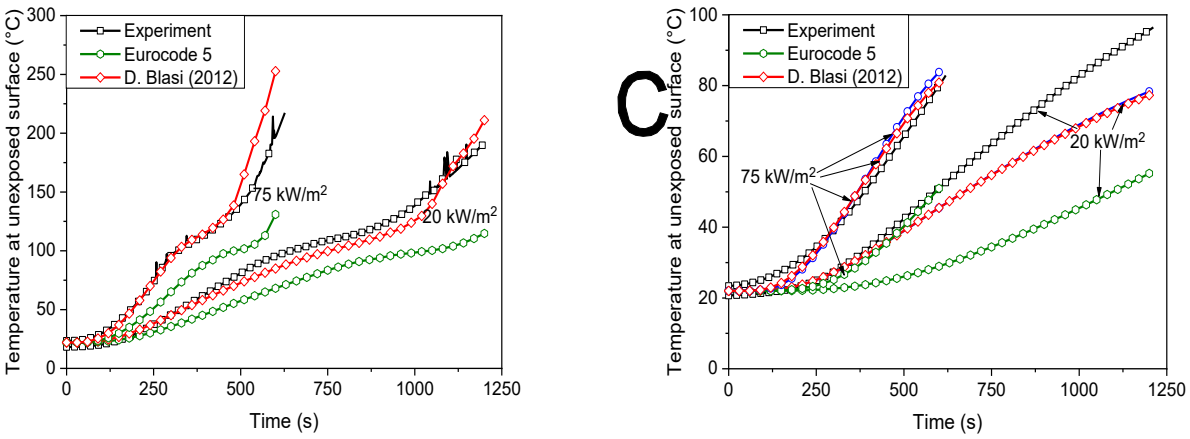

(a) Uncompressed samples

(b) Compressed samples

Figure 8: Temperature profiles at the unexposed surface

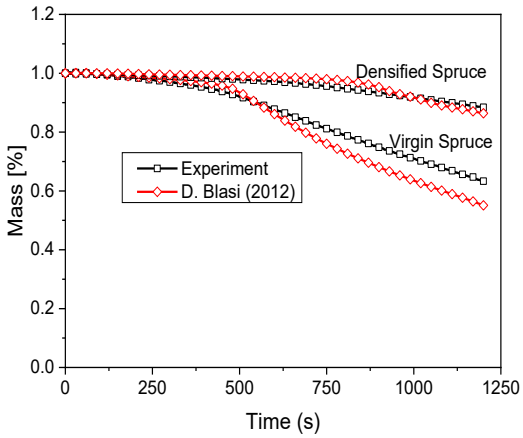

(a) Heat flux of 20 kW/m^2

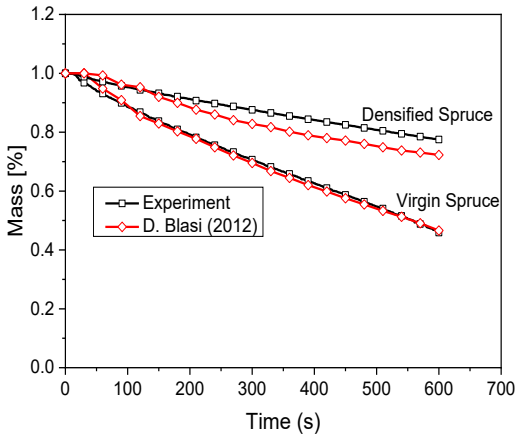

(b) Heat flux of 75 kW/m^2

Figure 9: Comparison of mass loss

(xem tiếp trang 66)

References

1. *L.A. Lowden, T.R. Hull, Flammability behavior of wood and review of the methods for its reduction, Fire Sci. Rev. 2 (2013) 4. http://www.fresciencereviews. com/content/2/1/4.*
2. *Osorio, Andres F., Hidalgo, Juan P., and Evans, Philip D. (2018). Enhancing the fire performance of engineered mass timber and its implications to the fire safety strategy. 2018 World Conference on Timber Engineering, WCTE 2018, Seoul, Korea, August 20-23, 2018. World Conference on Timber Engineering (WCTE).*
3. *W. Gan, C. Chen, Z. Wang, J. Song, Y. Kuang, S. He, R. Mi, P. B. Sunderl and L. Hu, Dense. Self-Formed Char Layer Enables a Fire-Retardant Wood Structural Material Advanced Functional Materials https://doi.org/10.1002/adfm.201807444.*
4. *K. Yue, J. Wu, L. Xu, Z. Tang, Z. Chen, W. Liu, L. Wang. Use impregnation and densification to improve mechanical properties and combustion performance of Chinese fr, Constr. Build. Mater. 241 (2020), 118101.*
5. *G. Chen, C. Chen, Y. Pei, S. He, Y. Liu, B. Jiang, M. Jiao, W. Gan, D. Liu, B. Yang, L. Hu. A strong, flame-retardant, and thermally insulating wood laminate, Chem. Eng. J. 383 (2020), 123109.*
6. *F. Richter and G. Rein. The Role of Heat Transfer Limitations in Polymer Pyrolysis at the Microscale, Front. Mech. Eng. 4:18.doi: 10.3389/fmech.2018.00018.*
7. *I. Vermesi, M. J. DiDomizio, F. Richter, E. J. Weckman, G. Rein. Pyrolysis and spontaneous ignition of wood under transient irradiation: Experiments and a-priori predictions, Fire Safety Journal (In press), https://doi.org/10.1016/j.fresaf.2017.03.081.*
8. *F. Richter, G. Rein, A multiscale model of wood pyrolysis in fire to study the roles of chemistry and heat transfer at the mesoscale, Combust. Flame 216 (2020) 316–325.*
9. *M.J. Antal, G. Varhegyi, E. Jakab. Cellulose pyrolysis kinetics: revisited, Ind. Eng. Chem. Res. 37 (1998) 1268–1275, https://doi.org/10.1021/ie970144v.*
10. *B. Peters, C. Bruch. Drying and pyrolysis of wood particles: experiments and simulation, J. Anal. Appl. Pyrol. 70 (2003) 233–250.*
11. *Lautenberger, Chris, and Fernandez-Pello, Carlos. A model for the oxidative pyrolysis of wood. United States: N. p., 2009. Web. doi:10.1016/J. COMBUSTFLAME. 2009.04.001.*
12. *S.R. Wasan, P. Rauwoens, J. Vierendeels, B. Merci. Application of a simple enthalpy-based pyrolysis model in numerical simulations of pyrolysis of charring materials, Fire Mater. Int. J. (2009), https://doi.org/10.1002/fam.1010.*
13. *P. Patel, T. R. Hull, A. A. Stec and R. E. Lyon. Influence of Physical Properties on Polymer Flammability in the Cone Calorimeter, Polymers for Advanced Technologies 22(7):1100–1107.*
14. *D. Cancellieri, V. Leroy-Cancellieri, E. Leoni, A. Simeoni. Kinetic study of thermal degradation of peats by TGA, VI International Conference on Forest Fire Research.*
15. *Bilbao R, Mastral JF, Ceamanous J, Aldea ME. Modeling of the pyrolysis of wetwood, J Anal Appl Pyrol. 1996; 36; pp.81–97.*
16. *B. Moghtaderi. The state-of-the-art in pyrolysis modeling of lignocellulosic solid fuels, Fire Mater 2006;30:1–34.*
17. *Broström M., Nordina A., Pommer L., Branca C., Di Blasi C. Influence of torrefaction on the devolatilization and oxidation kinetics of wood, Journal of Analytical and Applied Pyrolysis 96 (2012) 100-109.*
18. *I. El-Houjeyri, V.-D. Thi, M. Oudjene, M. Khelifa, A. Sotato, Z. Guan. Experimental investigations on adhesive free laminated oak timber beams and timber-to-timber joints assembled using thermo-mechanically compressed wood dowels, Constr. Build. Mater. 222 (2019) 288–299.*
19. *Terrei L., Acem Z., Lardet P., Georges V., Boulet P., Parent G.. Experimental tools applied to the ignition study of spruce wood under cone calorimeter, Journal of Physics: Conference series volume 1107.*
20. *D.K. Shen, M.X. Fang, Z.Y. Luo, K.F. Cen. Modeling pyrolysis of wet wood under external heat flux, Fire Saf. J. 42 (2007) 210–217.*
21. *V.D. Thi, M. Khelif, M. Oudjene, M. El Ganaoui, Y. Rogaume. Finite element analysis of heat transfer through timber elements exposed to fire, Eng. Struct. 143 (2017) 11–21.*
22. *V.D. Thi, M. Khelifa, M. Oudjene, M. El Ganaoui, Y. Rogaume. Numerical simulation of fire integrity resistance of full-scale gypsum-faced cross-laminated timber wall, Int. J. Therm. Sci. 132 (2018) 96–103.*
23. *EN 1995-1-1:2004. Eurocode 5: design of timber structures – part 1. 1: general rules and rules for buildings, European Committee for Standardization, Brussels Belgium, (E).*
24. *ISO 834-1. Fire-resistance tests. Elements of building construction. Part 1: General requirements. International Organization for Standardization, Geneva, Switzerland; 1999.*

Yielding novel k-factor formula according to the aisc standard by machine learning

Nguyen Thanh Tung[1]

Abstract

The results of using machine learning via genetic programming (GP) to automatically generate novel effective length factor formula in accordance with AISC standard are presented in this article. The data points obtained from applying the numerical method equation solving for the transcendental equation for the effective length of the braced frame were fed into the machine learning algorithm. The the formula was compared to the AISC standard's numerical solution method for the equation. As a result, the error in the formula is negligible. Therefore, for greater convenience in practice, the the formula can completely replace the AISC standard's chart.

Key words: *Genetic Programming, Symbolic Regression, Machine Learning, Numeric Analysis Method, Effective Length Factor*

(1) MS, Lecturer, Faculty of civil engineering, Hanoi Architectural University,
Email: nguyenthanhtungb@gmail.com

Date of receipt: 15/4/2022
Editing date: 6/5/2022
Post approval date: 5/9/2022

1. Introduction

In stability analysis, the AISC standard [1] requires determining the effective length for columns in frames. The AISC standard included the concept of effective length factor for frame column design in 1961, and it is still used today.

When design for multi-storey frame columns, the effective length factor (K) greatly affects the critical buckling load. Intuitively, this concept is merely a mathematical method to alleviate the problem of calculating the critical stress for a column whose two ends are connected to the frame. The bending moment in the column due to the beam's gravity load does not significantly affect the overall stability of the frame in the elastic range, and only the axial force will have significant effect.

The AISC standard only has one method for calculating the effective length, which is depicted in Figure 2 [1]. The chart makes it possible to obtain the elastic solution of the K-factor without performing an actual stability analysis (which is rather complex). However, if engineers use software such as spreadsheets to automate calculations, charts are no longer valid. As a result, an analytic formula is required to facilitate practical application.

Many engineering problems require solutions to be derived from transcendental equations, experimental data, or numerical simulation data. But most experimental formulae are frequently derived from human experience and performed manually. This has the disadvantage of not providing an optimal formula and a good fit to the data.

A great difficulty is to find the analytic solution of a general equation that is impossible. Even polynomial equations with degrees greater than 5 do not have algebraic solutions (Abel–Ruffini theorem of 1813 [2]). Richardson's theorem [3], introduced in 1968, states that there is no general analytic solution for algebraic or transcendental equations.

As a result, using machine learning to automatically generate approximate formulas from data collected by numerical or experimental methods is a feasible and effective method. The machine learning method based on genetic programming (GP, John Koza 1990[4]) is popular among the methods to find the formula, also known as symbolic regression (SR)[4]. It has been used in

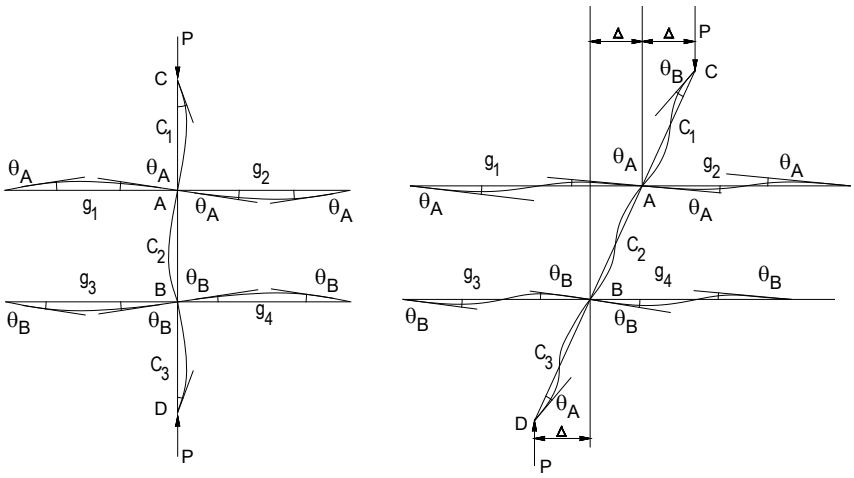

(a) Braced frame **(b) Unbraced frame**

Figure 1: Models for the K-factor of frame columns

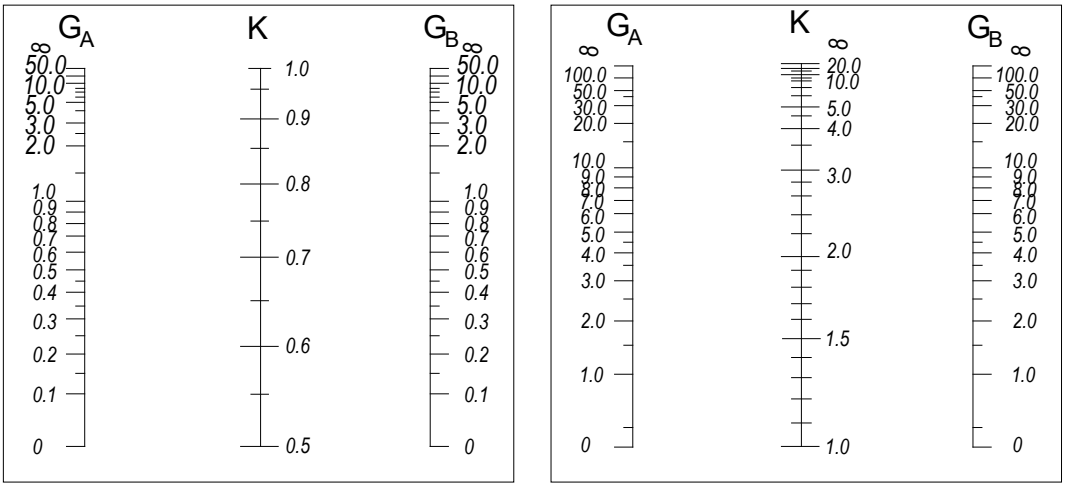

(a) Braced frame (b) Unbraced frame

Figure 2: Design chart for determining the effective length of the column in the frame

a variety of engineering disciplines, producing results that can be considered "inventions" that outperform humans[4]. However, the use of machine learning methods to create design formulas based on empirical data is still limited in the construction industry.

This paper presents a genetic programming-based machine learning method for determining the effective length of a braced frame column using data from numerical analysis. From there, a the formula is convenient in practice with high accuracy is proposed.

In published papers, the authors proposed the K-factor formula of frame columns that relate to the AISC's alignment chart method as following: Newmark 1949 [10]; Julian and Lawrence, 1959 [11]; Kavanagh, 1962 [12]; Johnston, 1976 [13]; LeMessurier, 1977 [14,15,16]; Lui, 1992 [17] ; Duan, King, Chen, 1993[18]; White and Hajjar, 1997 [19,20]. The Standards of steel structure involve formulas for K-factors including: European (prestandard-1992) [21], German, 2008 [22], France, 1966 [23], Russia, 2011 [24].

The K-factor formulas for frame columns in the above material do not coincide with the formula (10) found by GP in the article. The interpolation method is used in all of the K-factor formulas above. Therefore, they differ from the method described in the article in that knowing the form of the formula in advance (based on the builder's experience and knowledge) is required before identifying the formula's coefficients. In this paper, on the other hand machine learning method does not know the formula form in advance, it will automatically determine the formula form and coefficients (symbolic regression).

2. Effective length factor based on theoretical of stability

Frames are classified as braced or unbraced in AISC structural steel design standards[1]. When the stability of the structure is generally provided by walls, braces, or struts that are designed to carry all lateral forces in that direction, the column may be braced in that direction. When the resistance to lateral loads is caused by the bending of the columns, the column is not fully braced in that plane. There are no fully braced frames in practice, and there is no apparent distinction between braced and unbraced frames.

In the AISC [1] steel structure design standard, the interaction between a compression member and an adjacent member or a part of the structure is modeled as shown below.

The elastic stiffness of joints A and B is given by[1]

$$G_A = \frac{\sum\left(E_c I_c / L_c\right)_A}{\sum\left(E_g I_g / L_g\right)_A} \quad (1)$$

$$G_B = \frac{\sum\left(E_c I_c / L_c\right)_B}{\sum\left(E_g I_g / L_g\right)_B} \quad (2)$$

In which, the ∑ means the total stiffness of all elements connected to the joint on the instability plane of the column being considered. I_c is the moment of inertia, L_c is the length between the supports of the column. I_g is the moment of inertia, L_g is the length between the beam supports or other supporting members. I_c and I_g are in axis perpendicular to the buckling plane.

Galambos[5], 1968 solved this problem and gave the following transcendental equation to determine the effective length of the column in the frame.

Unbraced frame[1]:

$$\frac{G_A G_B(\pi/K)^2 - 36}{6(G_A + G_B)} = \frac{\pi}{K}\cot\left(\frac{\pi}{K}\right) \quad (3a)$$

Braced frame[1]:

$$\frac{G_A G_B}{4}\left(\frac{\pi}{K}\right)^2 + \left(\frac{G_A + G_B}{2}\right)\left[1 - \frac{\pi}{K}\cot\left(\frac{\pi}{K}\right)\right] + 2\frac{\tan\left(\pi/2K\right)}{\pi/K} - 1 = 0 \quad (3b)$$

3. Method of calculating effective length factor according to AISC

The AISC standard [1] relies on (3a) and (3b) to provide charts for convenient apply in practice. However, this leads to difficulties for applying in spreadsheet software

Where GA, GB is the relative stiffness ratio between the column and the beam at the ends A and B as shown in Figure 2 and is taken from (1) and (2).

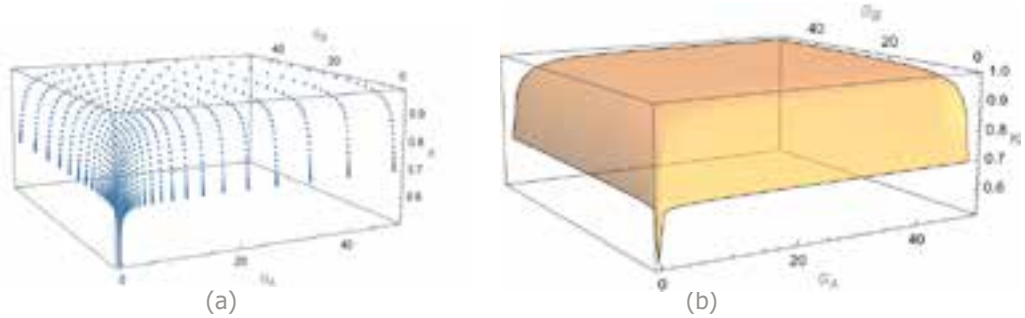

(a) (b)

Figure 3 : (a) Plot of the data set obtained from the numerical method for the equation (b) for learning and (b) Plot of learned K-factor formula (10)

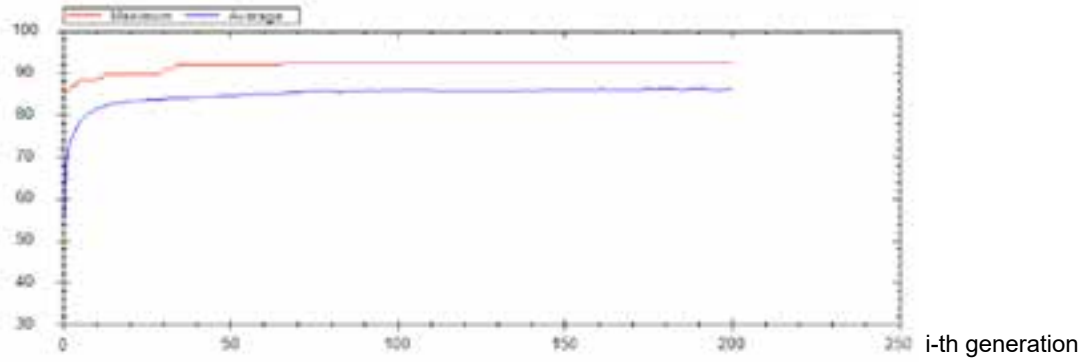

Figure 4: Graphs of maximum and average fitness values in evolution generations.

4. Application of Machine learning based on genetic programming to solve the problem of finding K-factor formulas for brace frames from numerical analysis data

4.1. Overview of machine learning by genetic programming

Machine learning has long been used in research [8], but it has exploded in popularity in recent years, thanks to researchers Yoshua Bengio, Geoffrey Hinton, Yann LeCun who won the Turing Award (Nobel Prize in IT) in 2018 [9] for developing a deep learning method. Deep learning, on the other hand, does not allow for the solution of the symbolic regression problem because it relies on an artificial neural network (ANN) and the learning process is just modifying the network's weights. As a result, in the domain of symbolic regression, the genetic programming method remains the most advantageous method.

In 1975, John Holland [6] published a genetic algorithm (GA) that approximates solving the combinatorial global optimization problem. This is an NP-hard problem [7], which is the most difficult class of problems for which there is currently no general solution for all problem instances. GA is used in a variety of fields, including machine learning. However, it does not allow for the solution of the symbolic regression problem. The symbolic regression problem could not be solved until the advent of genetic programming (in 1988, John Koza [4]). Genetic programming is based on genetic algorithms, but instead of data encoded in the form of string genome, it works on tree data structures genome.

4.2. Application of machine learning algorithms to learn the K-factor formula

The application of GP to learn the K-factor formula is described in this section as following.

Let

- KN:$\{G_A,G_B\}\rightarrow K$, $K\in\mathcal{R}+$ where K_N is K-factor value from the numerical solution to equation (3b).
- P is a sample (data point) for learning,
- $P=\{G_A,G_B,K_N(G_A,G_B)\}$, $G_A,G_B \in \mathcal{R}+$.
- T is the data set (data table) which is the set of samples $T=\{P_i\}$, i=1,…,n; n – number of samples.
- T_L is a data set for learning $TL=\{P_j\} \subset T$, j=1,…,l, l- the number of samples to be learned.
- T_T is the data set for evaluation (testing) $T_T=\{P_k\} \subset T$, k=1,…,t, t- the number of samples to be tested.

Two sets T_L and T_T satisfy the following constraint:

$T= T_L \cup TT$, $TL \cap T_T = \emptyset$, from $T=T_L \cup T_T \rightarrow n=l+t$. Typically, there is 80% learning data and 20% testing data i.e. l=0.8n and t=0.2n.

- $K_f^{i,j}:\{G_A,G_B\}\rightarrow K$, $K\in\mathcal{R}+$; where $K_f^{i,j}$ is i-th individual K-factor formula of j-th generation.
- $K_{GP}:\{T_L,B,P_r\}\rightarrow K_f^{best}$, where K_{GP} is a Genetic Programming learner that outputs as an explicit expression of K-factor formula; B – set of basic functions; P_r – set of parameters of a GP learner.
- $K_f^{best}:\{G_A,G_B\}\rightarrow K$, $K\in\mathcal{R}+$, where K_f^{best} is the best outputting K-factor formula,
- $\epsilon_k^{i,j}$ is the error in percentage between $K^{i,j}_f(G^k_A,G^k_B)$ and $K_N(G^k_A,G^k_B)$,

$$\epsilon_k^{i,j}= 100\times(K^{i,j}_f(G^k_A,G^k_B) - K_N(G^k_A,G^k_B))/K_N(G^k_A,G^k_B); \quad (4)$$

where i=1,…,m; m- the cardinality of the set $\{\epsilon ki,j\}$, i is i-th individual, j is j-th generation.

- ϵ is a member of the set of ϵ_k, $\epsilon \in \{\epsilon_k\}$, i=1,…,m,k=1,…,N,
- Var[ϵ] is the variance of ϵ, $Var[\epsilon]=E[(\epsilon-\mu)]$, where μ is expected value of ϵ, $\mu=E[\epsilon]$, E is mean of ϵ
- ϵ_{max}, ϵ_{min} is the maximum and minimum absolute errors between the value calculated by the learned formula and

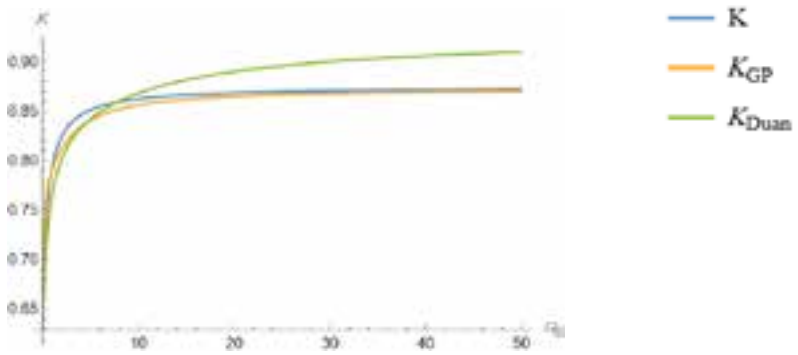

Figure 5: Graph of K(exact),K_{GP}(10),K_{Duan} (11) [18] with G_A=1, $G_B \in$ [0...50]

the numerical solution are given by ϵ_{max}, ϵ_{min} as following: $\epsilon max=max\{|\epsilon i|\}$, i=1,…,m; $\epsilon min=min\{|\epsilon i|\}$, i=1,…,m

- $\epsilon_k^{L,i,j}$, ϵ_k^T is learn and test error, i=1,…,m,k=1,…,N, k is k-th sample in T_L.
- $\epsilon^{L,i,j}$, ϵ^T is a member of the set of { $\epsilon_k^{L,i,j}$ },{ $\epsilon_k T$ }.
- $\epsilon^L{}_{max}$, $\epsilon^L{}_{min}$ and $\epsilon^T{}_{max}$, $\epsilon^T{}_{min}$ is the maximum and minimum absolute errors for learn and test sets.

From above definitions, the fitness function F is implemented as follows:

$$F(K^{i,j}_f (G_A,G_B))=(100-Var[\epsilon^{L,i,j}]) \quad (5)$$

Where i is i-th individual, j is j-th generation.

Convergence condition[4]:

$$Max(F(K_f^{i,j} (G_A,G_B)) - F(K_f^{i,j-1} (G_A,G_B)))\rightarrow 0 \quad (6)$$

The GP learning stage with fitness function F, by input T_L,B and output K_{GP}:$\{T_L,B,P_r\}\rightarrow K^f_{best}$;

$$K_f^{best} =arg_{(i)} max(F(K^{i,j}_f (G_A,G_B))). \quad (7)$$

The GP evaluation stage is to score the learned model based on statistics variables: $Var[\epsilon^T]$, $\epsilon^T{}_{max}$, $\epsilon^T{}_{min}$, the lower the values, the higher the quality of the learned model.

4.3. Data set for training and evaluation

The data set for the machine learning algorithm to learn the bracing effective length formula is based on the numerical method of solving equations (3b). After extensive testing, it is clear that the function of calculated length increases rapidly when the stiffness G_A,G_B is low and slowly as the stiffness increases (figure 3a). As a result, the final learning data set contains 2500 data points with increasing distances, as determined by the square rule. This achieves the required accuracy without necessitating the use of an excessive number of data points to learn.

$$G^{i+1}{}_A= G^i{}_A +\Delta^2 , G^{i+1}{}_B= G^i{}_B +\Delta^2, i=1..n \quad (8)$$

Where: Δ is the basic step size Δ = 0.1, n- number of data points of variable G_A, G_B, n=50.

The data used to train machine learning is divided into two sets: learning data set (80%) and testing data set (20%). Overfitting can be avoided by dividing the data set into two parts. Overfitting causes the learned model to be less generalizable, lowering prediction accuracy. This means that some range the the accurary of will be high while others will be low, which should always be avoided when using machine learning.

4.4. Parameters of the genetic programming algorithm

Viewing the plot, one can see that the shape of the data obtained from the numerical method is a monotonically increasing function that is not quite rapidly increasing, as shown in the figure 3, indicating that exponential functions are unnecessary. On the other hand, because the plot is not acyclic, trigonometric functions are unnecessary. The following operators are used from there:

B={+(Plus),-(Minus),×(Times),/(Divide),

^(Power),√ (Square Root), $\tan^{-1}$ (Arctan)} (9)

The following are the ideal parameter values for the problem under examination, as determined by a series of trials with various parameters:

Table 1: Parameters for the algorithm GP

Parameters	Values
Population size	1000
Generations	200
Crossover	0.9
Mutation	0.05
Reproduction	0.2
Maximum initial level	5
Maximum operation level	6

The algorithm starts to converge with number of generations > 100, then the objective function value cannot be improved further. After a number of different runs, the best fitness K-factor formula of braced frame column formula was obtained (Fig. 3b):

$$K=\tan^{-1}\left(\tan^{-1}\begin{pmatrix}1.49\tan^{-1}(0.26G_A)\tan^{-1}(0.26G_B)\\+0.23\left(\tan^{-1}(4.58G_A)+\tan^{-1}(4.58G_B)\right)\\+0.55\end{pmatrix}\right)+0.055 \quad (10)$$

4.5. Result evaluation

The statistical parameters of the machine-learning-discovered formula are listed in the table below:

Table 2: Statistical parameters of the learned formula

Parameters	Values
$Var[\epsilon^T]$	0.15%
$\epsilon^T{}_{max}$	2 %
$\epsilon^T{}_{min}$	2.83×10^{-7}%

According to table 2, the maximum absolute error value is only 2%, showing that the given formula is not overfit. The variance throughout the range is 0.15 %, which is a tiny error. The current best formula by Duan (11) [18] has a maximum absolute error value of 5%. A comparison of exact solutions obtained by numerical approach (K), machine learning formula (10) (K_{GP}), and Duan (K_{Duan}) is shown in the graph below:

Where, the KDuan [18] is

$$K_{Duan} = 1 - \frac{1}{5+9G_A} - \frac{1}{5+9G_A} - \frac{1}{10+G_AG_B} \quad (11)$$

5. Conclusion

The research findings demonstrate the advantages of using machine learning to find practical formulas based on data from experiments or numerical methods. It enables formulas with tiny errors across the entire data domain and differs from other methods for its automability. Furthermore, machine learning enables the successful learning of a wide variety of data types and problems./.

References

1. *ANSI/AISC 360-16 An American National Standard Specification for Structural Steel Buildings*
2. *Ruffini, Paolo (1813). Riflessioni intorno alla soluzione delle equazioni algebraiche generali opuscolo del cav. dott. Paolo Ruffini ... (in Italian). presso la Societa Tipografica.*
3. *Richardson, Daniel (1968). "Some Undecidable Problems Involving Elementary Functions of a Real Variable". Journal of Symbolic Logic. 33 (4): 514–520. JSTOR 2271358. Zbl 0175.27404*
4. *Koza, J.R. (1990). Genetic Programming: A Paradigm for Genetically Breeding Populations of Computer Programs to Solve Problems, Stanford University Computer Science Department technical report STAN-CS-90-1314..*
5. *Theodore V. Galambos. Guide to Stability Design Criteria for Metal Structures. John Wiley & Sons, 1988.*
6. *John Holland. Adaptation in Natural and Artificial Systems (1975, MIT Press)*
7. *Knuth, Donald (1974). "Postscript about NP-hard problems". ACM SIGACT Novels. 6 (2): 15–16. doi:10.1145/1008304.1008305. S2CID 46480926.*
8. *Samuel, Arthur (1959). "Some Studies in Machine Learning Using the Game of Checkers". IBM Journal of Research and Development. 3 (3): 210–229. CiteSeerX 10.1.1.368.2254. doi:10.1147/rd.33.0210.*
9. *Fathers of the Deep Learning Revolution Receive ACM A.M. Turing Award Bengio, Hinton and LeCun Ushered in Major Breakthroughs in Artificial Intelligence*
10. *Newmark NM. A simple approximate formula for effective end-fixity of columns. J Aeronaut Sci 1949;16(2)*
11. *Julian, O.G. and Lawrence, L.S. (1959) Notes on J and L Nomographs for Determination of Effective Lengths.*
12. *Kavanagh, T.C. (1962), "Effective Length of Framed Columns," Transactions, Part II, ASCE, Vol. 127, pp. 81–101.*
13. *Johnston, B.G. (ed.) (1976), Guide to Stability Design for Metal Structures, 3rd Ed., SSRC, John Wiley & Sons, Inc., New York, NY.*
14. *LeMessurier, W.J. (1976), "A Practical Method of Second Order Analysis, Part 1—PinJointed Frames," Engineering Journal, AISC, Vol. 13, No. 4, pp. 89–96.*
15. *LeMessurier, W.J. (1977), "A Practical Method of Second Order Analysis, Part 2—Rigid Frames," Engineering Journal, AISC, Vol. 14, No. 2, pp. 49–67.*
16. *LeMessurier, W.J. (1995), "Simplified K Factors for Stiffness Controlled Designs," Re structuring: America and Beyond, Proceedings of ASCE Structures Congress XIII, Boston, MA, ASCE, New York, NY, pp. 1,797–1,812.*
17. *Lui, E.M. 1992. A Novel Approach for K-Factor Determination. AISC Eng. J., 29(4):150-159.*
18. *Duan L, King WS, Chen WF. K-factor equation to alignment charts for column design. ACI Struct J 1993;90(3):242–8.*
19. *White, D.W. and Hajjar, J.F. (1997a), "Design of Steel Frames without Consideration of Effective Length," Engineering Structures, Elsevier, Vol. 19, No. 10, pp. 797–810.*
20. *White, D.W. and Hajjar, J.F. (1997b), "Buckling Models and Stability Design of Steel Frames: a Unified Approach," Journal of Constructional Steel Research, Elsevier, Vol. 42, No. 3, pp. 171–207.*
21. *Eurocode 3, Design of steel structures – part 1.1: general rules and rules for buildings (European prestandard ENV 1993-1-1:1992),*
22. *DIN 18800-2: Stahlbauten – Teil 2: Stabilitätsfälle – Knicken von Stäben und Stabwerken*
23. *Regles de calcul des constructions en acier CM66. Editions Eyrolles, Paris, France; 1966.*
24. *СВОД ПРАВИЛ СП 16.13330.2011 СТАЛЬНЫЕ КОНСТРУКЦИИ Актуализированная редакция СНиП 11-23-81 Издание официальное*

Application of convolutional neural network for detecting concrete cracks

Tu T. Nguyen[(1)], Hiep H. Vu[(2)] and Kien T. Doan[(3)]

Abstract

Deep learning continues to growing in popularity and expanding for civil engineering applications thanks to easy access to massive sets of labeled data, increased computing power, and the availability of pre-trained models built by experts. In this paper, a Convolutional Neural Network (CNN) method is employed to classify the crack/non-crack aerial images captured on the surface of concrete structures. The CNN model was trained and validated using the available experimental data of 4000 previously published images. The trained CNN model was then tested with 330 unseen images. It was shown that the proposed CNN model can classify the crack/non-crack images with an accuracy level of 93%.

Key words: *Deep Learning, Convolutional Neural Network, Crack Detection, Concrete Crack*

(1) Dr., Faculty of Civil Engineering, Hanoi Architectural University,
Email: <tunt@hau.edu.vn>

(2) Assoc. Prof., Faculty of Civil Engineering, Hanoi Architectural University,
Email: <vuhoanghiep@hau.edu.vn >

(3) Dr., Faculty of Civil Engineering, Hanoi Architectural University,
Email: <kiendt@hau.edu.vn >

Date of receipt: 15/4/2022
Editing date: 6/5/2022
Post approval date: 5/9/2022

1. Introduction

Crack on concrete structures is a significant indication of possible reinforcement corrosion, spall development, or overload conditions. Thus, monitoring the cracks on the structure surface would provide important information to evaluate the safety level of the structure as well as to have an appropriate rehabilitation plan. Manual visual inspections using human labor are proven as an effective method to detect surface cracks in concrete, however, the method is time-consuming, labor-intensive, and sometimes exposes risks to the inspectors. With the development of aerial vehicle (AV) devices and machine learning-based techniques, more and more automated AV-based visual inspections are available at an affordable cost and high level of accuracy. The technique itself consists of two parts: (i) image data collection, and (ii) data processing.

The process of collecting aerial image data has been conducted by many investigators [1-6]. For example, Jong et al. [1] used unmanned aerial vehicles (UAV) to capture the images from the lower part of slab desks in bridges. Chen et al. [3] employed UAV to take aerial images of different types of typical ground targets namely buildings, roads, mountains, and riverways to study the aftermath of an earthquake strike. Li and Zhao [5] obtained the image dataset using a smartphone from the surface of a pylon and anchor room of a suspension bridge. In a recent study, Zhou and Song [6] utilized the high-resolution, vehicle - mounted to collect aerial images from the concrete roadways.

With regard to image data processing, various popular convolutional neural network systems such as VGG [7], GoogLeNet [8], and ResNet [9] have been proposed. In recent years, the applications of deep learning to address engineering issues have been widely used among researchers [10-15]. Related to the application of CNN, Zhang et al. [10] applied a deep learning technique for road crack detection using images captured from smartphones. Maeda et al. [11] developed a mobile phone application to detect road surface defects. The application of the CNN approach for defects detection was also found in a study by Tong et al. [12] with images from a ground-penetrating radar.

In this paper, the CNN-based model was developed to identify crack/non-crack images collected on the surface of a concrete structure. The CNN model was adapted from the pre-trained, open-sourced model developed by Google and distributed through TensorFlow. Available experimental data was collected from the concrete roadways with a vehicle-mounted laser imaging system. The CNN-based model was developed with the PYTHON environment.

2. Methodology

This section presents brief description of the data collection process, as well as the method to pre-process and generate aerial image data, were presented. In addition, a predictive model called CNN was employed to detect the surface concrete cracks using the datasets mentioned in the previous sections. The structure of the CNN model, the title of layers, their roles in the system, and some basic steps to train the model were also briefly discussed. Detailed information is presented in the subsequent sections.

2.1. Data set and data augmentation

Data used in this study were obtained from an available, published source [6]. Experimental data were collected from the concrete

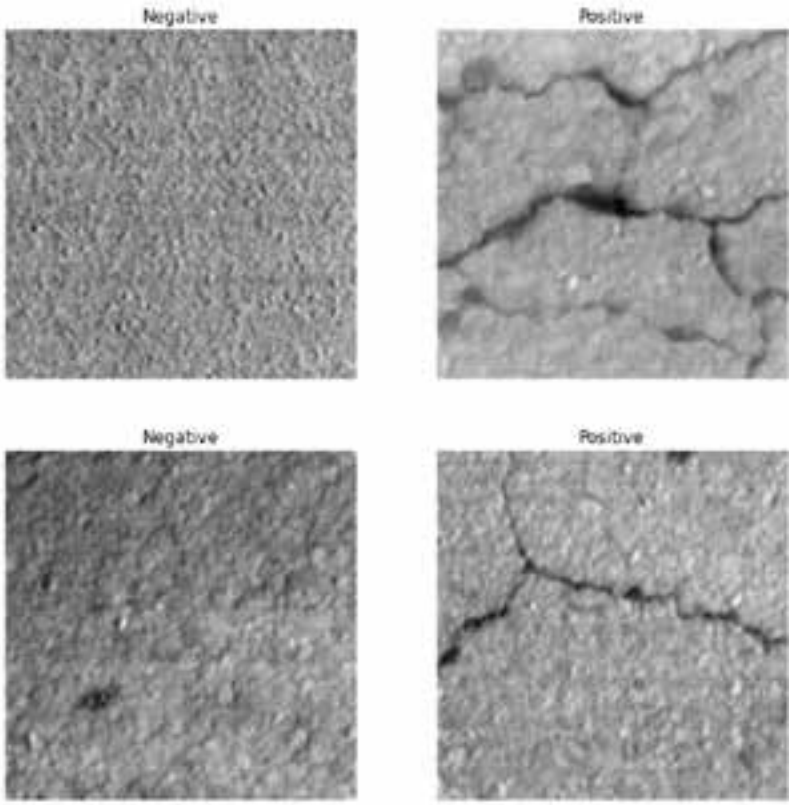

Figure 1: Inputs from different groups loaded with CNN model

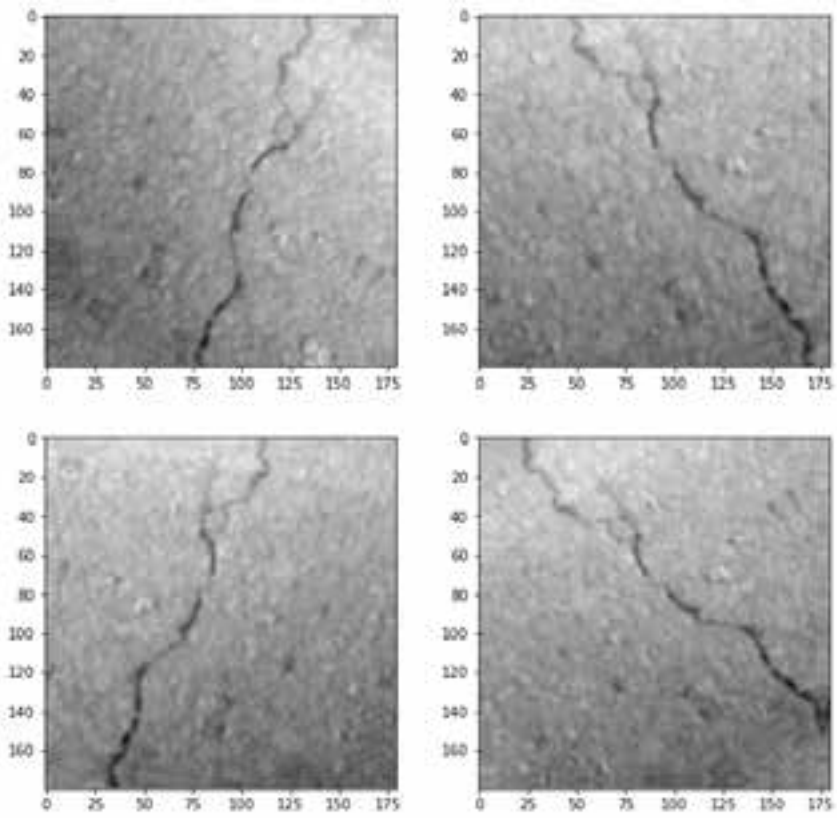

Figure 2: An example of image argumentation

roadways using a camera module is mounted 2.13 m above the ground on a vehicle. The images were captured while the vehicle was running at a speed of less than 9.83m/s. Detailed data collecting processes can be found in [6]. The raw data obtained from the field were then pre-processed to remove the unwanted effects of surface variations, scanning noises, and non-crack patterns. The final data set were generated using the sliding window technique [16], classified and documented in the "crack" and "non-crack" folders. A total of 4000 images are generated for each type of image data. Figure 1 presents some images from the positive/crack and negative/non-crack groups loaded by the proposed CNN model.

2.2. Convolutional Neural Network

The structure of a standard CNN model consists of an input layer, convolutional layers, pooling layers, and fully connected layers with an activation function to produce the output. The role of the convolutional layer is to apply the convolution to the raw input data and pass the results to the next layer. The pooling layer is extracted the dominant features from the input, usually using the maximum pooling or average pooling technique. The fully connected layers convert the two-dimensional features obtained from the previous layers into a one-dimensional vector and feed it into a softmax function to generate the outputs. Figure 3 illustrates a structure of a typical CNN model.

The CNN model used in this study has one node in the input layer and two nodes (i.e., crack or non-crack) in the output layer. To train the CNN model, the cracks and non-cracks images were loaded from the two separate folders and preprocessed to reduce the size of the pictures to 180 by 180 pixels before feeding to the proposed CNN model. In this study, about 90% of the entire inputs were used to train and validate the model, and 10% of the database was used for testing the accuracy of the trained CNN model.

3. Results and discussion

As previously mentioned, the trained CNN model was used to classify the crack and non-crack images in the test set. The following section present the prediction capabilities of the proposed model for the 330 unseen images in the testing dataset were presented. The performance of models would be evaluated through various performance metrics including Accuracy, Precision, Recall, and $F_{1-score}$. The confusion matrix and AR indicator would also be briefly discussed.

3.1. Model performance metrics

Accuracy refers to the ratio of the number of correctly predicted crack and non-crack images to the total number of input images.

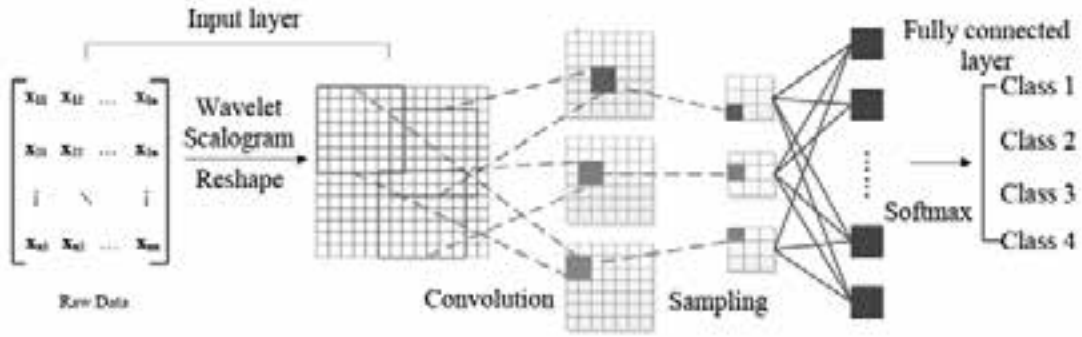

Figure 3: Architecture of CNN model

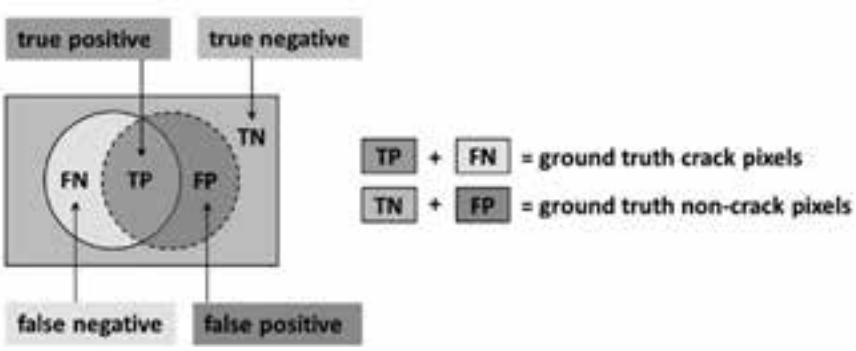

Figure 4: The schematic diagram for the performance metrics

Precision can be understood as the number of correctly predicted crack images divided by the number of crack images predicted by the classifier. The recall is the percentage of the number of correctly predicted crack images to the total number of cracked images. $F_{1-score}$ is the harmonic mean of precision and recall. Accuracy, Precision, Recall, and $F_{1-score}$ can be calculated through equations (1a-1d) using true-positive (TP), true negative (TN), false-positive (FP), and false-negative (FN), as illustrated in Figure 4.

$$\text{Accuracy} = \frac{TP + TN}{TP + FP + TN + FN} \quad (1a)$$

$$\text{Precision} = \frac{TP}{TP + FP} \quad (1b)$$

$$\text{Recall} = \frac{TP}{TP + FN} \quad (1c)$$

$$F_{1-score} = 2 \times \frac{\text{Precsion} \times \text{Rcall}}{\text{Precision} + \text{Recall}} \quad (1d)$$

An alternative way to present the performance results is using a confusion matrix. The columns of a confusion matrix represent the true value, and the rows show the predicted values assigned by the predictive model. The element aij (i is the row, and j is the column) indicates that the model assigned the value as i while the true value as in the database is I. The elements in the diagonal of the confusion matrix (aii in the light green cells) are the components correctly classified by the model. Additionally, an accuracy rate (AR) indicator (i.e., the percentage of predicted images that accurately matched the actual one) is also calculated for each group in the entire test set.

3.2. Model performance evaluation

A total of 330 images (i.e., 165 crack images and 165 non-crack images) in the training dataset were employed to test the trained CNN model. Performance results of the CNN model for the testing dataset are listed in Table 1. As can be seen, the trained CNN model can classify the crack/non-crack images at a high level of accuracy with an F1−score value of 93.0%. It is worth noting that high accuracy, precision, and recall values indicate a high positive detection rate, low false-positive rate, and low false-negative rate, respectively.

Table 1: Statistic on the performance metrics of CNN model

Accuracy (%)	Precision (%)	Recall (%)	$F_{1-score}$ (%)
93.0	98.8	88.6	93.4

Table 2: Confusion matrix for testing performance of CNN model

	Actual		
Prediction	Crack	Non-crack	Sum
Crack	163	21	184
Non-crack	2	144	146
Sum	165	165	330
AR (%)	98.8	87.3	93.0

The performance of the CNN model in terms of a confusion matrix for the testing dataset is presented in Table 2. It is interesting to note is that CNN showed a high level of accuracy in classifying the crack images with an AR value of 98.8%. The model, however, produced some misclassification for the non-crack group. To be specific, misidentified 21 non-crack images as crack ones.

4. Conclusions and recommendations

In this paper, a novel method using the Deep Learning approach to detect cracks on concrete surface is presented and discussed. The CNN model was developed using the available aerial images obtained from past publications. The trained CNN models were then utilized to categorize 330 images in the testing dataset. In terms of model performance,

the CNN model demonstrated a high precision in detecting concrete cracks. In future studies, the proposed CNN application is recommended to integrate with a computer and a camera system mounted on a vehicle to test the crack recognition capability of the software for the concrete road in Vietnam./.

References

1. *Jong-Woo, K.; Sung-Bae, K.; Jeong-Cheon, P.; Jin-Won, N. Development of Crack Detection System with Unmanned Aerial Vehicles and Digital Image Processing. Proceedings of the World Congress on Advances in Structural Engineering and Mechanics (ASEM15), Incheon, Korea, 25–29 August 2015; pp. 1–11.*
2. *Aldea, E.; Hégarat-Mascle, S.L. Robust crack detection for unmanned aerial vehicles inspection in a contrary decision framework. J. Electr. Imaging 2015, 24, 1–16, doi: 10.1117/1.JEI.24.6.061119.*
3. *Jinhong Chen, Haoting Liu, Jingchen Zheng, Ming Lv, Beibei Yan, Xin Hu, Yun Gao, Damage Degree Evaluation of Earthquake Area Using UAV Aerial Image. International Journal of Aerospace Engineering, Vol. 2016, Article ID 2052603, 10 pages, 2016. https://doi.org/10.1155/2016/2052603.*
4. *Peng, X., Zhong, X., Zhao, C., Chen, Y. F., Zhang, T. (2020). The Feasibility Assessment Study of Bridge Crack Width Recognition in Images Based on Special Inspection UAV. Advances in Civil Engineering, 2020, 8811649. https://doi.org/10.1155/2020/8811649.*
5. *S. Li and X. Zhao. Image-based concrete crack detection using convolutional neural network and exhaustive search technique. Advances in Civil Engineering, Vol. 2019.*
6. *Zhou, S., & Song, W. (2021). Deep learning-based roadway crack classification with heterogeneous image data fusion. Structural Health Monitoring, 20(3), 1274–1293. https://doi.org/10.1177/1475921720948434.*
7. *K. Simonyan and A. Zisserman. Very deep convolutional networks for large-scale image recognition. 2014, https://arxiv.org/abs/1409.1556.*
8. *C. Szegedy. Going deeper with convolutions. Proceedings of the IEEE Conference on Computer Vision and Pattern Recognition, pp. 1–9, Boston, MA, USA, June 2015.*
9. *K. He, X. Zhang, S. Ren, and J. Sun. Deep residual learning for image recognition. Proceedings of the IEEE Conference on Computer Vision and Pattern Recognition, pp. 770–778, Boston, MA, USA, June 2016.*
10. *L. Zhang, F. Yang, Y. D. Zhang, and Y. J. Zhu. Road crack detection using deep convolutional neural network. Proceedings of the IEEE International Conference on Image Processing (ICIP), pp. 3708–3712, IEEE, Phoenix, AZ, USA, September 2016.*
11. *H. Maeda, Y. Sekimoto, T. Seto, T. Kashiyama, and H. Omata. Road damage detection using deep neural networks with images captured through a smartphone. 2018, https://arxiv. org/abs/1801.09454.*
12. *Z. Tong, J. Gao, and H. Zhang. Recognition, location, measurement, and 3D reconstruction of concealed cracks using convolutional neural networks. Construction and Building Materials, Vol. 146, pp. 775–787, 2017.*
13. *Nguyen, T. T., Ngoc, L. T., Vu, H. H., & Thanh, T. P. (2021). Machine learning-based model for predicting concrete compressive strength. International Journal of Geomate, 20(77), 197-204.*
14. *Nguyen, T.T., Pham, D. H., Pham, T.T., and Vu, H.H. (2020). Compressive strength evaluation of Fiber-Reinforced High Strength Self-Compacting Concrete with artificial intelligence. Advances in Civil Engineering, 2020, 3012139. https://doi.org/10.1155/2020/3012139.*
15. *Pham, T. T., Nguyen, T. T., Nguyen, L. N., Nguyen, P. V. (2020). A neural network approach for predicting hardened property of Geopolymer concrete. International Journal of GEOMATE, Oct. 2020, Vol.19, Issue 74, pp.193–201. ISSN: 2186-2982 (P), 2186-2990 (O), Japan, https://doi.org/10.21660/2020.74.72565.*
16. *Cha YJ, Choi W and Buyukozturk O. Deep learning-based crack damage detection using convolutional neural networks. Comput Aided Civ Inf 2017, 32: 361–378.*
17. *Dung CV. Autonomous concrete crack detection using deep fully convolutional neural network. Automat Constr 2019, 99: 52–58.*
18. *Srivastava N, Hinton G, Krizhevsky A. Dropout: a simple way to prevent neural networks from overfitting. J Mach Learn Res 2014, 15: 1929–1958.*

Strength reduction of mudstone embankment...

(tiếp theo trang 30)

due to increased water content is inevitable. For the reason, it is important to develop design and quality control methods for weak rock embankments that take into account the reduction in strength due to water absorption and retention in order to improve durability and long-term performance./.

References

1. *M. Takagi, S. Yokota, K. Suga, S. Yasuda and H. Ota. The actual situation of the slope of earthfill that collapsed by an earthquake disaster in the Tomei Expressway Makinohara district. 55th Geotechnical Engineering Symposium, 193-196, 2010 (in Japanese).*
2. *H. Nakamura. Study on Design and Construction Method of High Performance Embankment on Expressway. Doctoral Dissertation. Department of Environmental Field Engineering, Graduate School of Engineering, Hokkaido University, 2014 (in Japanese).*
3. *H. Shima and S. Imagawa. Compressive settlement of slaking materials (weak rock) and its countermeasures. Tsuchi-to-Kiso. Japan Geotechnical Society, Vol.28, No.7, 45-52, 1980 (in Japanese).*
4. *NEXCO Test Methods, Test method for slaking of rocks, NEXCO Test Method 110, 2015 (in Japanese).*
5. *NEXCO Test Methods, Test method of crushing of rocks, NEXCO Test Method 109, 2015 (in Japanese).*
6. *Japanese Industrial Standards, Method for unconfined compression test of soils, JIS A 1216, 2020.*
7. *Japanese Industrial Standards, Test method for soil compaction using a rammer, JIS A 1210, 2020.*

Finite element modeling of reinforced concrete shear wall subjected to static loading

Khiem Van Giang[(1)], Hien Manh Nghiem[(2)] and Chuong Tien Nguyen[(3)]

Abstract

This paper presents a numerical modeling of RC shear walls using SSI3D finite element program. The objective of this research is to develop the full-scale model lab test of reinforced concrete (RC) shear wall. The wall is subjected to axially and laterally monotonic loading up to failure. The concrete performance is represented by 20-node solid elements that have ability of modeling the cracking in tension and failure in compression. The main steel reinforcing bars and stirrup are modeled by nonlinear bar elements that only axial stress-strain behavior is considered. The analysis results show that the concrete reaches to failure states in both tension and compression while the rebars only yield in tension.

Key words: *concrete shear wall, finite element model, nonlinear material, model lab test*

(1) MS, Lecturer, faculty of civil engineering, Hanoi Architectural University,
Email: <khiemgv@hau.edu.vn>

(2) Ph.D, Lecturer, faculty of civil engineering, Hanoi Architectural University,
Email: <hiennm@hau.edu.vn>

(3) Ph.D, Lecturer, faculty of civil engineering, Irrigation University,
Email: <nguyentienchuong@gmail.com>

Date of receipt: 15/4/2022
Editing date: 6/5/2022
Post approval date: 5/9/2022

1. Introduction

Reinforced concrete (RC) shear walls are considered as most effective elements of the lateral resisting force systems against the lateral forces of earthquake and wind loads in high-rise and mid-rise multi-story buildings due to their high lateral stiffness and strength. The RC walls also carry the vertical loads including both dead and live loads transferred from beams and slabs. Wall-frame systems provide the necessary strength and stiffness to satisfy the demands produced by both vertical and lateral loads.

Several researchers [1-4] reported that improperly designed RC shear walls may suffer severe damage, and some even collapsed during strong earthquakes such as in the recent Chile earthquake on February 27, 2010 and the Christchurch earthquake on February 22, 2011 in New Zealand. The walls were the lack of boundary transverse reinforcement, thin, and relatively high levels of axial force that suffered great damages [4]. To control the performance level of RC shear walls effectively, the earthquake-induced behavior of RC shear walls is necessary to investigate based on both model tests and nonlinear analyses.

Previous experimental studies on shear walls were focused on the load carrying capacity, hysteretic characteristics, and deformation ductility [1,5]. Wang and Jiang [1] conducted seven tests of shear wall with different geometries with aspect ratio of two and reinforcement configurations to assess the damage behavior of shear wall members under horizontal cyclic loading. Deng et al. [5] carried out four quasi-static tests of RC shear walls with low concrete strength and reinforcement ratio to investigate large axial compression ratio, stiffness, strength and energy dissipation capacity.

The current design standards for structures [6,7], the shell element that combines a membrane element with a plate element is widely used in modeling the elastic behavior of reinforced concrete wall system. The nonlinear analyses of structures with RC shear walls are very computationally expensive and not appropriate in practical but it still can be used in special purposes such as model test design and model test verification, etc. In this study, model tests of RC shear wall are analyzed using nonlinear finite element method to serve for the design of the model tests. The results of the model tests will be used to develop and calibrate a new nonlinear finite element that combining both concrete and reinforcements in one element and verify the behavior factor (q) of the current design code of earthquake resistances in Vietnam [7].

2. Finite element analyses

2.1. Preliminary design

The RC shear wall in the model test has dimensions of 3.0mx0.8mx0.15m (Height x Width x Thickness). The cross section and vertical section of the RC

Table 1: Concrete material

Parameter	Unit	Value
Young's modulus	MPa	27000
Poisson's ratio	-	0.2
Compressive strength	MPa	25
Tensile strength	MPa	1

Table 2: Steel reinforcement material

Parameter	Unit	Value
Young's modulus	MPa	200000
Poisson's ratio	-	0.3
Yield strength	MPa	360a

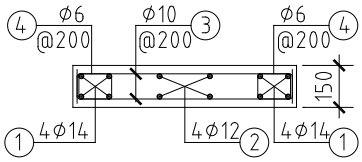

a) Cross section

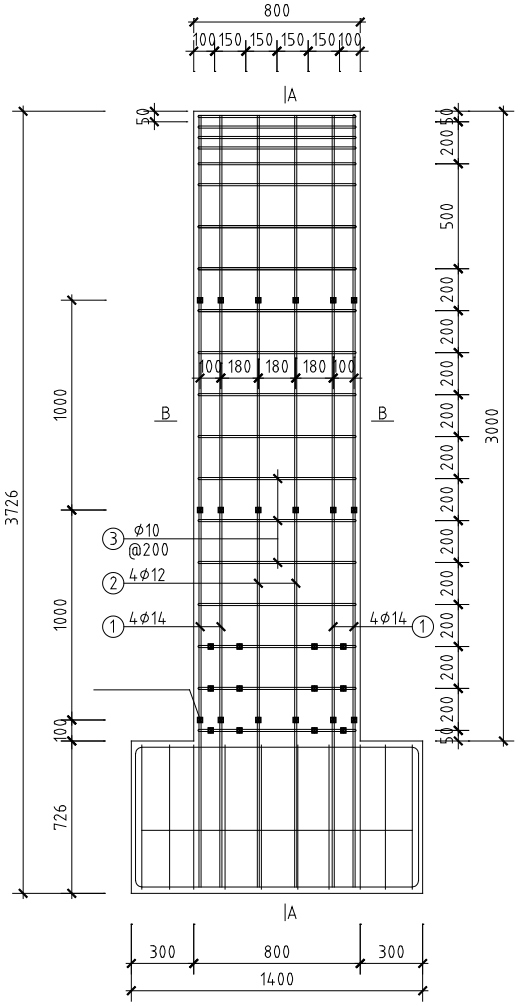

b) Vertical section

Figure 1: Details of RC shear wall

shear wall are shown in Figure 1. The material parameters of the concrete and reinforcement are presented in Table 1 and Table 2.

2.2. Element type

The finite element computer code SSI3D is used in the analyses [8]. A twenty-node solid element is used to model the RC shear wall. The solid element has twenty nodes with three degrees of freedom at each node. Figure 2 shows the twenty-node solid element in the local coordinate system. The element is capable of plastic deformation, cracking in three orthogonal directions. The nonlinear bar element is adopted to model the longitudinal rebars and stirrups. An assumption can be made that rebars and concrete are fully bonded at their interface.

2.3. The behavior of steel reinforcements

The stress-strain relationship of steel material, both in tension and in compression, is assumed to be elastic-

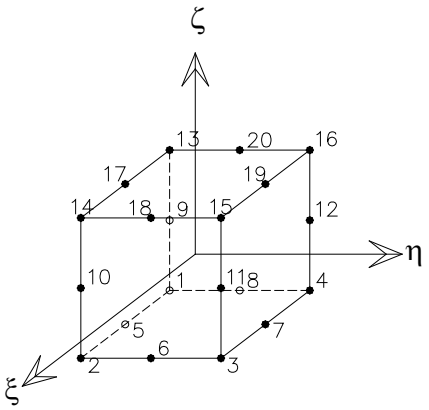

Figure 2: Twenty-node solid element

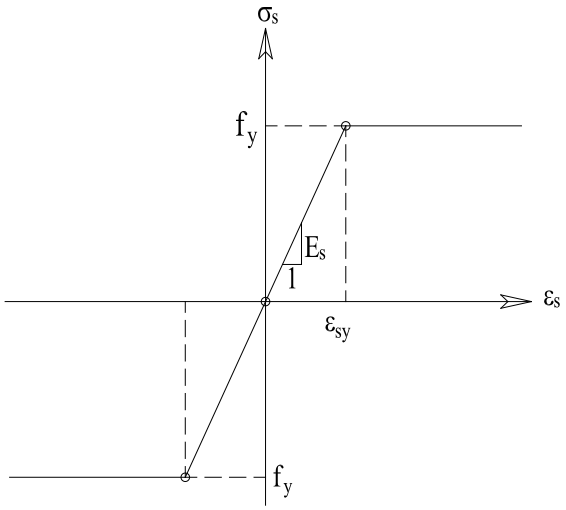

Figure 3: The stress-strain relationship for steel reinforcement

perfectly plastic, and the strain hardening of steel is neglected, as shown in Figure 3. The normal stress in the section is calculated as:

$$\sigma_s = E_s \varepsilon_s \quad (1)$$

where ε_s is Young's modulus of steel; ε_s is axial strain of steel.

The normal stress should not be greater than the yield strength of the steel material, $-f_y \le \sigma_s \le f_y$:

$$-f_y \le \sigma_s \le f_y \quad (2)$$

The yield strength is determined as:

$$f_y = E_s \varepsilon_{sy} \quad (3)$$

where ε_y is yield axial strain.

2.4. The behavior of concrete in compression

Many mathematical models of concrete are currently used in the analysis of reinforced concrete structures. For the nonlinear analysis, the stress-strain relation of concrete should be considered in both compression and tension.

In this study, elastic perfectly plastic model is adopted. The concrete stress-strain relation exhibits a linear elastic

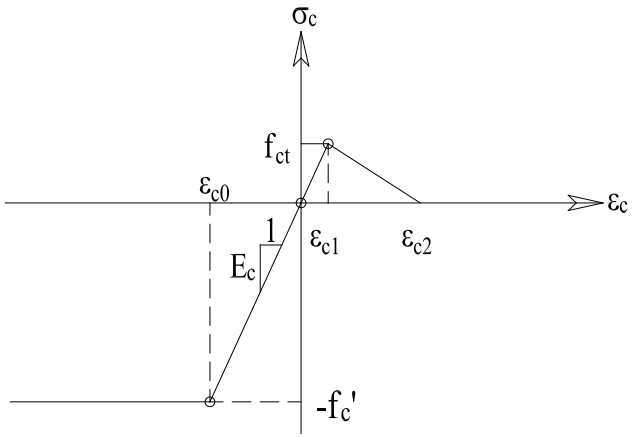

Figure 4: The stress-strain relationship for concrete

response up to the compressive strength. Beyond the compressive strength, the concrete stress-strain relation exhibits perfectly-plastic. The model can be represented by Tresca model in three-dimensional (3D) finite analyses that is already existed in the SSI3D software [8]. The behavior of the concrete represents the monotonic stress-strain relation for concrete under compression as depicted in Figure 4 and Eq. (4):

$$\begin{aligned} &\sigma_c = E_c\varepsilon_c \quad if\ \ \varepsilon_c \geq \varepsilon_{c0} \\ &\sigma_c = -f_c' \quad\ \ if\ \ \varepsilon_c < \varepsilon_{c0} \end{aligned} \tag{4}$$

where f_c' is ultimate compressive strength; ε_c is strain (positive in tension and negative in compression); ε_{c0} is a corresponding strain to f_c'; E_c is Young's modulus of concrete.

2.5. The behavior of concrete in tension

This study also accounted for the stress-strain relationship of concrete in tension. Idealized stress-strain curves for concrete in tension are shown in Figure 4. For plain concrete, the curve is linear up to cracking stress f_{ct} then gradually reduced to zero [9]. The stress-strain relationship of concrete in tension can be given in the following forms:

$$\begin{cases} \sigma_c = E_{ct}\varepsilon_c & if\ \ \varepsilon_c \leq \varepsilon_{c1} \\ \sigma_c = f_{ct} - E_{cr}(\varepsilon_c - \varepsilon_{c1}) & if\ \ \varepsilon_{c1} \leq \varepsilon_c \leq \varepsilon_{c2} \\ \sigma_c = 0 & if\ \ \varepsilon_c > \varepsilon_{c2} \end{cases} \tag{5}$$

where f_{ct} is tensile strength; ε_{ct} is a corresponding strain to f_{ct}; E_{ct} is Young's modulus of concrete in tension; and E_{cr} is slope of the stress-strain curve beyond the tensile strength.

2.6. Analysis results

Four analyses are performed to determine the maximum lateral load at different axial loads as presented in Table 3. Based on the lateral load-displacement curves at the top of the wall as shown in Figure 5, the maximum lateral loads are corresponding to the load values at the end of the curves that the shear wall cannot suffer more load. The highest lateral load is corresponding to the axial load of 250kN.

Table 3: Maximum lateral load

Axial load, P (kN)	Maximum lateral load, F_{max} (kN)
0	115
125	147
250	168
500	143

The maximum tensile and compressive stresses occur in the rebars at the boundaries. The tensile stress reach to the yield stress while compressive stress is much lower the yield stress. Figure 6 shows the plastic points in the RC shear wall. The concrete reaches to both failure states, tension or cracking indicated by blue color areas and compression failure illustrated by red color areas.

3. Conclusions

The three-dimension finite element analyses of the RC shear wall are performed to determine the maximum lateral load and failure states of the concrete and rebars for design purpose of the full-scale model tests. The RC shear wall is subjected to axially and laterally monotonic loading up to failure. The concrete performance is represented by

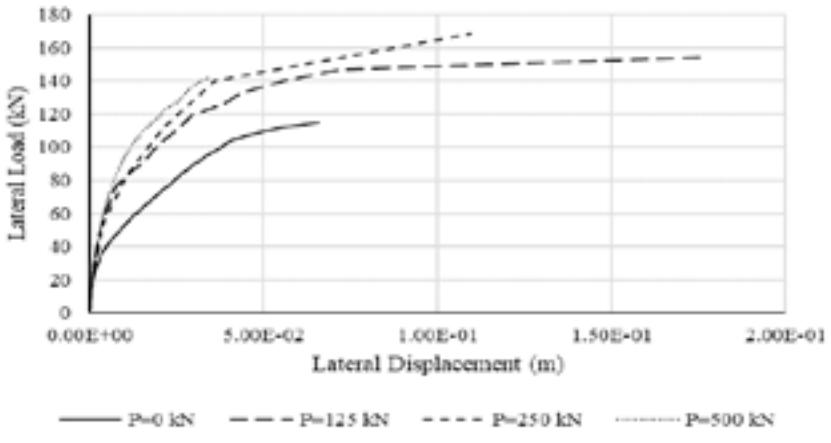

Figure 5: Lateral load-displacement curves at the top of the wall

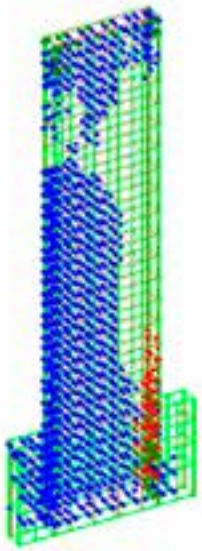

Figure 6: Plastic points in the RC shear wall

twenty-node solid elements that have ability of modeling the cracking in tension and failure in compression. The main steel reinforcing bars and stirrup are modeled by nonlinear bar elements that only axial stress-strain behavior is considered. The analysis results show that the concrete reaches to failure states in both tension and compression while the rebars are only yield in tension. Based on the analysis results, two model tests of the shear walls with different configurations of rebars will be manufactured. The tests will be carried out to verify the new finite element the behavior factor of the current design code of earthquake resistant in Vietnam that the shear walls will be subjected to lateral dynamic and axial static loads simultaneously./.

References

1. *Jiang H., Wang B. and Lu X. Experimental study on damage behavior of reinforced concrete shear walls subjected to cyclic loads. Journal of earthquake engineering, 17(7), 958-971, 2013.*
2. *Wallace J.W. Behavior, design, and modeling of structural walls and coupling beams. Lessons from recent laboratory tests and earthquakes. International Journal of Concrete Structures and Materials, 6(1), 3-18, 2012.*
3. *Kam W.Y. and Pampanin S. The seismic performance of RC buildings in the 22 February 2011 Christchurch earthquake. Structural Concrete, 12(4), 223-233, 2011.*
4. *Earthquake Engineering Research Institute (EERI). EERI Special Earthquake Report-June 2010: The Mw 8.8 Chile Earthquake of February 27, 2010. EERI Newsletter, 2010.*
5. *Deng K.L., Pan, P., Shi Y.Y., Miao Q.S., Li W.F. and Wang T. Quasi-static test of reinforced concrete shear wall with low concrete strength and reinforcement ratio. In Applied Mechanics and Materials, Trans Tech Publications Ltd. 188, 106-111, 2012.*
6. *Eurocode 8. Design of structures for earthquake resistance. Brussels: European Committee for Standardization, (2005).*
7. *TCVN 9386-2012. Design of structures for earthquake resistances.*
8. *Nghiem H.M. Soil-pile-structure interaction effects on high rises under seismic shaking. University of Colorado at Denver, 2009.*
9. *Bangash, M.Y.H. Concrete and concrete structures: Numerical Modeling and Applications. Elsevier Science Publishers Ltd., London, England, 1989.*

Experimental and numerical investigation...

(tiếp theo trang 53)

properties of wood as a function of temperature (density and thermal conductivity) suggested by the Eurocode 5 for native (virgin) wood were applied to both uncompressed and compressed samples. It can be seen that the results from the developed FE-model match well the experiments in both cases, while the Eurocode 5 model is accurate in the case of uncompressed wood for which it is dedicated.

The mean experimental and simulated charring depths for both uncompressed and compressed spruce are summarized in Table 2 for the different heat flux values. It can be observed a fairly good correlation between experimental and numerical values.

Table 2: Comparison between experimental and numerical charring depths (mm)

	Heat flux (kW/m^2)	Exposed time (min)	Charring depth (Experiment)	Charring depth (Present Model)
Virgin spruce	20	20	12	13
	75	10	15	16
Densified spruce	20	20	3	3,5
	75	10	7	7

The mass loss for the heated square plates (compressed and uncompressed) was simulated and compared to the experimentally measured loss masses during the cone calorimeter tests (Figure 9). It can be seen as a fairly good correlation.

4. Conclusion

The thermal behavior and degradation of uncompressed (virgin) and thermomechanically-compressed spruce have been studied experimentally and numerically. Several square samples measuring 100 mm x 100 mm and 19 mm thick, have been exposed to fire under a cone calorimeter using two different heat fluxes. In addition, a predictive three-steps pyrolysis finite element model has been developed and successfully implemented in the Abaqus software via the user-subroutine UMATHT. Based on the obtained results, the following conclusions can be drawn:

- Densified wood exhibits reduced charring rate and masse loss as compared to the normal (uncompressed) wood.

- An extension of Blasi's multi-reactions pyrolysis model has been proposed to deal with the temperature profile of wet wood exposed to fire. Kinetic multi-reactions pyrolysis finite element models are more general, predictive, and accurate, while the Eurocode 5 approach is not accurate to predict the thermal behavior of densified wood as it is not calibrated and validated./.

Estimating the face-to-face reinforcement ratio of short rectangular reinforced concrete columns based on two uniaxial bendings separately

Vu Huy Hoang[1]

Abstract

This paper presents a new technique to design RC columns of the rectangular section, subjected to axial compression and uni- or biaxial bending. Distributed bars around the perimeter are considered as an equivalent thin tube. Using the same steel area for two separate couples of axial compression and uniaxial bending is a trick to solve the equilibrium equations for the optimum steel ratio between faces b and h.

Key words: *: RC column, bar distribution, uniaxial bending, biaxial bending*

(1) Lecturer, faculty of civil engineering, Hanoi Architectural University, Email: <hoangvptv@gmail.com>

Date of receipt: 15/4/2022
Editing date: 6/5/2022
Post approval date: 5/9/2022

1. Introduction

The reinforcement concrete short column (RC column) under biaxial bending can be checked for strength (analysis problem) or designed for reinforcement (design problem). For analysis problem, all parameters of section must be designated, including section shape and dimensions, reinforcement layout, class of concrete and steel. Interaction curve or surface then is established in a process of iterations in which concrete section will be divided into a grid of discrete elements (D. G. Row and T. Paulay in [1] divide the concrete section into a grid of 400 discrete rectangular elements, each with dimensions of 1/20 of the section width by 1/20 of the section depth), making it labored work and must usually take advantage of the electronic computer [2]. Some simplified methods based on uniaxial bending have been suggested, such as methods of superposition, equivalent uniaxial eccentricity method [2], reciprocal load method, load contour method [3].

The design problem is more complicated [2] and often limited to reinforcement determination, in which other data, including section parameters, are known. There are two approaches so far: one using a trial and adjustment procedure with computer aid and other using prepared charts. The former required a reinforcement pattern (i.e., the steel bar layout) to be assumed (predefined by software in most cases) and the reinforcement content (i.e., the reinforcement area) successively corrected until the section capacity approached the required value [1][2]. The latter makes use of a large number of charts limited to rectangular sections [2] and has been developed by some researchers. Design charts created by D. G. Row and T. Paulay [1], in which the reinforcement pattern is assumed to be uniformly distributed as a thin tube with 0.25Ast (total reinforcement area) in each face of the section (for the purpose of computation the reinforcement was still divided into ten discrete units per face [1][2]). Weber charts were made of four, eight, 12, and 16 bar columns (the bars are considered individually rather than as an equivalent thin tube) [1]. Design charts published by Brettle and Warner are for rectangular sections which contain 16 or more bars subject to compression and biaxial bending [1].

The two approaches require a fixed reinforcement pattern: the former uses a program-specific pattern; the latter uses the ratio of Ash/Asb of 1,0 (Ash and Asb are the reinforcement areas of face b and h of the rectangular section, respectively). In fact, reinforcement areas of two adjacent faces should not be equal and are related to internal forces and section dimensions, meaning that there will be a direction that is more force-bearing than the other.

Obviously, there is a need for developing a method to determine the ratio of reinforcement areas of two adjacent faces (termed the face-to-face reinforcement ratio) of a rectangular column that in turn will be the reinforcement pattern for building up the interaction surface.

This article will introduce a way to estimate the questioned ratio, but to its extent will be limited to the case of a column subjected to two combinations of uniaxial bendings.

The thin tube as described by T. Paulay [1] will be used to reduce unknown factors. There are two variables qb and qh (substituted for Asb and Ash), that come out in the procedure, in turn requiring two equations corresponding to two selected combinations to solve.

In this article, the ratio of qh/qb is termed reinforcement pattern and the value of qb (or qh) represents for reinforcement content.

Dividing a concrete section into parts will not create functions, and therefore not appropriate for solving solutions qb and qh; thus the method must start with the creation of functions of the resultant forces, similar to that of circular sections [4].

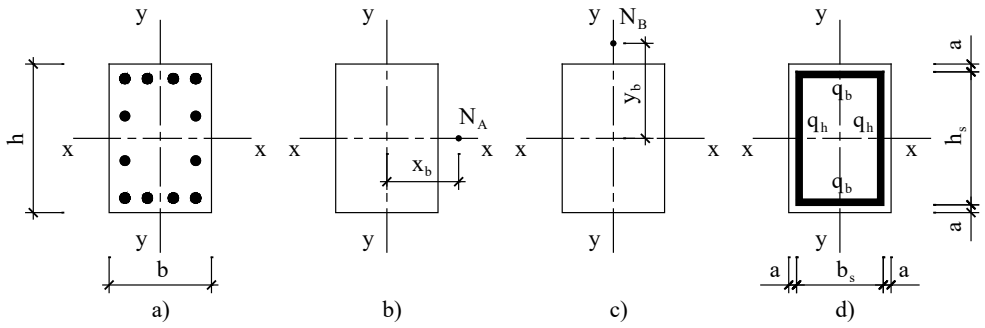

a) Column section

b) Case A: Uniaxial bending about y axis

c) Case B: Uniaxial bending about x axis

d) Steel bars to be converted to a thin tube

Figure 1: Rectangular RC column section

2. Estimating the face-to-face reinforcement ratio of rectangular RC columns based on two uniaxial bendings separately

Examining a rectangular section with distributed reinforcement as shown in Figure 1a. The section is subjected to two sets of uniaxial forces in different directions, separately, termed case A (NA, MyA) and case B (NB, MxB), as shown in Figures 1b, c.

Translate steel bars on each edge into a thin tube as shown in Figure 1d acquired

$$q_b = \frac{n_b A_{s1}}{b_s}; q_h = \frac{n_h A_{s1}}{h_s} \quad (1)$$

where

nb, nh – number of bar spacings along width (b) and depth (h) of cross section;

As1 – steel bar cross-sectional area;

bs, hs – width and depth of thin tube. bs = b - 2a, hs = h - 2a, where a is the distance from the centroid of the bar to the near edge.

a) Assumptions, sign conventions and scope

The assumptions of reinforcement concrete columns are used in this section, including that plane sections will remain plane after loaded; the tensile strength of the concrete is ignored.

The paper is limited to the following:

Cross section of column is rectangular, reinforcements are provided symmetrically.

The number of reinforcement bars on each edge is large enough to be translated into a thin tube. The number of bars is greater than or equal to five will satisfy this assumption [5].

Axial force is compressive. The strain of outer fiber in the concrete gets its limit of εcu at the ultimate limit state.

Concrete use bi-linear stress-strain relation, steel use tri-linear stress-strain relation.

To begin, formulars of the resultant forces of a typical rectangular section with respect to a neutral axis located at the bottom of the section will be established, as helpers for the next section.

The sign convention of stress/strain is such that compression positive, tension negative.

b) Resultant forces of rectangular section with respect to a neutral axis located at the bottom

It can be inferred from strain distribution [ε] that

$$\frac{\varepsilon}{t} = \frac{\varepsilon_0}{z} \Leftrightarrow t = \frac{\varepsilon z}{\varepsilon_0} \quad (2a)$$

$$dt = \frac{z}{\varepsilon_0} d\varepsilon \quad (2b)$$

Axial force function N and moment function M are

$$N = \int_0^{\varepsilon_0} \sigma dA = \frac{bz}{\varepsilon_0} \int_0^{\varepsilon_0} \sigma d\varepsilon = \frac{bz}{\varepsilon_0}\left[P_{(\varepsilon_0)} - P_{(0)}\right]$$

$$= \frac{bz}{\varepsilon_0}\left[P_{(\varepsilon_0)} - 0\right] = \frac{bz}{\varepsilon_0} P_{(\varepsilon_0)} \quad (3)$$

$$M = \int_0^{\varepsilon_0} t\sigma dA = \frac{bz^2}{\varepsilon_0^2} \int_0^{\varepsilon_0} \varepsilon\sigma d\varepsilon = \frac{bz^2}{\varepsilon_0^2}\left[T_{(\varepsilon_0)} - T_{(0)}\right]$$

$$= \frac{bz^2}{\varepsilon_0^2}\left[T_{(\varepsilon_0)} - 0\right] = \frac{bz^2}{\varepsilon_0^2} T_{(\varepsilon_0)} \quad (4)$$

where

$$P = \int \sigma d\varepsilon \; ; \; P_{(0)} = 0 \text{ and } T = \int \varepsilon\sigma d\varepsilon \; ; \; T_{(0)} = 0 \quad (5)$$

The group of $\sigma_{(\varepsilon)}$, $P_{(\varepsilon)}$, $T_{(\varepsilon)}$ is named a set of functions with respect to strain ε.

c) Resultant forces of rectangular RC section

Studying a rectangular RC section with thin tube provided as figure below.

The reinforcement densities of each side are qb and qh, respectively. Section width and depth are b and h. The width and depth of the thin tube are bs and hs. The following expressions are formed

$$\varepsilon_{s1} = \frac{z-a}{z}\varepsilon_{cu} \; ; \; \varepsilon_{s2} = \frac{z-a-h_s}{z}\varepsilon_{cu} \quad (6)$$

c.1 Resultant forces of concrete

Substitute εcu for ε0 in equations (3) and (4), acquired

$$N_b = \frac{bz}{\varepsilon_{cu}} P_{(\varepsilon_{cu})} \; ; \; M_b = \frac{bz^2}{\varepsilon_{cu}^2} T_{(\varepsilon_{cu})} - N_b\left(z - \frac{h}{2}\right) \quad (7)$$

where Mb is the resultant moment of compression zone about centroidal axis (x-x axis).

c.2 Resultant forces of steel

Break thin tube qh into upper part and lower part by neutral axis, still using expressions (3) and (4), acquired

$$N_s = q_b b_s \sigma_{s1} + q_b b_s \sigma_{s2} + 2\frac{q_h(z-a)}{\varepsilon_{s1}} P_{(\varepsilon_{s1})}$$

$$+ 2\frac{q_h(h_s - z + a)}{\varepsilon_{s2}} P_{(\varepsilon_{s2})} = s_n q_b + u_n q_h \quad (8a)$$

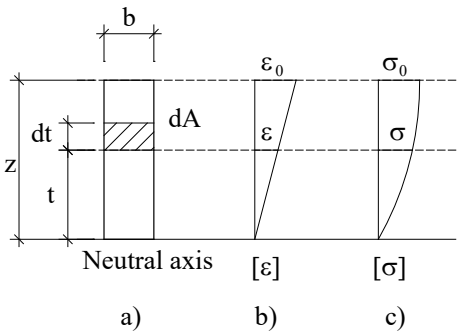

Figure 2: Calculation scheme

a) Section b) Strain distribution
c) Stress distribution

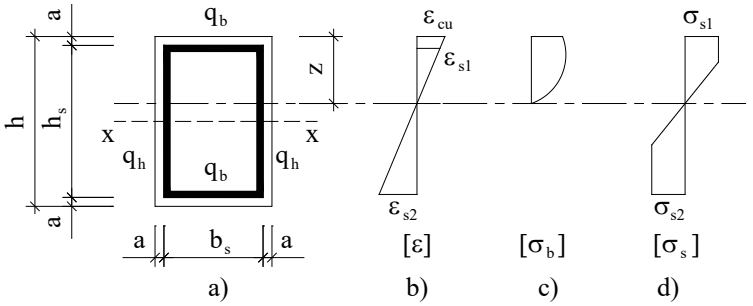

Figure 3: Calculation scheme

a) Rectangular RC section b) Strain distribution
c) Stress distribution of concrete d) Stress distribution of reinforcement

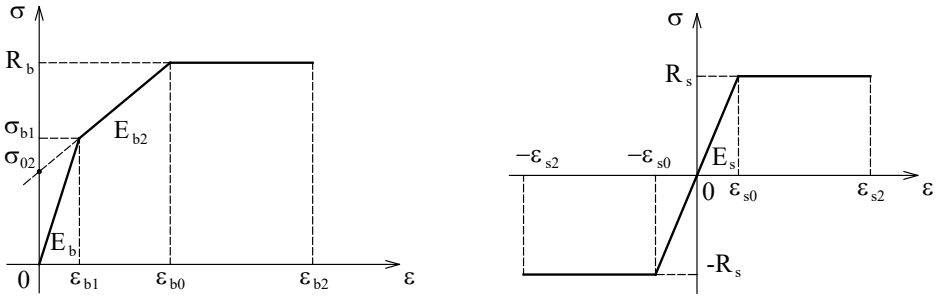

a) Concrete using tri-linear curve b) Steel using bi-linear curve

Figure 4: Strain-stress diagram per TCVN 5574-2018

$$M_s = q_b b_s \sigma_{s1}(z-a) + q_b b_s \sigma_{s2}(z-h_s-a) + 2\frac{q_h(z-a)^2}{\varepsilon_{s1}^2} T_{(\varepsilon_{s1})} - 2\frac{q_h(h_s-z+a)^2}{\varepsilon_{s2}^2} T_{(\varepsilon_{s2})}$$

$$-N_s\left(z-\frac{h}{2}\right) = s_m q_b + u_m q_h \quad (8b)$$

where Ns and Ms are the resultant force and moment of the thin tube about the centroidal axis, respectively.

$$s_n = b_s(\sigma_{s1}+\sigma_{s2});$$

$$s_m = b_s\left[\sigma_{s1}(z-a)+\sigma_{s2}(z-h_s-a)\right] - s_n\left(z-\frac{h}{2}\right) \quad (9a)$$

$$u_n = \frac{2z}{\varepsilon_{cu}}\left[P_{(\varepsilon_{s1})} - P_{(\varepsilon_{s2})}\right];$$

$$u_m = \frac{2z^2}{\varepsilon_{cu}^2}\left[T_{(\varepsilon_{s1})} - T_{(\varepsilon_{s2})}\right] - u_n\left(z-\frac{h}{2}\right) \quad (9b)$$

c.3 Consequences

Combining (7) and (8) results in

$$N = N_b + s_n q_b + u_n q_h \quad (10a)$$

$$M = M_b + s_m q_b + u_m q_h \quad (10b)$$

There are three variables in the set of equations (10); those are qb, qh and compression zone depth z.

d) Function set of concrete and steel as per TCVN 5574-2018 [6]

Relation of stress and strain of concrete and steel is illustrated in Figure 4 below

Based on definitions in (5), the formulars of σ, P, T of concrete and steel are formed and listed in Table 1 and Table 2, respectively.

e) Establishing expression for estimating face-to-face reinforcement ratio

Rewrite (10) using matrix form

$$\begin{bmatrix} N \\ M \end{bmatrix} = \begin{bmatrix} N_b \\ M_b \end{bmatrix} + \begin{bmatrix} s_n & u_n \\ s_m & u_m \end{bmatrix} \begin{bmatrix} q_b \\ q_h \end{bmatrix} \quad (11)$$

Transforming expression (11) produces

$$\begin{bmatrix} q_b \\ q_h \end{bmatrix} = \begin{bmatrix} s_n & u_n \\ s_m & u_m \end{bmatrix}^{-1} \begin{bmatrix} N-N_b \\ M-M_b \end{bmatrix} = \frac{1}{C}\begin{bmatrix} u_m\Delta N - u_n\Delta M \\ -s_m\Delta N + s_n\Delta M \end{bmatrix} \quad (12)$$

where

$$C = s_n u_m - s_m u_n \quad (13a)$$

$$\Delta N = N - N_b \quad (13b)$$

$$\Delta M = M - M_b \quad (13c)$$

For set of forces B (NB, MxB), bending about x-axis, there are three unknown factors qb, qh and compression zone depth yb

Table 1: Function set of concrete using tri-linear curve

Functions	$0 \le \varepsilon_b \le \varepsilon_{b1}$	$\varepsilon_{b1} \le \varepsilon_b \le \varepsilon_{b0}$	$\varepsilon_{b0} \le \varepsilon_b \le \varepsilon_{b2}$
σ	$E_{b2}\varepsilon_b + \sigma_{b02}$	$E_{b2}\varepsilon_b + \sigma_{b02}$	R_b
P	$\frac{E_{b2}\varepsilon_b^2}{2} + \sigma_{b02}\varepsilon_b - \frac{\sigma_{b02}\varepsilon_{b1}}{2}$	$\frac{E_{b2}\varepsilon_b^2}{2} + \sigma_{b02}\varepsilon_b - \frac{\sigma_{b02}\varepsilon_{b1}}{2}$	$R_b\varepsilon_b + \frac{(\varepsilon_{b0} - \varepsilon_{b1})\sigma_{b02} - R_b\varepsilon_{b0}}{2}$
T	$\frac{E_b\varepsilon_b^3}{3}$	$\frac{E_{b2}\varepsilon_b^3}{3} + \frac{\sigma_{b02}\varepsilon_b^2}{2} - \frac{\sigma_{b02}\varepsilon_{b1}^2}{6}$	$\frac{R_b\varepsilon_b^2}{2} + \frac{(\varepsilon_{b0}^2 - \varepsilon_{b1}^2)\sigma_{b02} - R_b\varepsilon_{b0}^2}{6}$
Notes:	$E_{b2} = \frac{R_b - \sigma_{b1}}{\varepsilon_{b0} - \varepsilon_{b1}}$		$\sigma_{b02} = \frac{\varepsilon_{b0}\sigma_{b1} - \varepsilon_{b1}R_b}{\varepsilon_{b0} - \varepsilon_{b1}}$

Table 2: Function set of steel using bi-linear curve

Functions	$-\varepsilon_{s2} \le \varepsilon_s \le -\varepsilon_{s0}$	$\varepsilon_{s0} \le \varepsilon_s \le \varepsilon_{s2}$	$\varepsilon_{s0} \le \varepsilon_s \le \varepsilon_{s2}$
σ	$-R_s$	$E_s\varepsilon_s$	R_s
P	$-R_s\varepsilon_s - \frac{R_s\varepsilon_{s0}}{2}$	$\frac{E_s\varepsilon_s^2}{2}$	$R_s\varepsilon_s - \frac{R_s\varepsilon_{s0}}{2}$
T	$\frac{E_b\varepsilon_b^3}{3}$	$\frac{E_s\varepsilon_s^3}{3}$	$\frac{R_s\varepsilon_s^2}{2} - \frac{R_s\varepsilon_{s0}^2}{6}$

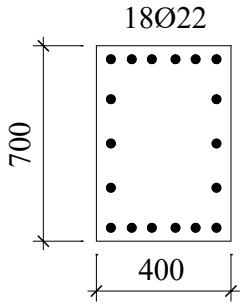

Figure 5: Steel bar layout

$$\begin{bmatrix} q_{bB} \\ q_{hB} \end{bmatrix} = \begin{bmatrix} (u_{mB}\Delta N_B - u_{nB}\Delta M_B)/C_B \\ (-s_{mB}\Delta N_B + s_{nB}\Delta M_B)/C_B \end{bmatrix} \quad (14)$$

For set of forces A (NA, MyA), bending about y-axis, there are three unknown factors qb, qh and compression zone depth xb, noted the swap of qb and qh in cases A and B

$$\begin{bmatrix} q_{bA} \\ q_{hA} \end{bmatrix} = \begin{bmatrix} (-s_{mA}\Delta N_A + s_{nA}\Delta M_A)/C_A \\ (u_{mA}\Delta N_A - u_{nA}\Delta M_A)/C_A \end{bmatrix} \quad (15)$$

Because the values of expression (14) and (15) are the same, then

$$\Delta q_b = q_{bA} - q_{bB} = \frac{-s_{mA}\Delta N_A + s_{nA}\Delta M_A}{C_A} - \frac{u_{mB}\Delta N_B - u_{nB}\Delta M_B}{C_B} = 0 \quad (16a)$$

$$\Delta q_h = q_{hA} - q_{hB} = \frac{u_{mA}\Delta N_A - u_{nA}\Delta M_A}{C_A} - \frac{-s_{mB}\Delta N_B + s_{nB}\Delta M_B}{C_B} = 0 \quad (16b)$$

There are only two variables, xb and yb, in set of equations (16). Solve this for xb and yb, in respect of case A and B, respectively; now that NbA, snA, unA, MbA, smA, umA are taken, thence qb, qh will be determined from expression (15).

The face-to-face reinforcement ratio can now be expressed by thin tube densities or by reinforcement areas:

$$k_q = \frac{q_h}{q_b} \text{ or } k_s = \frac{A_{sh}}{A_{sb}}$$

Set of equations (16) are non-linear systems. Moreover, functions such as Nb, sn, un, Mb, sm, um are piecewise-defined functions so that to solve exactly for solutions is impossible. In practice, approximate root-finding algorithms can be adopted, such as the trial-and-error method, the Newton-Raphson method...

3. Illustration

A rectangular column section of 400x700mm is subjected to five load combinations as shown in Table 3. Concrete utilizes class B25; the grade of steel is CB400-V. Distance from centroid of steel bar to the near edge is 25mm. Ask for section reinforcement.

Table 3: Design forces

Combo name	Combo discription	N (kN)	M_y ($kN.m$)	M_x ($kN.m$)
O	1,0*D*+1,0*L*	4187,6	42,6	25,2
A	1,0*D*+0,9*L*+0,9W_x	4066,3	**312,1**	28,5
B	1,0*D*+0,9*L*+0,9W_y	3991,5	47,3	**603,9**
C	1,0*D*+0,5*L*+1,0E_x+0,3E_y	3964,8	281,9	175,4
D	1,0*D*+0,5*L*+0,3E_x+1,0E_y	3933,1	96.8	541,6

where D, L, W_x, W_y, E_x, E_y denote for dead load, live load, wind load and earthquake load in X and Y directions, respectively.

Solution:

Because the axial forces in combinations are almost equal, then two combinations corresponding to M_{xmax} and M_{ymax} will be selected; i.e., combos A and B in Table 3. The moments M_x of combo A and My of combo B are insignificant (they were produced due to the irregularity of the plan) and can be ignored, meaning that combos A and B can be treated as two uniaxial bendings in estimating process, fetching the

values of (4066,3kN; 312,1kN.m) for combo A and (3991,5kN; 603,9kN.m) for combo B which will be used as the inputs.

$$b_s = b - 2a = 400 - 2\times 25 = 350mm;$$
$$h_s = h - 2a = 700 - 2\times 25 = 650mm$$

a) Material parameters

$$R_b = 14,5MPa\ ; E_b = 30000MPa\ ; \varepsilon_{b0} = 0,002;$$
$$\varepsilon_{cu} = \varepsilon_{b2} = 0,0035\ ; \sigma_{b1} = 0,6R_b = 8,7MPa$$

$$\varepsilon_{b1} = \frac{\sigma_{b1}}{E_b} = 0,00029\ ;\ E_{b2} = \frac{R_b - \sigma_{b1}}{\varepsilon_{b0} - \varepsilon_{b1}} = 3392MPa;$$

$$\sigma_{b02} = \frac{\varepsilon_{b0}\sigma_{b1} - \varepsilon_{b1}R_b}{\varepsilon_{b0} - \varepsilon_{b1}} = 7,716MPa$$

$$R_s = 350MPa\ ;\ E_s = 210000MPa;$$

$$\varepsilon_{s0} = \frac{R_s}{E_s} = 0,00167$$

b) Determination of x_b, y_b

Let x_b varies from 0 through 400mm; y_b varies from 0 through 700mm; find out the value pair (x_b, y_b) of (334,9mm; 592,1mm) which reconciles with set of equations (16). For these values, the last calculation step is as follows:

For combo B

- Resultant forces of concrete

$$P_{(\varepsilon_{cu})} = R_b\varepsilon_{cu} + \frac{(\varepsilon_{b0} - \varepsilon_{b1})\sigma_{b02} - R_b\varepsilon_{b0}}{2}$$
$$= 42,847kN/m^2$$

$$T_{(\varepsilon_{cu})} = \frac{R_b\varepsilon_{cu}^2}{2} + \frac{(\varepsilon_{b0}^2 - \varepsilon_{b1}^2)\sigma_{b02} - R_b\varepsilon_{b0}^2}{6}$$
$$= 0,08418kN/m^2$$

$$N_b = \frac{by_b}{\varepsilon_{cu}}P_{(\varepsilon_{cu})} = 2899,4kN\ ;$$

$$M_b = \frac{by_b^2}{\varepsilon_{cu}^2}T_{(\varepsilon_{cu})} - N_b\left(y_b - \frac{h}{2}\right) = 261,7kN.m$$

- Value of reinforcement functions

$$\varepsilon_{s1} = \frac{y_b - a}{y_b}\varepsilon_{cu} = 0,003352\ ;$$

$$\varepsilon_{s2} = \frac{y_b - a - h_s}{y_b}\varepsilon_{cu} = -0,00049$$

$$\sigma_{s1} = R_s = 350MPa\ ;\ \sigma_{s2} = E_s\varepsilon_s = -102,91MPa$$

$$P_{(\varepsilon_{s1})} = R_s\varepsilon_{s1} - \frac{R_s\varepsilon_{s0}}{2} = 880,95kN/m^2\ ;$$

$$P_{(\varepsilon_{s2})} = \frac{E_s\varepsilon_{s2}^2}{2} = 25,211kN/m^2$$

$$T_{(\varepsilon_{s1})} = \frac{R_s\varepsilon_{s1}^2}{2} - \frac{R_s\varepsilon_{s0}^2}{6} = 1,8036kN/m^2;$$

$$T_{(\varepsilon_{s2})} = \frac{E_s\varepsilon_{s2}^3}{3} = -0,008235kN/m^2$$

$$s_n = b_s\left(\sigma_{s1} + \sigma_{s2}\right) = 86482kN/m;$$

$$u_n = \frac{2y_b}{\varepsilon_{cu}}\left[P_{(\varepsilon_{s1})} - P_{(\varepsilon_{s2})}\right] = 289533kN/m$$

$$s_m = b_s\left[\sigma_{s1}(y_b - a) + \sigma_{s2}(y_b - h_s - a)\right] - s_n\left(y_b - \frac{h}{2}\right)$$
$$= 51518kN$$

$$u_m = \frac{2y_b^2}{\varepsilon_{cu}^2}\left[T_{(\varepsilon_{s1})} - T_{(\varepsilon_{s2})}\right] - u_n\left(y_b - \frac{h}{2}\right)$$
$$= 33610kN$$

$$C = s_nu_m - s_mu_n = -12010\times 10^6\,kN^2/m$$

- Compute q_b, q_h

$$\Delta N = N - N_b = 1092,2kN;$$
$$\Delta M = M - M_b = 342,2kN.m$$

$$q_b = \frac{u_m\Delta N - u_n\Delta M}{C} = 5,19mm;$$

$$q_h = \frac{-s_m\Delta N + s_n\Delta M}{C} = 2,22mm$$

Similar to combo B, with combo A

$$q_b = 5,2mm;\ q_h = 2,21mm$$

With the value pair of x_b = 334,9mm, y_b = 592,1mm, the values of qb and qh in both cases A and B are almost equal (slight differences arise due to calculation inaccuracy), which means that this value pair of (xb, yb) is the solution of equation set (16).

c) Reinforcement detailing

Steel reinforcements Asb and Ash along edges b and h are

$$q_b = 5,2mm \Rightarrow A_{sb} = q_bb_s = 1820mm^2$$
$$q_h = 2,22mm \Rightarrow A_{sh} = q_hh_s = 1443mm^2$$

Select bar size of 22mm, cross-sectional area is 380mm^2; then the number of spacing between bars along edges b and h are

$$n_b = \frac{A_{sb}}{A_{s1}} = 4,79 \Rightarrow \begin{cases} n_b = 5 \\ n_h = 4 \end{cases}$$
$$n_h = \frac{A_{sh}}{A_{s1}} = 3,8 \qquad (17)$$

The face-to-face reinforcement ratio

$$k_s = \frac{A_{sh}}{A_{sb}} = \frac{n_h}{n_b} = 0,8$$

Reinforcement layout is shown in Figure 5, representing the reinforcement pattern (value of 0,8) and reinforcement content (bar size of 22mm). This is just a preliminary arrangement of steel bars.

As declared in [7], "the critical load combinations may be difficult to discern without methodically checking each combination", so the interaction surface must be established, and for each combination, its force set (N, M_x, M_y) shall be checked. If a combination is over strength, reinforcement

Table 4: Checking for strength through combinations

Combo name	Design forces			Ultimate strength			Safety factor
	N (kN)	M_y (kN.m)	M_x (kN.m)	N_u (kN)	M_{uy} (kN.m)	M_{ux} (kN.m)	
O	4187,6	42,6	25,2	6049,7	61,5	36,4	1,445
A	4066,3	312,1	28,5	4130,3	317,0	28,9	1,016
B	3991,5	47,3	603,9	4012,2	47,5	607	**1,005**
C	3964,8	281,9	175,4	4113,4	292,5	182	1,037
D	3933,1	96,8	541,6	4061,9	100	559,3	1,033

Table 5: Total reinforcement area comparison

Combo name	$k_{q1} = b_s/h_s = 0{,}583$			$k_{q2} = q_h/q_b = 0{,}427$		
	q_b (mm^2/mm)	q_h (mm^2/mm)	A_{st} (mm^2)	q_b (mm^2/mm)	q_h (mm^2/mm)	A_{st} (mm^2)
O	0,9	0,48	1257	1	0,43	1261
A	4,62	2,49	6064	5,24	2,24	6579
B	4,91	2,64	**6871**	5,38	2,3	**6752**
C	4,39	2,36	6145	4,97	2,12	6233
D	4,58	2,46	6407	5,03	2,15	6314

content will be adjusted (bar size to be increased) while reinforcement pattern remains, and so on.

The results of checking for strength of the section shown in Figure 5 through combinations are shown in Table 4, in which the overall safety factor is the minimum value of 1,005. Although the provided reinforcement area has been chosen to be greater than required (see expression (17)), the margin is still pretty small (1,005 is very close to 1,0) this is because of the consideration of My in addition to combo B (for the scope of the article, the calculation process of the values in Tables 4 and 5 is not expressed here).

The reliability of the face-to-face reinforcement ratio k_s (meaning that its value can cause the total reinforcement area to be minimal) depends on the pick of two initial combinations. If the combination pair dominates the design, the result of the process (reinforcement layout in Figure 5) will be the final one. Sometimes these combinations are evident to be found. Especially in the case of buildings of simple shape plan, under wind load are often considered two directions of loading in company with major and minor axes of the plan. If the structure layout is simple and regular, these lateral loads will each produce a uniaxial bending effect to columns (the bending moment in the other direction still exists but is quite insignificant). Since the combinations which consist of lateral loads are commonly dominant in column design, the two combinations of these wind loads with vertical loads such as dead load and live load, still to be uniaxial bendings, will govern the design result. This is the case within the example.

The final reinforcement area acquired by the face-to-face reinforcement ratio suggested in the article has considered the effect of loadings, and therefore will in theory be optimized than that in the case of a predefined reinforcement pattern. Table 5 displays the comparison between total reinforcement area with respect to face-to-face reinforcement ratio $k_q=q_h/q_b$ (instead of k_s) of the two cases: k_{q1} represents the case in which total reinforcement area to be divided equally to four faces of the column, i.e. $A_{sb}=A_{sh}=A_{st}/4$, results in $k_{q1}=(A_{sh}/h_s)/(A_{sb}/b_s)=b_s/h_s$; k_{q2} is obtained via the example, using the calculated values of q_h=2,22mm and q_b=5,2mm (it is more reasonable to compare with calculated values than provided ones). The comparison results show that total reinforcement area acquired from k_{q2} (6752 mm_2) is smaller than that of k_{q1} (6871 mm^2), meaning that the face-to-face reinforcement ratio of the example is more optimizing than the specific one (the difference between these two values depends on design forces, section aspect ratio… and will not be discussed here).

4. Conclusions

By describing the interaction curve via piecewise-defined functions of the concrete compression zone and the steel thin tube, the proposed method has handled the problem of two variables qb and qh, making the design process possible, thence the required face-to-face reinforcement ratio can be obtained as a helper of the next step of finding reinforcement content.

Because the result is just an initial guess, so the assumption with respect to the number of bars on a face mentioned above is not restricted, meaning that it can be less than five. This is the same way manipulated in Paulay's example [1], in which the calculated results were obtained through charts derived from thin tubes but the final bar layout was set up with four bars at corners.

Besides limitations mentioned above, the article has not dealt with some exceptions in calculation (such as coefficient C of expression (13) equals zero, range of x_b, y_b…). These will be exposed in other documents./.

References

1. *D. G. Row and T. Paulay, Biaxial flexure and axial load interaction in short rectangular reinforced concrete columns, Bulletin of the N.Z.*
2. *R. Park and T. Paulay, Reinforced Concrete Structures, 1975, John Wiley & sons Inc*
3. *David Darwin, Charles W. Dolan and Arthur H.Nilson, Design of concrete structures - 15th edition, 2016, McGraw-Hill Education, 2 Penn Plaza, New York, NY 10121, USA*
4. *Phạm Phú Tình, Thiết kế cột tròn bằng cách sử dụng biểu đồ tương tác, Tạp chí KHCN Xây dựng - số 3/2017*
5. *Phạm Phú Tình, Lê Thị Thanh Hà, Báo cáo tổng kết kết quả đề tài nghiên cứu khoa học cấp trường: Thiết kế cấu kiện cơ bản bê tông cốt thép bằng đồ thị, theo TCVN 5574:2012, Trường đại học Kiến trúc Hà Nội, 2016*
6. *TCVN 5574-2018 Reinforcement concrete structure - Design standard, Construction Publishing House*
7. *ACI 318-19: Building Code Requirements for Structural Concrete*

Study on a novel exterior RCS hybird joint by ABAQUS

Nguyen Viet Phuong

Abstract

Hybrid RCS frames consisting of reinforced concrete (RC) column and steel (S) beam are used frequently in practice for mid- to high-rise buildings because of their several advantages. One of the key elements in RCS frames is the beam-column joints. This paper provides the validation of ABAQUS 3D finite element model by the experimental results. Test specimens consist of four specimens of new exterior RCS hybrid joint that the European Project SMARTCOCO investigated with the aim to ease the construction process and avoid additional on-site work.A steel profile is welded to the steel beam and totally encased into a RC column. Four full scale exterior hybrid joints were tested at Structures Laboratory of the INSA de Rennes under monotonic loading. Finally some parametric studies were conducted to find out the suitable configuration of the steel part and the effects of concrete class to the joint behavior.

Key words: *Exterior RCS hybrid joint, ABAQUS software, 3D finite element, L_e length*

Lecturer, faculty of civil engineering,
Hanoi Architectural University,
Email: nguyenphuong.bt.hau@gmail.com
ĐT: 0914859909

Date of receipt: 16/4/2021
Editing date: 20/5/2021
Post approval date: 5/9/2022

1. Introduction

Hybrid RCS frames consisting of reinforced concrete (RC) column and steel (S) beam are used frequently in practice because of their advantages such as reduction in structure's weight, covering large spans, increasing the lateral stiffness, convenience in adoption of strong column- weak beam criterion in tall buildings and enhanced ductility and energy dissipation capacities[1]. One of the key elements in RCS frames is the beam-column joints.The connections between a RC column and a steel beam can be classified into twotypes: continuous beam through (CBT) and continuous column through (CCT). In CBTconnections, the beam runs through the joint continuously and the column envelopes thebeam at the connection. It provides a ductile behaviour under seismic loading but orthorgonal moment connection in the panel zone may be labor-intensive. The CBT joints are primarily problematic due to possible congestion of vertical rebarspassing through the continuous beam and difficulties in pouring and compacting concretein such location, especially for the middle CBT connection[1]. On the contrary, with the CCT connection, the column runs continuously through thejoint. The face bearing plates (FBP), cover plate or shear studs are placed in the jointarea. The beams are connected directly to the plates by penetration weld.

A number of joint configurations have been presented in many articles of many researchers such as Kanno and Deierlein (2000), Nishiyama et al (2004), Mirghaderi and Eghbali (2013), Zibasokhan et al (2016) and their respective advantages, shortcomings listed. Nearly all proposed solutions require significant additional on-sitelabor work. The European Project SMARTCOCO (2012-2016) investigated the behavior of a new RCS joint belonging to theCBT group of jointswith the aim to ease the construction process and avoid additionalon-site work. In this type of joint, a steel profile named by the embedded steel profile is welded to the beam and totally encasedinto the RC column (see Figure 1). Some shear studs along the embedded steel profileare also used to improve the strength and the ductility of the joint.

This paper provides the comparison between the numerical results using ABAQUS and the experimental results from four specimens of new exterior RCS hybrid joint. Four full scale exterior hybrid joints were prepared and tested at Structures Laboratory of the INSA de Rennes. After that, some parametric studies were conducted to find out the configuration of the steel part that leads to the better performance of the beam-column joint and the effects of concrete class to the joint behavior.

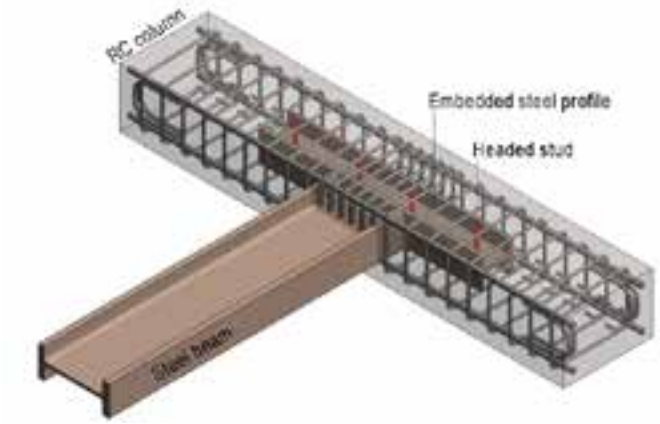

Figure 1. Novel exterior RCS joint detail proposed within SMARTCOCO project

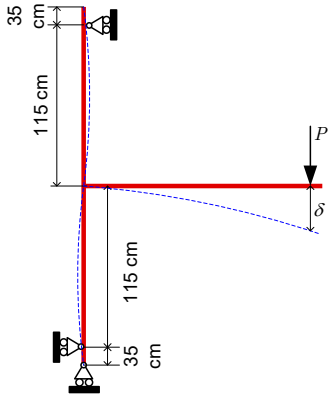

Figure 2. Test setup

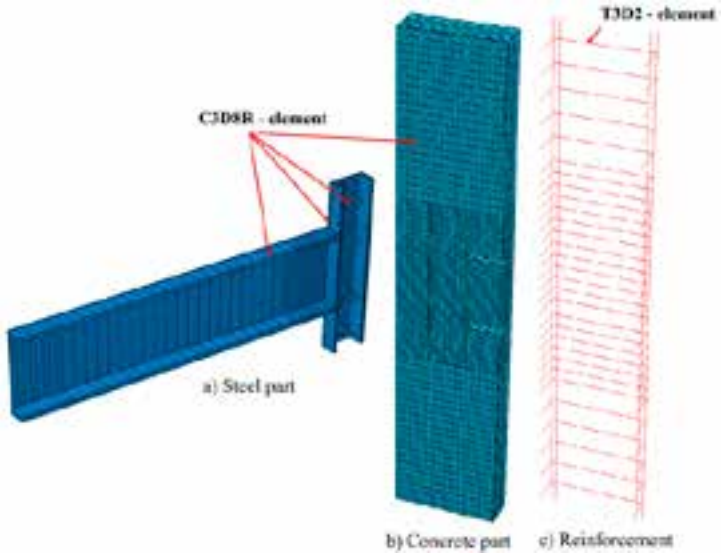

Figure 3. Finite element type and mesh of all components

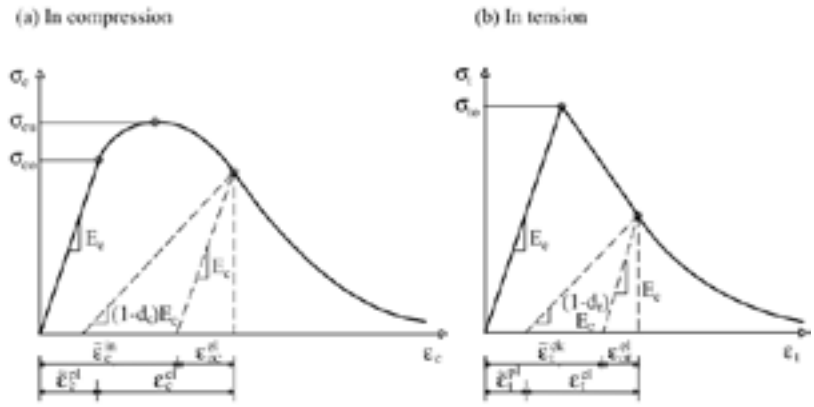

Figure 4. Stress-strain curve of concrete under uniaxial loading [8]

2. Experimental test of novel RCS hybrid joint

Four exterior RCS hybrid joints between steel beam and reinforced concrete column were tested at the Structures Laboratory of INSA Rennes from the end of 2015 to the beginning of 2016. The specimens are planar beam-column connections with 40cm x 60cm rectangular column with 3m length and HEM450 steel beam with 2m length (modified to 200mm flange width). All specimens have the same size, geometry and longitudinal reinforcing bar arrangements. The primary differences between the specimens are the concrete resistance (C40 and C60) and the total length (anchorage length) of the embedded profile in the RC column (L_e = 1m and 1,5m). The embedded steel profile is HEM200. The four specimens are labelled: HJS1 (with L_e=1m and C40), HJS2 (with Le = 1m and C60), HJS3 (with L_e=1,5m and C40) and HJS4 (with L_e=1,5m and C60).

For all specimens, eight ϕ32 bars were used for the longitudinal reinforcement. The shear reinforcements consist of ϕ16 provided at 70mm spacing inside the joint region and at 140mm spacing in the reinforced concrete part outside the joint region. At both ends of the column, ϕ20 U-bars were used for anchorage. Steel grade S460 and S500B were used for steel profiles and reinforcing bars, respectively.Several different instruments were used in the testing of the specimens. They can be divided into 4 types: (1) six inclinometers for recording absolute rotation at six cross-sections; (2) thirteen displacement sensors LVDTs(three for controlling the beam displacement, two for measuring the joint distortion and eight for determining the concrete column's displacement); (3) seventeen single strain gages for monitoring the transverse and longitudinal stresses; (4) five rosette gages for measuring the shear stresses.Monotonic concentrated load was put on the end of the steel beam by a hydraulic of 1500 capacity. The loading was applied in displacement-controlled manner by 3 steps: Firstly, did two initial cycles with an amplitude 1mm and displacement speed of 0,05mm/s; secondly, did the monotonic loading up to a displacement of 60mm with a speed of 0,02mm/s and finally, did the monotonic loading up to a displacement of 60mm up to 200mm with a speed of 0,1mm/s.The test setup was shown in Figure 2.

3. Finite element model for RCS hybrid joint by ABAQUS

ABAQUS is a powerful numerical tool used for component and system modeling and finds application in various fields. It is used to solve multi-degree and multi-physics transient problems. ABAQUS has several built-in models to predict the behavior of materials as well as the provision to add user defined models. The program offers a wide range of options regarding element types, material behavior and numerical solution controls, as well as graphic user interfaces, auto-meshers, and sophisticated post-processors and graphics to speed the analyses[2]. In this article, this commercial software is employed to develop reliable three-dimensional finite element model for the hybrid steel-concrete specimens of the experimental program.

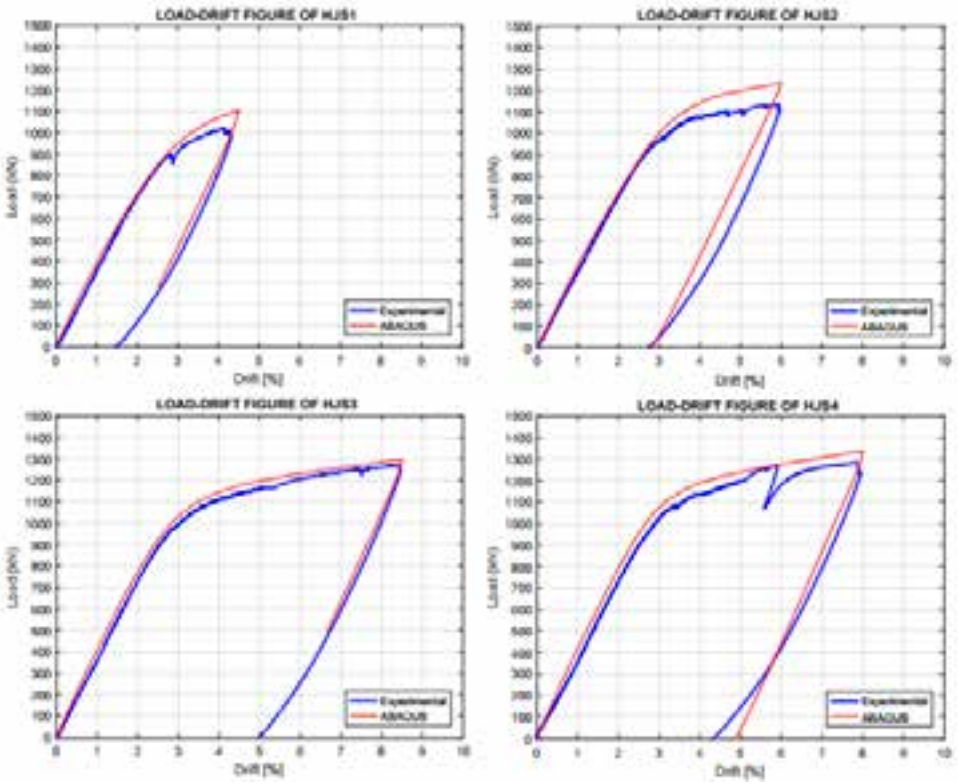

Figure 5. Numerical-experimental comparison of load-drift curve

a) Selection of finite element type and meshing

Because of the symmetry of thespecimen geometry, support conditions and loading, only half specimen is modelled withthe purpose of saving the computing. Each component of specimens consisted of concrete column, reinforcing rebars, steel beam, embedded steel profile and headed studs are modelled separately and assembled to produce the complete specimen model.The reinforced concrete column, the steel beam, the embedded steel profile were modelled by solid C3D8R element and T3D2 elements were chosen for the reinforcing bars (shown in Figure 3). In order to achieve the reliable results, the fine mesh was created in the connection zone. The mesh size depends on each element, each different increment and is from about 5mm to about 50mm.

b) Material modeling

In finite element model, concrete needs to be modelled with the Concrete Damaged Plasticity (CDP) parameters. The value of these parameters found out in articles of [3], [4], [5], [6] and [7] can be shown in Table 1. The uniaxial stress-strain curve of concrete in compressive and tensile behavior with two uniaxial damage variables in tension and compression can be determined by Eurocode 2 [8] and by Kratzig and Polling (2004) [9] (shown in Figure 4). These two uniaxial damage variables in compression and tension are specified in the options "Concrete Compression Damage" and "Concrete Tension Damage" in ABAQUS.The Poisson's ratio of concrete is taken equal to 0,2.

Table 1. The Concrete Damaged Plasticity in ABAQUS

Dilation angle	Eccentricity	f_{b0} / f_{c0}	K	Viscosity paramater
36	0.1	1.15	0.6667	0.01

The Von-Mises yield criterion with isotropic hardening rule is used for modeling the structural steel included steel beam and encased steel profile, the reinforcement and theheaded studs connected to the steel profile. In ABAQUS, the yielding stress and the elastic modulus are taken equal to 460 MPa and 210000 MPa for structural steel, respectively. For the reinforcing steel bar and headed studs, these parameters are taken equal to 500 MPa for the yield stress and 200000 MPa for the Young Modulus. For simplicity, the elastic-perfectly plastic model is used for the reinforcements and the elastoplastic model with hardening is considered for the structural steels.

Table 2. Numerical-experimental comparison of the initial stiffness and the applied loads at 4% drift

Specimen	Applied load at 4% drift			Initial stiffness		
	Experimental (kN)	Numerical (kN)	Error (%)	Experimental (kNm/rad)	Numerical (kNm/rad)	Error (%)
HJS1	1011.04	1070.52	5.88	213.91	221.89	3.73
HJS2	1076.16	1146.19	6.51	215.98	226.41	4.83
HJS3	1114.43	1149.92	3.18	303.03	311.26	2.72
HJS4	1135.56	1189.42	4.74	345.42	349.21	1.10

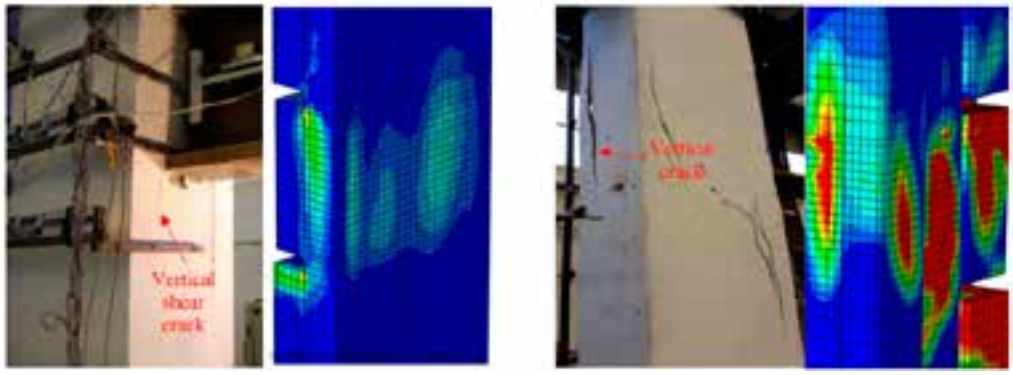

Figure 6. Comparison between crack pattern and damage plastic zone in ABAQUS

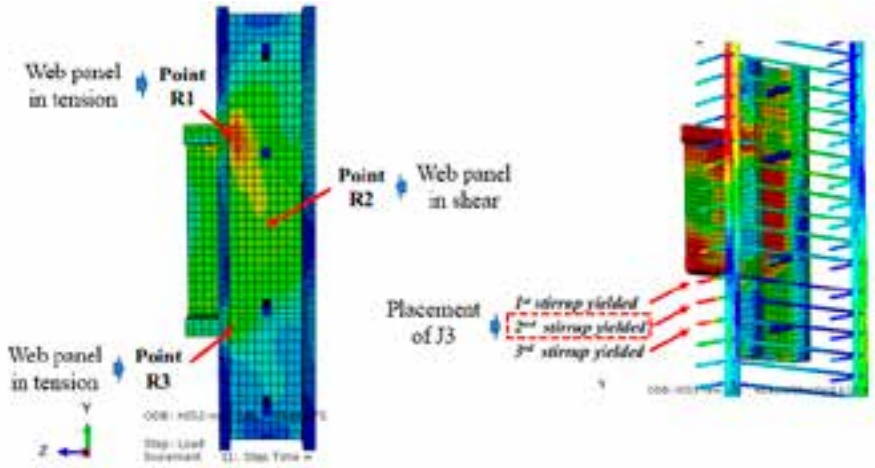

Figure 7. Location of the rosettes R1, R2, R3 and the strain gage J3

c) Interaction conditions between components, boudary conditions and loading

In addition, contact interactions between components play an important role in the specimen behavior, especially for the composite models. In this study, the reinforcing bars such as vertical longitudinal bars and stirrups are fully anchored in concrete so that embedded constraint method can be used for the interaction between rebars and concrete surrounding. For the interaction between concrete column, encased steel profie and shear studs, the general-self contact elements (available in ABAQUS library) are chosen to model the interaction between these components. The extremities of column is restrained in both vertical and horizontal directions by means of hinges. As mentioned before, symmetric of the specimen is exploited and only half of specimen can be modelled. Instead of applying a force at the steel beam end, a vertical displacement is applied to each node of the end cross-section of the steel beam.

4. Validation of the numerical results by experimental test

In order to validate the accuracy of the finite element model, four test specimens weremodelled. The results obtained in the numerical analysis, in terms of load-drift responses ofthe stresses at several points, were compared with the results obtained in the experimentaltests in the same terms. As can be seen in Figure 5 and Table 2, the numerical results were in good agreement with the experimental ones, both in terms of initial stiffness and ultimate loads. The initial stiffness can be defined as the intersection point between the initial tangent at the beginning of the joint moment-joint rotation curve with the slope of kjand the tangent in the inelastic domain presented by the slope of kj=10. It can be noticed that the initial stiffness obtained in the numerical analysis is higher than the one obtained in the experimental tests. This difference appears due to the fixing set between the test specimen and the supports.If the results obtained in the numerical analysis andin the experimental tests are compared at the limit stage, it can be observed that the values of the ultimate forces and ultimatedisplacements are quite close for all tested elements.

Four main types of cracks were observed from the experimental tests: (1) horizontal cracks under the beam flange; (2) diagonal shear cracks in the shear panel; (3) vertical cracks below the steel beam bottom flange; and (4) splitting cracks due to loss of adhesion between reinforcement and concrete. Figure 6 shows three types of cracks (first, third and fourth ones) observed from the experimental test and damage plastic zones observed from the numerical model by ABAQUS. The location of cracks and damage plastic zones and also the value of applied load corresponding to their appearance time are quite similar in all specimens. In addition, in order to compare the behavior of the encased steel profile and stirrups with the experimental results, we look at the Von Mises stress evolution of the three points where the rosettes R1, R2 and R3 were pasted and the point of the strain gage J3 (shown in Figure 7).

Table 3 presents the numerical-experimental comparison of the applied loads leading to different yielding and the drifts corresponding to different component strength: steel web panel in tension; steel web panel in shear; steel web panel in compression; and second yielded stirrup. The error between experimental and numerical is from 0.68% to 12,12%. The sequence of yielding appearance in steel profile is also similar for all specimens. Good agreement between the numerical study and experimental test can be observed.

Due to all previous comparison results between experimental and numerical study, they mean that the numerical analysis by ABAQUS can be a reliable method to predict the exterior RCS hybrid joint behavior.

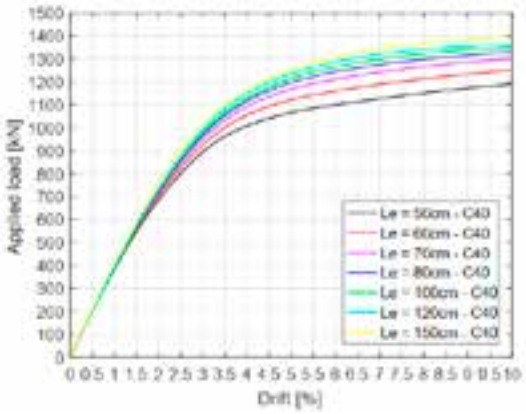

Figure 8. Load-drift curves for different anchorage length

Figure 9. Plastic bending moment and initial stiffness in cases of different anchorage length

5. Parametric studies for novel RCS hybrid joint

Using the 3D FE model which was successfully validated against experimental resultsof the studied RCS joint, a set of parametric studies was undertaken to understand thebehavior of the joint as the components of the joint varied. The goal of this parametricstudy is to find out the configuration of the steel part that leads to the better performanceof the beam-column joint. Therefore, the geometrical properties of the beam and the RCcolumn are unchanged. The behavior of the joint is firstly investigated for the change ofthe length of encased profile. Because the height of steel beam is 478mm, the first value of encased steel profile's length is chosen from 500mm to the maximum of 1500mm. Let consider the parametric study in case of the concrete class of C40 with the differentanchorage length. Then, the influence of the concrete class on the joint responseis studied. In addition to the case of 1m and 1,5m anchorage length which are presentedabove, five other cases are considered: Le= 0,5m, Le= 0,6m, Le= 0,7m, Le= 0,8mand Le= 1,2m. Corresponding to each case of anchorage length, four concrete class areconsidered: C30, C40, C50 and C60. The input values of material have been taken fromthe Eurocode standard.

As can be seen in Figure 8 and Figure 9, the global behavior keeps almost unchanged when Le is greater than80 cm. In the opposite side, the different behavior between the cases of the anchoragelength that is less than 80cm

Table 3 - Numerical-experimental comparison of the yielding time

	Specimen	Applied load			Drift		
		Experimental (kN)	Numerical (kN)	Error (%)	Experimental (kN)	Numerical (kN)	Error (%)
Column web panel in tension	HJS1	633.4	574.3	-9.33	1.79	1.54	-14.0
	HJS2	645.3	652.7	1.15	1.81	1.78	-1.66
	HJS3	668.8	639.3	-4.41	1.88	1.61	-14.4
	HJS4	683.7	696.5	1.87	1.87	1.74	-6.95
Column web panel in shear	HJS1	844.9	830.8	-1.67	2.53	2.43	-3.95
	HJS2	878.7	945.0	7.55	2.55	2.76	8.24
	HJS3	871.4	893.2	2.50	2.51	2.39	-4.78
	HJS4	835.7	937.0	12.12	2.31	2.44	5.63
Column web panel in compression	HJS1	825.6	805.8	-2.40	2.45	2.33	-4.90
	HJS2	969.3	962.7	-0.68	3.10	2.83	-8.71
	HJS3	889.4	924.1	3.90	2.44	2.50	2.46
	HJS4	960.0	991.0	3.23	3.13	2.62	-16.3
Yielding of J3	HJS1	1017	1040.0	4.32	3.68	3.91	6.25
	HJS2	1118	1218.0	9.44	5.54	4.11	-25.8
	HJS3	1131	1173.2	3.73	4.84	5.45	12.6
	HJS4	1251	1272.3	1.70	6.06	6.89	13.7

can be observed. It can be explained that the encased steelprofile can be considered to be totally anchored into the RC column in cases of lengthmore than 80cm. Therefore, the behavior of the hybrid joint can be considered similarlyto the composite joint.Furthermore, it is observed that the stiffness of the joint is not much influenced by the anchorage length.

For the encased steel profile, the similar first yielding point can be found at the location of the point R1 in all specimens. It is noted that the yield stress at the point R1 corresponds to the yielding of the steel web panel in tension and this observation is also found in the experimental test. After that, the point R2 (web panel in shear) and R3 (web panel in compression) are the next ones reached to the yield stress. Figure 10 shows the bending moment corresponding to the yield stress at the locations of three point R1, R2, R3 and two first yielding stirrups in cases of different anchorage length. The quite similar behavior for the bending moment and the sequence of yielding appearance can be collected with the differences of anchorage length. The resistance of steel web panel almost increases followed by the increase of anchorage length of encased steel profile.For the stirrup stresses, two stirrups below the steel beam bottom flange yieldedfirst because of the high compressive pressure caused by the rotation of the steel beam. As can be seen, the stress of the stirrupsbelow the steel beam depends on the anchorage length of the encased steel profile.

As can be seen in Figure 11, the global behavior of the joint is much influencedby the concrete class in case of the anchorage length which is less than 80cm. When thelength is greater than 80cm, the global behavior seems to be unchanged in cases of differentconcrete class. The resistance of RCS joint improves with the higher concrete class. Theresult for the initial stiffness shows that in all cases of the anchorage length, the joint initialstiffness is dependent on the concrete class. However the plastic bending moment is notmuch influenced by the different concrete class, especially for the anchorage length whichis greater than 80cm.

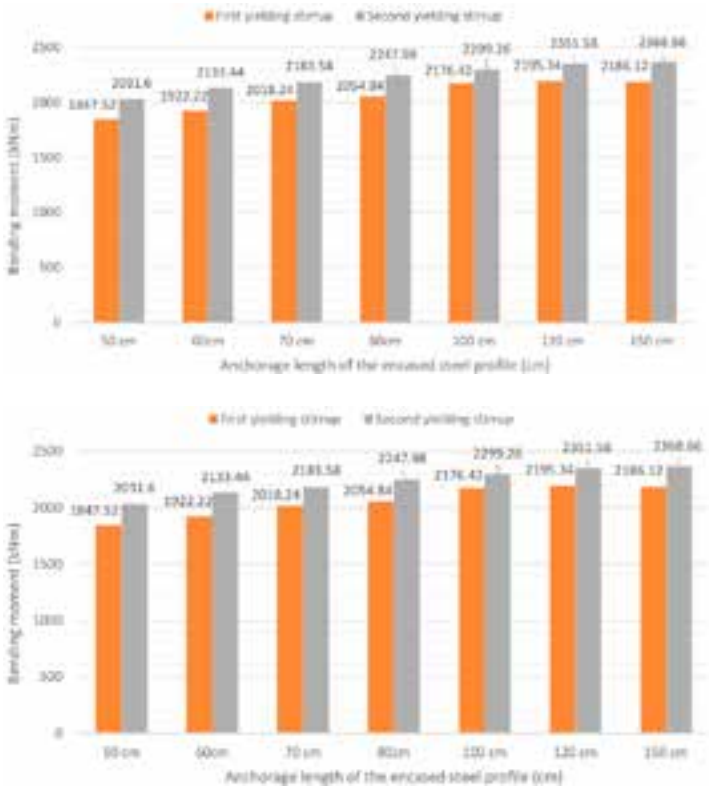

Figure 10. Bending moment corresponding to the yield stress in cases of different anchorage length

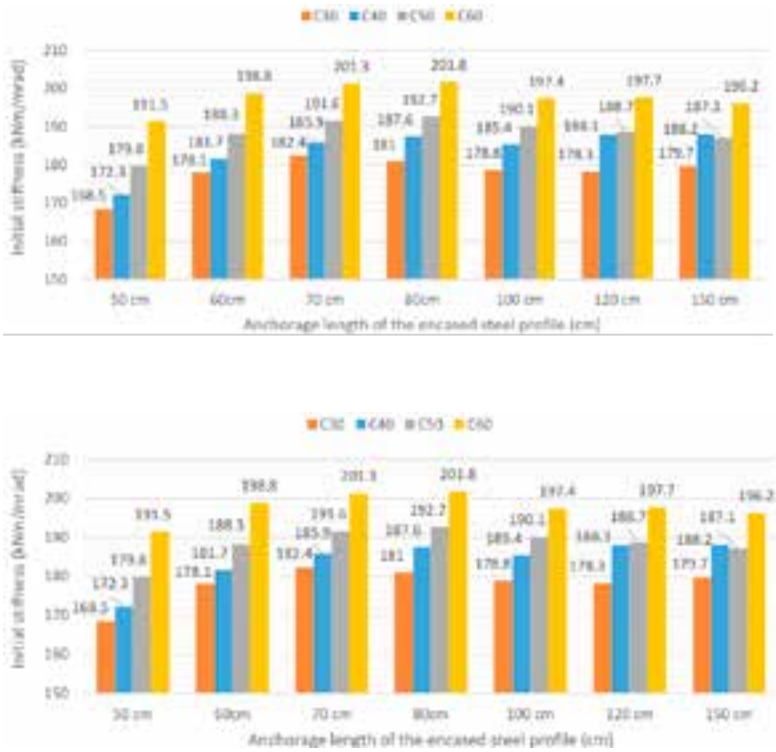

Figure 11. Plastic bending moment and initial stiffness in cases of different anchorage length

Conclusions

In this article, a numerical study using ABAQUS software was conducted and its results were compared with the experimental tests for novel exterior RCS hybrid joint at the Structures Laboratory of INSA Rennes. After validating the suitable and reliable results, a set of parametric studies were conducted to investigate the influence of the anchorage length of the encased steel profile and the influence of the concrete class. Due to the previous resultes in this article, the following conclusions can be drawn:

(xem tiếp trang 91)

Real situation and solutions for solid waste management in Tien Yen district (Quang Ninh province)

Bui Thi Ngoc Lan

Abstract

This article discusses the solid waste management status in Tien Yen district, Quang Ninh province. As a result, we have achieved exceptional results that significantly contribute to raising awareness of the hazards of solid waste to the environment and human life. Concurrently, this paper demonstrates solid waste management challenges and hurdles, as well as essential solutions to overcome problems in Tien Yen district (Quang Ninh province), thereby contributing to the protection of the environment and human life.

Key words: *: Solid waste management; real situation; solutions*

PhD. Bui Thi Ngoc Lan
Constructions Economic and Investment Department,
HaNoi Architectural University
Email: lanbtn@hau.edu.vn

Date of receipt: 18/8/2022
Editing date: 01/9/2022
Post approval date: 5/9/2022

1. Introduction

As a result of socioeconomic development and rapid population growth, municipalities are currently producing an increasing amount of solid garbage. As a result, one of the top priorities for environment protection and sustainable development is solid waste management. The localities of Vietnam in general and Tien Yen district (Quang Ninh province) in particular, are increasingly developing and growing in terms of socioeconomic development, the rapid increase of the population, particularly the urban population, has created great pressure on the environment when the amount of solid waste is increasing due to a variety of emission sources.

Meanwhile, solid waste control and management remain limited, increasing the likelihood of severe impacts on the ecosystem and having a highly detrimental influence on the environment, as well as on health and life of local people. As a result, the proposal of some solutions to solid waste management in Tien Yen district (Quang Ninh province) is a critical and required task for the community.

2. The scope and method of case study

The current state of solid waste management in Tien Yen district, Quang Ninh province, is the subject of this paper's investigation. The article employed analysis, synthesis, and data processing methods to clarify the current condition, constraints, and difficulties in solid waste management in Tien Yen district, Quang Ninh province. The research findings primarily rely on secondary material gathered from publications, books, periodicals, and television.....

3. Tien Yen district solid waste management situation

Tien Yen district, Quang Ninh province, is undergoing economic and social development, with an increase in the number of manufacturing, commerce and service enterprises. On the one hand, creating jobs for employees; on the other hand, increasing the amount of solid waste generated in the district, putting strain on the environment.

In accordance with Decree No. 38/2015/ND-CP on the management of solid waste and scrap: “Solid waste is defined as waste that is solid or viscous (also known as sludge) and is discharged from manufacturing, business, service, daily life or other activities”.

Currently, due to a lack of appropriate management systems, rules, policies, solid waste poses numerous health risks (including some infectious diseases, odors, ...), as well as environmental consequences (water pollution, soil pollution and air pollution...). The Asian Productivity Organization (AOP) published a report on Solid Waste Management: Issues and Challenges in Asia in 2007, this report included a chapter on Viet Nam, which pointed out that the management of MSW, to a certain extent, is inadequate, particularly in urban regions of the country. The report stated that there were practices of uncontrolled and long-term storage of waste, disposalon site, nonengineered landfills and use of waste to fill-up the vacant areas. These practices have resulted in the percolation of water soluble hazardous components of the waste to the groundwater and contaminating the groundwater. The discharge of waste withoutadequate treatment in waterbodies, such as the rivers, is causing a contamination of surface water which is making the water unusable for drinking and becoming harmful to aquatic life. Open burning of the waste affects the air quality of the region [6].

Identify goals and offer some efficient solid waste management solutions that will contribute to improving environmental protection and boosting the long-term development of areas in general and the Tien Yen district in particular. Within the scope of the research, the paper focuses on examining and evaluating the current state of solid waste management in the Tien Yen area in order to identify

flaws and limitations and to take appropriate measures to address those issues.

Rick LeBlanc, the author of a scientific article, contends that: “Solid waste management is defined as the discipline associated with control of generation, storage, collection, transport or transfer, processing and disposal of solid waste materials in a way that best addresses the range of public health, conservation, economic, aesthetic, engineering and other environmental considerations” [7].

The primary goal of solid waste management is reducing and eliminating adverse impacts of waste materials on human health and the environment to support economic development and superior quality of life. This is to be done in the most efficient manner possible, to keep costs low and prevent waste buildup [7].

The Government issued Decree No. 38/2015/ND-CP on April 24, 2015, plainly stating: “Management of hazardous waste, household waste, common industrial waste, liquid waste products, wastewater, industrial pollutants, other particular wastes and environmental preservation in the import of scrap are all included in solid waste management “[3].

Currently, the rapid economic and population growth is accompanied by an increase in waste production, which harms long-term economic and social development. The environment and people's livelihoods are negatively impacted in numerous ways by the deficiencies and inadequacies in solid waste management, notably as follows:

In the regions, numerous industrial clusters, hotels, offices and residential zones have high population density;

Figure 1. Tien Yen district landfill pollutes the ecosystem [8]

production and business activities are carried out on a regular basis..... As a result, there are numerous sources of solid waste creation, such as: (i) Family; (ii) Places used for commerce and services (markets, hotels, supermarkets, restaurants, etc.); (iii) Offices (offices, schools, hospitals, etc.); (iv) Public places (bus stations, parks, amusement parks, streets ...); (v) Services for cleaning (street sweeping, tree trimming ...); (vi) Manufacturing plants; (vii) Industrial parks, industrial clusters and craft villages….. These emission sources are causing an increase in the amount of home solid waste (which accounts for the lion's share), medical solid waste, industrial solid waste and so on in the communities, particularly in cities, making soil degradation,

Figure 2. Tien Yen district waste treatment with manual incinerators [4],[5]

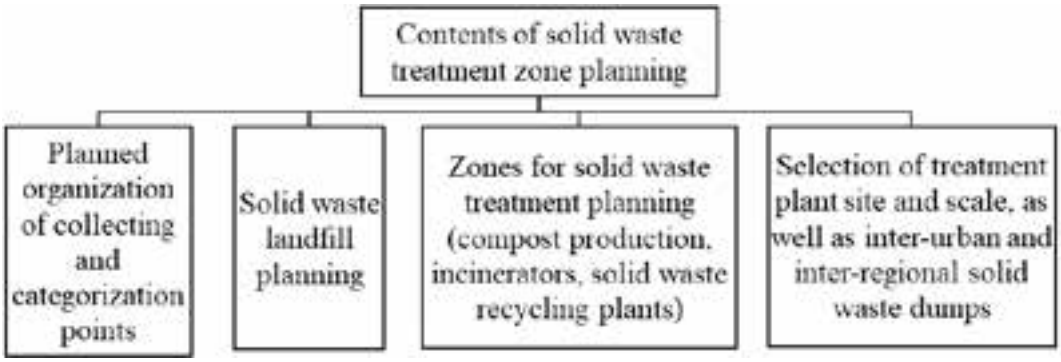

Figure 3. Solid waste treatment zone planning content

Figure 4. Solid waste segregation at the source

air pollution and water quality deterioration, endangering people's health and lives.

In recent years, in localities in general and in Tien Yen district in particular, a big percentage of people have turned to non-agricultural jobs and people's consumption has also changed. As a result, prior recycling initiatives have become overburdened with waste, jeopardizing land, water, air and human health.

Tien Yen town and communes in the district arrange daily waste collection after identifying dangers associated with solid waste management difficulties, concentrate on bringing to the landfill's treatment area of Cong To village, this is the location where domestic garbage from the district's eight communes and municipalities is gathered. However, over time, the landfill has become overburdened and the treatment procedure has become obsolete, negatively impacting the lives of nearby residents [8]. As a result, the district's policy was to close this landfill and transport it to the Tien Yen solid waste treatment complex, which was created in Tai Noong village, Dong Hai commune, with a capacity of 400 tons/day. The maximum design capacity for managing and eliminating home garbage is 250 tons per day and night; the maximum design capacity for treating industrial and medical waste is 150 tons per day and night [1].

However, solid waste in the Tien Yen area has not been classified at the source; the rate of solid waste collection in the Tien Yen district is approximately 70%, with rubbish collected and transported to the main dump; basic treatment by burial, manual burning and lime sprinklement [2].

For construction solid waste, preliminary classification is performed, the garbage can be used to generate economic value: plastic, packaging, iron and steel …. are sold to agencies scrap purchasing division.

Đối với chất thải rắn xây dựng, việc phân loại thực hiện một cách sơ bộ, các chất thải có thể tận dụng được mang lại giá trị kinh tế: nhựa, bao bì, sắt thép..... được bán cho các cơ sở thu mua phế liệu. Other non-recyclable waste must be mixed with household waste, such as dirt, sand, concrete, broken bricks and tiles....(a component is utilized for additional reasons such as leveling and foundation leveling.....).

There are also many difficulties in treating medical solid waste because of the medical stations in Tien Yen area, only Tien Yen hospital has invested in developing a wastewater and solid waste treatment system, the hazardous waste satisfies the standard; on average, 10-15kg of hazardous waste can be handled per day; there are three medical stations nearby that have carried hazardous waste to the hospital for treatment. The remaining medical stations are 10-30 kilometers away and staff is scarce, making it difficult to transport and collect rubbish from the stations to the incinerator, simple methods of hazardous waste disposal include burial or manual burning in brick kilns using charcoal fuel [2].

In terms of household waste treatment, most people gather according to household and treat themselves in the traditional rural manner (self-burning). Toxic waste from agricultural output, as well as industrial and handicraft production facilities, has received little attention, primarily self-collect, rent or dispose of according to rules [2].

4. Provide some solutions

4.1 Plan for and locate solid waste treatment zones that are appropriate for local conditions.

The planning of a solid waste management and treatment system that includes both municipal solid waste and hazardous waste in a synchronized and environmentally friendly manner is critical in zoning planning.

Cities must prioritize the planning of solid waste management and treatment systems during the development phase; the specific requirements are detailed in Figure 3 below:

Simultaneously, carry out socioeconomic growth in tandem with Environment protection in a holistic manner, with a plan to limit the adverse impacts of solid waste on the natural urban environment, thereby avoiding environmental

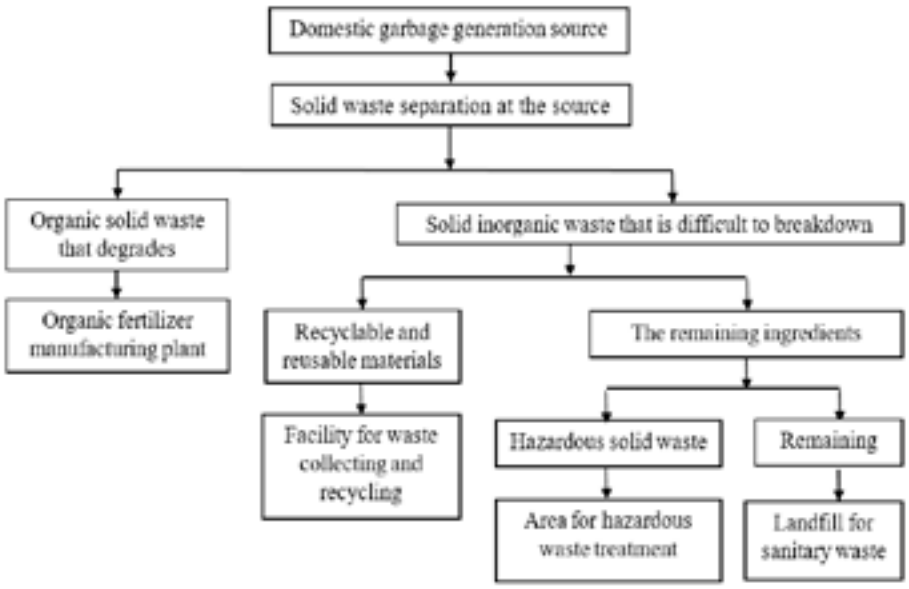

Figure 5. The sequence of classification, collection and treatment of domestic solid waste

damage. natural landscape and reduce pollution of the air, land and water environments caused by exhaust gas, wastewater and garbage.

To establish an acceptable location for a solid waste treatment area, solid waste generated by living quarters and other works must be identified at the source, then collected and delivered to transfer stations located throughout each region and commune. The waste will be preliminarily handled at the transfer station by compacting and sorting each form of recyclable waste, resulting in a source of "clean" biodegradable organic solid waste (food solid waste, food waste, etc.). branches, leaves, wood, paper and so on), no hazardous wastes in everyday life (cleaning chemicals, pesticides, rat poisons, plant protection, etc), the waste is then transferred by mobile vehicle to the Tien Yen solid waste treatment complex in Dong Hai commune to be composted and processed into organic fertilizers, micro-organic fertilizers and high-quality bio-fertilizers.

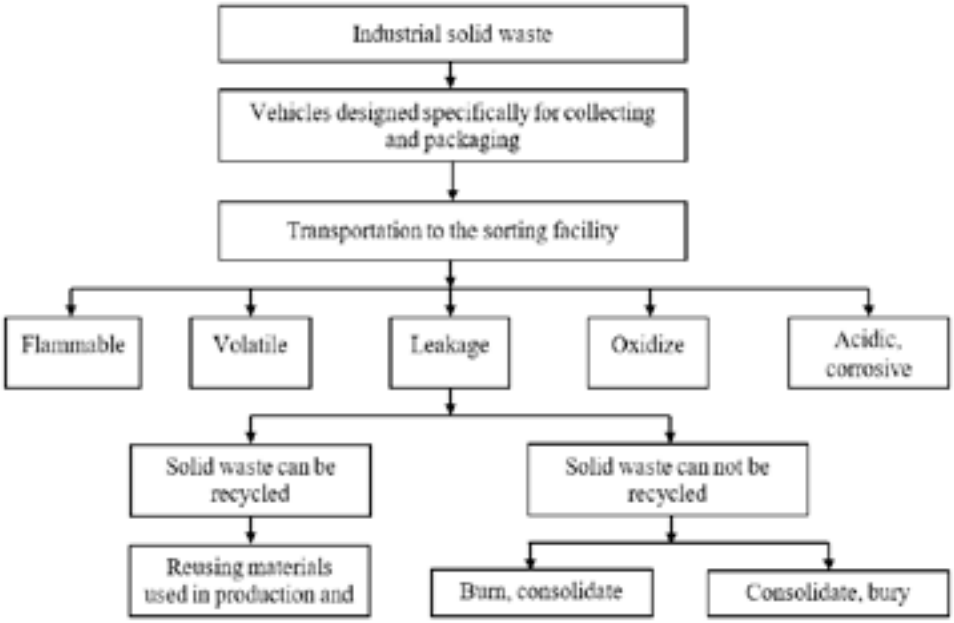

Figure 6. The sequence of industrial solid waste classification, collection and treatment

4.2 Separate and treat solid waste at the source

Solid waste collection and segregation are critical components of solid waste management. Tien Yen district can research and implement a number of specific measures to treat solid waste thoroughly and effectively, including:

- Set a target and aggressively apply it on the collection rate as follows: The household solid waste collection rate is 85%, while the industrial, construction and hospital solid waste collection rates are 95%. Towards forming a model of a circular society, encouraging sorting, 3R (Reduce, Reuse, Recycle) treatment measures and minimizing waste waste, with the long-term goal of applying technology treated by incineration which is now widely used in countries such as Japan, Germany, Switzerland, the Netherlands and others.

- In order to treat residential solid waste: Separation of biodegradable organic waste (vegetables, leftovers, etc.) from non-biodegradable inorganic garbage at the source (rubber, plastic, metal, etc.) and be labeled. Increase the efficiency and volume of reuse and recycling processes. Encourage the best possible use of food waste to produce organic fertilizer and animal feed. Raise environmental awareness and contribute to the objective of "sustainable development and green growth."

Improper solid waste disposal results in accumulated waste that becomes a problem for both the environment and the community. Biodegradable materials decay and degrade under unique, unregulated and unhygienic conditions as a result of massive garbage disposal. It becomes a breeding habitat for dangerous insects and infectious organisms after a few days of decomposition. A foul odor is produced, which detracts from the area's aesthetic appeal. As a result, solids collection time management is both required and critical.

To reduce polluting odors, solid waste collection locations should be treated with biological products; decomposing solid waste and hard-to-decompose solid waste are easy to treat.

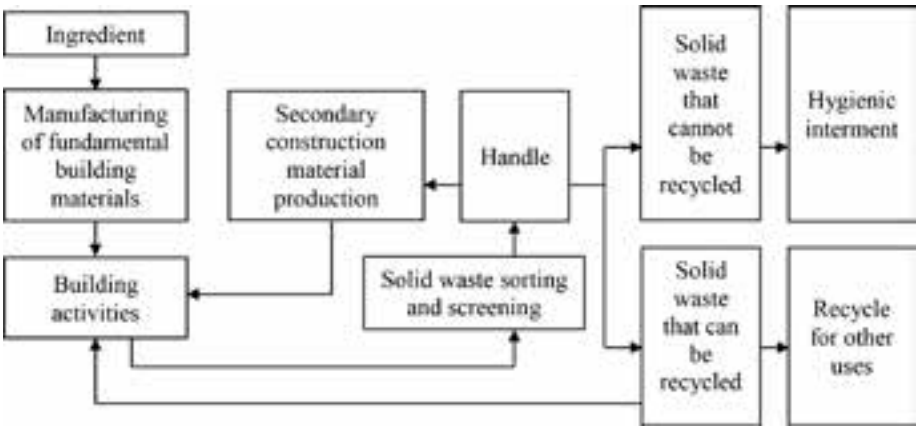

Figure 7. The sequence of construction solid waste classification, collection and treatment

- For the treatment of industrial solid waste:

+ Solid industrial waste can be recycled and utilized: It will be stored in a separate garbage container before being sold to recycling units or enterprises that need to utilize this waste in the manufacturing process.

+ Solid industrial waste can not be recycled and utilized: These

garbage will be collected and handled at landfills after being collected and stored in separate bins with distinct labels and colors to distinguish them

+ Industrial solid waste that is hazardous: Production facilities contracted with permitted functional units gather the waste, which is subsequently delivered to the combined treatment area for burning in compliance with laws.

- For the treatment of medical solid waste:

+ Medical solid waste in general: To be kept in separate containers and be transferred to a landfill by the household garbage collection unit. Medical solid waste is collected and sent to medical waste treatment clusters in accordance with rules.

+ Medical solid waste that is hazardous: To be treated where hazardous solid waste is generated during the course of living and producing in order to ensure environmental cleanliness and human life safety. In particular, considering the recent problematic developments of the Covid-19 pandemic, medical solid waste disposal should be given top priority and attention. To avoid illness transmission to the community, ensure strict collection, transportation and treatment; Prioritize treatment based on the cluster model of medical facilities and hazardous waste treatment facilities with the role of treating medical waste in the community to ensure the shortest collecting distance from the point of creation to the treatment facility.

- Treatment of construction solid waste: Investors or contractors are responsible for contracting with this unit to collect, sort and transport materials using specialized equipment. Because construction solid waste has a very high reusable composition, classifying it at the source will have significant economic benefits as well as help safeguard the environment for the building sector.

- Treatment of other hazardous solid waste: Set up a centralized hazardous solid waste treatment station to use hazardous solid waste generated during everyday life and production to provide environmental sanitation and safety during the hazardous solid waste treatment process.

- Zones of planned solid waste treatment, Prioritize advanced treatment technology investment projects, can sort and recycle rubbish, compost organic waste and burn hazardous waste in an incinerator, only bury the rubbish that cannot be treated, 15% maximum burial rate. The landfill must meet environmental sanitation standards and include a leachate collection and treatment system. Incinerators must have exhaust gas treatment systems and operating modes must prevent the production of dioxins and furans.

4.3 Increase the effectiveness of state and local solid waste management policies

Increase the district's application of guidelines and regulations for solid waste classification at the source in urban areas, handicraft zones and craft villages. Improve the organizational structure of the solid waste management system at each level and sector on a continuous basis, focusing on decentralization, explicitly allocating roles and improving the management apparatus at all levels and localities.

Improve the administration of collection locations, transfer stations and solid waste treatment facilities, assist municipalities in conducting a study of collection, classification, transportation, transshipment facilities, dispose of rubbish at authorized solid waste disposal sites. Investigate and implement investment attraction methods, advantageous processes and regulations to encourage active investor interest in the establishment of solid waste treatment zones.

Comprehensive solid waste management legislation in the area; Propagating and rallying individuals to effectively implement the Environmental Protection Act, provide legal incentive mechanisms for solid waste reduction and recycling, to limit solid waste creation and enhance solid waste separation at the source in accordance with rules.

5. Conclusion

One of the primary sources of pollution in the environment is solid waste, specifically, contaminating land, water, air and negatively impacting people's life. As a result, improving solid waste management practices such as prevention, reduction, monitoring, categorization, collection, transportation, reuse, recycling and solid waste treatment is critical. The essay examines the current state of the solid waste management in Tien Yen district (QuangNinh province) as well as its limitations. The deficiencies of solid waste management will be addressed to some extent if some of the aforementioned solutions are successfully implemented, so helping to prevent future adverse effects on the environment and the lives of the inhabitants in the Tien Yen district./.

References

1. *Viet Anh (2018), Quang Ninh: Investor designated for a VND 250 billion project to treat solid waste, Newspaper for bidding*
2. *Dinh Hong Duyen and partner (2014), Evaluation of the existing state of the environment in Tien Yen district, Quang Ninh province, Science and Development Journal*
3. *Government (2015), The Government issued Decree No. 38/2015/ ND-CP on garbage and scrap management on April 24, 2015.*
4. *Pham Hoach (2020), Quang Ninh:Tightening solid waste management, classification and treatment at the source, on the website https://baotainguyenmoitruong.vn*
5. *QNP (2017), Planning for solid waste in Quang Ninh: A new decision for a new vision, on the website https://doanhnghiep.quangninh.gov.vn*
6. *R.L.Vermaa, G.Borongana, M.Memonb (2016), Municipal solid waste management in Ho Chi Minh city, Viet Nam, current practices and future recommendation, International Conference on solid waste management, 5IconSWM 2015*
7. *Rick LeBlanc (2020), An Introduction to Solid Waste Management, The balance small business, on https://www.thebalancesmb.com*
8. *Quang Ninh Television (2019), Tien Yen's "super-giant" dump pollutes the ecosystem.*

Road development reality in Dienbien province, Vietnam

Nguyen Cong Giang, Bui Thi Ngoc Lan

Abstract

DienBien province holds a particularly important position in terms of national security in the Northwest region and throughout Vietnam. Furthermore, with historical tourist areas, nature tourism and agro-forestry development, DienBien province has a lot of potential to develop services and tourism. However, because the road network in DienBien province has not been fully developed, it cannot promote socioeconomic development in the surrounding area. Many transportation development planning projects in DienBien province have been issued and completed; the development of the road network has yielded some results, but there are still many difficulties and problems. This article discusses the reality of road development in DienBien province from 2016 to 2020. Concurrently, this article demonstrates problems and obstacles in road development and proposes necessary solutions for future road development problems in DienBien province.

Key words: *Exterior RCS hybrid joint, ABAQUS software, 3D finite element, L_e length*

(1)PhD. Nguyen Cong Giang
Geotechnical Engineering and Underground Construction Department
HaNoi Architecture University
Email: giangtokyo1963@gmail.com
(2)PhD. Bui Thi Ngoc Lan
Construction Economic and Investment Department
HaNoi Architecture University
Email: lanbtn@hau.edu.vn

Date of receipt: 20/6/2022
Editing date: 01/7/2022
Post approval date: 5/9/2022

Introduction

DienBien province is a mountainous province on Vietnam's northwest border that plays a critical role in national security. DienBien has a natural area of 9.541,25 km^2 and borders Lai Chau province to the north, Son La province to the east and northeast, China's Yunnan province to the northwest, Laos to the west and southwest and is approximately 462km from Hanoi. Only DienBien province in Vietnam shares a common border with Laos and China, spanning 455,573 km (in which, the Vietnam - Laos border is 414,712 km; Vietnam - China border is 40,861 km). Tay Trang international border gate, A Pa Chai entrance, Huoi Puoc main border gate, Si Pa Phin sub-border gate and Na Bung border gate are among the border gates with China and Laos. These vital border crossings provide numerous benefits in terms of socioeconomic development, promoting economic development and exchange with other countries. This is an excellent opportunity to promote international trade by developing DienBien into the main transit area on the Northern Trans-Asian road, which connects Vietnam's Northwest region with the Northern Laos region - Southwest China..

DienBien province has a diverse tourism potential, including both natural and historical tourism resources. DienBien has a diverse terrain, numerous rivers, lakes and beautiful landscapes,... Natural tourism resources are plentiful, but not in every province. DienBien also has many historical sites associated with Vietnam's construction and defense, such as national historical sites (particularly the DienBien Phu battlefield), historical relics (Ban Phu citadel, Sam Man citadel, Muong Tinh cave...), De Cat tunnel, Muong Thanh bridge and so on. Muong Phang relic site, Hill A1... They are extremely valuable assets for developing historical tourism. DienBien province, in particular, has a multi-ethnic culture with 19 major ethnic groups: Thai, H'Mong, Kinh, Dao, Kho Mu, Ha Nhi, Lao, Hoa, Khang,... Each ethnic group has distinct characteristics in terms of language, customs and culture,.... creating a colorful picture of DienBien culture and having a significant impact on tourism development.

Concurrently, DienBien province has abundant surface water resources, diverse agro-forestry product potential and favorable weather and climate for agro-forestry development and agro-forestry product processing. Demand for agro-forestry products is expected to rise; businesses are gradually shifting their investment to DienBien in the fields of agriculture and forestry, as well as rural areas with abundant land resources and a variety of mechanisms and policies to encourage and attract investment. It is undeniable that DienBien province is critical to the Northwest region's and Vietnam's economic development strategies.

With the characteristics of a mountainous border province, wide terrain and distance from major cities, the development of a road traffic is a necessary condition for socio-economic development. DienBien province must determine the construction synchronously building and developing a road traffic that plays a particularly important role, serving the needs of passenger and tourist transport, agro-forestry goods transport, promoting trade and socio-economic development, ensuring the safety of citizens.

DienBien province has prioritized road traffic development, following the resolutions of the Provincial Party Committee and the Provincial People's Committee on the organization and implementation of the socioeconomic development plan, as well as

the relevant agencies and organizations. With many specific solutions, sectors and localities have focused on leading and directing the development and implementation of the road development program. DienBien's road traffic development planning has been completed and the province's road transport infrastructure is being completed and upgraded. However, the pace of road development is slow, not synchronized, not commensurate with the potential, has not been invested in accordance with the plan and it takes a long time to travel between DienBien and other localities. There are still numerous difficulties and problems to be resolved. In order to promote the long-term development of the road traffic and the socioeconomic environment, this article examines the current state of road development in DienBien province from 2016 to 2020. Next, proposes necessary solutions to the problems and development of the road network in DienBien province.

Literature review

In appropriate contexts and locales, new roads can promote sizeable economic and social benefits. If poorly planned or implemented, however, new roads can provoke serious cost overruns, corruption and environmental impacts, while generating sparse economic benefits and intense social and political conflict [5]. The road network is thought to play an important role in the national transportation system, as well as in the process of socioeconomic development, national defense and security and improving people's living standards. When the road transport is smooth and safe, it will be easier to carry out the tasks of socioeconomic development, national defense, safety and social order. As a result, localities in general and DienBien province in particular, must develop road transport to serve economic development, create conditions for goods to circulate, reduce transportation costs, facilitate import and export, promote production, circulation, investment and development to contribute to the province's economic growth.

DienBien province is a large mountainous province in the Northwest with advantages in natural resources, soil, climate and topography, ... These conditions are ideal for the growth of industrial crops, fruit trees, specialized rice cultivation, tourism and service industries. Furthermore, they serve as the foundation for the growth of processing industries, trade, tourism, import-export and investment attraction. Besides, in planning road development, planners often face a challenge to reconcile various interests and interpretations on the ultimate goals which complicate the discussion decision-making processes [6]. DienBien province has recently focused on road transport planning in order to develop a synchronous road network, carry out socioeconomic development tasks, ensure national defense and security.

Implementation of Decision No. 44/QD-UBND dated February 4th, 2012 issued by the People's Committee of DienBien province on approving the adjustment of the Master Plan on the road network for the period 2011-2020, with a view toward 2030. After 8 years, by the end of 2020, DienBien province will have 9.568,23 km of roads, including: 06 national highways (NHs) totaling 745,43 km, 20 provincial roads totaling 604,7 km, 102 district roads totaling 1.161 km and rural roads totaling 7.927,58 km. Furthermore, 100% of communes have quality roads that allow cars to reach the commune center, with 95.3% of communes having roads to the commune center and 4.7% only being accessible by car during the dry season.

Many significant road construction projects in DienBien province have been completed, including: the rehabilitation and upgrade of NH 279; the project of renovating and upgrading NH 12, section MuongCha - DienBienPhu city; and the construction of the SiPaPhin - MuongNhe route.….[1]. However, there are numerous challenges that must be overcome in the development of the road network in DienBien province; development is not commensurate with potential and road transport infrastructure has not been invested synchronously. As a result, traveling between towns is difficult. This article discusses the reality of road development in DienBien province from 2016 to 2020. Concurrently, this article identifies problems and impediments to road development and proposes solutions to address these issues and promote socioeconomic development in DienBien in the future.

Research methodology

The development of road network in Dien Bien province is the subject of this paper's investigation. The article employed data analysis, synthesis, and treatment methods to clarify the current status, constraints, and challenges in the process of road transport development in Dien Bien province from 2016 to 2020. The research findings mostly rely on secondary data gathered from Dien Bien province reports, books, journals, and statistical yearbooks, which are then analyzed using the SWOT (strengths, weaknesses, opportunities, and threats) method to establish the best solutions.

Result research

- Regarding the reality of road network development in DienBien province:

According to the Department of Transport of Dien Bien province's report summarizing the work in 2020 and implementing the tasks in 2021, the road traffic in Dien Bien province currently has a total length of 9.568,23 km, including national highways (NHs), provincial roads, district roads, urban roads, commune roads, border patrol roads and village roads..… [2].

ased on the data in Table 1, the article charts the scale of road types in DienBien province by the end of 2020 in Figure 1. From the chart, it is clear that the majority of roads in DienBien are commune roads, village roads and intra-field roads; there is no interchange connection with neighboring localities; and there is no freeway; the system of national highways and provincial roads has not yet developed, with national highways accounting for approximately 8% and provincial roads accounting for approximately 6% of the total length of roads in the province.

- Current situation of national highway network in Dien Bien province

National highways managed by the central government are inter-regional roads that connect externally, are important routes connecting DienBien province with key economic regions in the region and connect traffic hubs big pine.

According to the summary data of DienBien Department of Transport, the national highway (NH) system has 06 routes with a total length of 751 km in 2016, of which the cement concrete pavement has 68,2 km, the asphaltic concrete pavement has 302,7 km and the bituminous penetration macadam pavement has 380,1 km (of which, The Directorate for Roads of Vietnam has entrusted the Department of Transport with the management of 620,9

km). DienBien province upgraded and expanded 160 km of national highway surface from 2016 to 2020 to ensure smooth traffic (especially on national highways) [3].

NH 12, NH 6, NH 279, NH 279B, NH 279C and NH 4H currently connect DienBien province to neighboring provinces. In which, the NH 12 section through DienBien province, running along Dien Bien Phu city through Muong Cha district to MuongLay town, has a length of 188,63 km of grade IV mountain road; the extended NH 12 has a length of 84,03 km of grade VI mountain road.

NH 6 runs through DienBien province, passing through Tuan Giao, Tua Chua, Muong Cha and Muong Lay districts, about 112 km long, with 95 km of grade VI mountain road and 17 km of grade IV mountain road.

NH 279, section through Dien Bien province, 130,3 km long, grade IV Dien Bien – rural road, running through Tuan

Table 1: Road classification in Dien Bien province based on pavement layer [2]

No.	Road network	Unit	Quantities	Scale
1	National highways	Km	745,43	100%
1.1	Cement concrete pavement	Km	68,20	9,15%
1.2	Asphaltic concrete pavement	Km	335,64	45,03%
1.3	Bituminous penetration macadam pavement	Km	341,59	45,82%
2	Provincial roads	Km	604,70	100%
2.1	Cement concrete pavement	Km	46,40	7,67%
2.2	Asphaltic concrete pavement	Km	17,40	2,88%
2.3	Bituminous penetration macadam pavement	Km	335,10	55,42%
2.4	Aggregate pavement	Km	156,80	25,93%
2.5	Earth road	Km	49,00	8,10%
3	District roads	Km	1.161,00	100%
3.1	Cement concrete pavement	Km	206,30	17,77%
3.2	Asphaltic concrete pavement	Km	9,60	0,82%
3.3	Bituminous penetration macadam pavement	Km	447,80	38,57%
3.4	Aggregate pavement	Km	240,10	20,68%
3.5	Earth road	Km	257,20	22,15%
4	Urban roads	Km	216,40	100%
4.1	Cement concrete pavement	Km	55,90	25,83%
4.2	Asphaltic concrete pavement	Km	67,80	31,33%
4.3	Bituminous penetration macadam pavement	Km	75,10	34,70%
4.4	Aggregate pavement	Km	1,80	0,83%
4.5	Earth road	Km	15,80	7,30%
5	Commune roads	Km	2.859,80	100%
5.1	Cement concrete pavement	Km	727,10	25,42%
5.2	Bituminous penetration macadam pavement	Km	214,90	7,51%
5.3	Aggregate pavement	Km	480,90	16,82%
5.4	Earth road	Km	1.436,90	50,24%
6	Border patrol routes	Km	74,20	100%
6.1	Cement concrete pavement	Km	74,20	100%
7	Village roads	Km	2.395,70	100%
7.1	Cement concrete pavement	Km	812,90	33,93%
7.2	Bituminous penetration macadam pavement	Km	27,40	1,14%
7.3	Aggregate pavement	Km	162,40	6,78%
7.4	Earth road	Km	1.393,00	58,15%
8	Intra-field roads	Km	1.511,00	100%
8.1	Cement concrete pavement	Km	48,30	3,20%
8.2	Bituminous penetration madacam pavement	Km	15,60	1,03%
8.3	Aggregate pavement	Km	22,30	1,48%
8.4	Earth road	Km	1.424,80	94,29%

Source: DienBien Department of Transport, 2020

Giao district, Muong Ang district, Dien Bien Phu city and Dien Bien district to Tay Trang border gate. NH 279B is 11,5 km long and has a grade VI mountainous road, while NH 279C is 68,2 km long and has a grade V mountainous road.

NH 4H, section through DienBien province, running along Muong Cha, Nam Po and Muong Nhe for 190.2 km, grade V mountain roads, 02 national highways 4H1 for 13,2 km and 4H2 for 37 km, grade VI mountain roads.

In general, the national highway system in Dien Bien province has invested in basic arterial roads reaching grade IV in mountainous areas. The main arteries connecting DienBien province to neighboring provinces and the capital Hanoi are relatively easy to navigate. However, because the topography of Dien Bien province is high mountainous, building transportation infrastructure is especially difficult, so the density of national highways over 100 km2 is the lowest in the country.

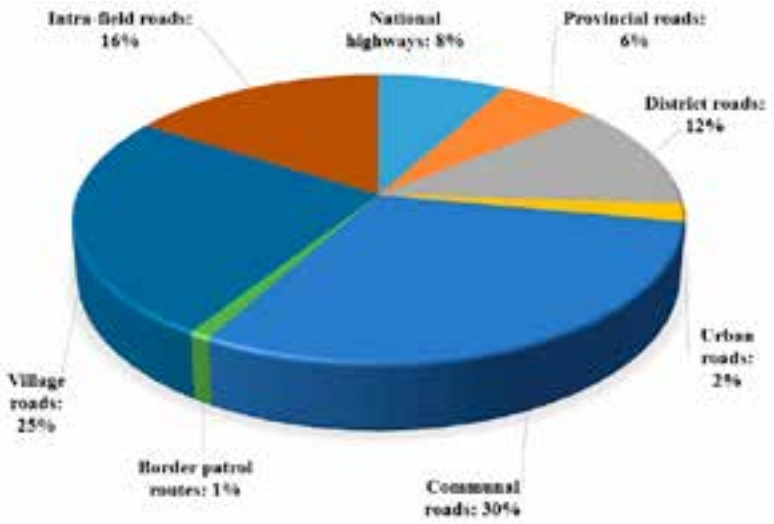

Figure 1. Road type scale in DienBien province by 2020
Source: DienBien Department of Transport, 2020

- The current condition of locally managed roads

Internal traffic routes managed locally include provincial roads, district roads, urban roads, commune roads, village roads and so on. In which, the provincial road (PR) system serves as internal roads connecting localities, while some routes serve as radial axes, ring roads and so on. DienBien provincial road system currently has 06 roads, the Department of Transport manages 140 km of routes (including lines PR 139, PR 140, PR 141, PR 142, PR 143, PR 150) and 17 districts manage 467,8 km of routes.

Although not yet heavily invested in, Dien Bien province's provincial road system has ensured relatively stable and convenient transportation and travel demand.

Regarding the current state of rural transport routes: To develop the rural transport system in the province, in accordance with the motto of the State and the people to collaborate, in difficult capital source conditions, the situation of rain and floods. difficult developments..... In recent years, the rural transportation system has grown in both quantity and quality, with a total length of 7.927,58 km, of which 2.509,9 km are concrete and asphalt roads and the road surface is distributed. The remaining distance is 4.511,9 km on the ground. The number of communes with car roads to the commune center is 129/129 communes, with 123/129 communes, wards and townships having a car road to the commune center that can travel in all seasons of the year, accounting for 95,3% and the remaining 6 communes having roads that can only be accessed by car in the dry season, accounting for 4,7%. (Hang Lia, Tia Dinh, Phu Hong, Sa Dung, Muong Khong and Nam Chua communes) [1].

Figure 2. The current state of national highways in DienBien province
Source: DienBien Department of Transport, 2020

- The current state of the road surface structure of major transport routes

Based on the data from the report summarizing the work in 2020 and implementing the tasks in 2021 of the DienBien province Department of Transport, Figure 5 shows the percentage of road surface structures in DienBien province by the end of 2020.

The chart above (Figure 5) shows that, while the road transport system of DienBien

province has been invested and developed to meet people's travel needs, the quality of the road surface structure is still backward, has not been invested synchronously, the technical scale is not up to standard and the majority of them are grade IV and VI roads with low quality road surface (mainly asphalt, graded and dirt roads); It is still very difficult to travel in many remote and remote areas, especially during the rainy season and especially in some communes that do not have access to villages. One of the factors affecting DienBien province's socioeconomic development is its underdeveloped road transportation system.

Discussion

- Limitations and difficulties

The most significant constraint and difficulty in developing the road transport system in DienBien province is a lack of investment capital for road construction, upgrading and renovation, which leads to inter-regional and intra-regional connectivity still face numerous challenges. DienBien province will require tens of thousands of billions of dong to invest in, upgrade and renovate projects in order to develop the road transportation system. The total capital demand anticipated to implement road planning is 51.696 billion VND (of which, in the period of 2020 - 2030, it is 28.483 billion VND) [1].

However, a number of national highways under the Ministry of Transport's public investment plan for the 2016-2020 period have yet to be invested according to the approved plan. A number of national highway construction projects are underway but have yet to be completed due to a lack of capital allocation and disbursement, forcing the projects to halt construction, resulting in unfinished construction and traffic disruptions; traffic safety difficulties and potential hazards. The majority of local roads, such as provincial roads, district roads, commune roads and village roads have not been invested, or have been invested but not in accordance with the scale of planning approved by the competent authority, due to the province of DienBien's lack of investment capital.

Table 2. SWOT analysis of Dien Bien province's road network development

Strengths (S)	Weaknesses (W)
(1) Dien Bien province has land exchange conditions with China and Laos via the A Pa Chai opening (Yunnan, China); Tay Trang international border gate (Phong Saly, Laos); Huoi Puoc main border gate (Luong Pha Bang, Laos); and Si Pha Phin and Na Bang secondary border gates (Phong Saly, Laos) (2) The development of intra-provincial and inter-regional road transport is aided by cultural, historical and sightseeing tourism resources. (3) Dien Bien province land fund for efficient growth of road traffic, lowering the cost of site clearance compensation	(1) The topography is difficult, severely fractured, with steep hills and mountains covering a significant region. (2) Weak infrastructure, particularly the transportation system, is not commensurate with the potential for development. Particularly in some sections of the national highway, such as NH 12, the Pom Lot - Chieng So section, NH 4H, NH 6, provincial roads and district roads have low density and poor quality road networks, making it difficult to connect urban areas and other regions of the province. (3) Because the industry has not yet developed, it cannot serve as a driving force for the advancement of transportation in general and road transport in particular. (4) DienBien province currently has a very low road density of 0.95 km/100 km^2, which is lower than the provinces in the Northwest region and the entire country. The provincial road density per 1000 population is also lower than the national and Northwest region averages. (5) The grades of provincial and district roads are low, making them vulnerable to the effects of climate change, such as natural disasters, floods, storms, landslides and due to heavy vehicle traffic. The running portion of the roadbed is extremely narrow. In many places, the road pavement structure is unsafe. (6) There are numerous aggregate pavement and earth roads that have not been hardened.
Opportunities (O)	**Threats (T)**
(1) Connect to a variety of economic development corridors (2) Modes of transportation that work well together, increase the capacity of road transportation. (3) Technology, science and technology are becoming more advanced in the service of road traffic construction. (4) There is a great opportunity to establish the region's trucking service center. (5) There are prospects for economic development in tourism, trade, agriculture and forestry as road traffic routes to A Pa Chai open up.	(1) Climate change causes landslides on slopes, which are hazardous to vehicles and road users. (2) Provincial and district road grades are poor and readily ruined by heavy truck loads. (3) Industrial development is slow, road upgrades and renovations fall short of expectations. (4) When district and commune roads are upgraded, the safety of forest resources is likely to suffer. (5) Production establishments, small firms, poor and near-poor residents continue to dominate, making it difficult for the state and people to collaborate on road traffic construction. (6) The state's construction money will not endure forever and the province's income is insufficient to pay for road traffic development on its own.

The second difficulty stems from DienBien province's complex mountainous terrain. Road traffic projects primarily pass through mountainous areas with complex geology in unpredictable weather conditions, such as heavy rains and floods, which have a direct impact on the work. Engineering design is relatively large, construction policies frequently change and raw material prices fluctuate, resulting in slow construction progress.

- The cause of the limitations

Because of the small economic scale of DienBien province, which is backward and one of the poorest provinces in Vietnam, commodity production is slow to develop, so attracting non-budget investment is still limited. Inadequate specific mechanisms and policy breakthroughs to encourage and create an environment and conditions for mobilizing resources, attracting investment and constructing a road transportation system. While resources are dependent on the central budget, there is a lack of investment capital, infrastructure development is not synchronized, the technical level remains low and socialization of resources for investment in transportation network development has not been implemented.

The mismatch between the allocated capital and the demand for consultancy has an impact on the investment in building the information interface; most projects' capital plans are delayed, resulting in the project's cancellation. are stretched and delayed in completion, reducing capital investment efficiency. Specifically, from the end of 2019 to the present, due to the complicated development of the Covid-19 pandemic, climate change, unusual weather, prolonged rain and floods, as well as the rapid increase in modes of transportation, many vehicles carry a large load, which makes road construction difficult.

The paper conducts a SWOT analysis based on the collected road transport development systems to identify strengths and weaknesses and to seek knowledge and opportunities to develop the road network in DienBien province.

- Solutions for road network development in DienBien province

DienBien is a disadvantaged province with significant socioeconomic development challenges, DienBien is ranked fifth from the bottom of Vietnam in terms of economic development. As a result, in order to foster socioeconomic development, Dien Bien province must focus on developing the road transport system in order to connect commercial and cultural exchange with the Northwest area and the entire territory of Vietnam.

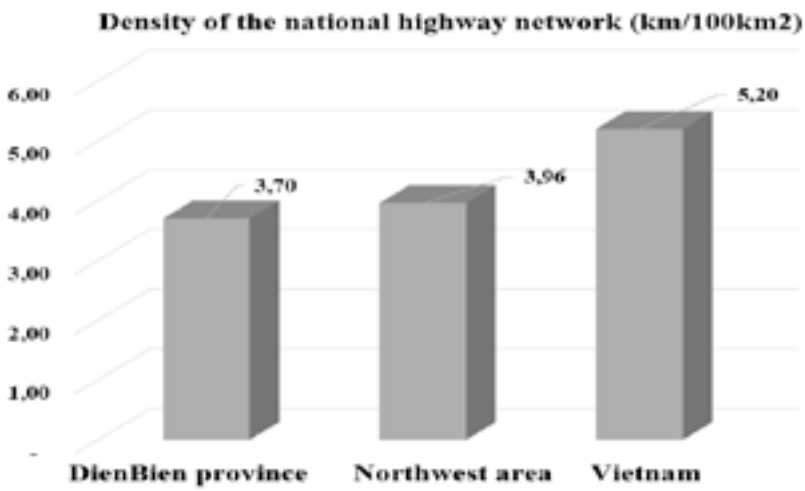

Figure 3. The density of the national highway network in DienBien province in comparison to the region and the entire country
Source: DienBien Department of Transport, 2020

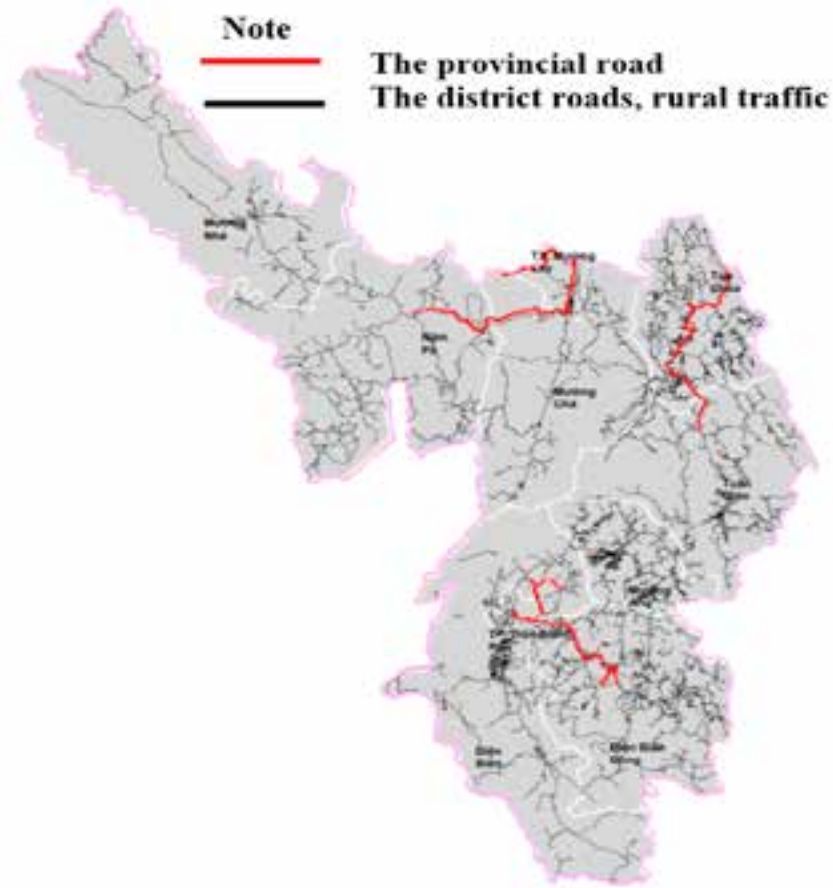

Figure 4. The current state of provincial road in DienBien province
Source: DienBien Department of Transport, 2020

Firstly, strengthen inter-sectoral coordination among state agencies, particularly in planning and devising policies for the growth of the road transport system in line with the transportation infrastructure development strategy. Priority projects for investment include the development of information interface infrastructure, the construction of new roadways, the improvement of national highways and

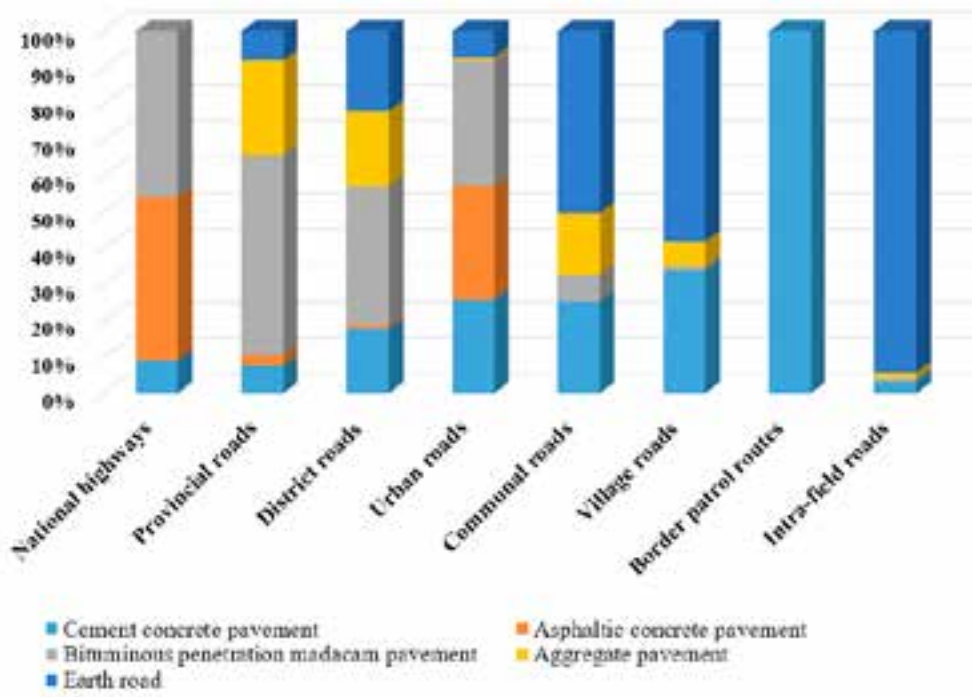

Figure 5. DienBien province's percentage of road surface structure types by 2020
Source: DienBien Department of Transport, 2020

provincial roads. Some noteworthy projects are given special consideration, including: (i) To build a highway network connecting Tuan Giao - Muong Ang - Dien Bien Dong - Dien Phu city - Tay Trang border gate connecting Son La; It is proposed to build the Dien Bien - Son La route before 2030 with a minimum scale of grade III, 2 lanes serving socioeconomic development and laying the groundwork for the completion of the Dien Bien - Son La expressway; (ii) Extending the national highway and provincial road network, to strengthen highway connectivity and links between cities, production hubs and border gates; (iii) Proposal to establish a high-speed line connecting with Lai Chau province to increase connectivity; proposal to construct a bridge linking Tua Chua to Lai Chau.

Secondly, taking advantage of land exchange conditions with China and Laos via openings, border gates....to create a comprehensive plan for connecting international road traffic with China and Laos, to take advantage of the two countries' markets and expand bilateral trade. Create a plan to update the national highway in order to connect the expressway on time, to connect interregional national routes with locations after 2030. Complete the goal of restoring and modernizing provincial roads that connect the region between Dien Bien Phu city and Muong Lay town, as well as districts throughout the province. Prioritize the achievement of the goal of upgrading the provincial national highway system by 2025, largely conform to grade IV road specifications, Provincial highways have steadily been finished, upgraded and improved to meet grade V and VI criteria and rural roads to be upgraded, renovated and concretized, concrete is used on all district roads and 70% of commune-level roads. At the same time, several districts are prioritizing investment in new rural roads linking with recently divided communes and to construct, renovate, upgrade routes linking with historical relic places in order to capitalize on the province's historical tourism development potential.

Thirdly, emphasize the critical role that the military plays in securing national security, abundant tourism resources and excellent opportunity to establish a regional transportation service hub. To promote investment, to ask for and benefit from the central government's investment in national highways, which are lifelines and are especially important for socioeconomic development and security guarantee - national defense in the province, such as the renovation and improvement of NH 6, NH 12, NH 279 and NH 279B, which connects the provinces of SonLa and LaiChau; in which NH 6 is a clear route that plays an important role in improving connectivity with the capital of Hanoi. Implement strategies to effectively promote internal resources and increase investment promotion from a variety of legal capital sources (for example, PPPs, from official development aid (ODA), primarily from the World Bank, ADB, JICA and the others), in order to gradually develop the road transport infrastructure approved during the planning period 2021-2030, including: (i) Upgrading 87 km of segment PR 139 of the Muong Nha-Sa Dung, grade V mountain road; (ii) Upgrading 77 km of the PR 139B Keo Lom-Sam Kha segment (SonLa province, Sop Cop district), grade V mountain road; (iii) Additional 49 km of Huoi So-Ta Phin route, grade V mountain road under PR 140; (iv) Additional 34,5 km of Deo Gio - Ta Sin Thang route, grade V mountain road under PR 140B; (v) Upgrading 68 km of the Quang Lam-Nam Khum Ban route (Km169+550/ NH.4H) grade V mountain road under PR 145E.

Conclusion

The road transport system is an important factor that contributes significantly to the economic development of each country, area and location. It is a powerful tool

for promoting economic, cultural and social growth. Furthermore, increasing road network has a great influence on the natural environment, society and the economy. The requirements for provinces and countries are to research and direct the development of road transport in a socioeconomically sustainable and effective manner. The article's study findings were based on a SWOT analysis to identify strengths and weaknesses, as well as challenges and possibilities for developing the Dien Bien province's road transport system. After that, offer some solutions to to overcome the flaws, enhance the strengths and possibilities for local road network development. It can be stated that the above solutions, if implemented properly, will contribute to the development of road network and create circumstances for the socioeconomic development of Dien Bien province./.

References

1. *Hung Nguyen (2020), DienBien Transportation - Resources must be mobilized for synchronized growth, on the website https:// tapchicongthuong.vn/*
2. *DienBien Province's Department of Transportation (2021), Report summarizing work in 2020 and tasks to be completed in 2021.*
3. *Trinh Long (2021), Dien Bien - Improve transportation infrastructure to create a driving force for development, on the website http://consosukien.vn/*
4. *DienBien Province People's Committee, Decision no.44/QD-UBND issued by the DienBien Province People's Committee on approving the adjustment of the Master Plan on the road network for the period 2011-2020, with a view toward 2030.*
5. *Mohammed Alamgir and partners (2017), Economic, Socio-Political and Environmental Risks of Road Development in the Tropics, Current Biology Review.*
6. *Gede B. Suprayoga and partners (2017), Coping with strategic ambiguity in planning sustainable road development: Balancing economic and environmental interests in two highway projects in Indonesia, Impact Assessment and Project Appraisal.*

Study on a novel exterior RCS hybird joint by ABAQUS

(tiếp theo trang 78)

- The numerical results were in good agreement with the experimental ones, both in terms of initial stiffness and ultimate loads.

- The numerical analysis by ABAQUS can be a reliable method to predict the exterior RCS hybrid joint behaviorin monotonic loading.

- For anchorage length beyond 80cm, the joint stiffness, the plastic bending moment and the initial stiffness remain unchanged.

- The joint resistance improves with higher concrete class for anchorage length below 80cm. The latter remain unchanged for the anchorage length greater than 80cm. The plastic bending moment is not much affected by the difference of the concrete class while the joint initial stiffness dependent on the concrete class./.

References

1. *Zibasokhan, H., F. Behnamfar, and K. Behfarnia, The new proposed details for moment resisting connections of steel beam to continuous concrete column. Advances in Structural Engineering, 2016. 19(1): p. 156-169.*
2. *Nguyen, Q.-H., et al., Finite Element analysis of a hybrid RCS beam-column connection., in The 3rd International Conference CIGOS 2015 on « Innovations in Construction».2015: Paris, France, 11-12 May 2015.*
3. *Michal, S. and W. Andrzej, Calibration of the cdp model parameters in abaqus. The 2015 World Congress on Advances in Structural Engineering and Mechanics (ASEM15), Incheon, Korea, 2015.*
4. *Lubliner, J., et al., A plastic-damage model for concrete. International Journal of Solids and Structures, 1989: p. 299-326.*
5. *Lee, J. and G.L. Fenves, A plastic-damage concrete model for earthquake analysis of dams. Earthquake Engineering & Structural Dynamics, 1998. 27(9): p. 937-956.*
6. *Kmiecik, P. and M. Kaminski, Modelling of reinforced concrete structures and composite structures with concrete strength degradation taken into consideration. Archives of Civil and Mechanical Engineering, 2011. 11: p. 623-636.*
7. *Alfarah, B., F. Lopez-Almansa, and S. Oller, New methodology for calculating damage variables evolution in plastic damage model for rc structures. 2017. 132: p. 70-86.*
8. *Eurocode-2, Design of concrete structures-Part 1: General rules and rules for buidings. EN1992-1-1. 2005: European Committee for Standardization.*
9. *Kratzig, W.B. and R. Polling, An elasto-plastic damage model for reinforced concrete with minimum number of material parameters. Computers & Structures, 2004. 82(15-16): p. 1201-1215.*

Cultural heritage conservation and sustainable development - Case study of Tien Yen, Quang Ninh, Vietnam

Ngo Thi Kim Dung

Abstract

Tien Yen, Quang Ninh is a locality with a favorable geographical position, a place of convergence and connection of ethnic groups in the Northeast of Vietnam. This region has a large and diverse natural area, and a unique history and culture. Those advantages make Tien Yen a valuable cultural heritage. From the perspective of heritage conservation, this study is conducted to understand the cultural heritage system of Tien Yen. This study is to answer the question which potentials Tien Yen cultural heritage system have that contribute to the sustainable development goals of Tien Yen locality. We discuss strategies to handle those cultural heritages, which balance between preserving historical values and traditional cultural identities of the locality, while also ensure integrating and developing sustainably. The main methods used in the research are field survey, document research, synthesis, and analysis. The results have shown many potentials of cultural heritage in Tien Yen. In this paper, multiple approaches, and model of preserving and utilizing Tien Yen cultural heritage to meet the goal of sustainable development are also discussed.

Key words: *Cultural Heritage, Sustainable Development, Historic Town, Heritage Conservation*

PhD. Ngo Thi Kim Dung,
Hanoi Architectural University
Email: dungnkhau@gmail.com

Date of receipt: 7/9/2022
Editing date: 3/10/2022
Post approval date: 5/10/2022

1. Introduction

Currently, sustainable development has become an urgent global need as well as an inevitable trend of the development process, and Vietnam is not an exception to that trend. Tien Yen is a district with a low starting point and the economy following the model of Agriculture-Forestry-Fisheries, specially based on agriculture with backward farming methods. The per capita incomes of ethnic minorities is significantly lower than those of general population. Thus, poverty still exists. Despite these challenges, Tien Yen has advantageous geographical location. Tien Yen is Quang Ninh's second-largest land of seas, hills and plains with rich natural ecosystems. In addition, Tien Yen is also a locality with rich historical and cultural traditions, a place of convergence and connection of ethnic groups in the Northeast with many unique traditional cultural values [1].These advantages have brought Tien Yen rich and diverse cultural heritage resources. Faced with such a situation, many questions have been raised: What must be done, how can the locality's traditional cultural identities and historical values be preserved while simultaneously integrating and developing sustainably? Where should sustainable development start? What is the most appropriate and effective strengths for sustainable development?

From the perspective of heritage conservation, this study is conducted with the goal of understanding the cultural heritage system of Tien Yen, identifying their potential to contribute to sustainable development. On that basis, the author discusses how to conserve and exploit cultural heritage to reach the goal of sustainable development.

2. Research Methods

In this study, the author used the following main methods: (1) Field survey in Tien Yen; (2) Document research (3) Synthesis, and analysis the characteristics of cultural heritage, compare with the content and objectives of sustainable development to identify the potential of cultural heritage of Tien Yen. These methods are basis for discussing about the models and approaches to conserving and exploiting cultural heritage, thereby reaching sustainable development goals.

3. Research results

3.1 Sustainable development

"Sustainable development is development that meets the needs of the present without compromising the ability of future generations to meet their own needs" [2]. The United Nations Summit on Sustainable Development has emphasized 7 priority areas for sustainable development including employment; energy; city; food security and sustainable agriculture; country; ocean and disaster preparedness [3]. In 2015, the United Nations adopted 17 Sustainable Development Goals. The issue of resource conservation including cultural heritage is mentioned as follows: Intensify efforts to protect and conserve the world's cultural and natural heritage to achieve the goal of making cities and human settlements become inclusive, secure, resilient and sustainable (Goal 11.4); Conservation and sustainable use of oceans, seas and marine resources for sustainable development (Goal 14); Protect and develop forests sustainably, conserve biodiversity, develop ecosystem services, combat desertification, prevent degradation and restore land resources (Goal 15).

The "sustainable development in Vietnam" strategy has been implemented since 2002. Basically, Vietnam's sustainable development goals coincide with the set goals of the United Nations [4]. To realize the common goal of the country, Tien Yen district has determined that "Promoting potentials and comparative advantages of natural resources and geographical location, setting Agriculture-Forestry-Fisheries as the foundation, Commercial Services as the "breakthrough" for a rapid development step". The economic structure determined by 2030 is Agriculture 30%, Industry-Construction 25% and Services 40% (including Trade, Tourism and Transport Services) [1].

3.2 Cultural Heritage in Tien Yen

Heritage means something inherited, a part of a culture that is passed on from one generation to the next. It may include monuments, buildings or natural landscapes. Existing cultural heritages of Tien Yen include:

3.2.1 Historical and cultural relics

The amount of ranked historical and cultural relics in Tien Yen remains modest. At provincial level, there are Khe Tu historical site, Khe Giao historical site, Dien Xa victory historical site on 4th street, An Long pagoda, Tien Lang commune and Dai Vuong Temple (Temple of Monsignor Hoang Can).

3.2.2. Architectural heritage

The architectural heritage of Tien Yen includes 2 main kinds (1) Western-style architecture - the works of the French built during the invasion of our country (Now only a few typical works remain, e.g. Headquarters of Tien Yen District Party Committee, Tien Yen High Fort, Tien Yen Church); (2) Eastern-style architecture comprising religious architecture (Linh Quang Pagoda; Dong Dinh Communal House; Tree Si Temple; Quan Am Pagoda)) and residence architecture (Houses of the Chinese, Vietnamese, and ethnic minority)

3.2.3 Urban Heritage.

Along with historical-cultural relics and architectural heritages, Tien Yen has heritages associated with the formation and development of urban areas. Due to the lack of proper attention, most of urban heritage in Tien Yen disappeared, but still only a few mainly located in the center of Tien Yen town. For instance, the archaeological site of Hon Ngo on Dong Hai commune is footprint of human life in Tien Yen; Con Chim, Ben Chau, and Old Street, the famous trading areas of the North East in the past, are the mark of the feudal urban area foundation in Tien Yen. The old hand-drawn ferries given by modern bridges; works with architectural and cultural characteristics of France (bridges, ferries, roads, forest rangers, churches, warehouses, hospitals, prisons, water towers, harbors, blockhouses, graveyards) and Chinese housing are the urban legacies of Western colonial domination periods. [6].

3.2.4. Scenic spots

Due to topographical features, most of the mountainous communes of Tien Yen are situated around streams, including hot streams. Streams form many waterfalls such as Pac Sui, Ca Nhay waterfall, Khe Luc mi waterfall, Khe xom waterfall. The system of winding rivers and streams surrounding the hills and mountains creates charming and poetic scenes. With the advantage of a 35km long coastline, Tien Yen also has scenic spots such as Mui Pagoda Port, Mui Long Vang, and Loc Vang Island. The diverse vegetation system (evergreen forest; mixed forest; mangrove forest, tidal flats and riparian mud flats) associated with rich species of flora and fauna has increased the value and attractiveness of the natural landscape here [7].

3.2.5 Intangible cultural heritage

Along with the tangible cultural heritages, Tien Yen has a diverse and rich system of intangible cultural heritages. They are Traditional Festivals (Long Tong Festival of the Tay, Le Cap Sac (maturity ritual) of the Dao, Le hoi Cau mua (Soil and grain ceremonies) of the San Chi, Dai Phan festival of the San Diu); Performing arts (Batting, call-and-response singing, San Co, playing bronze trumpets of the Dao Thanh y and the Dao Thanh phan, Soong co of the San Chi, Then singing of the Tay, and Soong co of the San Diu); Traditional cuisine (Tien Yen chicken, Nodding cake, Five-color sticky rice, etc…) [5].

Figure 1: Ranked Historical and Cultural Relics of Tien Yen [5]

3.3 Assessment of cultural heritage potential for sustainable development of Tien Yen.

Based on the content and objectives of sustainable development presented in Section 3.1 and the significance of the heritage characteristics presented in Section 3.2, the author assess the potential of Tien Yen heritage in sustainable development process as follows (See Table 1).

4. Discussion

Research results in sections 2 and 3 show that the diversity of Tien Yen's cultural heritage brings a lot of potential to make a major contribution to the sustainable development of locality. Typically, natural heritage with wild beauty and untouched landscapes is somewhat more prominent in quantity and quality with landscapes. The architectural and construction heritages are of small scale, but sparsely scattered as well; thereby, not really typical values. Relics recognized and ranked at the provincial level account for a small percentage of the total. However, according to the author's opinion, the unrecognized heritage resources have great potential to contribute to the socio-economic development and sustainable development of Tien Yen. To convert the potential into reality, it is necessary to have appropriate strategies, policies and solutions, with the participation of relevant sectors.

4.1 Conservation approach.

In the history of heritage conservation, there are many different perspectives, philosophies and approaches. The most common are the material factors-based approaches, heritage values-based approaches and approaches to living heritage. The traditional approaches focus on the protection of monuments, individual structures and their surroundings. The contemporary approaches consider heritage in a broader context and is closely related to urban planning and architecture. In the context of Tien Yen, cultural heritage should be seen as an important component of sustainability. Therefore, the approach to living heritage is considered appropriate. With this approach, heritage is seen

as an essential component of life. Treating heritage is not only focused on the past but is articulated with the needs and aspirations of modern life. The needs and opinions of the people are carefully considered to promote new value, taking people as the center and focusing on collective governance. Communities together with experts determine the values, meanings and protect and exploit the heritage. Heritage is approached comprehensively, holistically and integrated across fields and aspects, in the interaction between the city and its people. Cultural heritage conservation is integrated in the sustainable development strategy, urban planning and design [13,14].

4.2 Some models of conservation and promotion of cultural heritage values of Tien Yen.

4.2.1 Preservation of status quo

Preservation of the status quo means keeping the original state and image, reflecting the meanings and contents that the heritage contains along with the history of its existence and development. This model covering the identification, valuation, protection, preservation, restoration, and maintenance of heritage can be applied to ranked heritages and relics (According to the law on heritage conservation) and monuments, landscapes under local management (According to regulations of local).

4.2.2 Heritage adaptive conservation model

It is a conservation model in which the value of heritage is inherited and perfected in the development process. The heritage is preserved the original value and simultaneously provided with new functions and new values, aiming at ensuring its sustainable existence in the contemporary community and society. This model can be applied to heritage sites not governed by the Law on Cultural Heritage.

4.2.3 Cultural heritage conservation model through tourism development.

This model aims to make heritage live with social life through linking heritage with tourism economic activity. Heritage is exploited as an asset, bringing benefits to all parties involved. The benefits obtained from tourism activities will influence back to the activities of the heritage, thereby creating conditions for the heritage to exist and sustainable development. As a result, the value of cultural heritage is continuously increased, and at the same time brings great benefits to the resident community as the owner of the cultural heritage. To possibly conserve cultural heritage through tourism development, it is necessary to develop a system of solutions as follows:

In terms of institutions and policies, it is necessary to supplement regulations on the roles and interests of the community in heritage conservation and tourism development. Decentralization of heritage management to local authorities and communities is consistent with practice. In addition, it is necessary to build policies on socialization of heritage and relic conservation activities.

Regarding the construction and development of resources for tourism, it is necessary to ensure the essential elements of infrastructure such as convenient transportation, tourism facilities, services for guests, health and safety and Human Resources, etc...

Regarding planning, it is necessary to conduct planning of tourist routes and spots in accordance with the actual situation and potential and then encourage the development of tourism types associated with community culture, respecting cultural diversity and combining tangible and intangible cultural heritage:

Planning by topic.

- Ecotourism is a business activity promoting natural resources, which is considered the biggest advantage of Tien Yen town, including river cruises; visit the coastal mangrove

Figure 2: Architectural heritage [5]

Figure 3: Some typical urban heritages (Old Town, Ben Chau, Hon Ngo) [5]

Figure 4: Scenic spots [5]

forest, visit the sand dunes, parrot tiger beach, Mui yellow heart, Loc Vang Island, etc…

- Cultural and historical tourism in the center of Tien Yen town, the old quarter, the walking street, the historical - cultural relics and the experience of intangible cultural heritage.

- Travel to experience, explore agricultural and aquaculture production activities.

Planning by route, point.

The routes and points that have been approved for use today have not really exploited the existing heritage of Tien Yen. Some places where many types of heritage can be added for exploitation are:

Dai Duc Commune is a mountainous commune with over 90% of the San Chi ethnic group, and the convergence of a diverse and rich heritage system compromising many large and small streams coming from above to form waterfalls such as Nam Vam waterfall, Co Bay waterfall, Khe Luc My waterfall, A Chu Lan waterfall; Con Rong Stream known as Tuyet Tinh Coc on the mountain; Hot spring located in Khe Lac village. Besides streams, Dai Duc has many famous mountains and hills such as Love hill, a area of more than 200 hectares of pine forest; Thong Chau peak with full of myrtle flowers and cornflowers at an altitude of nearly 1,500m, where we can observe the whole Dai Duc commune and Dam Ha area; terraces and housing of the San Chi. Dai Duc is also a place to maintain many types of intangible cultural heritage such as crafts of forging, carpentry, wickerwork, bamboo and rattan; traditional cuisine with many popular folk delicacies; traditional ceremonies such as the Soil and Grain Ceremonies, Soong Co call-and-response singing as one of the most famous and attractive cultural features in the cultural life of the San Chi. The habit of residence of the San Chi is also an attractive content for tourists. To increase the attractiveness of the site, it is possible to study the restoration of a few villages with traditional houses of the San Chi just for sightseeing and accommodation in the form of Homestay.

Phong Du Commune is a commune where many ethnic minorities live, of which the Tay account for 40%. The heritage system of Phong Tu is also diverse, including Dinh Dong communal house relic - where the Dong Dinh communal house festival is held (In essence, it is the Long Tong festival, in which the Tay come down to the fields to pray for a good harvest in the new year) with typical Tay rituals such as "Lau Then" ceremony, incense offering ceremony, god worshiping ceremony and the festival such as stick push, tug of war, crossbow shooting, cake wrapping contest, national costume performance contest. The Tay ethnic culture and sports area has been built with 49 Tay ethnic households here, which is a favorable condition for organizing attractions to experience the resident culture, Then singing – the standard cultural features, etc. Besides, Phong Du also has many beautiful natural landscapes such as the terraced field area, Khe xom waterfall, etc.

Yen Than Commune is a commune with outstanding potential attracting tourists including Ngau Vo Leng Peak (Trau Dam Peak), Pac Sui Waterfall, Dao ethnic culture house, resident population of 39 Dao households in Pac Soi village. Additionally, it owns intangible cultural heritage such as Le Cap Sac (maturity ritual), call-and-response singing, singing on the wedding day, brocade embroidery and traditional cuisine.

Along with holding independent tourist sites, it is necessary to plan to connect tourist sites of communes and districts together to form inter-commune and inter-district tourist routes, especially, for adjacent localities with great tourism potential such as Binh Lieu, Dam Ha to increase the quality and effectiveness of tours.

Table 1: Potential of Tien Yen cultural heritage [8,9,10,11,12].

	Heritage Potential.	Contribution content	Contribution method
Economy	Transform livelihoods, ensure growth, employment, and income; Promote economic investment and tourism; Capacity building, local innovation and entrepreneurship.	Eradicate hunger, alleviate poverty and promote sustainable agricultural development (Goal 1.2); Ensure sustainable, inclusive, and continuous economic growth (Goal 8).	Through economic development, especially tourism development. Tourism development makes a breakthrough in local economic development
Society	Improve quality of life; Increase the welfare of all parties involved in the heritage; Meet the need for emotional exchange and be in a community group; be creative, shining and recognized as successful person.	Ensure healthy lives and promote well-being for people of all ages (Goal 3)	Development of investment and tourism projects. Encourage the community to participate in cultural heritage conservation and operation activities.
	Maintain the identity and cohesion of the community; Preserve memories, create urban images and symbols; Strengthen social inclusion, develop dialogue and recognize cultural diversity.	Promote peaceful, civilized society, make access to justice for all; Effectively build institutions. (Goal 16)	Cultural Heritage Conservation as a core locality and regional component.
Environment	Provide tangible records and information, knowledge about climate change; Experience in responding to environmental and climate hazards and disaster risk management; Create jobs for ethnic minorities.	Sustainable and resilient urban and rural development; reasonable distribution of population and labor by region. Timely and effective response to climate change and natural disasters (Goal 11.13)	Through strategies and planning of urban development, socio-economic development and tourism development.
	Maintain marine ecosystems; Anti-corrosion, erosion, landslide; Limit damage caused by high tides and sea level rise.	Conservation and sustainable use of oceans, seas and marine resources for sustainable development (Goal 14)	Rational exploitation of marine ecosystems, development of agriculture and aquaculture.
	Natural heritage, vegetation, forest ecosystems are still relatively intact and unspoiled.	Protection and sustainable development, biodiversity conservation, anti-desertification, prevention of degradation and restoration of land resources (Goal 15)	Forestry development, forest protection and exploitation. Develop ecosystem services

5. Conclusion.

The cultural heritage system in Tien Yen is a part of the present built from the past, a part of the living culture passed down from generation to generation. The system is diverse, rich in both number and form. Its presence strongly contributes to the quality of life, enhances the sense of identity, promotes a sense of pride and patriotism, and improves social cohesion. The heritage system also encourages urban and community resilience. These cultural heritages contribute to local sustainable development goals with outstanding potentials, including economic potential, social potential, and environmental potential. To effectively utilize the potentials and strengths of this cultural heritage system, local authorities need to have appropriate strategies, orientations, models, and approaches for each type of heritage. Examples of effective strategies are status quo, adaptive conservation, conservation through tourism development. With appropriate preservation and utilization, Tien Yen's cultural heritage will be a strong driving force for the sustainable development of the locality./.

References

1. *People's Committee of Quang Ninh province, Tien Yen district socio-economic development master plan to 2020, vision to 2030, Quang Ninh 2015.*
2. *The World Commission on Environment and Development, Brundtland report, 1987.*
3. *"The Future We Want", The United Nations Conference on Sustainable Development, Rio+20 , 2012.*
4. *Government of the Socialist Republic of Vietnam, Resolution No. 136/NQ-CP on sustainable development, 2020.*
5. *http://disanquangninh.gov.vn/en/*
6. *Tran Thi Kim Dung, Tien Yen City (Quang Ninh): The process of formation and transformation, Master Thesis, University of Pedagogy, Thai Nguyen University, 2015.*
7. *Dinh Hong Duyen et al., Results of environmental status assessment in Tien Yen district, Quang Ninh province, Journal of Science and Development, Hanoi University of Agriculture, vol. 12, no. 1:, 2014*
8. *The Committee on Culture of United Cities and Local Governments, Cultural Heritage and Sustainable Cities. Key Themes and Examples in European Cities, 2018*
9. *Mladen Obad Šćitaroci, Bojana Bojanić Obad Šćitaroci, Ana Mrđa, Cultural Urban Heritage.Development, Learning and Landscape Strategies, 2019.*
10. *Dr. Amira Elnokaly and Dr. Ahmed Elseragy, Sustainable Heritage Development: Learning from Urban Conservation of Heritage Projects in Nonwestern Contexts, European Journal of Sustainable Development (2013), 2, 31- 54.*
11. *R Rostami, S M Khoshnava , and H Lamit, Heritage contribution in sustainable city, Universiti Teknologi Malaysia, Skudai. 81310, Johor, Malaysia, IOP Conf. Series: Earth and Environmental Science 18 (2014) 012086 doi:10.1088/1755-1315/18/1/012086*
12. *Jamieson, D, Sustainability and beyond, Ecological Economics 24: 183-192, 1998*
13. *EFILW: European Foundation for the Improvement of Living and Working Conditions, Reports from European Conference on Urban Innovations, Dublin, 1994*
14. *United States National Trust for Historic Preservation, The Pocantico Proclamation on Sustainability and Preservation, 2009.*

Kinetic ofammonium removal by anammox rocessusingbiomass carrier felibendy

Nguyen Thi My Hanh[(1)], Tran Thi Hien Hoa[(2)]

Abstract

Ammonium removal from domestic wastewater has attracted increasedattention due to the serious water pollution consequences such as eutrophication ofwater bodies. To remove ammonium from septic tank wastewater of the dormitory,the anammox process was conducted in the fixed bed reactor using Felibendy biomass carrier. In the research, three kinetic models including first order, Grau second order, Stover Kincannon model were studied to describe the process kinetics of the ammonium removal in the AX. Stover Kincaanon proved to be the most suitable for simulating ammonium performance in fixed bed reactor using Felibendy.

Key words: *Anammox process, kinetic model,domestic wastewater, biomass carrier Felibendy*

(1) Water Enginerring Department, Hanoi Architectural University, ĐT: 0919776168, Email: hanhpro77@gmail.com,

(2) Water Supply & Sanitation Division, Hanoi University of Civil Engineering, ĐT: 0916511818, Email: hoatth@nuce.edu.vn

Date of receipt: 26/9/2022
Editing date: 19/10/2022
Post approval date: 21/10/2022

1. Introduction

The domestic wastewater containing nitrogen compounds could be toxic to aquatic life, causing depleting dissolved oxygen levels and theeutrophication in receiving water bodies. To remove nitrogen in the domestic wastewater, themost widely technology was theconventional nitrification-denitrification process. But theconventional process was limited by high operational costs and external additionof organic matter for the denitrification step. In contrast, the Anammoxprocess has recently received more attentionin applied research for domestic wastewater treatmentdue to its more advantages compared withthe conventional technology such asno need the addition of external carbon, less sludgeproduction and low energy consumption.

Nitrogen treatment technology by anammox process is a combination of two partial nitrification processes and anammox process.Firstly, partial nitrification processconvertspartially ammonium to nitrite according to equation (1):

$$NH4^+ + 0{,}83O_2\ 0{,}45NH_4^+ + 0{,}55NO_2^- + 0{,}55H_2O + 1{,}1H^+ \quad (1)$$

Secondly, anoxic combination of ammonium and nitrite to form dinitrogen gas by anammox process following equation (2):

$$NH_4^+ + 1{,}32NO_2^- + 0{,}066HCO_3^- + 0{,}13H^+ \rightarrow 1{,}02N_2 + 0{,}26NO_3^- + 0{,}066CH_2O_{0,5}N_{0,15} + 2{,}03H_2O \quad (2)$$

When studying the application of the Anammox process, an important task is to determine the kinetic model describing the treatment process.In 2012, Ni et al. [4] applied 5 types of kinetic models including Monod, Contois, firstorder, Grau secondorder andStover Kincannon for UASB reactor using granular sludge.In the study of Niu et al [5], the total nitrogen removal efficiency of the UASB model was simulated and predicted bysubstrate removal model of StoverKincannon, Monod, firstorder and Grau second order. The study of Abyar et al. [2] also used four kinetic models including firstorder, secondorder Grau, StoverKincannon and Monod models, the Stover - Kincannon model. The above studies showed that three types of kinetic models that are most suitable to describe the kinetics of Anammox process are first-order kinetic model, Grau second-order kinetic model and Stover-Kincannon model. However, the kinetic parameters of these processes are different for different wastewater types, substrate concentrations and operating conditions of each model [1], [6].Therefore, this study focuses on whether the model is suitable to decribe the performance of Anammox process using Felibendy biomass carrier to remove nitrogen from domestic wastewater.

2. Kinetic approaches

2.1. First order substrate removal model

The change rate of substrate concentration can be illustrated as:

$$-\frac{dS}{dt} = \frac{Q.S_0}{V} - \frac{Q.S_e}{V} - K_1.S_e \quad (1)$$

Since the (-dS/dt) is negligible under pseudo steady state to the Eq. (1) can be modified as:

$$\frac{Q.S_0}{V} - \frac{Q.S_e}{V} = \frac{S_0 - S_e}{HRT} = K_1.S_e \quad (2)$$

$$\frac{S_0 - S_e}{HRT.S_e} = K_1 \quad (3)$$

where S_0 and S_e express the substrate concentration in the influent and effluent, respectively and K_1 is the first order substrate removal rate constant

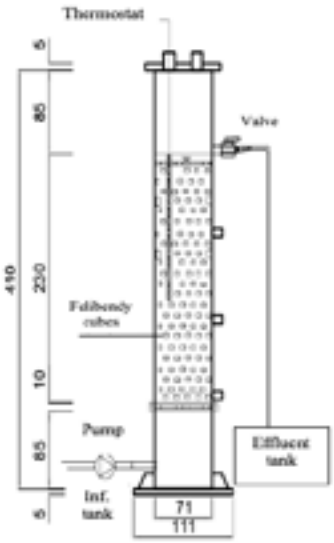

Figure 1. Schematic diagram of the experiment

Figure 2. Felibendy cubes

(1/day).The value of K1 can be obtained by plotting (S_0–S_e)/HRT) versus S_e, that mean K_1 can be obtained from the slope of the line.

2.2. Grau second order substrate removal model

The equation of second order kinetic model is expressed as:

$$-\frac{dS}{dt} = K_2.X.\left(\frac{S_e}{S_0}\right)^2 \quad (4)$$

where So and Se express the substrate concentration in the influent and effluent, X is the average biomass concentration in the reactor (g/L), and K_2 is the second-order substrate removal rate constant (1/d).

By linearization of Eq (4), the following equation can be obtained:

$$\frac{S_0 HRT}{S_0 - S_e} = HRT - \frac{S_0}{K_2 X} \quad (5)$$

When (S_0-S_e)/S_0 express the substrate removal efficiency and is symbolized as E, HRT is the hydraulic retention times (days), E_q (5) can be modified as follows:

$$\frac{HRT}{E} = a.HRT + b \quad (6)$$

where a=S_0/(K_2X) and b is a constant. a, b can be obtained by plotting HRT/E versus HRT in Eq.(6).

2.3. Stover Kincannon model

The Stover Kincannon model is used for determining the change rate of substrate concentration at steady state which can be expressed by Eq (7):

$$-\frac{dS}{dt} = \frac{Q.(S_0 - S_e)}{V} = \frac{U_{max}\left(\frac{Q.S_0}{V}\right)}{K_B + \left(\frac{Q.S_0}{V}\right)} \quad (7)$$

where dS/dt, substrate removal rate (g/L day); S_0 and S_e are the influent and effluent substrate concentration (g/l); V, the reactor volume (L); Q, the flow rate (L/day); U_{max}, the maximum utilization rate constant (g/L day) and K_B is the saturation value constant (g/L day).

If $(dS/dt)^{-1}$ is taken as V/[Q(S_0 – S_e)], which is the inverse of the loading removal rate andachieved Eq. (8):

$$\left(-\frac{dS}{dt}\right)^{-1} = \frac{K_B}{U_{max}}.\frac{HRT}{S_0} + \frac{1}{U_{max}} \quad (8)$$

The maximum utilization rate constant Umax and the saturation value constant K_B can be obtained by plotting HRT/(S_0-S_e) verus HRT/S_0 in Eq. (8).

3. Materials and methods

3.1. Reactor configuration

The schematic diagram of Anammox reactor (AX) was shown in Fig.1. The AX reactor is plastic cylindrical column which had an inner diameter of 7.1 cm and total height of 41 cm.The AX reactor contains biomass carrier called Felibendy, a product of Kuraray company, has porous structure with resin ofEVOH and core of PET (polyethylene terephthalate). In this study, Felibendy cubes with numbers of poreswill support for attached Planctomycetes bacteria

The AXreactor was enclosed with a thermostatateto maintain a constant temperature of 33-35^{0}C, and also was covered with black cloth to avoid growth of phototropic bacteria. Daily purging by nitrogen gas was used to reduce dissolved oxygen (DO) levels in the influent medium to below 0.5 mg/L.

3.2. Domestic wastewater and operationphases

Generally, the raw wastewater from dormitory's septic tankcontains nitrogen compounds, most of which exits in form of ammonium.So, this experiment used synthetic wastewater (simulating domestic wastewater) with ammonium as the main nitrogen component.The wastewater used for the AX reactor is the effluent of the PN reactor, which has nitrite to ammonium ratio of aprociately 1:1.

Withaiming to investigate the nitrogen removal performance of the anammox reactor, the NLR was increased stepwise through raising influent concentrations of ammonium and nitrite or by shortening HRT. So that, the study was conducted in 4 phases: Phase 1 has an HRT of 9 hours and an ammonium/nitrite concentration of 19.5±0.58 mgN/L; Phase 2 and phase 3 had ammonium/nitrite concentration of 39.55±0,64mgN/L and HRT decreased from 9h to 6h. Stage 4 kept HRT at 6h and increased ammonium/nitrite concentration to 56.55±0,44mgN/L.

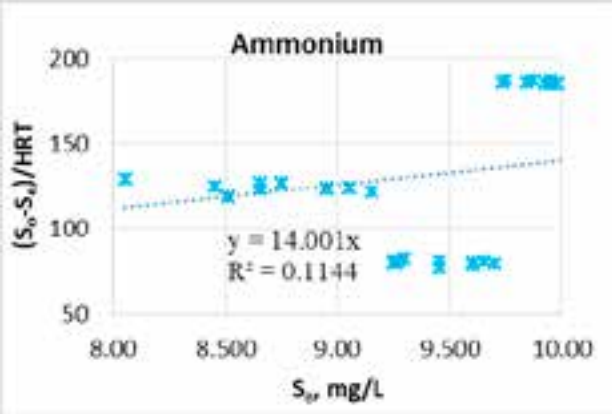

Figure 3. First order kinetic model plot

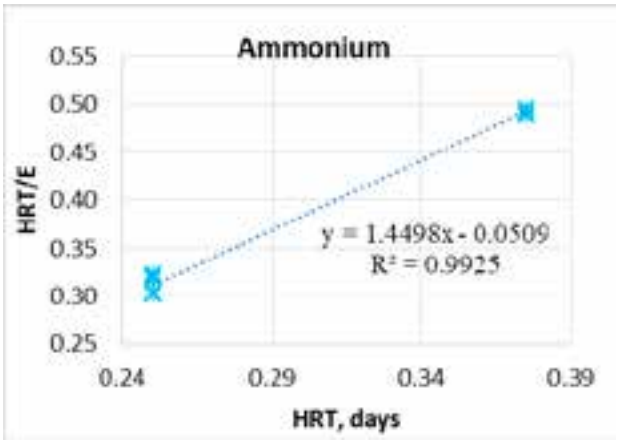

Figure 4. Second order Grau kinetic model plot

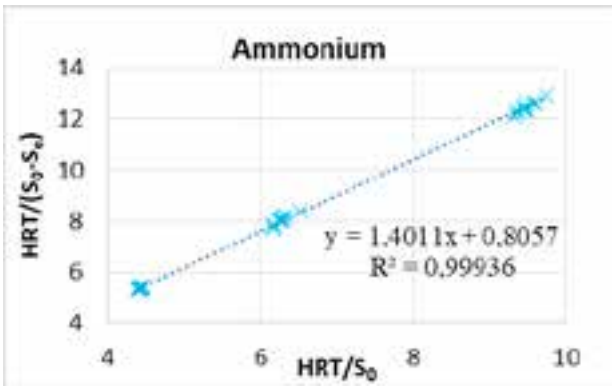

Figure 5. Stover Kincannon kinetic model plot

3.4. Analysis

The influent and effluent samples were analyzed immediately or stored in a refrigerator at 4^0C until the analyses were carried out. Measurements of ammonium, nitrite, and nitrate were performed according to the Standard methods. Ammonium and nitrite were measured by using colorimetric method; nitrate was analyzed by using ultraviolet spectrophotometric method. Total nitrogen concentration was determined by the sum of ammonium nitrogen, nitrite nitrogen and nitrate nitrogen concentration. Data based on arithmetic means of three or more measurements obtained at pseudosteadystate were adopted for kinetic study.

4. Results and discussion

From the data analyzed in the experiment such as influent substrate concentration (S_0), effluent substrate concentration (S_e), hydraulic retention time (HRT), reaction model volume (V), inflow rate (Q), process efficiency (E) establishes a correlation relationship between the parameters of the kinetic equation. Using Microsoft Excel software, set up linear equations to describe the kinetic process.

4.1. First order substrate removal model

First-order substrate removal model was applied to the AX reactor at pseudo-steady-state (Fig.3). The value of K_1 was obtained from the slope of the line by plotting ($S_0 - S_e$)/ HRT versus $S_e$as 14,001d^{-1} and the determination coefficient (R^2) was 0.911.

The ammonium concentration in effluent (Se) is predicted from the approximate curve in Fig.3 as follows:

$$S_e = \frac{S_0}{14.001HRT+1} \quad (9)$$

4.2. Grau second order model

The values of a and b in Eq. 6 were calculated to be 1.4498 and 0.0509 from the intercept and slope of the approximate curve shown in Fig. 4. The determination coefficient (R^2) of this model was 0.9925, indicating that Grau second-order substrate removal model was suitable for simulation of nitrogen removal performance in the AX reactor.

The formula for predicting effluent substrate concentration for the ammonx process is given by:

$$S_e = S_0\left(1 - \frac{HRT}{1.4498HRT - 0.0509}\right) \quad (10)$$

4.3. Stover Kincannon model

The Stover Kincannon model plot is shown in Fig. 5. Saturation value constant (K_B) and maximum utilization rate (U_{max}) were determined as 1.241 g/L/d and 1.738 g/L/d, respectively. A plot of the V/Q(S_i-S_e) against (V/QS_i) showed a satisfactory linear correlation (R^2 = 0.999).

The ammonium concentration in effluent (Se) is predicted by Stover Kincannon as follows:

$$S_e = S_0 - \frac{1.738}{1.241 + \frac{S_0}{HRT}} \quad (11)$$

4.4. Evaluation of the kinetic model

Three kinetic models were applied to simulate the ammonium removal performance in the fixed bed reactor using Felibendy biomass carrier. The linear regression lines set up with each kinetic model have a coefficient of determination R^2 and summarized in Table 1.

A low R^2 value means a high dispersion of the data, which means that the accuracy of the established equation is not high. Therefore, it is necessary to choose a kinetic model with the highest R^2 coefficient to describe the performance of biological treatment. In this research, the StoverKincannon model has the highest R^2, that means the Stover-Kincannon model is the most suitable and applicable for predicting the effluent substrate concentration and efficiecncy of process.

Table 1. Comparison of kinetic models applied to anammox process

Models	Reactor	NLR (g/L/d)	HRT (d)	Constant		R^2	Ref.
First order				K_1			
	Fixed bed	0.015-0.226	0.25-0.5	14.001		0.9111	This study
	MBBR	0.43-0.72	0.2-0.3	11.64		0.8043	[4]
	UASB	1.5-12	0.93-7.34	0.458		0.43	[5]
	Column	0.08-1.94	0.25-1.0	7.44		0.756	[3]
Second order Grau				a	b		
	Fixed bed	0.015-0.226	0.25-0.5	0.0509	1.4498	0.992	This study
	MBBR	0.43-0.72	0.2-0.3	1.0287	0.0936	0.998	[4]
	UASB	1.5-12	0.93-7.34	1.13	0.087	0.93	[5]
	Column	0.08-1.94	0.25-1.0	1.136	0.0554	0.991	[3]
Stover Kincannon				U_{max}	K_B		
	Fixed bed	0.015-0.226	0.25-0.5	1.738	1.241	0.999	This study
	MBBR	0.43-0.72	0.2-0.3	12.1	11.4	0.999	[4]
	UASB	1.5-12	0.93-7.34	0.892	1.019	0.94	[5]
	Column	0.08-1.94	0.25-1.0	6.41	7.37	0.993	[3]

The results of this study are similarity to the results of several other studies. However, the difference between these kinetic coefficients suggests that the rate of substrate removal is mainly dependent on the nature of the substrate, the reactor structure, the metabolism and the microorganisms in the reactor rather than concentration of that substrate [7].

5. Conclusions

Biokinetic models such as first-order, Grausecondorder and StoverKincannon models were applied for the anammox process in fixed bed reactor using Felibendy carrier. StoverKincannon model for ammonium removalgave thehighestcorrelation coefficients of 99.9%. Therefore, StoverKincannon model may be used in the design of the anammox process to remove nitrogen in domestic wastewater./.

References

1. *Abbas, G., Wang, L., Li, W., Zhang, M., & Zheng, P. (2015), "Kinetics of nitrogen removal in pilot-scale internal-loop airlift bio-particle reactor for simultaneous partial nitrification and anaerobic ammonia oxidation", Ecological Engineering, 74, 356–363.*
2. *Abyar, H., Younesi, H., Bahramifar, N., Zinatizadeh, A. A., &Amini, M. (2017), "Kinetic evaluation and process analysis of COD and nitrogen removal in UAASB bioreactor", Journal of the Taiwan Institute of Chemical Engineers, 78, 272–281.*
3. *Huang, X.-W., Wei, Q.-Y., Urata, K., Tomoshige, Y., Zhang, X.-H., &Kawagoshi, Y. (2014), "Kinetic study on nitrogen removal performance in marine anammox bacterial culture", Journal of Bioscience and Bioengineering, 117(3), 285–291.*
4. *Ni, S.-Q., Sung, S., Yue, Q.-Y., & Gao, B.-Y. (2012), "Substrate removal evaluation of granular anammox process in a pilot-scale upflow anaerobic sludge blanket reactor", Ecological Engineering, 38(1), 30–36.*
5. *Niu, Q., Zhang, Y., Ma, H., He, S., & Li, Y.-Y. (2016), "Reactor kinetics evaluation and performance investigation of a long-term operated UASB-anammox mixed culture process", International Biodeterioration & Biodegradation, 108, 24–33.*
6. *Qiao, L., Xu, W., Mao, S., Li, Y., & Zhang, Y. (2019), "Study on the expanded culture and kinetics of anammox bacteria in the upper flow packed bed", Science of The Total Environment, 650, 1173–1181.*
7. *Wang, C., Wu, H., Zhu, B., Song, J., Lu, T., Li, Y. Y., &Niu, Q. (2020). Investigation of the process stability of different anammox configurations and assessment of the simulation validity of various anammox-based kinetic models, RSC Advances, 10(64), 39171-391*

Lễ công bố quyết định công nhận Hội đồng trường và Chủ tịch Hội đồng trường Đại học Kiến trúc Hà Nội nhiệm kỳ 2022 - 2027

Ngày 26/4/2022 tại Trường Đại học Kiến trúc Hà Nội, Bộ Xây dựng đã công bố Quyết định công nhận Hội đồng Trường và Quyết định công nhận Chủ tịch Hội đồng Trường nhiệm kỳ 2022- 2027. Đồng chí Nguyễn Văn Sinh - Uỷ viên Ban Cán sự Đảng, Thứ trưởng Bộ Xây dựng đến dự và phát biểu tại buổi Lễ.

Tham dự buổi Lễ có bà Nguyễn Thị Thanh Hằng - Phó Vụ trưởng, Vụ Tổ chức cán bộ, Bộ Xây dựng; ông Đào Việt Dũng - Vụ trưởng Vụ Tài chính Kế hoạch, Bộ Xây dựng; đồng chí Nguyễn Quốc Hùng - Phó trưởng phòng An ninh chính trị nội bộ PA03 Công an Thành phố Hà Nội.

Về phía Trường Đại học Kiến trúc Hà Nội có PGS. TS.KTS. Lê Quân - Bí thư Đảng uỷ, Hiệu trưởng Nhà trường; PGS.TS.KTS. Phạm Trọng Thuật - Phó Bí thư Đảng uỷ, Chủ tịch Hội đồng Trường. Dự buổi Lễ còn có đại diện các thầy cô trong Đảng uỷ, Ban Giám hiệu, Hội đồng Trường; đại diện lãnh đạo các Khoa, Phòng ban chức năng cùng đại diện cán bộ, viên chức, giảng viên, sinh viên trong toàn Trường.

Tại buổi Lễ, bà Nguyễn Thị Thanh Hằng - Phó Vụ trưởng, Vụ Tổ chức cán bộ, Bộ Xây dựng đã công bố các Quyết định:

- Quyết định số 285/QĐ-BXD ngày 06/4/2022 về việc công nhận Hội đồng Trường, Trường Đại học Kiến trúc Hà Nội nhiệm kỳ 2022 - 2027 (gồm 17 thành viên);

- Quyết định số 286/QĐ-BXD ngày 06/4/2022 về việc công nhận Chủ tịch Hội đồng Trường, Trường Đại học Kiến trúc Hà Nội nhiệm kỳ 2022 - 2027 đối với ông Phạm Trọng Thuật - PGS.TS.KTS, Phó Bí thư Đảng uỷ, Chủ tịch Hội đồng Trường nhiệm kỳ 2017 - 2022.

Việc thành lập Hội đồng trường này được thực hiện theo Luật 34/2018/QH14 và Luật sửa đổi, bổ sung một số điều của Luật Giáo dục Đại học.

Hội đồng Trường, Trường Đại học Kiến trúc Hà Nội là tổ chức quản trị, đại diện quyền sở hữu của Nhà trường, có quyền quyết nghị các vấn đề mang tính chiến lược, quan trọng liên quan tới các hoạt động và sự phát triển của Trường. Việc thành lập Hội đồng Trường và phê chuẩn Chủ tịch Hội đồng Trường đánh dấu bước tiến của Trường Đại học Kiến trúc Hà Nội trong việc đổi mới hệ thống cơ cấu tổ chức, bộ máy lãnh đạo nhằm nâng cao chất lượng, hiệu quả hoạt động.

Phát biểu tại buổi Lễ, đồng chí Nguyễn Văn Sinh - Uỷ viên Ban Cán sự Đảng, Thứ trưởng Bộ Xây dựng hoan nghênh và biểu dương thành tích của tập thể lãnh đạo, cán bộ, viên chức, học viên, sinh viên, của Trường Đại học Kiến trúc Hà Nội về những cố gắng và đóng góp của Nhà trường trong sự nghiệp đào tạo nguồn nhân lực chất lượng cao cho ngành Xây dựng và cho đất nước. Đạt được những thành tích đó, ngoài sự cố gắng nỗ lực của Thầy và trò Nhà trường, còn có sự hỗ trợ, giúp đỡ của Bộ Xây dựng, các cơ quan Trung ương và địa phương, sự hợp tác giữa Nhà trường với các cơ quan, đối tác; các cơ sở đào tạo trong nước, khu vực và thế giới.

Để làm tốt nhiệm vụ của Nhà trường, nhất là trong bối cảnh hội nhập Quốc tế, một trong những giải pháp quan trọng đó là phát triển nguồn nhân lực chất lượng cao, phát triển khoa học công nghệ. Việc đào tạo nguồn nhân lực có chất lượng trong thời kỳ hội nhập Quốc tế, đòi hỏi đội ngũ Thầy và trò Nhà trường phải thực sự cố gắng, vượt qua mọi khó khăn và thử thách trong thời gian tới.

Thứ trưởng Nguyễn Văn Sinh tin tưởng Nhà trường sẽ có những bước phát triển mới to lớn hơn trong thời gian tới, tập thể Nhà trường luôn đoàn kết, sáng tạo, chủ động đi đầu trong việc đổi mới và phát triển Nhà trường.

Phát biểu nhận trọng trách mới, PGS.TS.KTS. Phạm Trọng Thuật - Chủ tịch Hội đồng Trường nhiệm kỳ 2022 - 2027 bày tỏ lời cảm ơn đến lãnh đạo Bộ Xây dựng, Ban Giám hiệu Nhà trường, các cán bộ, giảng viên Trường Đại học Kiến trúc Hà Nội đã tin tưởng tín nhiệm và ủng hộ. Thay mặt các thành viên Hội đồng Trường, PGS.TS.KTS. Phạm Trọng Thuật khẳng định sẽ nỗ lực thực hiện tốt trọng trách được giao, đồng thời phát huy cao độ tinh thần đoàn kết, nhất trí trong Trường để thực hiện thắng lợi các mục tiêu của Nhà trường đã đề ra, đóng góp tích cực hơn nữa vào sự nghiệp đào tạo nhân lực, bồi dưỡng cán bộ phục vụ cho ngành Xây dựng, đưa Trường Đại học Kiến trúc Hà Nội trở thành một Trường uy tín sánh ngang tầm khu vực và trên Thế giới.

Thay mặt Đảng uỷ, Ban Giám hiệu, PGS.TS.KTS. Lê Quân - Bí thư Đảng uỷ, Hiệu trưởng Nhà trường gửi lời chúc mừng đến cá nhân Chủ tịch Hội đồng Trường Phạm Trọng Thuật cũng như tập thể Hội đồng Trường. Hiệu trưởng Lê Quân bày tỏ hy vọng trong thời gian tới, Hội đồng Trường sẽ phối hợp cùng tập thể Ban Giám Hiệu cùng các cán bộ, giảng viên Nhà trường quyết tâm đưa Trường Đại học Kiến trúc Hà Nội ngày càng phát triển.

Khai mạc triển lãm Kiến trúc - Nội thất đương đại V.ICON

Ngày 26/3/2022, tại Tầng 1 Tòa nhà Interior, Trường Đại học Kiến trúc Hà Nội đã diễn ra lễ khai mạc Triển lãm Kiến trúc - Nội thất đương đại V.ICON do Khoa Nội thất Trường Đại học Kiến trúc Hà Nội phối hợp cùng Chi hội Kiến trúc - Nội thất trực thuộc Hội Kiến trúc sư Việt Nam tổ chức. Triển lãm hướng tới kỷ niệm ngày Kiến trúc Việt Nam 27/4 và kỷ niệm ngày thành lập Khoa Nội thất Trường Đại học Kiến trúc Hà Nội.

Tới dự lễ khai mạc có sự hiện diện của đại diện các ban ngành, tổ chức: Bộ xây dựng; Vụ Khoa học công nghệ - Bộ xây dựng; Hội Kiến trúc sư Việt Nam; Ban Giám hiệu Trường Đại Học Kiến trúc Hà Nội; Lãnh đạo các Khoa: Kiến trúc, Khoa Thiết kế Mỹ thuật, Viện hợp tác quốc tế. Đại diện các đoàn thể đơn vị trực thuộc Trường: Đoàn thanh niên, Viện Kiến trúc nhiệt đới; Đại diện các doanh nghiệp, nhà tài trợ, các Kiến trúc sư, Nhà thiết kế, các thầy cô, các em sinh viên và đông đảo khách mời quan tâm tới sự kiện.

Triển lãm quy tụ những tác phẩm kiến trúc nội thất của những Kiến trúc sư, Nhà thiết kế hàng đầu của Chi hội Kiến trúc Nội thất và Khoa Nội thất, được ban tổ chức tuyển chọn kỹ lưỡng, mang đến những triết lý thiết kế mới mẻ, sáng tạo xứng đáng là đại diện "Icon" của kiến trúc nội thất đương đại. Bên cạnh đó các gian triển lãm giới thiệu sản phẩm từ các doanh nghiệp, nhãn hàng nội thất uy tín giúp cho khách tham quan triển lãm và đặc biệt là sinh viên có cái nhìn thực tiễn về hoạt động nghề nghiệp nội thất. Triển lãm là động lực để các nhà thiết kế cùng chung tay xây dựng một phong cách Kiến trúc, Nội thất Việt Nam đương đại.

Phát biểu khai mạc triển lãm, PGS.TS.KTS Lê Quân - Hiệu trưởng Trường Đại học Kiến Trúc Hà Nội bày tỏ: "Trong khí đầu xuân, Trường Đại học Kiến trúc rất vui mừng khi tổ

chức Triển lãm Kiến trúc - Nội thất đương đại. Đây là một trong những hoạt động mở đầu, khởi động cho chuỗi các hoạt động trong năm 2022 của Nhà trường - Một năm đánh dấu sự bước qua, phục hồi sau dịch bệnh. Triển lãm thể hiện một sức sống bật lên qua những khó khăn. Hy vọng trong năm tới, ngành nội thất nói riêng và sinh viên nói chung cũng sẽ có 1 sức sống mới trong bối cảnh phát triển của ngành nội thất như hiện nay."

Chia sẻ về triển lãm, PGS.TS.KTS Vũ Hồng Cương, Trưởng Khoa Nội thất Đại học Kiến trúc Hà Nội, Chủ tịch Chi hội Kiến trúc Nội thất cho biết: "Triển lãm Triển lãm Kiến trúc - Nội thất đương đại (V.ICON) giới thiệu các tác phẩm của chính các thành viên trong Chi hội Nội thất và giảng viên trường Đại học Kiến trúc Hà Nội đã thực hiện trong suốt 2 năm dịch bệnh khó khăn vừa qua. Triển lãm không chỉ mang tới cái nhìn thực tiễn cho khách tham quan và sinh viên trường Đại học Kiến trúc Hà Nội mà còn là một sự kiện giao lưu kết nối giữa các hoạt đào tạo với thực tiễn nghề nghiệp; Giữa giảng viên với người làm nghề; Giữa các nhà cung ứng với nhà thiết kế; Giữa chuyên gia và các em sinh viên."

Thông tin bên lề Triển lãm:

- Chuỗi sự kiện Talk show:

1. Talkshow "Học gì từ truyền thống?" - Diễn giả KTS. Lê Thành Vinh

2. Talkshow "Sống!" - Diễn giả HS. Lê Thiết Cương & NĐK. Đinh Công Đạt

3. Talkshow "Chuyện nghề nội thất" - Diễn giả KTS. Đồng Minh Hậu & KTS. Nguyễn Văn Sinh

Trường Đại học Kiến trúc Hà Nội hưởng ứng Kỷ niệm 72 năm ngày Kiến trúc Việt Nam

Sáng 27/04/2022, tại Trường Đại học Kiến trúc Hà Nội đã diễn ra chuỗi sự kiện chào mừng Kỷ niệm 74 năm Ngày Kiến trúc Việt Nam (27/4/1948 - 27/4/2022).

Chương trình có sự tham dự của: Ông Vi Quốc Phương - Phó Chủ tịch Huyện Tiên Yên - Bắc Giang; ông Nguyễn Đức Dương - Phó Tổng Giám đốc Công ty Joton, Giám đốc Chi nhánh Hà Nội; ông Lưu Minh Soi - Tổng Giám đốc Công ty CP Blue Crystals; đại diện Công ty TNHH Friendship, Công ty Khóa Huy Hoàng, Công ty Sàn SPC, Công ty MB Windows cùng đại diện các doanh nghiệp hợp tác khác với Khoa Kiến trúc và Trường Đại học Kiến trúc Hà Nội.

Phía đại diện của Trường Đại học Kiến trúc Hà Nội có sự tham dự của PGS.TS.KTS Lê Quân - Hiệu trưởng Nhà trường; PGS.TS.KTS. Phạm Trọng Thuật - Chủ tịch Hội đồng Trường; các Phó Hiệu trưởng Nhà trường: PGS.TS.KTS. Nguyễn Tuấn Anh, TS.KTS. Ngô Thị Kim Dung, PGS.TS. Lê Anh Dũng cùng đại diện lãnh đạo Khoa Kiến trúc, đại diện một số Khoa, Phòng ban trong Trường; các Kiến trúc sư cùng các em sinh viên…

Mở đầu chương trình là Lễ trao giải Cuộc thi Thiết kế ý tưởng phố đi bộ Tiên Yên (Bắc Giang).

Cũng tại sự kiện này, chương trình đã công bố danh sách và trao chứng nhận cho 3 Kiến trúc sư Asean: TS.KTS Vương Hải Long; ThS.KTS Lê Minh Hoàng và KTS Lê Quốc Anh.

Phát biểu tại lễ kỷ niệm, PGS.TS.KTS. Lê Quân - Hiệu trưởng Trường Đại học Kiến trúc Hà Nội đã ôn lại truyền thống 74 năm ngày thành lập Hội Kiến trúc sư Việt Nam.

Ngày 27/4/1948, Chủ tịch Hồ Chí Minh đã gửi thư cho các kiến trúc sư ở Đại hội lần thứ I, chính thức thành lập Đoàn Kiến trúc sư Việt Nam (nay là Hội Kiến trúc sư Việt Nam) tại làng Thản Sơn, xã Chiến Thắng, huyện Lập Thạch, tỉnh Vĩnh Yên. Năm 2011, Thủ tướng Chính phủ đã quyết định lấy ngày 27/4 hàng năm là Ngày Kiến trúc Việt Nam.

Trải qua 74 năm hình thành và phát triển, Hội Kiến trúc sư Việt Nam nói riêng và ngành Kiến trúc nói chung đang không ngừng trưởng thành lớn mạnh, có nhiều đóng góp quan trọng vào sự nghiệp xây dựng và bảo vệ Tổ quốc. Những công trình kiến trúc quan trọng, những tác phẩm kiến trúc có giá trị về nghệ thuật tạo nên những dấu ấn đặc sắc và làm giàu thêm cho nền kiến trúc thế giới đều có những đóng góp của giới kiến trúc sư, Hội Kiến trúc sư và ngành Xây dựng Việt Nam…

Cũng trong khuôn khổ chương trình đã diễn ra Lễ ký kết tài trợ giải thưởng AA giữa Khoa Kiến trúc, Trường Đại học Kiến trúc Hà Nội với Công ty cổ phần L.Q Joton và Tọa đàm với chủ đề "Thiết kế đặc thù và hợp tác trong Kiến trúc".

Tọa đàm là hoạt động được tổ chức thường xuyên tại Trường Đại học Kiến trúc Hà Nội nhằm lấy ý kiến của các chuyên gia, các kiến trúc sư và các Hội cơ sở… từ đó tiếp thu các đóng góp để đổi mới ngày càng chất lượng hơn, tạo được tiếng vang trong xã hội. Tọa đàm lần này nhận được nhiều các ý kiến đóng góp từ các kiến trúc sư giàu kinh nghiệm, uy tín trong giới nghề nhằm nâng cao chất lượng.

NCS Hoàng Huệ Quân bảo vệ thành công luận án tiến sĩ chuyên ngành kỹ thuật cơ sở hạ tầng

Ngày 22/4/2022, Trường Đại học Kiến trúc Hà Nội tổ chức đánh giá Luận án Tiến sĩ cấp trường cho nghiên cứu sinh Hoàng Huệ Quân với đề tài: "Nghiên cứu công trình lọc ODM-2F để loại bỏ cặn lơ lửng trong xử lý nâng cao nước thải đô thị nhằm mục đích tái sử dụng", chuyên ngành Kỹ thuật Cơ sở Hạ tầng, mã số 62.58.02.10. Người hướng dẫn khoa học là GS.TSKH. Trần Hữu Uyển và PGS.TS. Nghiêm Vân Khanh.

Với những kết quả đạt được trong luận án, Nghiên cứu sinh Hoàng Huệ Quân đã hoàn thành mục đích và nhiệm vụ nghiên cứu. Luận án có những đóng góp thiết thực vào việc: Nghiên cứu đánh giá thực trạng về tái sử dụng nước thải, xây dựng cơ sở lý thuyết và lựa chọn công nghệ xử lý nâng cao nước thải; Nghiên cứu thực nghiệm xác định các thông số/chỉ tiêu để xây dựng phương pháp tính toán công trình lọc ODM-2F; Nghiên cứu ứng dụng phương pháp tính toán vào thiết kế công trình lọc ODM2F trong xử lý nâng cao nước thải sinh hoạt để tái sử dụng cho mục đích cấp nước chữa cháy, tưới cây, rửa đường cho khu đô thị điển hình.

Hội đồng đánh giá đây là một công trình nghiên cứu khoa học độc lập, nghiêm túc, bám sát và đáp ứng được những yêu cầu của luận án Tiến sĩ. Nghiên cứu sinh đã vận dụng lý thuyết để phân tích, đánh giá thực trạng giải quyết vấn đề nghiên cứu. Kết quả phân tích và một số nhận định có chất lượng khoa học. Đề tài nghiên cứu có ý nghĩa sâu sắc cả về lý luận và thực tiễn.

Với kết quả 07/07 phiếu tán thành, Hội đồng đã thông qua Nghị quyết và đề nghị Trường Đại học Kiến trúc Hà Nội cấp văn bằng học vị Tiến sĩ cho Nghiên cứu sinh Hoàng Huệ Quân.

Lễ khánh thành xưởng đồ án I.902 và trao giải thưởng cuộc thi Tổ kén - Xưởng sáng tạo

Sáng 16/3/2022 tại Trường Đại học Kiến trúc Hà Nội đã diễn ra lễ khánh thành Xưởng đồ án I902 và trao giải thưởng cho các sinh viên đạt giải tại cuộc thi Tổ kén - Xưởng sáng tạo. Lễ khánh thành cũng là sự kiện chào mừng Ngày Hội Pháp ngữ 2022.

Dự buổi lễ, về phía Tổ chức Đại học Pháp ngữ AUF có ngài Ciril Michelet - Phó Giám đốc phụ trách Hành chính của AUF.

Về phía Trường Đại học Kiến trúc Hà Nội có PGS.TS.KTS. Lê Quân - Hiệu trưởng Nhà trường; TS.KTS.Nguyễn Thái Huyền - Phó Viện trưởng Viện Đào tạo và Hợp tác quốc tế cùng đại diện lãnh đạo các Khoa có sinh viên tham dự cuộc thi Tổ Kén - Xưởng sáng tạo.

Cuộc thi Tổ Kén - Xưởng sáng tạo là một cuộc thi thiết kế không gian học tập dưới hình thức một xưởng học mùa hè (Workshop d'été/Summer workshop) do Tổ chức Đại học Pháp ngữ AUF tài trợ. Mục tiêu của cuộc thi là tạo ra một không gian đặc biệt dành cho các sinh viên Kiến trúc, nơi diễn ra không chỉ các hoạt động học tập chuyên ngành mà còn có những chương trình mang tính kết nối cộng đồng sinh viên như hội họp, văn nghệ, diễn đàn. Đây là cơ hội để đẩy mạnh mối liên hệ giữa các sinh viên Việt Nam và sinh viên nước ngoài của Viện Đào tạo và Hợp tác quốc tế, từ đó xây dựng một mạng lưới sinh viên bền chặt, không chỉ trong học tập mà còn trong cuộc sống hàng ngày. Cuộc thi không chỉ dừng lại ở việc xây dựng ý tưởng, mà ý tưởng xuất sắc nhất sẽ được chọn lựa để đưa vào thi công thực tế.

Phát biểu khai mạc buổi lễ, PGS.TS.KTS. Lê Quân - Hiệu trưởng Trường Đại học Kiến trúc Hà Nội cho rằng: Với một không giản nhỏ nhưng sinh viên đã cố gắng xây dựng được các ý tưởng sáng tạo, tổ chức một không gian cho chính mình để tổ chức các sự kiện, lớp học cũng như không gian tổ chức các triển lãm, sinh hoạt của sinh viên… Sự hợp tác, chia sẻ của Tổ chức AUF cũng là một động lực tốt giúp cho sinh viên phát huy được sức sáng tạo, đặc biệt sinh viên Pháp ngữ của Nhà trường trong chương trình liên kết đào tạo giữa Trường Đại học Kiến trúc Hà Nội, Trường Đại học Kiến trúc Toulouse, Trường Đại học Kiến trúc cảnh quan Bordeaux và Trường Đại học Kiến trúc Normandie. Hiệu trưởng Lê Quân cũng bày tỏ sự vui mừng được đứng trong một không gian có sự thay đổi, một không khí rất trẻ trung, tươi trẻ và đầy sáng tạo của các em sinh viên.

GS. Ciril Michelet - Phó Giám đốc Tổ chức Đại học pháp ngữ AUF bày tỏ sự vui mừng khi đến tham dự buổi lễ khánh thành xưởng đồ án I 902 và cho biết đây là một phần của cuộc thi Le Cocoon.

Theo GS. Ciril Michelet, từ năm 2009, một khóa đào tạo kiến trúc và cảnh quan nói tiếng Pháp đã được thành lập trong Trường Đại học Kiến trúc Hà Nội. Khóa học này là kết quả của sự hợp tác giữa Nhà trường và 4 Trường Đại học Quốc gia Pháp về kiến trúc và cảnh quan (Trường Đại học Kiến trúc Toulouse, Trường Đại học Kiến trúc cảnh quan Bordeaux, Trường Đại học Kiến trúc Normandie và Trường Đại học Kiến trúc Grenoble). Đây là các Trường đã nhận được sự hỗ trợ lâu dài từ AUF.

Đại diện AUF cho biết AUF cũng muốn đóng góp vào việc đào tạo ra các Thạc sĩ Kiến trúc. Đây là một liên kết thiết yếu trong lĩnh vực nghiên cứu kiến trúc bằng tiếng Pháp. Kể từ năm 2021, AUF đã thực hiện chiến lược 5 năm 2021-2025. Nhiều cơ hội kêu gọi các dự án đang xuất hiện, và AUF hy vọng có thể liên kết Trường Đại học Kiến trúc Hà Nội với các đối tác hàng đầu của AUF…

Cũng tại lễ khánh thành xưởng đồ án, ban tổ chức cuộc thi đã trao giải thưởng cho các sinh viên đạt giải tại cuộc thi Tổ kén - Xưởng sáng tạo.

THỂ LỆ VIẾT VÀ GỬI BÀI CHO TẠP CHÍ KHOA HỌC KIẾN TRÚC – XÂY DỰNG

1. Bài gửi đăng tạp chí phải là công trình nghiên cứu của tác giả, chưa đăng và chưa gửi đăng ở bất kỳ tạp chí nào khác.
2. Bài gửi đăng bằng tiếng Việt hoặc tiếng Anh, được đánh máy tính, in trên 1 mặt giấy khổ A4 thành 2 bản (phông chữ Arial (Unicode), cỡ chữ 11; lề trên và lề dưới 3cm; lề phải và lề trái 3cm).
3. Các hình vẽ phải rõ ràng, chuẩn xác. Nếu bài có ảnh thì phải gửi kèm ảnh gốc độ phân giải 200dpi. Hình vẽ và ảnh phải được chú thích đầy đủ.
4. Các công thức và các thông số có liên quan phải được chế bản bằng phần mềm Mathtype (kể cả công thức hoặc các thành phần của công thức có trên các dòng văn bản).
5. Tài liệu tham khảo chính, trích dẫn phải có đủ các thông tin theo trình tự sau: Họ tên tác giả (hoặc chủ biên), tên sách (tên bài báo/tạp chí, tên báo cáo khoa học), nơi xuất bản, nhà xuất bản, năm xuất bản, trang trích dẫn (tối đa 10 tài liệu tham khảo chính).
6. Ghi rõ họ, tên, học hàm, học vị, nơi làm việc, số điện thoại, e-mail của tác giả kèm theo một file chứa nội dung bài báo.
7. Bài viết phải có tên bằng tiếng Việt và tiếng Anh, các từ khóa tìm kiếm. Mỗi bài cần kèm theo phần tóm tắt bằng tiếng Việt và tiếng Anh (cỡ chữ 10, tối đa là 150 từ) cung cấp những nội dung chính của bài viết.
8. Cấu trúc bài báo gồm các phần: dẫn nhập, nội dung khoa học và kết luận (viết thành mục riêng). Bài báo phải đưa ra được các kết quả nghiên cứu mới hoặc các ứng dụng mới hay phải nêu được hiện trạng, những hướng phát triển cơ bản của vấn đề được đề cập, khả năng nghiên cứu, phát triển và ứng dụng tại Việt Nam. Bài giới thiệu tổng quan không quá 10 trang; công trình nghiên cứu và triển khai ứng dụng không quá 8 trang.
9. Với bài thông tin khoa học, tin ngắn: Là các bài dịch tổng thuật, tổng quan về các vấn đề khoa học công nghệ xây dựng kiến trúc có tính thời sự.
10. Không trả lại bản thảo cho những bài không đăng./.